
Electronic Thesis and Dissertation Repository

9-5-2013 12:00 AM

Development of Nanostructured LiMPO₄ (M=Fe, Mn) as Cathodes for High Performance Lithium-Ion Batteries

Jinli Yang

The University of Western Ontario

Supervisor

Xueliang(Andy) Sun

The University of Western Ontario

Graduate Program in Mechanical and Materials Engineering

A thesis submitted in partial fulfillment of the requirements for the degree in Doctor of Philosophy

© Jinli Yang 2013

Follow this and additional works at: <https://ir.lib.uwo.ca/etd>

 Part of the [Nanoscience and Nanotechnology Commons](#)

Recommended Citation

Yang, Jinli, "Development of Nanostructured LiMPO₄ (M=Fe, Mn) as Cathodes for High Performance Lithium-Ion Batteries" (2013). *Electronic Thesis and Dissertation Repository*. 1597.

<https://ir.lib.uwo.ca/etd/1597>

This Dissertation/Thesis is brought to you for free and open access by Scholarship@Western. It has been accepted for inclusion in Electronic Thesis and Dissertation Repository by an authorized administrator of Scholarship@Western. For more information, please contact wlsadmin@uwo.ca.

DEVELOPMENT OF NANOSTRUCTURED LiMPO_4 (M=Fe, Mn) AS CATHODES
FOR HIGH PERFORMANCE LITHIUM-ION BATTERIES

(Thesis format: Integrated-Article)

by

Jinli Yang

Graduate Program in Mechanical and Materials Engineering

A thesis submitted in partial fulfillment
of the requirements for the degree of
Doctor of Philosophy

The School of Graduate and Postdoctoral Studies
The University of Western Ontario
London, Ontario, Canada

© Jinli Yang 2013

Abstract

Olivine LiFePO_4 has garnered the most interest because of its environmental benignity, high safety and theoretical capacity. However, the major limitation for LiFePO_4 is the intrinsically poor electronic conductivity and ionic conductivity. The sluggish kinetics for LiFePO_4 could be overcome by reducing the size, coating with conductive carbon, or doping with isovalent ions. The decrease of the size to nanoscale could shorten the diffusion time of Li ions in LiFePO_4 during intercalation/deintercalation process, but the nano-size active material usually accompanies with low tap density. Carbon coating and carbon addition could alleviate the poor electronic conductivity. However, simple or nonuniform carbon coating cannot obtain an ideal electrochemical performance due to the fact that the electrons could not reach some positions where Li ions charge/discharge takes place. The research in this thesis aims at developing high electrochemical performance of the LiFePO_4 composite.

In this research, we proposed as follows: (1) three dimensional (3D) porous LiFePO_4 in microscale. The porous strategy could allow efficient percolation of the electrolyte through the electrode, favoring the electrolyte access to active materials via the pores, then make full use of electrode material; (2) the nanosized LiFePO_4 anchors in the 3D conducting network. This could achieve fast electronic and ion conduction, leading to high performance of the composites.

Therefore, we first reported 3D porous LiFePO_4 with N-CNTs, CNTs and graphene fabricated by using sol-gel approach. The highly conductive and uniformly dispersed N-CNTs and graphene nanosheets incorporated into 3D interlaced porous LiFePO_4 , which could facilitate the electric and lithium ion diffusion rate, thus resulting in high performance of LiFePO_4 electrodes.

We also reported the nanosized and unfolded graphene modified LiFePO_4 composites. The LiFePO_4 nanoparticles anchored to 3D conducting unfolded graphene network resulted in almost theoretical capacity (171 mAh g^{-1}). One-dimensional LiFePO_4 @CNTs nanowires have been prepared, while 3D CNTs conducting network structure was also obtained simultaneously. The LiFePO_4 @CNTs nanowires can give excellent cycling stability and rate capability.

The effect of Mn concentration on the morphology of LiFePO_4 and the electrochemical performance have been investigated

In summary, the discoveries in this thesis contribute to a better understanding and design on LiFePO_4 candidate and provide novel hierarchical nanostructured materials as electrodes applied in LIBs as power sources for EVs or HEVs.

Keywords: LiFePO_4 , Olivine, Hierarchical structure, CNTs, N-CNTs, Graphene, Three dimensional conducting network, Core-shell, Nanowires, Lithium ion batteries

Co-Authorship Statement

1.

Title: Hierarchically Porous LiFePO_4 /Nitrogen-doped Carbon Nanotube Composite for Lithium Ion Batteries Cathodes

Authors: **Jinli Yang**, Jiajun Wang, Xifei Li, Doniniu Wang, Jian Liu, Guoxian Liang, Michel Gauthier, Yongliang Li, Ruying Li, Xueliang Sun

The final version of this manuscript has been published in *Journal of Materials Chemistry*, 2012, 22, 7537-7543.

Jinli Yang: carry out all the experiments; finish the initial draft and the followed modifications of the manuscript.

Dr. Xueliang Sun: the experiment was under the supervision of Dr. Xueliang Sun

Jiajun Wang: modification the manuscript and discussion of the experiment

Xifei Li: modification the manuscript and the discussion of the electrochemical testing

Dongniu Wang: modification the manuscript and discussion of the experiment

Jian Liu: provide N-CNTs

Guoxian Liang and Michel Gauthier: modification the manuscript, financial support

Ruying Li: characterization help and discussion

Yongliang Li: TGA testing

2.

Title: 3D Porous LiFePO_4 -graphene Hybrid Electrodes with Enhanced Performance for Li-ion Batteries.

Authors: **Jinli Yang**, Jiajun Wang, Doniniu Wang, Xifei Li, Dongsheng Geng, Guoxian Liang, Michel Gauthier, Ruying Li, Xueliang Sun

The final version of this manuscript has been published in *Journal of Power Sources*, 2012, 208, 340-344.

Jinli Yang: carry out all the experiments; finish the initial draft and the followed modifications of the manuscript.

Xueliang Sun: the experiment was under the supervision of Dr. Xueliang Sun

Jiajun Wang: modification the manuscript and discussion of the experiment

Dongniu Wang: modification the manuscript and discussion of the experiment

Xifei Li: modification the manuscript

Dongsheng Geng: provide graphene

Guoxian Liang and Michel Gauthier: modification the manuscript, financial support

Ruying Li: characterization help and discussion

3.

Title: $\text{LiFePO}_4/\text{graphene}$ as a Superior Cathode Material for Rechargeable Lithium Batteries: Impact of Stacked Graphene and Unfolded Graphene.

Authors: **Jinli Yang**, Jiajun Wang, Yongji Tang, Dongniu Wang, Xifei Li, Yuhai Hu, Ruying Li, Guoxian Liang, Tsun-Kong. Sham, Xueliang Sun

This work has been published in *Energy Environmental Science*, 2013, 6, 1521-1528.

Jinli Yang: carry out all the experiments; finish the initial draft and the followed modifications of the manuscript.

Xueliang Sun: the experiment was under the supervision of Dr. Xueliang Sun

Jiajun Wang: modification the manuscript and discussion of the experiment

Yongji Tang: modification the manuscript and synchrotron Fe K-edge characterization, Raman

Dongniu Wang: modification the manuscript and discussion of the experiment, synchrotron C K-edge characterization

Xifei Li: modification the manuscript

Yuhai Hu: provide graphene

Guoxian Liang: modification the manuscript, financial support

Ruying Li: TEM characterization and discussion

Tsun-Kong Sham: discussion of all synchrotron analysis, modification the manuscript

4.

Title: In-situ Self-catalyzed Formation of Core-shell $\text{LiFePO}_4\text{@CNTs}$ Nanowire for Ultra-high Rate Performance Lithium-ion Batteries.

Authors: **Jinli Yang**, Jiajun Wang, Yongji Tang, Dongniu Wang, Biwei Xiao, Xifei Li, Ruying Li, Guoxian Liang, Tsun-Kong Sham and Xueliang Sun

The final version of this manuscript has been published in *Journal of Materials Chemistry A*, 2013, 1, 7306-7311.

Jinli Yang: carry out all the experiments; finish the initial draft and the followed modifications of the manuscript.

Xueliang Sun: the experiment was under the supervision of Dr. Xueliang Sun

Jiajun Wang: modification the manuscript and discussion of the experiment

Yongji Tang: modification the manuscript and synchrotron Fe K-edge characterization, Raman

Dongniu Wang: modification the manuscript and discussion of the experiment, synchrotron C K-edge characterization

Biwei Xiao: TGA testing

Xifei Li: modification the manuscript

Guoxian Liang: modification the manuscript, financial support

Ruying Li: TEM characterization

Tsun-Kong Sham: discussion of all synchrotron analysis, modification the manuscript

5.

Title: Peapod-like $\text{LiFePO}_4\text{-C}$ nanowires synthesised by hydrothermal Route for Li-Ion Batteries

Authors: **Jinli Yang**, Dongniu Wang, Xifei Li, Ruying Li, Guoxian Liang, and Xueliang Sun

The final version of this manuscript is to be submitted for publishing.

Jinli Yang: carry out all the experiments; finish the initial draft and the followed modifications of the manuscript.

Xueliang Sun: the experiment was under the supervision of Dr. Xueliang Sun

Dongniu Wang: modification the manuscript and discussion of the experiment,

Xifei Li: modification the manuscript

Guoxian Liang: modification the manuscript, financial support

Ruying Li: TEM characterization

6.

Title: Binary olivine $\text{LiFe}_x\text{Mn}_{1-x}\text{PO}_4/\text{C}$ ($x=0.3, 0.5$ and 0.7) solid solution as cathode materials for lithium ion batteries.

Authors: **Jinli Yang**, Dongniu Wang, Xifei Li, Yongji Tang, Biwei Xiao, Guoxian Liang, Ruying Li, Tsun-Kong Sham, Xueliang Sun

The final version of this manuscript is to be submitted for publishing.

Jinli Yang: carry out all the experiments; finish the initial draft and the followed modifications of the manuscript.

Xueliang Sun: the experiment was under the supervision of Dr. Xueliang Sun

Dongniu Wang: modification the manuscript and discussion of the experiment, synchrotron characterization

Xifei Li: modification the manuscript

Yongji Tang: modification the manuscript

Biwei Xiao: TGA testing

Guoxian Liang: modification the manuscript, financial support

Ruying Li: TEM characterization

Tsun-Kong Sham: discussion of all synchrotron analysis, modification the manuscript

7.

Title: High-Performance Carbon- LiMnPO_4 Nanocomposite as Cathode for Lithium Ion Batteries

Authors: **Jinli Yang**, Dongniu Wang, Xifei Li, Guoxian Liang, Ruying Li, Tsun-Kong Sham, Xueliang Sun

The final version of this manuscript is to be submitted for publishing.

Jinli Yang: carry out all the experiments; finish the initial draft and the followed modifications of the manuscript.

Dr. Xueliang Sun: the experiment was under the supervision of Dr. Xueliang Sun

Dongniu Wang: modification the manuscript and discussion of the experiment

Xifei Li: modification the manuscript

Guoxian Liang: modification the manuscript, financial support

Ruying Li: characterization

Tsun-Kong Sham: discussion of all synchrotron analysis, modification the manuscript

To my dear husband: Dongniu Wang

An honest Man, a responsible comrade, and a steadfast lover

*Your strong support and love give me a lot of encouragement in this
reaserch road.*

By this thesis

To gave us a memory in our youth.....

Acknowledgments

This thesis is the summary of my Ph.D. work. It was carried out in Dr. Sun's Nanomaterials and Energy group at Western University, Canada. Here, I would like to express my thanks to all the guys who accompany with me in these years.

First, I would like to express my deep gratitude to my supervisor, Dr. Xueliang (Andy) Sun, who is the Canada Research Chair in Development of Nanomaterials for Clean Energy and a professor in Department of Mechanical & Materials Engineering at Western. I really appreciate that he provides me an opportunity to study in his group. Dr. Sun is kind, knowledgeable, patient and passionate. In this four years, with his extensive and comprehensive help, I know how to get ideas, how to design experiment and how to efficiently characterize samples and how to finish papers. In a word, he is a role model for me in my future career.

I also appreciate the help of Dr. Tsun-Kong Sham, a very nice professor. He is the God father of Canadian Light Sources (CLS) and a professor in Department of Chemistry in Western. In 2008, we met each other in Harbin Institute of Technology (HIT), the school where I pursued my bachelor and master degree. At that time, he gave me a new insight to the scientific research. Dr. Sham gave me a lot of help on synchrotron analysis. His patience and sense of humor encourage me a lot in these years. My family members will cherish his kindness and support.

I am very grateful to Mrs. Ruying (Kathy) Li, Dr. Sun's wife and a research engineer in the group. She trained me a lot of skills on characterizing techniques. Mrs. Li is a very hard-working lady. She not only supported my experiments in my thesis work, but also provided assistance on my life. Her kindness and generosity warm me a lot in heart in these years.

I would like to sincerely thank my advisory committee members: Dr. Jun Yang and Dr. Liying Jiang-two professors in MME in western. They provided very valuable advices to my studies in every stage. Also, particularly I would also like to thank my examiners of my thesis defense Dr. Jeff Wood, Dr. Liying Jiang, Dr Chunbao Xu (Western University) and

Dr. Steen Schougaard (Université du Québec à Montréal) for their careful examination, insightful suggestions and comments.

I deeply appreciate Dr. Guoxian Liang, director in Clariant Inc. (former Phostech Lithium Inc.), for his four years strong support. I have been working on a project collaborated with Clariant company. I would like to thank Dr. Liang for his valuable suggestions on my papers and financial support.

I would like to express my acknowledgement to Dr. Henry Huang and Dr. Quanming Yang, who worked in Springpower International Company. They guided me to set up cells and also the preparation of the electrodes. Due to their preliminary support, I could extend my further study in this thesis.

Many thanks to all my group members in Dr. Sun's group, Dr. Yong Zhang, Dr. Jiajun Wang, Dr. Liang Li, Dr. Gaixia Zhang, Dr. Shuhui Sun, Dr. Xifei Li, Dr. Dongsheng Geng, Dr. Xiangbo (Henry) Meng, Dr. Mihnea Ioan Ionescu, Dr. Yu Zhong, Dr. Mohammad Norouzi Banis, Dongniu Wang, Harmid Norouzi Banis, Yongliang Li, Jian Liu, Biwei Xiao, Biqiong Wang, Xia Li, Andrew Lushington, and Dr. HosseinYadegari. It was so much pleasure to work with so many nice people. Without your collaboration and generous help, my project could not have been done so smoothly. I wish all of them good luck in the future.

Also, I would like to thank the help from Mr. Fred Pearson and Ms. Carmen at McMaster University for their help of HRTEM.

Specially, I would like to express my love to parents and parents-in-law. They always give me strong support, encouragement and whole understanding. I would also like to thank my brothers, brothers-in-law, sisters and sisters-in-law, who gave me a lot of support and happiness in my life.

Here, I would like to say some words to my be-loved husband, Dongniu Wang, a very charming guy. He is an honest, responsible and intelligent person. He is so supportive and caring for me when I am feeling down. In these years, He always accompanies with me, even when I am willful and making trouble. When I was tired, he gave me a shoulder to lean on. He is the big gift god gave me. I will cherish and spend my life with him together. I would

also like to say “thanks” to my lovely Leo and Eva, two cute bears, who provide me a lot of happiness.

Jinli Yang

CMLP 1325, Western University

London, ON, Canada

June, 2013

Table of Contents

Abstract	ii
Co-Authorship Statement.....	iv
Acknowledgments.....	xi
Table of Contents	xiv
List of Tables	xx
List of Figures	xxi
List of Appendices	xxvi
List of Abbreviations	xxvii
Chapter 1	1
1 Introduction.....	1
1.1 Introduction to lithium-ion batteries	1
1.1.1 Fundamental of lithium-ion batteries.....	1
1.1.2 Development and challenges of cathode materials.....	5
1.1.3 Solutions to address the limitations	10
1.2 Thesis objectives.....	14
1.3 Thesis organization	16
1.4 References.....	18
Chapter 2.....	25
2 Experimental, Characterization Techniques and Electrochemical Measurements	25
2.1 Experimental.....	25
2.1.1 Synthesis of N-CNTs via chemical vapor deposition (CVD) method.....	25
2.1.2 Synthesis of graphene via chemical method.....	26
2.1.3 Synthesis of hierarchical porous LiFePO ₄ /Nitrogen-doped carbon nanotube composite via sol-gel route	26

2.1.4	Synthesis of hierarchical LiFePO ₄ -graphene hybrid electrodes by sol-gel method.....	28
2.1.5	Synthesis of stacked graphene and unfolded graphene modified LiFePO ₄ via sol-gel route.....	29
2.1.6	Synthesis of one-dimensional core-shell LiFePO ₄ @CNTs nanowires via sol-gel method.....	29
2.1.7	Synthesis of peapod like LiFePO ₄ /C nanowires via hydrothermal method	30
2.1.8	Synthesis of LiMnPO ₄ /C nanocomposites via ball-milling and CVD route	31
2.2	Characterizations.....	32
2.2.1	Physical characterizations (SEM, TEM, XRD, EDX, BET, RAMAN, Synchrotron)	32
2.2.2	Electrochemical characterization	35
2.3	References.....	37
Chapter 3	38
3	Hierarchically Porous LiFePO ₄ /Nitrogen-doped Carbon nanotube Composite for Lithium Ion Batteries Cathodes	38
3.1	Introduction.....	39
3.2	Experimental	40
3.2.1	Synthesis of porous LiFePO ₄ /Nitrogen-doped carbon nanotube composite and LiFePO ₄ / carbon nanotube composite.....	40
3.2.2	Physical characterization	41
3.2.3	Electrochemical characterizations	41
3.3	Results and discussion	42
3.4	Conclusions.....	52
3.5	Acknowledgements.....	52
3.6	Supporting Information.....	53
3.7	Reference	55

Chapter 4.....	58
4 3D Porous LiFePO ₄ /Graphene Hybrid Electrodes with Enhanced Performance for Li-ion Batteries	58
4.1 Introduction.....	59
4.2 Experimental	60
4.2.1 The procedures of materials synthesis	60
4.2.2 Physical characterization	60
4.2.3 Electrochemical measurements.....	61
4.3 Results and discussion	61
4.4 Conclusions.....	67
4.5 Acknowledgments.....	67
4.6 Supporting Information.....	68
4.7 References	69
Chapter 5.....	71
5 Stacked Graphene and Unfolded Graphene Impact on Morphology of LiFePO ₄ as Superior Cathode Material for Rechargeable Lithium Batteries.....	71
5.1 Introduction.....	73
5.2 Experimental	75
5.2.1 Preparation of LiFePO ₄ /Stacked graphene and LiFePO ₄ /unfolded graphene composites.....	75
5.2.2 Physical Characterization.....	76
5.2.3 Electrochemical measurements.....	76
5.3 Results and Discussion	76
5.4 Conclusions.....	88
5.5 Acknowledgements.....	89
5.6 Supporting Information.....	90
5.7 References.....	92

Chapter 6.....	96
6 In-situ Self-catalyzed Formation of Core-shell LiFePO ₄ @CNTs Nanowire for High Rate Performance Lithium-ion Batteries	96
6.1 Introduction.....	97
6.2 Experimental part.....	98
6.2.1 Synthesis of LFP@CNTs nanowire composites	98
6.2.2 Physical Characterization.....	98
6.2.3 Electrochemical Measurements	99
6.3 Results and discussion	99
6.4 Conclusions.....	108
6.5 Acknowledgements.....	108
6.6 Supporting Information.....	109
6.7 References	113
Chapter 7.....	116
7 Peapod-like LiFePO ₄ -C Nanowires Synthesised by Hydrothermal Route for Li-Ion Batteries.....	116
7.1 Introduction.....	117
7.2 Experimental	119
7.2.1 Synthesis of pea-pod like LiFePO ₄ nanowire	119
7.2.2 Physical characterization	119
7.2.3 Electrochemical Measurements	120
7.3 Results and discussion	120
7.4 Conclusions.....	125
7.5 Acknowledgements.....	126
7.6 Supporting information.....	126
7.7 References	127
Chapter 8.....	130

8	Binary Olivine $\text{LiFe}_x\text{Mn}_{1-x}\text{PO}_4/\text{C}$ ($x=0.3, 0.5$ and 0.7) Solid Solution as Cathode Materials for Lithium-ion Batteries	130
8.1	Introduction.....	131
8.2	Experimental	132
8.2.1	Preparation of $\text{LiFe}_x\text{Mn}_{1-x}\text{PO}_4/\text{C}$ ($x=0.3, 0.5$ and 0.7) series.....	132
8.2.2	Physical characterization	133
8.2.3	Electrochemical Characterization	133
8.3	Results and discussion	133
8.4	Conclusion	144
8.5	Acknowledgements.....	144
8.6	Supporting information.....	145
8.7	References.....	147
	Chapter 9.....	151
9	High-Performance Carbon- LiMnPO_4 Nanocomposite as Cathode for Lithium Ion Batteries.....	151
9.1	Introduction.....	152
9.2	Experimental	154
9.2.1	Synthesis of LiMnPO_4/C nanoparticles	154
9.2.2	Physical characterization	154
9.2.3	Electrochemical measurements.....	154
9.3	Results and discussions.....	155
9.4	Conclusion	159
9.5	Acknowledgement	160
9.6	References.....	160
	Chapter 10.....	163
10	Conclusions and Future Perspectives.....	163
10.1	Conclusions.....	163

10.2Future perspectives	166
Appendices.....	168
Curriculum Vitae	173

List of Tables

Table 1.1 The space group and lattice parameters of LiFePO_4 and FePO_4 [37].....	9
-----------------------------------------------------------------------------------------------------	---

List of Figures

Figure 1.1 Comparison of the different battery technologies in terms of volumetric and gravimetric energy density [10].	2
Figure 1.2 Schematic of the working mechanism for a lithium-ion battery [12].	3
Figure 1.3 Electrode materials for rechargeable lithium ion batteries in the view of potential and capacity [13].	4
Figure 1.4 Crystal structures of various cathode materials (red-O, blue-Li, green-Co for LiCoO_2 ; red-O, green-Mn, purple-Li for LiMn_2O_4) [34].	6
Figure 1.5 Olivine structure of LiFePO_4 [35].	7
Figure 1.6 Structure of lithiation and delithiation phase of LiFePO_4 (blue-Li, green- PO_4 , red- FeO_6) [36].	8
Figure 1.7 Structure of LiFePO_4 depicting the curved trajectory of Li ions [42].	10
Figure 1.8 (a) Electron-transfer pathway for LiFePO_4 particles partially coated with carbon. (b) Designed ideal structure for LiFePO_4 particles with typical nano-size and a complete carbon coating. (c) Preparation process for the C/ LiFePO_4 composite [56].	11
Figure 1.9 Structure of the olivine LiMnPO_4 with Pnma space group [82].	13
Figure 2.1 Schematic illustration of ultrasonic spray pyrolysis [1].	25
Figure 2.2 Experimental setup of sol-gel process.	27
Figure 2.3 Images of the obtained composites and the schematics.	28
Figure 2.4 Synthesis procedures for the pristine and graphene modified LiFePO_4 .	29
Figure 2.5 Schematics to illustrate the synthetic procedure of the LFP@CNTs nanocomposites.	30

Figure 2.6 Hydrothermal oven set up (Thermo).	31
Figure 2.7 Ball milling set up (Retsch, PM 200) used in this system.....	32
Figure 2.8 Image of SEM (Hitachi S-4800) device.	33
Figure 2.9 Image of TEM equipment (H-7000, Hitachi).....	34
Figure 2.10 Image of Raman facility (HORIBA Scientific LabRAM HR).....	34
Figure 2.11 Image of glove box.....	35
Figure 2.12 Image of the working station for the battery testing (Arbin, BT2000).	36
Figure 3.1 SEM and TEM images of CNTs (a, b and e) and N-CNTs (c, d and f).	43
Figure 3.2 EDX elemental mappings (a, b and c) and Raman spectra (d) for N-CNTs.	44
Figure 3.3 Powder X-ray diffraction patterns for porous LiFePO_4 and LiFePO_4 composite. * represents the impurity phase.....	45
Figure 3.4 SEM images of (a, b) porous LiFePO_4 ; (c, d) $\text{LiFePO}_4/\text{CNTs}$ composite; (e, f) $\text{LiFePO}_4/\text{N-CNTs}$ composite.	46
Figure 3.5 Raman spectra and TGA curves of the as synthesized porous LiFePO_4 and LiFePO_4 composites.....	47
Figure 3.6 (a) Charge-discharge profiles of porous LiFePO_4 , $\text{LiFePO}_4/\text{CNTs}$ and $\text{LiFePO}_4/\text{N-}$ CNTs cycled at a current rate of 17 mA g^{-1} ; (b) Discharge capacities during continuous cycling of lithium ion batteries at 17 mA g^{-1} ; (c) rate performance; (d) cycle performance of $\text{LiFePO}_4/\text{CNTs}$ and $\text{LiFePO}_4/\text{N-CNTs}$ cycled at a current rate of 850 mA g^{-1}	49
Figure 4.1 TEM image of (a) Graphene; SEM images of (b) Graphene, (c) and (d) Porous LiFePO_4 at different magnifications, (e) and (f) $\text{LiFePO}_4/\text{graphene}$ composite at different magnifications.....	63
Figure 4.2 Powder X-ray diffraction (XRD) pattern (a), Raman spectra (b) and TGA curve of the inset of (b): porous LiFePO_4 and $\text{LiFePO}_4\text{-Graphene}$ composite.	64

Figure 4.3 (a) Cyclic voltammograms (0.1 mV s^{-1}); (b) Charge-discharge profiles of porous LiFePO_4 , $\text{LiFePO}_4/\text{graphene}$ cycled at a current rate of 17 mA g^{-1} ; (c) Discharge capacities during continuous cycling of lithium cells at 17 mA g^{-1} ; (d) rate performance.	65
Figure 5.1 (a) SEM image and (b) TEM image of stacked graphene, (c) and (d) TEM images of unfolded graphene.	77
Figure 5.2 SEM images of (a) $\text{LiFePO}_4/\text{stacked graphene}$ composites and (b) $\text{LiFePO}_4/\text{unfolded graphene}$ composites; (c) TEM image of $\text{LiFePO}_4/\text{unfolded graphene}$ composites. (Inset showing selected area electron diffraction (SAED) pattern of unfolded graphene (circle area)); (d) High-resolution TEM image and SAED pattern (inset) of an individual LiFePO_4 nanoparticle on unfolded graphene (boxed area in (c)); (e) XRD spectrum of the $\text{LiFePO}_4/\text{unfolded graphene}$ and $\text{LiFePO}_4/\text{stacked graphene}$ composites; (f) Electron-transfer pathway for the $\text{LiFePO}_4/\text{stacked graphene}$ and $\text{LiFePO}_4/\text{unfolded graphene}$ compistes.....	79
Figure 5.3 SEM and TEM (inset) images of $\text{LiFePO}_4/\text{unfolded graphene}$ nanocomposite obtained with different annealing time: (a) 2 h. (b) 6 h. (c) 12 h. (d) 24 h; (e) Schematic image of LiFePO_4 growth on the unfolded graphene.	82
Figure 5.4 XRD patterns (a), Raman spectra (b), normalized absorption of Fe K-edge (c) and C K-edge (d) XANEs spectra for $\text{LiFePO}_4/\text{unfolded graphene}$ composites annealed at 700°C for various time.	84
Figure 5.5 (a) Cyclic voltammograms (0.1 mV s^{-1}); (b) charge-discharge curves at different cycle number for LFP/UG-12 and LFP/SG at a current rate of 17 mA g^{-1} ; (c) cycling profile tested at a current density of 17 mA g^{-1} between 2.5 and 4.2 V for LFP/UG and LFP/SG; (d) rate performance for LFP/UG-12.....	86
Figure 6.1 (a) and (b) SEM image of the as-prepared needle-like LFP@CNTs; (c) TEM image of the fabricated core-shell nanowire, and (d) the corresponding HRTEM image LFP@CNTs nanowire; (e) EDX Line scanning of LFP@CNTs core-shell nanowire, HRTEM image of single LFP@CNTs nanowire (inset); (f) Schematic illustration of the LFP@CNT core-shell Nanowire.....	102

Figure 6.2 TEM images of LFP@CNTs composites annealed for different time: (a) 5 h. (b) 10 h. (c) 20 h. (d) schematics of the morphology evolution.	104
Figure 6.3 XRD patterns (a) and TGA curves (b) of LFP@CNTs composites; normalized XANES spectra for LFP@CNTs composites: (c) Fe K edge; (d) C K edge.	106
Figure 6.4 (a) Cyclic voltammetry (CV) profiles for LFP@CNTs-10 at a scan rate of 0.1 mV s ⁻¹ ; (b) Galvanostatic cycle charge-discharge profiles in voltage range of 2.5-4.2 V at 0.2 C; (c) Cyclic performance at 0.2 C prepared at different annealing time and (d) Rate capabilities of LFP@CNTs-10 nanocomposites.	107
Figure 7.1 SEM images of LiFePO ₄ nanowires precursor, inset indicates low magnification graph.	121
Figure 7.2 SEM (a) and TEM (b) images of core-shell LiFePO ₄ /carbon nanowires annealed at 700 °C, inset shows the low magnification SEM image.	122
Figure 7.3 The morphology evolution of the of LiFePO ₄ precursor nanowires in function of hydrothermal reaction time.	123
Figure 7.4 XRD patterns of the as-obtained LiFePO ₄ /carbon nanowire and its precursor... ..	124
Figure 7.5 Cycle performances of the LiFePO ₄ /C nanowire and PPy modified composites.	125
Figure 8.1 XRD spectrum of the LiFe _x Mn _{1-x} PO ₄ /C composites. (Inset showing magnified XRD patterns in the range between 40° and 42°).	134
Figure 8.2 SEM images of the obtained LiFe _x Mn _{1-x} PO ₄ /C composites: (a), (b) x=0.3; (c), (d) x=0.5; (e), (f) x=0.7.	135
Figure 8.3 Micrographs of LiFe _{0.5} Mn _{0.5} PO ₄ /C composites: (a, b) TEM images; (c) High-resolution TEM image and (d) SAED pattern (circle area in (b)).	136
Figure 8.4 SEM images of obtained LiFe _{0.5} Mn _{0.5} PO ₄ /C with different annealing time. (a, b) 3 h; (c, d) 10 h.	138

Figure 8.5 XANES spectrum (transmission) of (a) Fe K edge and (b) Mn K edge spectra of $\text{LiFe}_{1-x}\text{Mn}_x\text{PO}_4$ solid solutions; FT magnitudes of (c) Fe K edge and (d) Mn K edge k^3 -weighted EXAFS spectra of $\text{LiFe}_{1-x}\text{Mn}_x\text{PO}_4$ solid solutions.....	139
Figure 8.6 (a) Cyclic voltammograms (0.1 mV s^{-1}) and (b) charge-discharge curves at different cycle number for $\text{LiFe}_x\text{Mn}_{1-x}\text{PO}_4/\text{C}$ ($x=0.3, 0.5$ and 0.7) at a current rate of 17 mA g^{-1}	142
Figure 8.7(a) Cycling profile tested at a current density of 17 mA g^{-1} between 2.2 and 4.5 V for $\text{LiFe}_x\text{Mn}_{1-x}\text{PO}_4/\text{C}$ ($x=0.3, 0.5$ and 0.7) composites; (d) rate performance for $\text{LiFe}_{0.5}\text{Mn}_{0.5}\text{PO}_4/\text{C}$	143
Figure 9.1 SEM images (a) and (b) of the $\text{Mn}_2\text{P}_2\text{O}_7/\text{C}$ with different magnifications.	155
Figure 9.2 SEM images (a) and (b) of the LiMnPO_4/C after annealed at 700°C	156
Figure 9.3 X-ray diffraction (XRD) patterns for the obtained products in both steps.....	157
Figure 9.4 The first two charge-discharge curves of LiMnPO_4/C nanocomposites at a rate of $1/20 \text{ C}$ at room temperature.	158
Figure 9.5 The cycle performance of the LiMnPO_4/C nanocomposites at a rate of $1/20 \text{ C}$ at room temperature. (top:charge curve; bottom: discharge curve).....	159

List of Appendices

Appendix I: PERMISSION FROM ROYAL SOCIETY OF CHEMISTRY (RSC) FOR PUBLISHED ARTICLE.....	169
Appendix II: PERMISSION FROM ELSEVIER FOR PUBLISHED ARTICLE	170
Appendix III: PERMISSION FROM ROYAL SOCIETY OF CHEMISTRY (RSC) FOR PUBLISHED ARTICLE.....	171
Appendix IV: PERMISSION FROM ROYAL SOCIETY OF CHEMISTRY (RSC) FOR PUBLISHED ARTICLE.....	172

List of Abbreviations

A

ALD atomic layer deposition

C

CLS Canadian light source

CNTs carbon nanotubes

CVD chemical vapor deposition

D

DMC dimethyl carbonate

E

EDX energy disperse X-ray spectroscopy

EVs electrical vehicles

EC ethylene carbonate

EXAFS extended X-Ray absorption fine structure

F

FESEM field emission scanning electron microscope

G

GNS graphene nanosheets

H

HEVs hybrid electrical vehicles

HRTEM high resolution transmission electron microscopy

L

LFP LiFePO_4

LIB lithium ion batteries

LMP LiMnPO_4

M

MWCNTS multiwalled carbon nanotubes

N

N-CNTs nitrogen-doped carbon nanotubes

NWs nanowires

NMP N-methylpyrrolidinone

O

1D one dimensional

S

SAED selected area electron diffraction

SEM scanning electron microscopy

SG stacked graphene

SGM spherical grating monochromator

SXRM soft X-ray microcharacterization

T

3D	three dimensional
TGA	thermogravimetric analysis
TEM	transmission electron microscope
2D	two dimensional
U	
UG	unfolded graphene
X	
XANES	X-ray absorption near edge structure
XAS	X-ray absorption spectroscopy
XRD	X-ray diffraction
XPS	X-ray photoelectron spectrometer

Chapter 1

1 Introduction

1.1 Introduction to lithium-ion batteries

1.1.1 Fundamental of lithium-ion batteries

It is now widely recognized that gaseous emissions from the burning of fossil fuels and biomass are polluting the air of large. Moreover, the rise of population and sophistication of modern society increase the dependence on the fossil fuels, and the depletion of the oil resources around the world which creates national vulnerabilities. From this point of view, the development of clean alternative energy sources is becoming an urgent need [1]. The most available alternative energy sources are solar radiation, wind and waves energy. In real application, all these alternative energy sources have been preferably converted to direct current (DC) electricity, and then transmitted for storage. The most commonly utilized energy carriers include electricity grid, electromagnetic waves, and chemical energy, where portable chemical energy is regarded as the most convenient form of energy storage; meanwhile, the converted electrical energy is well-matched with the storage system in battery [2-3].

All batteries consist of two electrodes (cathode and anode), which are separated by an ionically conductive electrolyte but an electronic insulator. Once the electrodes are connected by means of an external device, the chemical reactions will occur due to the different chemical potentials of the electrodes. However, the first generation of batteries is hard to be applied as real energy storage system. Since the introduction of the secondary (or rechargeable) batteries, the storage of the chemical energy could be realized by the charge current. In secondary or rechargeable batteries, a larger voltage applied in the opposite direction can cause the battery to recharge [4].

During the nineteenth and early twentieth centuries, the typical secondary batteries systems proposed by different electrochemical couples of Zn–MnO₂, lead–acid and Ni–Cd are commercialized [5]. Nevertheless, the consumption of the electrolyte in these batteries systems are inevitable, hence adversely affects the shelf life of these batteries.

Therefore, low-cost, high safety, rechargeable (secondary) batteries of high energy density and power density are pursued.

The energy density (electrical energy per unit of mass or unit of volume) is a function of the cell's voltage and capacity, which are determined by the intrinsic chemistry of the system. While the power density (the amount of power per unit of mass or unit of volume) is mainly relied on the chemicals the battery contains. In this case, the storage capability of a battery can be enhanced by the following ways: (1) high working voltage value from a large chemical potential difference between anodes and cathodes; (2) light weight (or small volume) of the reactants per exchanged electron while as small as possible; and (3) high reversibility of electrochemical reactions at both electrodes to maintain the batteries life as long as possible [5].

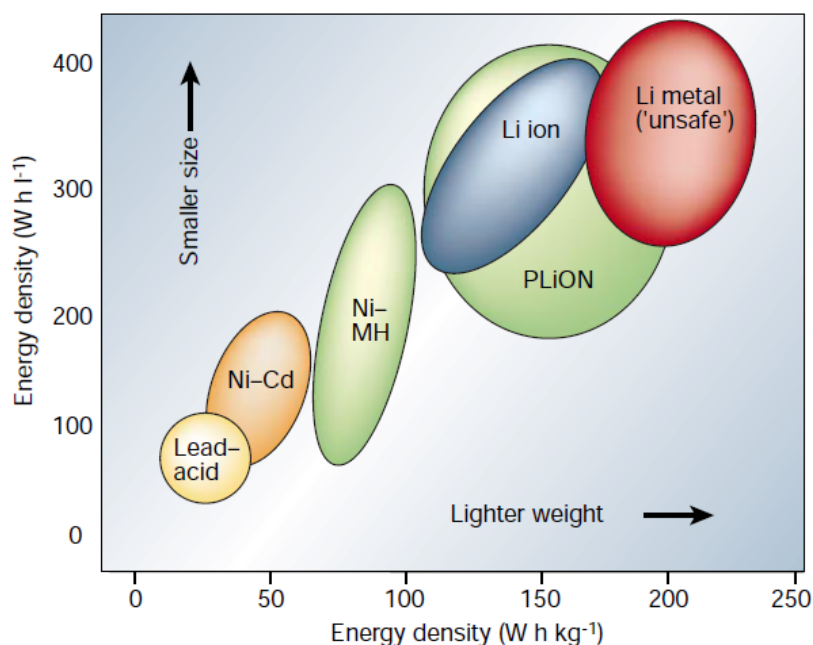


Figure 1.1 Comparison of the different battery technologies in terms of volumetric and gravimetric energy density [10].

Due to that Li is the most electropositive (-3.04 V versus standard hydrogen electrode) and as well as the lightest (equivalent weight $M=6.94$ g mol $^{-1}$, and specific gravity $\rho=0.53$ g cm $^{-3}$) metal, it was first introduced in the market with the assembly of primary

Li cells in the 1970s [6]. It soon encountered the drawback of this system, where dendritic Li metal growth during each subsequent discharge–recharge cycle, which led to explosion hazards. To circumvent the safety issues arising from the usage of Li metal, substituting Li metal for metallic Li as a second insertion material was raised by Murphy et al. [7] and Scrosati et al. [8] in end of the 1980s and early 1990s. Finally, the highly reversible, low voltage of Li-ion batteries (LiCoO₂/C) was commercialized by Sony Corporation in June 1991, with an energy density around 180 Wh kg⁻¹, which has a factor of 5 higher than that stored by the lead–acid batteries [9]. Compared with other batteries based system, rechargeable lithium batteries possess the highest energy density [10], as shown in Figure 1.1. Therefore, Li ion based batteries currently outperform other battery systems, accounting for 63% of worldwide sales values in portable batteries [11].

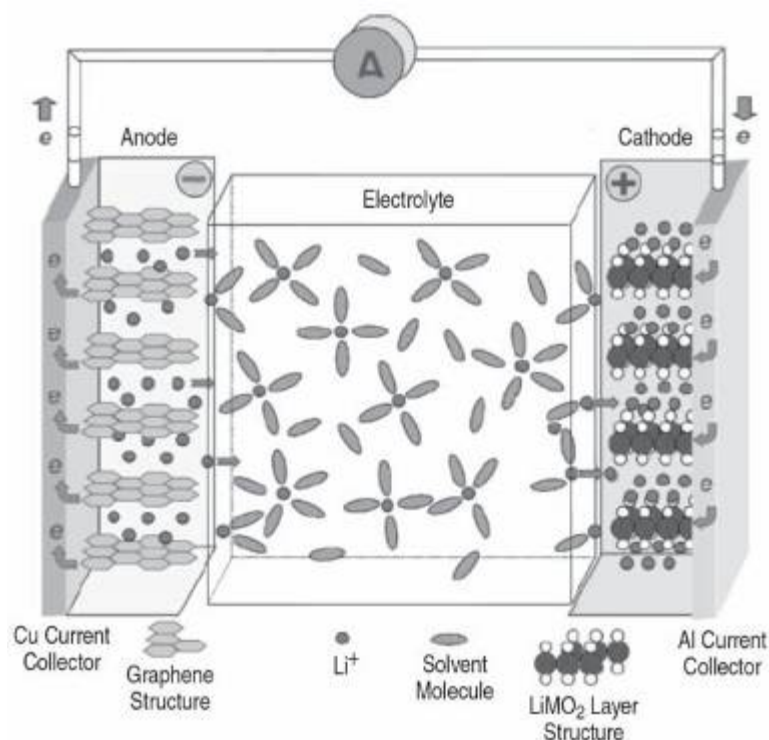


Figure 1.2 Schematic of the working mechanism for a lithium-ion battery [12].

The schematic of the working mechanism for a lithium-ion battery is illustrated in Figure 1.2. A combination of a negative lithium intercalation material (anode) with lithium intercalation material (cathode) having a more positive redox potential produces a Li-ion

transfer cell. Upon charging, lithium ions are released by the cathode (LiMO_2) and intercalated at the anode (graphite). When the cell is discharged, lithium ions are extracted by the anode and inserted into the cathode [12], which can be dictated in the following process:



Since the reaction is reversible, evaluation of its performance (cell potential, capacity or energy density) is related to the intrinsic properties of the positive and negative electrodes.

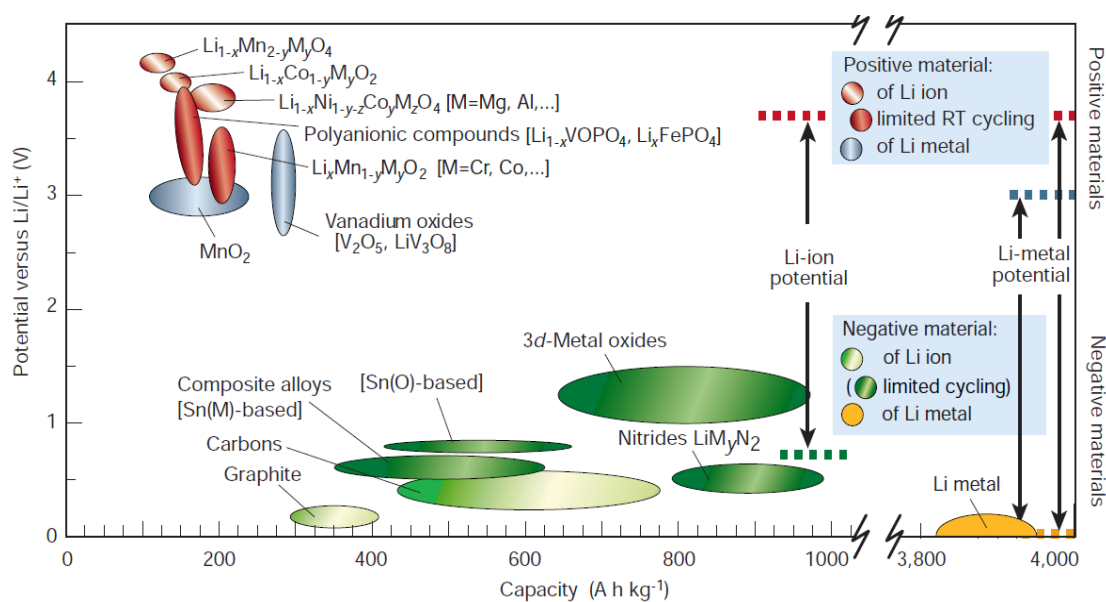


Figure 1.3 Electrode materials for rechargeable lithium ion batteries in the view of potential and capacity [13].

Retracing almost 40 years of the development of the rechargeable lithium ion battery, the suitable electrode materials for rechargeable lithium ion batteries are listed in Figure 1.3 [13]. For negative electrodes, graphite displays a practical value of 350 mA h g^{-1} (372 mA h g^{-1} for the LiC_6) [14]. The use of tin alloys as carbon alternatives will give larger capacities but accompany with larger volume change during the cycling. A reduction of the alloy size could tolerant the stress cracking in some extent [15]. Furthermore, applying a ‘buffer matrix’ could also compensate the expansion of the metallic alloys [16]. For rechargeable lithium ion batteries, since negative electrode is empty of Li, the

positive material requires air-stable Li-based compounds to function as Li sources, thus facilitating the cells assembly.

Lithium ion batteries have been widely used as power sources for consumer portable electronic devices in the past decades, and are considered for the transportation technology in the near future. The challenges facing the development of lithium ion batteries for electric vehicles (EVs) or hybrid electric vehicles (HEVs) are cost, safety, cell energy density (voltage \times capacity), rate capability, and shelf life [17]. Long shelf life requires avoiding of unwanted chemical reactions between the electrodes and the electrolyte and the retention of the electronic contact between the active materials and the current collector over many charge/discharge cycles, which requires the volume change versus state of charge that can be tolerated in an electrode unless the active materials are tethered to a current collector [1, 18, 19].

In addition, as the presence of both combustible material and an oxidizing agent, a risk of run-away reactions will result in fires or explosions. Although problems of instability could not be inevitable in a safer electrolyte composition, accidents are mainly a result of cramming more active material in the same volume as well as of applying unstable active materials which release O₂ over several charge/discharge cycles, leading to explosions [5, 17, 20]. As a result, developing stable active materials are essential if lithium-ion batteries are to fulfill their potential in the automotive market.

1.1.2 Development and challenges of cathode materials

Among the components in lithium-ion batteries, positive electrode is devoted much efforts due to that it plays an important role on costs and circumventing safety issues [21]. Since the first work reported by J. B. Goodenough [22], LiCoO₂ has been widely used in small batteries for portable electronics with the working voltage around 4 V versus Li/Li⁺. Although the reversible delithiation of LiCoO₂ beyond 0.5 Li is feasible, its use in large size batteries has been limited for safety reasons (charge cut-off voltage is around 4.2 V) [23-25]. Layered LiNiO₂ displayed comparable specific capacity to that of LiCoO₂ [26]. Nevertheless, Li_{1-x}NiO₂ suffers from exothermic oxidation of the organic electrolyte (thermal runaway) and structural collapse during the delithiation process [27]. Another

investigation of the layered structured cathode is LiMnO_2 with $\text{Mn}^{4+}/\text{Mn}^{3+}$ redox couples, the structure undergoes layered to spinel structural transition upon cycling, while the Mn will dissolve in the electrolyte, leading to the capacity fading [28-30].

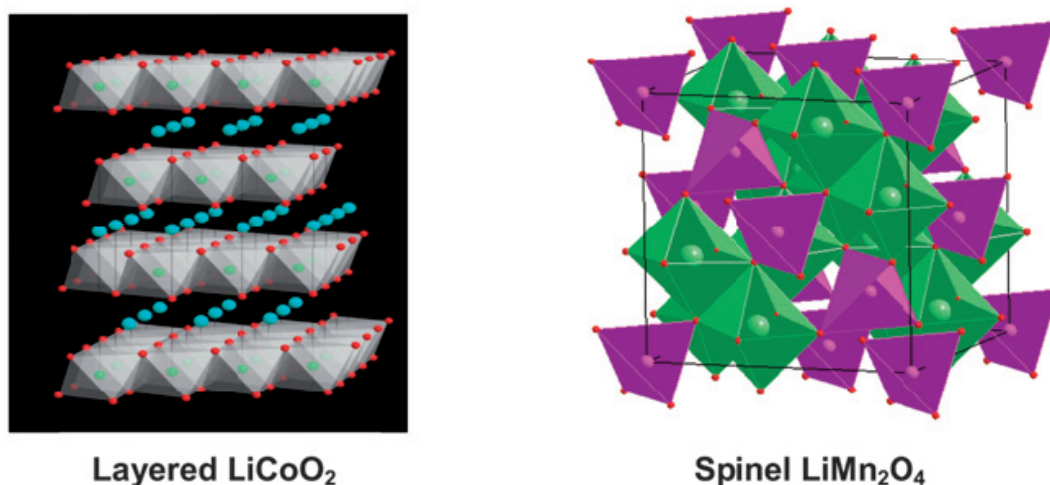


Figure 1.4 Crystal structures of various cathode materials (red-O, blue-Li, green-Co for LiCoO_2 ; red-O, green-Mn, purple-Li for LiMn_2O_4) [34].

The spinel LiMn_2O_4 with a strong edge-shared $[\text{Mn}_2]\text{O}_4$ octahedral framework has been recognized as a potential alternative cathode material for rechargeable lithium-ion batteries, although the specific capacity is less than LiCoO_2 , it possesses essential advantages of less toxicity and having an abundant materials source [31]. However, the disproportionation of Mn^{3+} occurs in presence of trace amounts of H^+ ions into Mn^{2+} and Mn^{4+} , resulting in a release of Mn^{2+} ions from the spinel lattice into the electrolyte, thus capacity fades upon cycling. Moreover, the reversible delithiation of Li is around 0.8 (4 V versus Li/Li^+), which limits the capacity to less than 120 mA h g^{-1} [32-34]. The structures of the LiMO_2 ($\text{M} = \text{Co}, \text{Ni}, \text{Mn}$) and LiMn_2O_4 are shown in Figure 1.4.

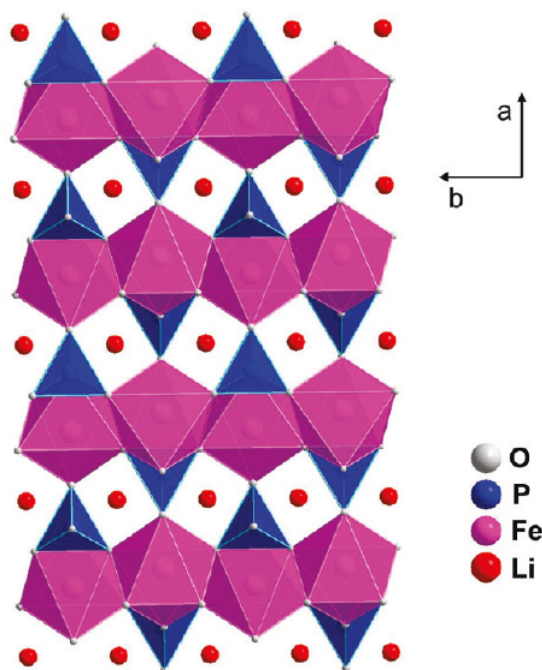


Figure 1.5 Olivine structure of LiFePO_4 [35].

Olivine LiFePO_4 has been emerging as a new positive electrode for rechargeable Lithium ion batteries in 1997 by J. B. Goodenough and co-workers in Austin [35-36]. The orthorhombic olivine LiFePO_4 (S.G.: Pbnm) consists of polyoxyanionic framework composed of LiO_6 octahedral, FeO_6 octahedral and PO_4 tetrahedral sites. The oxygen array is hexagonally close packed, where the octahedrals share both edges and faces as shown in Figure 1.5 [37]. The lithium ions reside in chains of edge-shared octahedral (LiO_6); divalent Fe^{2+} ions occupy the corner-shared octahedral (FeO_6); the phosphorus ions are located in tetrahedral sites (PO_4) [38]. The strong P-O covalent bonds in $(\text{PO}_4)^{3-}$ polyanion stabilize the $\text{Fe}^{3+}/\text{Fe}^{2+}$ redox couple through the Fe-O-X inductive effect, then avoid O_2 release at high states of charge, making LiFePO_4 the high thermal stability compared with other cathode candidates [39].

Besides, the positive LiFePO_4 candidate provides an attractive theoretical capacity of 170 mA h g^{-1} , and the electrochemical potential is 3.5 V, which is far below the oxidation potential of the electrolyte [40], giving a quite safe chemical environment. Moreover, the t_{2g} band of the redox couples ($\text{Fe}^{2+}/\text{Fe}^{3+}$) does not overlap with the 2p band of O^{2-} as well as the phase similarity of the lithiated and delithiated of LiFePO_4 induce both thermal

stability and electrochemically stability [41]. The excellent reversibility of the cells upon cycling is due to the striking similarity of the LiFePO_4 and FePO_4 structures, which are compared in Figure 1.6 [36]. FePO_4 is isostructural with heterosite. The lattice parameters and the space group of both LiFePO_4 and FePO_4 phases are listed in Table 1.1, both LiFePO_4 and FePO_4 have the same space group [37].

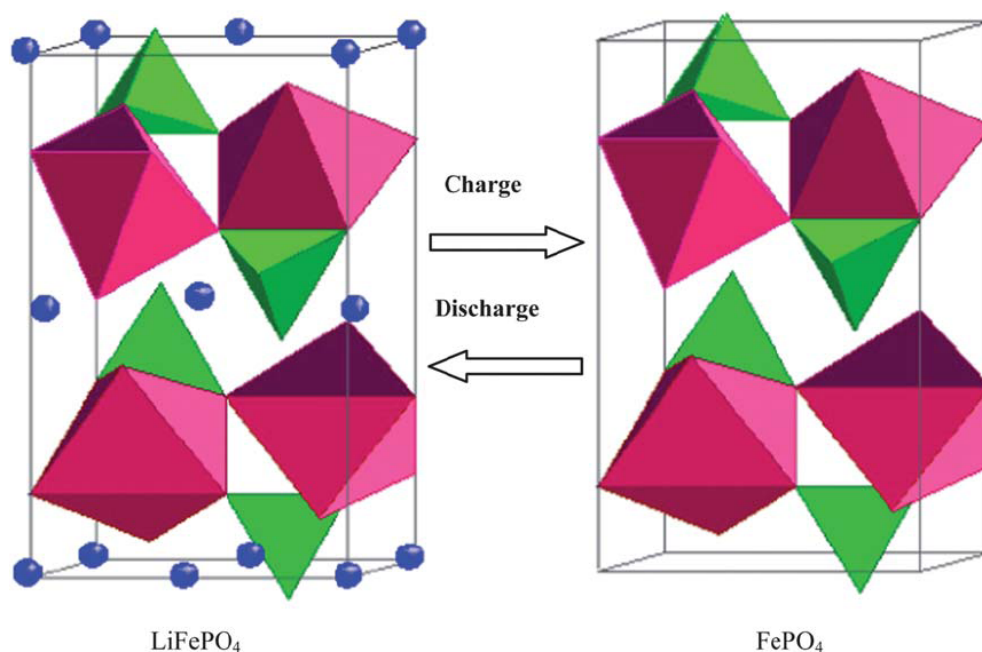


Figure 1.6 Structure of lithiation and delithiation phase of LiFePO_4 (blue-Li, green- PO_4 , red- FeO_6) [36].

Iron sources can be easily obtained from nature and are environmental benign. The low cost, environmental compatibility, high theoretical specific capacity of 170 mAh g^{-1} and especially a superior safety performance make LiFePO_4 a promising candidate for use as power supplies for EVs and HEVs.

However, from the lattice of this olivine structure, there is no continuous network of FeO_6 edge shared octahedral that might contribute to electronic conductivity, which results in the poor electronic conductivity of LiFePO_4 [38]. At room temperature, the electronic conductivity of pristine LiFePO_4 is only 10^{-9} to $10^{-10} \text{ S cm}^{-1}$, which is much lower than those of LiCoO_2 ($10^{-3} \text{ S cm}^{-1}$) and LiMn_2O_4 (2×10^{-5} to $5 \times 10^{-5} \text{ S cm}^{-1}$) [42].

By using the atomistic modeling technique and first-principle calculations, three possible migration paths were examined: the first pathway involves migration between adjacent Li sites in the [010] direction, paralleling to the b axis, with a jump distance of $2.9 \square 3.0$ Å; the second migration way is in the [001] direction, parallel to the c axis, with a jump distance of $4.6 \square 4.7$ Å; while the longest jump distance involves migration between the lithium channels in the [101] direction of $5.6 \square 5.8$ Å, as shown in Figure 1.7 [43]. The lowest Li ions migration energy for the pathway is along the [010] channel, with a nonlinear, curved trajectory between adjacent Li sites [44]. The one dimensional channel is easily blocked by the impurities and defects, leading to sluggish lithium ion diffusion kinetics [45]. The ionic diffusion coefficients in LiFePO_4 are therefore lower than the theoretical value.

Table 1.1 The space group and lattice parameters of LiFePO_4 and FePO_4 [37].

	LiFePO_4	FePO_4
Space group	Pbnm	Pbnm
a (Å)	6.008(3)	5.792 (1)
b (Å)	10.334(4)	9.821 (1)
c (Å)	4.693 (1)	4.788 (1)
Volume(Å ³)	291.392 (3)	272.357 (1)

Apparently, the low electronic and low ionic conductivities indicate the sluggish kinetics of LiFePO_4 in charge/discharge cycles, which is the main obstacle of LiFePO_4 used for practical applications in vehicles. Besides, how to improve the energy density of LiFePO_4 battery, while keeping a good power performance and cycle life, is an important task facing the industry.

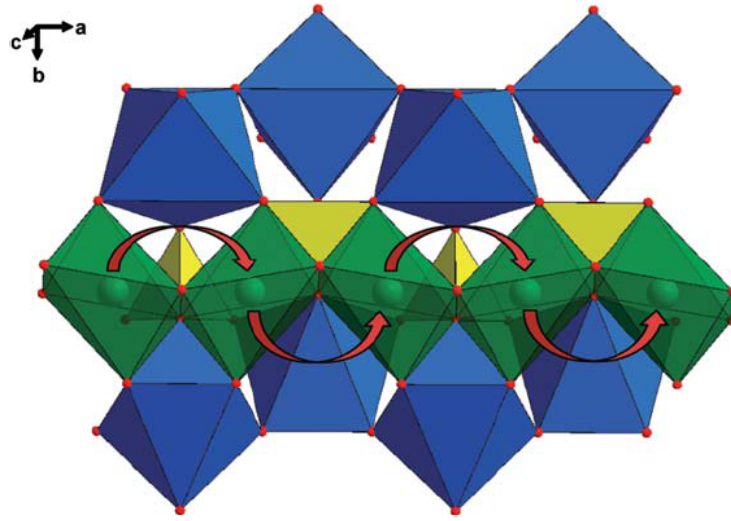


Figure 1.7 Structure of LiFePO₄ depicting the curved trajectory of Li ions [42].

1.1.3 Solutions to address the limitations

Many studies have been conducted in order to eliminate lithium diffusion limitations in LiFePO₄. Decrease the size to nanoscale dimension has been proved as one of the effective methods to solve the kinetic problems of LiFePO₄ [46, 47]. According to the formula [48],

$$L = (D\tau)^{1/2} \quad (1.2)$$

(where D and τ is the diffusion coefficient and time and L is the diffusion distance), the short diffusion lengths could shorten the diffusion time of Li ions in LiFePO₄ during intercalation/deintercalation process, also the relatively high surface area for the nano-sized particles enables fast charge transfer [49-52]. Moreover, the ionic diffusion constant on nanosized particles is proved much faster than in micrometre-size particles or bulk [53].

Up to now, to alleviate the poor electronic conductivity problem, additives were introduced to synthesize LiFePO₄/conductive material composites, such as dispersed carbon, metal powders, and intrinsically conducting polymers [54, 55]. Among of them, carbon coating and addition has been particularly attractive with respect to its high conductivity, low cost, and simplicity. However, the simple carbon coating or addition

cannot achieve an ideal rate performance especially for micro-sized LiFePO_4 . And uniform coating of LFP is also difficult to achieve [51, 56], as shown in Figure 1.8, so the electrode performance is limited in terms of rate capability. Also, the charge distribution is not homogenous in the perpendicular direction to the electrode surface at high charge/discharge rate for bulk LiFePO_4 material, which results in lower efficiency of active material [57].

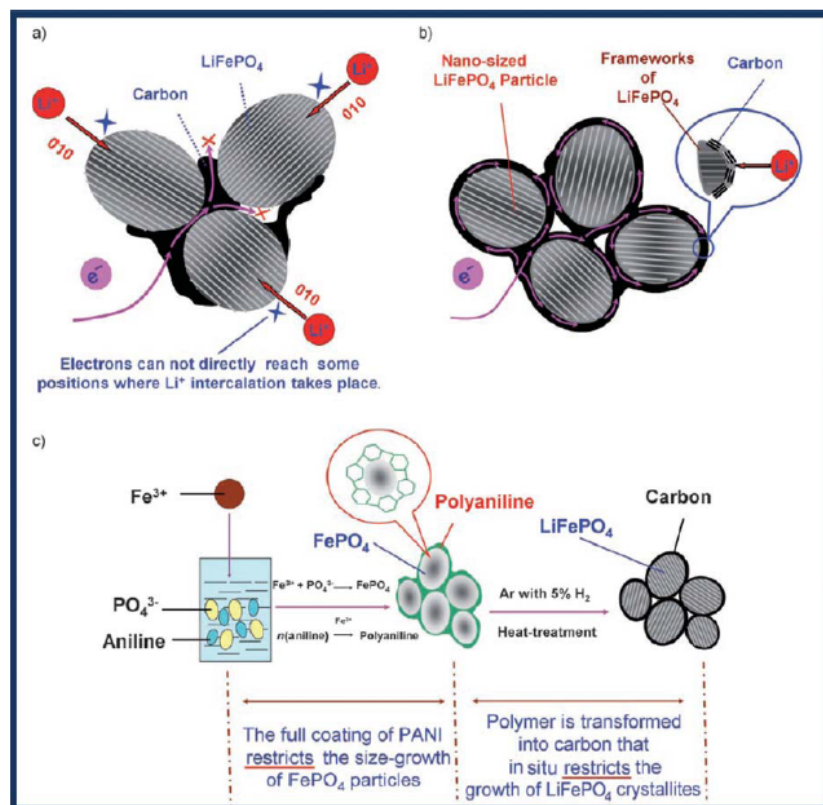


Figure 1.8 (a) Electron-transfer pathway for LiFePO_4 particles partially coated with carbon. (b) Designed ideal structure for LiFePO_4 particles with typical nano-size and a complete carbon coating. (c) Preparation process for the C/ LiFePO_4 composite [56].

The choice of a more appropriate carbon material such as carbon nanotubes (CNTs) or graphene is important for high-performance of the composite. Zhou [58] combined the advantages of porous LiFePO_4 and carbon nanotubes (CNTs), and developed $\text{LiFePO}_4/\text{CNTs}$ composites, yielding a high-performance cathode material for high-

energy and high-power lithium-ion batteries. Furthermore, graphene has recently been used as a 3D conducting matrix to grow and anchor insulating materials because of its superior conductivity, high mechanical strength, structural flexibility, and more importantly, high surface area (theoretical value of $2630 \text{ m}^2 \text{ g}^{-1}$) [59–61]. Ding et al. fabricated a LFP/graphene composite using a co-precipitation method [62]. In their work, the graphene suspension was prepared first, followed by the addition of a precursor into the solution, and finally the graphene-modified LFP was obtained by post-heat treatment. However, there were some unattached and aggregated LFP particles in the composites. In this case, the unattached LFP was not sufficiently utilized, thereby resulting in a limited enhancement of the specific capacity. Su et al. mechanically mixed graphene with LFP particles. This method did not adequately combine LFP and graphene because the graphene was not well dispersed, resulting in limited utilization of LFP active material (150 mA h g^{-1} at 0.1C) [63].

To make high capacity low cost LiFePO_4 large battery, it is desirable to reduce the amount of carbon and improve the quality of carbon coating.

In the case of improving electronic conductivity, doping with supervalent cations in LiFePO_4 lattice was recognized as an efficient method because it can improve the bulk conductivity, the lattice electronic conductivity of LiFePO_4 can be increased by a factor of eight orders, reaching values of $>10^{-2} \text{ S cm}^{-1}$ at room temperature, which was first introduced by Chiang et al. [38]. Recent work in the same group showed that doping can reduce the lithium miscibility gap, increase phase transformation and expand Li diffusion channels [64]. The mechanism is still not clear. Li site doping contributes much more to the increase of electronic conductivity than Fe site doping [65, 66]. Li site doping may affect the activation energy of Li ion transportation and block the one dimensional Li ion migration path [67, 68], which restrict the wide use of this technique in LiFePO_4 . Various models are proposed to explain the mechanism and kinetics in the charge/discharge cycles [69-71]. Up to now, the carbon coating and size reduction techniques are still widely introduced to prepare C/LiFePO_4 composites to address the poor electronic conductivity and poor ionic conductivity limitations.

The successful achievement from LiFePO_4 encouraged the great interest to other olivine typed LiMPO_4 ($\text{M}=\text{Mn}$, Co , and Ni) cathodes materials, which is even more attractive than LiFePO_4 because of higher theoretical energy density (energy density= specific capacity \times operating voltage) [72-77]. The other olivine typed LiMPO_4 ($\text{M}=\text{Mn}$, Co , and Ni) cathodes possess higher redox potentials (4.1, 4.8, and 5.1 V vs. Li^+/Li) thus higher energy density can be expected. Since working voltage higher than 4.5 V will cause stability problems of the battery system [72, 78-80], and the 4.1 V voltage plateau is compatible with the commercially used carbonate ester-based electrolyte [81], which makes LiMnPO_4 an exciting cathode material for next generation LIBs.

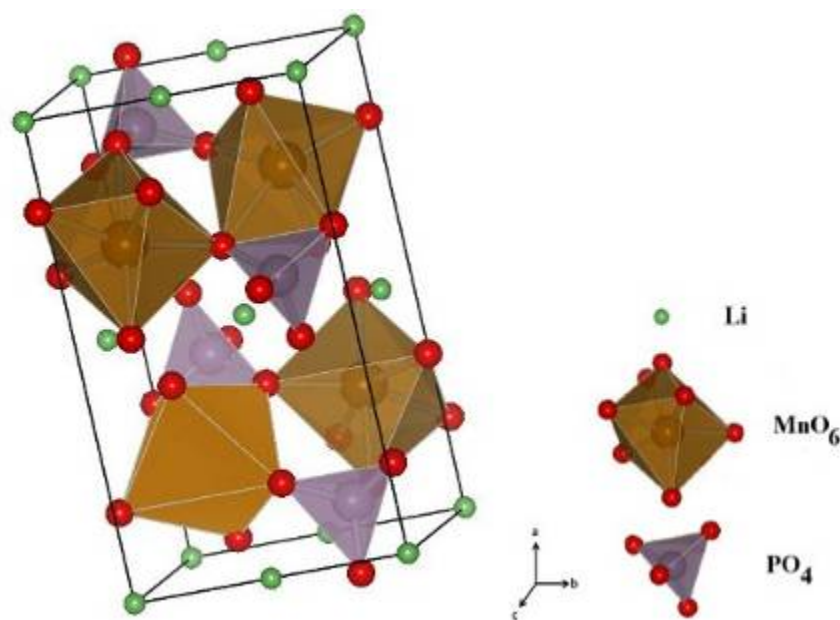


Figure 1.9 Structure of the olivine LiMnPO_4 with Pnma space group [82].

The divalent Mn^{2+} ions occupy the corner-shared octahedral 4c sites, and Li^+ resides in chains of edge-shared octahedral 4a sites, and the P atom is located in tetrahedral 4c site, respectively. The O atoms are in a hexagonal close-packed arrangement. The MnO_6 octahedra are separated by PO_4 tetrahedra and cannot form a continuous MnO_6 network, the olivine structure of LiMnPO_4 is shown in Figure 1.9 [82].

Because of the Jahn-Teller distortion triggered by the heavy polaronic holes located at the Mn^{3+} sites ($3d^4(t_{2g}^3 e_g^1)$) in delithiated MnPO_4 , and the interface strain between LiMnPO_4

and MnPO_4 during charge–discharge [83], the electronic conductivity of LiMnPO_4 is low ($< 10^{-10} \text{ S cm}^{-1}$), compared with $1.8 \times 10^{-8} \text{ S cm}^{-1}$ for LiFePO_4 [84], hence a poor rate capability and an insufficient utilization of Li ions are inevitable in the olivine host structure.

Similar to the LiFePO_4 electrode, the electrochemical behavior of LiMnPO_4 could also be improved by preparing nano-sized particles, carbon coating and cation doping.[85-89] Unfortunately, depositing carbon on LiMnPO_4 is more challenging due to the lower catalytic activity of Mn to carbon compared with Fe [90]. Moreover, given the even lower electrical conductivity of LiMnPO_4 ($< 10^{-12} \text{ S cm}^{-1}$) than LiFePO_4 ($1.8 \times 10^{-8} \text{ S cm}^{-1}$), quite a few amount of carbon additives (usually more than 10 wt.%) are required for achieving acceptable capacity and rate performances [91, 92]. Besides, Mn will dissolve into the electrolyte during the cycling, which will lead to very poor cycle performance [92].

From the case of LiFePO_4 studied for highly packed large-sized batteries, carbon coatings should be thin enough to allow easy penetration of lithium ions, more importantly, guarantee high capacity and energy density. Therefore, the novel gradient material (for example, forming core-shelled $\text{LiMnPO}_4@\text{LiFePO}_4$) might become a very competitive candidate for future LiMnPO_4 production.

1.2 Thesis objectives

LiFePO_4 has been recognized as a promising material applied for large size lithium-ion batteries due to its low cost, environmental compatibility, high theoretical specific capacity of 170 mA h g^{-1} and especially a superior safety performance. And three approaches can address the limitations existed in LiFePO_4 : (1) size reduction; (2) surface coating of conductive materials; (3) doping other element into LiFePO_4 .

For doping effect, there is still much debate about the precise substitution mechanisms whether the considerable increase in electronic conductivity is the doping effect or carbon contamination. Therefore, size reduction and carbon coating are the most widely used techniques in improvement of electronic conductivity of LiFePO_4 . Unfortunately, nano-

sized electrodes usually accompany with low tap density and a low volumetric capacity in practical battery application. Furthermore, more undesirable chemical reactions occurred at electrolyte/electrode interface layer will produce HF, which attacks the surface of LiFePO_4 , leading to poor cycle performance. The effective way to eliminate this problem is complete carbon coating. Full carbon coating plays a bifunctional role (conductivity improvement and protection barrier), ensuring LiFePO_4 particles getting electrons from all directions and avoiding the direct contact with the electrolyte, thus it could alleviate polarization and improve cycle life.

Another strategy is hierarchical nanostructure design. One way is developing of novel structured LiFePO_4 such as three dimensional (3D) porous LiFePO_4 architectures, another way is designing high-crystalline LiFePO_4 in nanosize anchored into three dimensional (3D) conductive networks. The strategy is feasible because it achieves fast electronic and ion conduction. In addition, the porous strategy also allows efficient percolation of the electrolyte through the electrode, favoring the access of electrolyte to active materials via the pores, and then making full use of electrode material.

From the experience of LiFePO_4 , carbon coating on LiMnPO_4 is key factor to improve the electrochemical performances. We also start preliminary work of how to get carbon coating layer on LiMnPO_4 .

In this case, we design our research objectives as follows:

- (1) Synthesis of 3D N-CNTs and CNTs modified porous LiFePO_4 composites as cathodes for Lithium ion batteries;
- (2) Synthesis of 3D Graphene modified porous LiFePO_4 composites as cathodes for Lithium ion batteries;
- (3) Synthesis of hierarchical LiFePO_4 nanoparticles anchored to 3D graphene conducting network as cathode for Lithium ion batteries;
- (4) Synthesis of one dimensional core-shell LiFePO_4 @CNTs by sol-gel route as cathode materials for Lithium-ion batteries;

(5) Synthesis of carbon-LiMnPO₄ nanocomposite as cathode for lithium ion batteries.

1.3 Thesis organization

This thesis includes ten chapters and satisfies the requirements on Integrated-Article form as outlined in the *Thesis Regulation Guide* by the School of Graduate and Postdoctoral Studies (SGPS) of the Western University. Specifically, it consists of the following sequence:

Chapter 1 presents an introduction to lithium ion batteries, which includes the working principles, applications and its challenges. Further, the history of cathodes materials and their challenges as well as the solutions are detailed described. The research objectives and the thesis organization of this study are also clearly addressed.

Chapter 2 lists experimental analytical techniques and electrochemical measurements, which were used to study and characterize physical and chemical properties of the obtained composites.

Chapter 3 compares N-CNTs and CNTs modified 3D porous LiFePO₄ with pristine porous LiFePO₄ prepared by sol-gel route. Highly conductive and uniformly dispersed N-CNTs incorporated into 3D interlaced porous LiFePO₄ will facilitate the electric and lithium ion diffusion rate, demonstrating N-CNTs modified composites can act as a promising cathode for high-performance lithium-ion batteries.

Chapter 4 presents graphene nanosheets modified 3D porous LiFePO₄ composites. Graphene nanosheets were incorporated into the porous hierarchical network homogenously, which greatly enhances the electrical conductivity and efficient use of the LiFePO₄, thus leading to an improved Li storage capability of the hybrid electrodes.

Chapter 5 describes the use of unfolded graphene as a three dimensional (3D) conducting network for LiFePO₄ nanoparticle growth. Compared with stacked graphene, which has a wrinkled structure, the use of unfolded graphene enables better dispersion of LiFePO₄ and restricts the LiFePO₄ particle size at nanoscale. More importantly, it allows each LiFePO₄ particle to be attached to the conducting layer, which could greatly

enhance the electronic conductivity and thereby realizing the full potential of the active materials, which is close to the theoretical capacity.

Chapter 6 explores in-situ self-catalyzed core-shell $\text{LiFePO}_4\text{@CNTs}$ nanowire fabricated by a two-step synthesis, where one-dimensional LiFePO_4 nanowire with a diameter of 20-30 nm encapsulated into CNTs, and 3D conducting networks of CNTs were obtained from in situ carbonization of polymer. Therefore, an excellent cycling stability and rate capability could be achieved benefiting from this one-dimensional core-shell structure.

Chapter 7 studies pea-pod like $\text{LiFePO}_4/\text{carbon}$ nanowires ($\sim 50\text{nm}$) synthesized by hydrothermal method. And the mechanism of the nanowires evolution is investigated. The nuclei of the nanowires are derived from the decomposition of the initial octahedral particles. The electrochemical properties $\text{LiFePO}_4/\text{carbon}$ nanowires are performed.

Chapter 8 systematically studies the solid solution of olivine $\text{LiFe}_x\text{Mn}_{1-x}\text{PO}_4/\text{C}$ ($x=0.3, 0.5$ and 0.7) as cathode materials for lithium ion batteries. It is found that the concentration of Mn substitution not only significantly affect the morphologies of obtained compounds from nanoparticles for Fe-rich phase to nanoplates for Mn-rich phase, but also is highly related to the electrochemical behaviors. The 50% Mn substitution forming a solid solution with the Fe in the olivine lattice was optimal for achieving the best electrochemical performance.

Chapter 9 presents LiMnPO_4/C nanoparticles with 15-20 nm fabricated by using a two step process. Carbon coating plays as a bi-functional role not only restrict the size, but also guarantees the layers on surface of LiMnPO_4 , which has very inert activity with carbon, thus good electrochemical performance is obtained.

Chapter 10 summarizes the results and contributions for this thesis work. Meanwhile, the outlook and future work is proposed.

1.4 References

- [1] J. B. Goodenough, Y. Kim, Chem. Mater., 2010, **22**, 587.
- [2] J.-M. Tarascon, N. Recham, M. Armand, J. Chotard, P. Barpanda, W. Walker, L. Dupont, Chem. Mater., 2010, **22**, 724.
- [3] <http://www.eia.doe.gov/fuelrenewable.html>. Accessed on 05/25/2009.
- [4] D. Linden, T. B. Reddy, (eds) Handbook of Batteries, 2002, 3rd edn (McGraw-Hill).
- [5] M. Armand, J.-M. Tarascon, Nature, 2008, **451**, 652
- [6] H. Ikeda, T. Saito, H. Tamura, in Proc. Manganese Dioxide Symp., 1975, Vol. 1 (eds A. Kozawa, & R. H. Brodd) (IC sample Office, Cleveland, OH).
- [7] D. W. Murphy, F. J. DiSalvo, J. N. Carides, J. V. Waszczak, Mat. Res. Bull., 1978, **13**, 1395.
- [8] M. Lazzari, B. Scrosati, J. Electrochem. Soc., 1980, **127**, 773.
- [9] T. Nagaura, K. Tozawa, Prog. Batteries Sol. Cells, 1990, **9**, 209.
- [10] J.-M. Tarascon, M. Armand, Nature, 2001, **414**, 359.
- [11] H. Takeshita, Proc. Conf. Power 2000, San Diego, 25 September 2000.
- [12] J. Goodenough, H.D. Abruna, and M.V. Buchanan, editors, Washington, D.C.: Office of Basic Energy Sciences, 2007, U.S. Department of Energy.
- [13] D. Guyomard, Electronics Vol. 9 (eds T. Osaka, & M. Datta), 2000, **253** (Gordon & Breach Science Publishers).
- [14] J. R. Dahn, et al. Industrial Chemistry Library, 1994, Vol. 5 (ed. G. Pistoia).
- [15] M. Winter, J. O. Besenhard, Electrochem. Acta, 1999, **45**, 31.

- [16] A. Anani, S. Crouch-Baker, R. A. Huggins, J. Electrochem. Soc., 1987, **134**, 3098.
- [17] P. G. Bruce, B. Scrosati, J.-M. Tarascon, Angew. Chem., 2008, **120**, 2972-2989; Angew. Chem. Int. Ed., 2008, **47**, 2930.
- [18] B. Scrosati, J. Hassoun, Y.-K. Sun, Energy Environ. Sci., 2011, **4**, 3287.
- [19] V. Etacheri, R. Marom, R. Elazari, G. Salitra, D. Aurbach, Energy Environ. Sci., 2011, **4**, 3243.
- [20] H. K. Liu, G. X. Wang, Z. P. Guo, J. Z. Wang, K. Konstantinov, J. Nanosci. Nanotechnol., 2006, **6**, 1.
- [21] X. Zhi, G. Liang, L. Wang, X. Qu, J. Zhang, J. Cui, J. Power Sources, 2009, **189**, 779.
- [22] K. Mizushima, P.C. Jones, P.J. Wiseman, J. B. Goodenough, Materials Research Bulletin, 1980, **15**, 783.
- [23] A.C. Dillon, Chem. Rev., 2010, **110**, 6856.
- [24] F. K. Lutgens, E. J. Tarbuck, Essentials of Geology 7th, 2000 edn (Prentice Hall, New York).
- [25] R. D. Ward, D. Brownlee, Rare Earth, 2000 (Copernicus, New York).
- [26] G. Yuan, M. V. Yakovleva, W. B. Ebner, Electrochem. Solid State Lett. 1998, **1**, 117.
- [27] J. R. Dahn, U. Von Sacken, M. W. Juzkow, H. Al-Janaby, J. Electrochem. Soc., 1991, **138**, 2207.
- [28] R. Armstrong, P. G. Bruce, Nature, 1996, **381**, 499.
- [29] F. Capitaine, P. Gravereau, C. Delmas, Solid State Ionics, 1996, **89**, 197.
- [30] S. Choi, A. Manthiram, J. Electrochem. Soc., 2002, **149**, A1157.

- [31] M. M. Thackeray, W. I. F. David, P. G. Bruce, J. B. Goodenough, *Mat. Res. Bull.* 1983, **18**, 461.
- [32] D. H. Jang, Y. J. Shin, S. M. Oh, *J. Electrochem. Soc.*, 1996, **143**, 2204.
- [33] H. Yamane, T. Inoue, M. Fujita, M. Sano, *J. Power Sources*, 2001, **99**, 60.
- [34] A. Manthiram, A. Vadivel Murugan, A. Sarkar, T. Muraliganth, *Energy Environ. Sci.*, 2008, **1**, 621.
- [35] A. K. Padhi, K. S. Nanjundaswamy, J. B. Goodenough, ECS Meeting Abstract, No. 58, Los Angeles, CA., May 5-10, 1996, vol. 96-1.
- [36] A. K. Padhi, K. S. Nanjundaswamy, J. B. Goodenough, *J. Electrochem. Soc.* 1997, **144**, 1188.
- [37] A. Michel, J. B. Goodenough, A. K. Padhi, K. S. Nanjundaswamy, C. Masquelier. 2003, US Pat., 6514640,
- [38] S. Y. Chung, J. T. Bloking, Y. M. Chiang, *Nat. Mater.*, 2002, **1**, 123.
- [39] S. Okada, S. Sawa, M. Egashira, J. Yamaki, M. Tabuchi, H. Kageyama, T. Konishi, A. Yoshino, *J. Power Sources*, 2001, **97–98**, 430.
- [40] J. B. Goodenough, A. K. Padhi, K. S. Nanjundaswamy, C. Masquelier. US Pat., 5910382, 1999.
- [41] G. Wang, H. Liu, S. Qiao, G. M. Lu, P. Munroe, H. Ahn, *Adv. Mater.*, 2011, **22**, 4944.
- [42] J. Molenda, A. Stoklosa, T. Bak, *Solid State Ionics*, 1989, **36**, 53.
- [43] B. L. Ellis, K. T. Lee, L. F. Nazar, *Chem. Mater.*, 2010, **22**, 691.
- [44] M. S. Islam, D. J. Driscoll, C. A. J. Fisher, P. R. Slater, *Chem. Mater.*, 2005, **17**, 5085.

- [45] H. Fang, Z. Pan, L. Li, Y. Yang, G. Yan, G. Li, S. Wei, *Electrochem. Commun.*, 2008, **10**, 1071.
- [46] A. S. Andersson, J. O. Thomas, B. Kalska, L. Haggstrom, *Electrochem. Solid-State Lett.*, 2000, **3**, 66.
- [47] N. Meethong, Y. H. Kao, M. Tang, H.-Y. Huang, W. C. Carter, Y.-M. Chiang, *Chem. Mater.*, 2008, **20**, 6189.
- [48] H. S. Zhou, D. L. Li, M. Hibino, I. Honma, *Angew. Chem.* 2005, 117, 807-812; *Angew. Chem. Int. Ed.*, 2005, **44**, 797.
- [49] M. Gaberscek, R. Dominko, J. Jamnik, *Electrochem. Commun.*, 2007, **9**, 2778.
- [50] R. Dominko, M. Bele, J. M. Goupil, M. Gaberscek, D. Hanzel, I. Arcon, J. Jamnik, *Chem. Mater.* 2007, **19**, 2960.
- [51] Y. S. Hu, Y. G. Guo, R. Dominko, M. Gaberscek, J. Jamnik, J. Maier, *Adv. Mater.* 2007, **19**, 1963.
- [52] V. Srinivasan, J. Newman, *J. Electrochem. Soc.*, 2004, **151**, A1517.
- [53] R. Malik, D. Burch, M. Bazant, G. Ceder, *Nano Lett.*, 2010, **10**, 4123.
- [54] S. H. Ju, Y. C. Kang., *Mater. Chem. Phys.*, 2008, **107**, 328.
- [55] J. F. Ni, H. H. Zhou, J. T. Chen, X. X. Zhang, *Chin. J. Inorg. Chem.* 2005, **21**, 472.
- [56] Y. Wang, Y. Wang, E. Hosono, K. Wang, H. Zhou, *Angew. Chem. Int. Ed.*, 2008, **47**, 7461.
- [57] J. Liu, M. Kunz, K. Chen, N. Tamura, T. J. Richardson, *J. Phys. Chem. Lett.*, 2010, **1**, 2120.
- [58] Y. Zhou, J. Wang, Y. Hu, R. O'Hayreb, Z. Shao, *Chem. Commun.*, 2010, **46**, 7151.
- [59] S. Park, R. S. Ruoff, *Nat. Nanotechnol.*, 2009, **4**, 217.

- [60] H. Wang, J. T. Robinson, G. Diankov, H. Dai, J. Am. Chem. Soc., 2010, **132**, 3270.
- [61] Y. Liang, H. Wang, H. S. Casalongue, Z. Chen, H. Dai, Nano Res., 2010, **3**, 701.
- [62] Y. Ding, Y. Jiang, F. Xu, J. Yin, H. Ren, Q. Zhuo, Z. Long, P. Zhang, Electrochem. Commun., 2010, **12**, 10.
- [63] F. Y. Su, C. H. You, Y. B. He, W. Lv, W. Cui, F. Jin, B. Li, Q. Yang, F. Kang. J. Mater. Chem., 2010, **20**, 9644.
- [64] N. Meethong, Y. -H. Kao, S. A. Speakman, Y. -M. Chiang. Adv. Funct. Mater., 2009, **19**, 1060.
- [65] D. Y. Wang, H. Li, S. S. Shi, X. J. Huang, L. Q. Chen, Electrochim. Acta, 2005, **50**, 2955.
- [66] J. Hong, C. S. Wang, X. Chen, S. Upreti, M. S. Whittingham, Electrochem. Solid-State Lett., 2009, **12**, A33.
- [67] C. Y. Ouyang, D. Y. Wang, S. Q. Shi, Z. X. Wang, H. Li, X. J. Huang, L. Q. Chen, Chin. Phys. Lett., 2006, **23**, 61.
- [68] D. Wang, C. Ouyang, T. Drezen, I. Exnar, A. Kay, N. H. Kwon, P. Guerec, J. H. Miners, M. Wang, M. Gratzel, J. Electrochem. Soc., 2010, **157**, A225.
- [69] C. Delmas, M. Maccario, L. Croguennec, F. L. Cras, F. Weill, Nat. Mater., 2008, **7**, 665.
- [70] C. Delacourt, P. Poizot, J.-M. Tarason, C. Masquelier, Nat. Mater., 2005, **4**, 254.
- [71] S. Yang, Y. Song, K. Ngala, P. Y. Zavalij, M. S. Whittingham, J. Power Sources, 2003, **119**, 239.
- [72] K. Zaghib, M. Trudeau, A. Guerfi, J. Trottier, A. Mauger, R. Veillette, C. M. Julien, J. Power Sources, 2012, **204**, 177.

- [73] P. Gibot, M. Casas-Cabanas, L. Laffont, S. Levasseur, P. Carlach, S. Hamelet, J. M. Tarascon, C. Masquelier, *Nat. Mater.*, 2008, **7**, 741.
- [74] C. Delacourt, L. Laffont, R. Bouchet, C. Wurm, J. B. Leriche, M. Morcrette, J. M. Tarascon, C. Masquelier, *J. Electrochem. Soc.*, 2005, **152**, A913.
- [75] T. Drezen, N. H. Kwon, P. Bowen, I. Teerlinck, M. Isono, I. Exnar, J. Power Sources, 2007, **174**, 949.
- [76] D. Y. Wang, H. Buqa, M. Crouzet, G. Deghenghi, T. Drezen, I. Exnar, N. H. Kwon, J. H. Miners, L. Poletto, M. Graetzel, *J. Power Sources*, 2009, **189**, 624.
- [77] K. Saravanan, V. Ramar, P. Balaya, J. J. Vittal, *J. Mater. Chem.*, 2011, **21**, 14925.
- [78] C. Delacourt, P. Poizot, M. Morcrette, J. M. Tarascon, C. Masquelier, *Chem. Mater.*, 2004, **16**, 93.
- [79] B. Ellis, P. S. Herle, Y. H. Rho, L. F. Nazar, R. Dunlap, L. K. Perry, D. H. Ryan, *Faraday Discuss.*, 2007, **134**, 119.
- [80] G. H. Li, H. Azuma, M. Tohda, *Electrochem. Solid-State Lett.*, 2002, **5**, A135.
- [81] B. Kang, G. Cedar, *J. Electrochem. Soc.*, 2010, **157**, A808.
- [82] A. Yamada, Y. Kudo, K. Y. Liu, *J. Electrochem. Soc.*, 2001, **148**, A747.
- [83] M. Yonemura, A. Yamada, Y. Takei, N. Sonoyama, R. Kanno, *J. Electrochem. Soc.*, 2004, **151**, A1352.
- [84] N. Meethong, H. Y. S. Huang, S. A. Speakman, W. C. Carter, Y. M. Chiang, *Adv. Funct. Mater.*, 2007, **17**, 1115.
- [85] S.-W. Oh, S. T. Myung, S.-M. Oh, K. H. Oh, K. Amine, B. Scrosati, Y.-K. Sun, *Adv. Mater.*, 2010, **22**, 4842.
- [86] S.-W. Oh, S. T. Myung, Y. S. Choi, K. H. Oh, Y.-K. Sun, *J. Mater. Chem.*, 2011, **21**, 19368.

- [87] Y. S. Choi, S. Kim, S. S. Choi, J. S. Han, J. D. Kim, S. E. Jeon, B. H. Jung, *Electrochim. Acta*, 2004, **50**, 833.
- [88] S. Kuroda, N. Tabori, M. Sakuraba, Y. Sato, *J. Power Sources*, 2003, **119-121**, 924.
- [89] Z. Bakenov, I. Taniguchi, *J. Electrochem. Soc.*, 2010, **157**, A430.
- [90] N. Ravet, M. Gauthier, K. Zaghib, J. B. Goodenough, A. Mauger, F. Gendron and C. M. Julien, *Chem. Mater.*, 2007, **19**, 2595
- [91] S.-M. Oh, H.-G. Jung, C. S. Yoon, S.-T. Myung, Z. Chen, K. Amine, Y.-K. Sun, *J. Power Sources*, 2011, **196**, 6924.
- [92] S.-M. Oh, S.-W. Oh, C.-S. Yoon, B. Scrosati, K. Amine, Y.-K. Sun, *Adv. Funct. Mater.*, 2010, **20**, 3260.

Chapter 2

2 Experimental, Characterization Techniques and Electrochemical Measurements

2.1 Experimental

2.1.1 Synthesis of N-CNTs via chemical vapor deposition (CVD) method

N-CNTs were synthesized by a CVD method [1], as shown in Figure 2.1. In detail, different concentration (0.5, 1 and 2g) of imidazole ($C_3H_4N_2$, 99%) and 200 mg of ferrocene ($Fe(C_5H_5)_2$, 98%) were added into 10 ml of acetonitrile (CH_3CN , 99.5%), after ultrasonication, the transparent solution was then transferred into the syringe for injection.

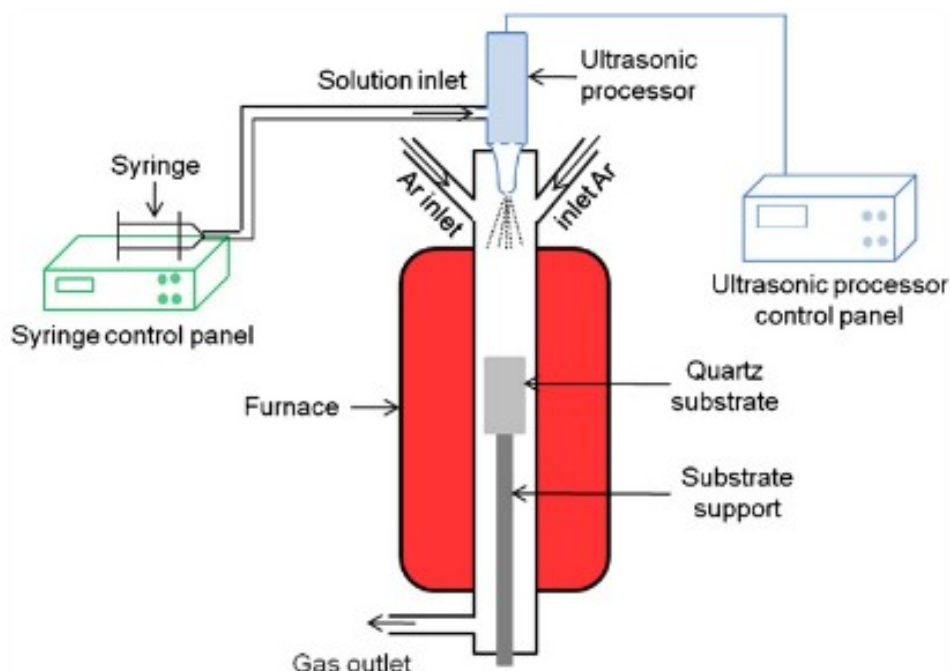


Figure 2.1 Schematic illustration of ultrasonic spray pyrolysis [1].

Before the reaction, Ar (99.999% in purity) gas was introduced into the quartz tube from both inlets for 20 min with a flow rate of 150 sccm. Then the furnace was heated to 850 °C at a rate of 60 °C min⁻¹. Once the furnace reached the desirable temperature, 6 ml of the solution was injected into the ultrasonic processor at different injection rates (0.25, 0.5 and 0.75 ml min⁻¹), then N-CNTs begin to grow. After injection of 6 ml of the precursor solution, the furnace starts to cool down to room temperature in the protection of Ar gas. Finally, N-CNTs were collected from the quartz plate.

2.1.2 Synthesis of graphene via chemical method

The stacked graphene with the size of around 10 μm was synthesized by a modified Hummers method [2, 3]. In detail, we first use concentrated sulfuric acid (23 ml) and sodium nitrate (NaNO₃, 0.5g) to oxidize the graphite powder (1g) to graphite oxide, after 2 hours, potassium permanganate (3g) was then added into the suspension with stirring for 5 days. Thereafter, 100 ml of diluted sulfuric acid was added in the above suspension, followed by the addition of hydrogen peroxide (140 ml) with 1 h stirring. The suspension was subsequently filtered and washed until reaching a neutral pH. After dried it at 60 °C in a vacuum oven, GO was obtained. The stacked graphene was prepared by 30 seconds thermal treatment of the as-obtained GO around 1050 °C in the furnace.

The unfolded graphene was reduced by hydrazine reduction of GO as-obtained in the distilled water [4]. After ultrasonication of GO (0.02 g mL⁻¹) in 2 L batches bath ultrasound (VWR B2500A-MT) for 3 h and following centrifugation, the centrifugate was collected. Single and few-layer graphene sheets were readily prepared, homogeneously and stably suspended in the solvent medium.

2.1.3 Synthesis of hierarchical porous LiFePO₄/Nitrogen-doped carbon nanotube composite via sol-gel route

Multiwalled carbon nanotubes (CNTs) purchased from Shenzhen Nanotech Port Co. Ltd. were used in this study. The diameter of CNTs is in the range of 40 to 60 nm. Nitrogen doped carbon nanotubes (N-CNTs) with similar diameter range were prepared by ultrasonic spray pyrolysis reported previously.

In situ sol-gel experiments [5] were conducted in aqueous solution under ambient atmosphere, as shown in Figure 2.2. In a typical synthesis, $\text{LiFePO}_4/\text{N-CNTs}$ and $\text{LiFePO}_4/\text{CNTs}$ composites were prepared by using an in situ sol-gel method as follows: first 80 mg N-CNTs were dissolved in 30 mL of water via strong ultrasonic agitation for 30min, then 1.039 g lithium dihydrogen phosphate (LiH_2PO_4) was dissolved in 100 mL of water and stirred at 80 °C for 1 h. Separately, 2.449 g iron (III) citrate($\text{FeC}_6\text{H}_5\text{O}_7$) dissolved in 70ml of water by stirring at 70 °C for 1h. The three solutions were mixed together and dried at 70 °C for 24 h.

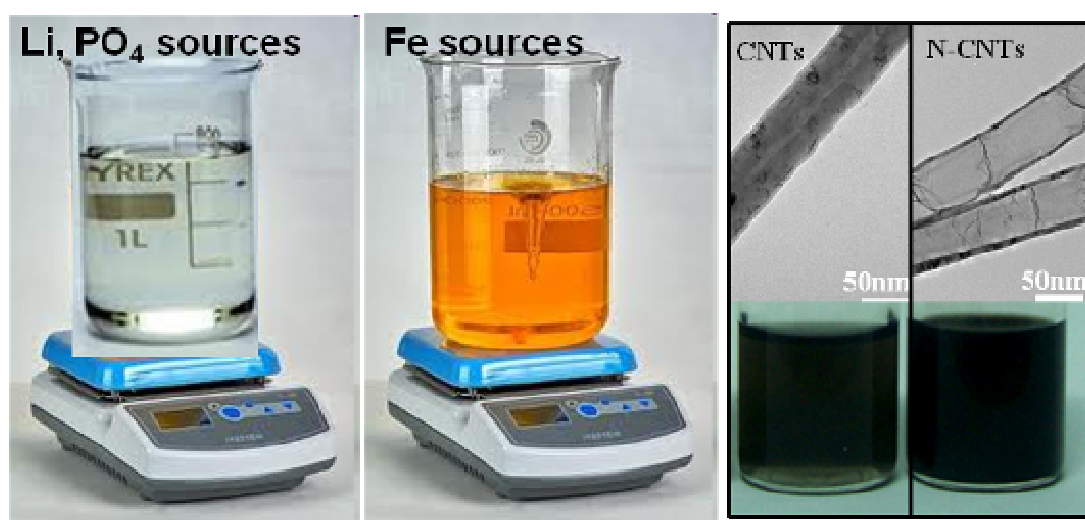


Figure 2.2 Experimental setup of sol-gel process.

After thorough grinding with a mortar and pestle, the obtained material was fired in an inert (argon) atmosphere at 700 °C for 10 h with a heating rate of 10 °C min⁻¹. The synthesis procedure of CNTs modified porous LiFePO_4 was the same as above. For the pristine porous LiFePO_4 , all the experimental parameters kept the same as above except without the addition of N-CNTs or CNTs, the obtained products is shown in Figure 2.3.

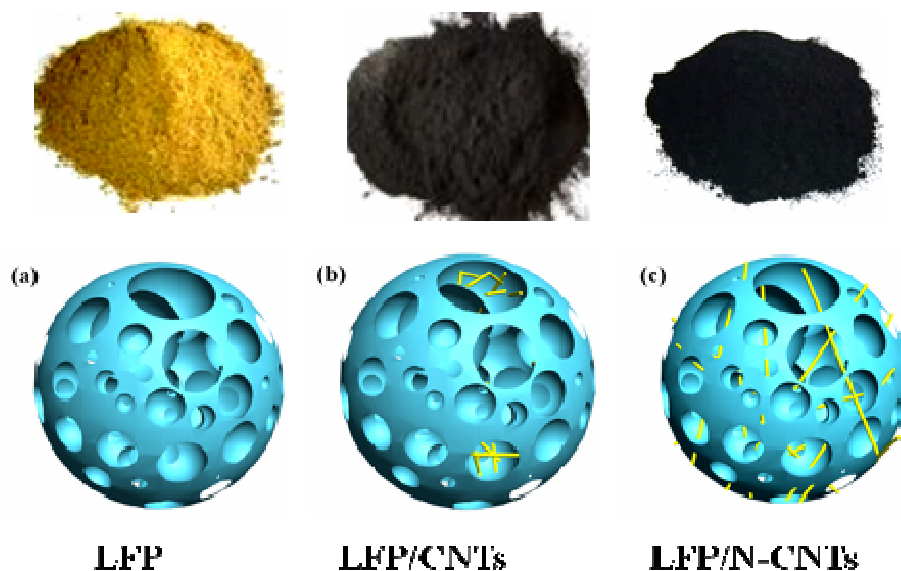


Figure 2.3 Images of the obtained composites and the schematics.

2.1.4 Synthesis of hierarchical LiFePO_4 -graphene hybrid electrodes by sol-gel method

Graphene nanosheets used in this study were prepared through the thermal expansion of graphite oxide. The synthesis procedures are shown in Figure 2.4. In a typical sol-gel route [5] of LiFePO_4 -graphene, 20 mg graphene nanosheets were firstly dissolved in 30mL of water via strong ultrasonic agitation for 30 min, then 1.039 g lithium dihydrogen phosphate and 2.449 g iron (III) citrate was dissolved in 170 ml of water by stirring at 70 °C for 1h. The two solutions were mixed together and dried at 70°C for 24 h. The obtained xerogel was fired in argon atmosphere at 700 °C for 10 h. For the pristine porous LiFePO_4 , graphene nanosheets were not added and all other experimental parameters were kept same as LiFePO_4 -graphene above.

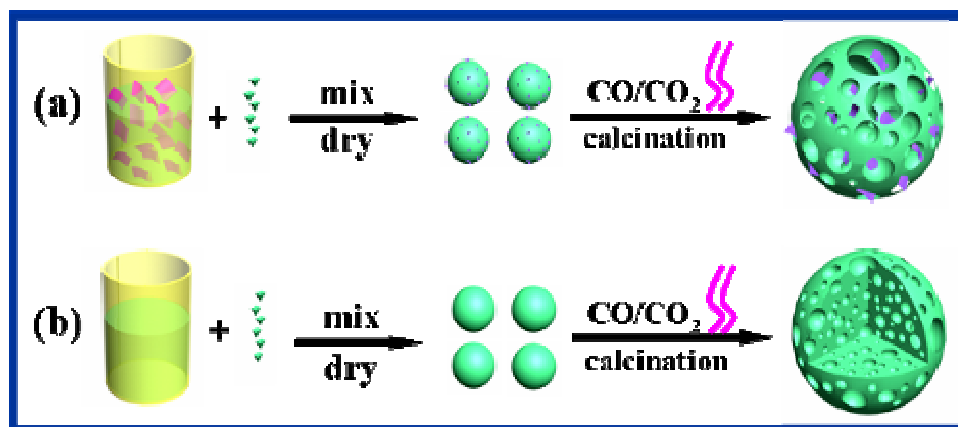


Figure 2.4 Synthesis procedures for the pristine and graphene modified LiFePO_4 .

2.1.5 Synthesis of stacked graphene and unfolded graphene modified LiFePO_4 via sol-gel route

The following describes a typical synthesis for LiFePO_4 /stacked graphene composites using sol-gel route [5]. First: 22.5 mg of stacked graphene was dissolved in 30 mL of water via strong ultrasonic agitation for 30 min. Next, 1.039 g lithium dihydrogen phosphate (LiH_2PO_4 , Sigma) was dissolved in 100 mL of water and stirred at 80 °C for 1 h. Separately, 1.739 g iron (II) acetate ($\text{Fe}(\text{AC})_2$, Sigma) was dissolved in 70 mL of water by stirring at 70 °C for 1 h. The two solutions and the stacked graphene suspension were mixed together and dried at 70 °C for 24 h.

For the LiFePO_4 /unfolded graphene composites, the procedure was similar, except that the stacked graphene solution was replaced with the unfolded graphene suspension (0.2 g L^{-1}). After thorough grinding of the xerogel followed by annealing in a furnace filled with an argon atmosphere at 700 °C and a heating rate of 10 °C min^{-1} , the composites were obtained.

2.1.6 Synthesis of one-dimensional core-shell LiFePO_4 @CNTs nanowires via sol-gel method

A typical synthesis for LFP@CNTs nanowires is shown in Figure 2.5. First: 100 mg PMMA was dissolved in 30 mL of water via strong ultrasonic agitation. Next, 1.039 lithium dihydrogen phosphate (LiH_2PO_4 , Sigma) was dissolved in 100 mL of water and

stirred at 70 °C for 1 h. Separately, 1.739 M iron (II) acetate ($\text{Fe}(\text{AC})_2$, Sigma) dissolved in 80 ml of water by stirring at 60 °C for 1h. The three solutions were mixed together and dried at 70 °C for 24 h. After thorough grinding of the xerogel followed by annealing in a furnace filled with an argon atmosphere at 700 °C and a heating rate of 10 °C min^{-1} , the composites were obtained.

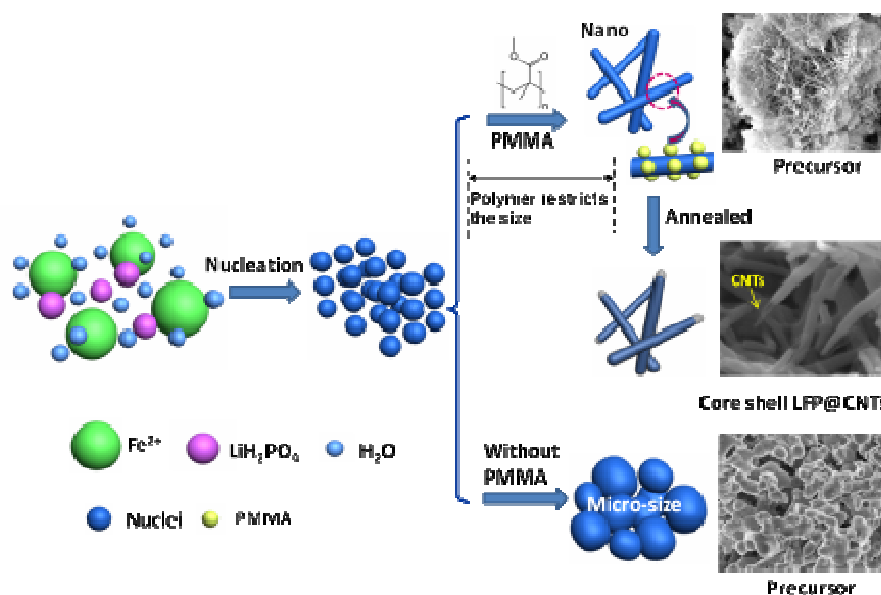


Figure 2.5 Schematics to illustrate the synthetic procedure of the LFP@CNTs nanocomposites.

2.1.7 Synthesis of peapod like LiFePO_4/C nanowires via hydrothermal method

In a typical synthesis process for preparing LiFePO_4 nanowires, lithium hydroxide (LiOH), ammonium dihydrogen phosphate ($\text{NH}_4\cdot\text{H}_2\text{PO}_4$) and ferrous sulfate ($\text{FeSO}_4\cdot 7\text{H}_2\text{O}$) (all from Aldrich) are used as starting materials, the starting precursor of Li:Fe:P is prepared in a molar ratio of 3:1:1 [6].

Metal salts were first dissolved in 8 ml de-ionized water. After stirring, 0.3 g nitrilotriacetic acid (NTA) surfactant and 7 ml isopropanol were added, followed by the addition of 1.6 mmol ascorbic acid to the suspension. The pH value of the mixture was adjusted to 5 by adding concentrated ammonia, and the concentration of LiOH in the precursor solution is 0.2 M. The mixed solution was then transferred into a 50 ml

stainless steel Teflon-lined autoclave. After stirring for 5 min followed by Ar-gas bubbling for 10 min to get rid of the oxygen the autoclave was sealed, kept at 200 °C for 20 h, and then naturally cooled to room temperature. After the hydrothermal reaction, the solution was centrifuged and washed with distilled water a number of times. The gray-white product was dried at 60 °C in a vacuum oven overnight. To get better crystallized LiFePO_4 and the carbon layer, the obtained material was treated at 700 °C for 1 h under Ar atmosphere. The equipment set up is shown in Figure 2.6.



Figure 2.6 Hydrothermal oven set up (Thermo).

2.1.8 Synthesis of LiMnPO_4/C nanocomposites via ball-milling and CVD route

The LiMnPO_4/C was prepared by the following procedures [7]. In the first step, 1.73 g manganese acetate was dissolved in 30 mL of water via strong ultrasonic agitation. Then, 500 mg citric acid was dissolved in the solution by stirring at 70 °C for 1 h, followed by the drop of the phosphoric acid. The molar ratio of Mn:P is 1:1. The dried xerogel was treated at 700 °C for 1 h.

In the second step, the composite from the first step was mixed with lithium hydroxide by ball-milling (Retsch, PM 200) for 5 h at 350 rpm, the set up of the ball-milling is shown in Figure 2.7. The final LiMnPO_4 was obtained through CVD thermal treatment at 700 °C for 10 h.



Figure 2.7 Ball milling set up (Retsch, PM 200) used in this system.

2.2 Characterizations

2.2.1 Physical characterizations (SEM, TEM, XRD, EDX, BET, RAMAN, Synchrotron)

In order to investigate the physical and chemical properties of the products as-obtained, a variety of analytical techniques have been performed in this thesis.

The scanning electron microscope (SEM) was used to determine the morphology and microstructure of the samples. The as-prepared samples were examined by SEM (Hitachi S-4800) operated at 5 kV coupled with energy dispersive X-rays (EDX). The instrument is shown in Figure 2.8.

Transmission electron microscopy (TEM) is another technique to get structural information. The regular TEM (H-7000, Hitachi) equipment is shown in Figure 2.9, while the high resolution TEM measurements were carried out with a JEOL JEM-2100, operated at 200 kV.

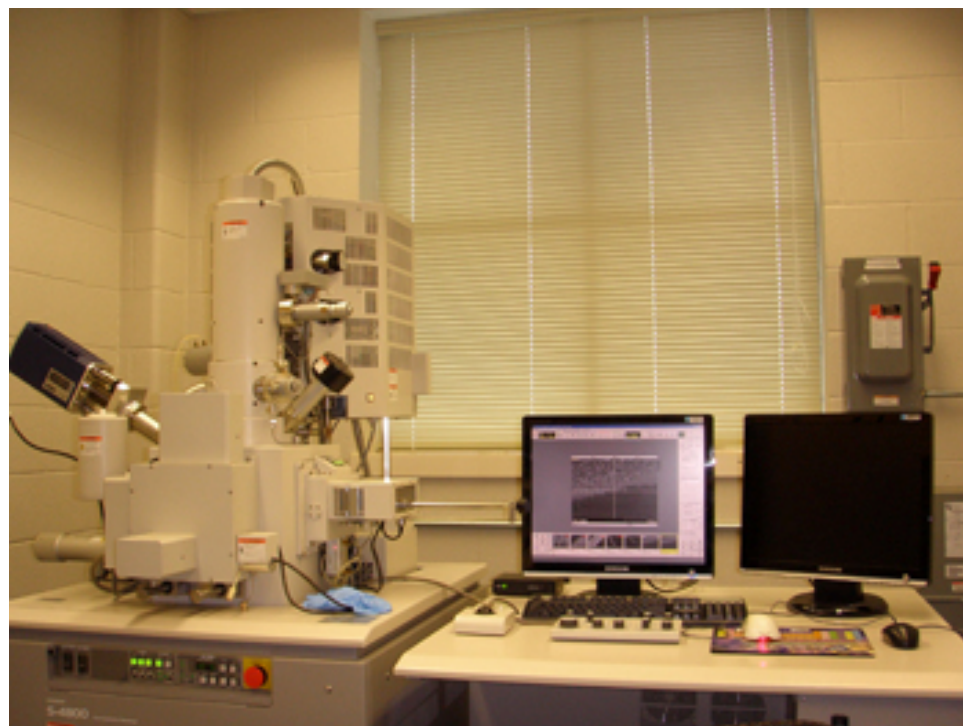


Figure 2.8 Image of SEM (Hitachi S-4800) device.

A Raman scattering spectroscopy apparatus (HORIBA Scientific LabRAM HR) equipped with a 532.4 nm laser was performed to study the phonon modes of elements, as shown in Figure 2.10. X-ray diffraction (XRD) is a versatile, non-destructive technique that reveals detailed information about the chemical composition and crystallographic structure of natural and manufactured materials. In our study, the XRD analysis was conducted on a Rigaku rotating-anode X-Ray diffractometer. The diffractometer employs Co Ka radiation (wavelength of 0.17902 nm), with monochromation is achieved using a curved crystal, diffracted beam, graphite monochromater. The instrument was operated at 45 kV and 160 mA. The experimental diffraction patterns were completed from 2 to 82° two-theta, at a rate of 10 degree per minute. N₂ adsorption/desorption isotherms were performed using a Folio Micromeritics TriStar II Surface Area Analyser.



Figure 2.9 Image of TEM equipment (H-7000, Hitachi).

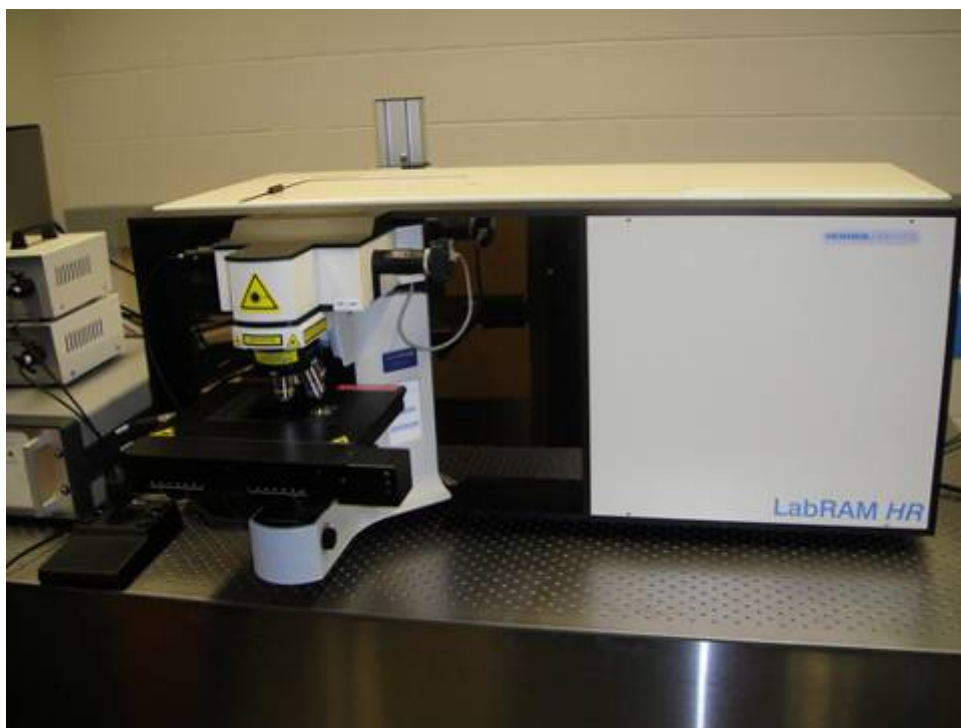


Figure 2.10 Image of Raman facility (HORIBA Scientific LabRAM HR).

X-ray absorption near edge structure (XANES) are performed on the Soft X-ray Microcharacterization Beamline (SXRMB, $\Delta E/E$: 10^{-4}) and undulator Spherical Grating Monochromator (SGM) beamline at the Canadian Light Source (CLS) located at the University of Saskatchewan in Saskatoon.

2.2.2 Electrochemical characterization

The electrochemical performances were conducted on coin-shape half cells (2352). The working electrode was fabricated by mixing the active material /acetylene black/polyvinylidene fluoride with a weight ratio 75:15:10, then grinding the mixture in a mortar and pestle. The resultant slurry, pasted on Al foil, was dried at 100 °C under vacuum for 24 h. The electrolyte was 1M LiPF_6 solution in a 1:1 mixture of ethylene carbonate (EC) and dimethyl carbonate (DEC). The coin cells (2352) were assembled in a high purity argon filled glove box, as shown in Figure 2.11.



Figure 2.11 Image of glove box.

2.2.2.1 Cyclic voltammetry (CV)

Cyclic voltamograms (CV) measurements were performed on an electrochemical workstation (Potentiostat/Galvanostat/EIS (VMP3)) over the potential range 2.5–4.2 V vs. Li^+/Li at a scanning rate of 0.1 mV s^{-1} . All the electrochemical measurements were conducted at room temperature and at least three cells are assembled and tested to confirm the consistence of CV results.

2.2.2.2 Battery test

The electrochemical performances were carried out using a computer-controlled Arbin BT-2000 Battery Test Station with coin-shape half cells between 2.2 and 4.5 V at different rates, and the working station is shown in Figure 2.12. Charge-discharge testing was conducted galvanostatically at different C rates using a computer controlled battery test system (Arbin BT-2000 Battery Test System) within the voltage range of 2.5–4.2 V (vs. Li^+/Li). To confirm the results, at least six cells were assembled for cycling and rate test.



Figure 2.12 Image of the working station for the battery testing (Arbin, BT2000).

2.3 References

- [1] J. Liu, Y. Zhang, M. Ionescu, R. Li, X. Sun, Appl. Surf. Sci., 2011, **257**, 7837.
- [2] W. S. Hummers, R. E. Offeman, J. Am. Chem. Soc., 1958, **80**, 1339.
- [3] D. Geng, Y. Chen, Y. Chen, Y. Li, R. Li, X. Sun, S. Ye, S. Knights, Energy Environ. Sci., 2011, **4**, 60.
- [4] D. Li, M. Muller, S. Gilje, R. Kaner, G. Wallace, Nat. Nanotechnol. 2008, **3**, 101.
- [5] Y. Zhou, J. Wang, Y. Hu, R. O'Hayre and Z. Shao, Chem. Commun., 2010, **46**, 7151.
- [6] G. Wang, X. Shen, J. Yao, J. Power Sources, 2009, **189**, 543.
- [7] T. Drezen, N.-H. Kwo, P. Bowen, I. Teerlinck, M. Isono, I. Exnar, J. Power Sources, 2007, **174**, 949.

Chapter 3

3 Hierarchically Porous LiFePO_4 /Nitrogen-doped Carbon nanotube Composite for Lithium Ion Batteries Cathodes

Recently, CNTs have been investigated as a carbon additive for lithium ion battery due to high conductivity, network structure, and high surface area. Compared with CNTs, N-CNTs possess even higher conductivity contributed from many active defects and good hydrophilic properties. As we know, nano-size LiFePO_4 material usually accompanies with low tap density and a low volumetric capacity in practical battery application. Therefore, developing of novel structured LiFePO_4 such as three dimensional (3D) porous LiFePO_4 architectures is a feasible strategy, since the porous strategy also allows efficient percolation of the electrolyte through the electrode, favoring the electrolyte access to active materials via the pores, then make full use of electrode material.

In this chapter, a porous composite of LiFePO_4 /nitrogen doped carbon nanotubes (N-CNTs) with hierarchical structure was prepared by sol-gel method independent of templates or surfactants. Highly conductive and uniformly dispersed N-CNTs incorporated into three dimensional (3D) interlaced porous LiFePO_4 will facilitate the electric and lithium ion diffusion rate. LiFePO_4 /N-CNTs composites deliver a reversible discharge capacity of 138 mAh g^{-1} at a current density of 17 mA g^{-1} , demonstrating N-CNTs modified composites can act as a promising cathode for high-performance lithium-ion batteries.

Note: This work has been published.

J. Yang, J. Wang, X. Li, D. Wang, J. Liu, G. Liang, M. Gauthier, Y. Li, R. Li, X. Sun, **J. Mater. Chem.** 2012, 22, 7537-7543.

3.1 Introduction

The past few years witness an unprecedented increase of interest in large scale batteries demand for energy storage to develop electric vehicle (EV) and hybrid electric vehicle (HEV) [1-5]. Since the pioneer work of Goodenough and co-workers [6], LiFePO_4 has become a promising material for large size lithium-ion batteries due to its low cost, environmental compatibility, high theoretical specific capacity of 170 mAh g^{-1} and especially a superior safety performance. Unfortunately, one of the main obstacles of LiFePO_4 for its practical applications is its poor rate capability, which can be attributed to sluggish kinetics of lithium-ion diffusion through the LiFePO_4 - FePO_4 interfaces and the poor electronic conductivity [7, 8].

The kinetics of the lithium ion extraction/insertion process can be facilitated by reducing the particle size [9, 10], doping with isovalent ions [11, 12], or coating with conductive carbon layer [13-15]. Decreasing the size of the LiFePO_4 crystallites to nanosize can shorten the distance of the lithium ion diffusion pathway and improve its rate capacity, but nano-size LiFePO_4 material usually accompanies with low tap density and a low volumetric capacity in practical battery application [16]. For doping effect, there is still much debate about the precise substitution mechanisms whether the considerable increase in electronic conductivity is the doping effect or carbon contamination [17]. Therefore, addition or coating with conductive carbon is the most widely used technique in improvement of electronic conductivity and rate performance of LiFePO_4 .

Nevertheless, the simple carbon coating or addition cannot achieve an ideal rate performance especially for micro-sized LiFePO_4 . Also, the charge distribution is not homogenous in the perpendicular direction to the electrode surface at high charge/discharge rate for bulk LiFePO_4 material, which results in lower efficiency of active material [18]. Therefore developing of novel structured LiFePO_4 such as three dimensional (3D) porous LiFePO_4 architectures is a feasible strategy because it achieves fast electronic and ion conduction [16]. In addition, the porous strategy also allows efficient percolation of the electrolyte through the electrode, favoring the electrolyte access to active materials via the pores, then make full use of electrode material [19-21].

Doherty [22] successfully prepared porous LiFePO_4 -carbon composites by using template method, which exhibited 100 mAh g^{-1} at a high discharge rate of 5 C. Considering the importance of carbon in the composite, the choice of a more appropriate carbon material such as carbon nanotubes (CNTs) is important for high-performance of the composite. Zhou [23] combined the advantages of porous LiFePO_4 and carbon nanotubes (CNTs), and developed $\text{LiFePO}_4/\text{CNTs}$ composites, yielding a high-performance cathode material for high-energy and high-power lithium-ion batteries. However, the CNTs were not quite uniformly dispersed in the modified composite, which leads to ineffective transfer of the electrons. Therefore, to make full use of the CNTs conductive network, uniform CNTs dispersion in the LiFePO_4 composite is critical.

It is widely accepted that nitrogen doped carbon nanotubes (N-CNTs) possess many active defects and hydrophilic properties, allowing more uniform dispersion of N-CNT into porous LiFePO_4 and leading to intimate contact with active material, In addition, N-CNTs could further enhance the electronic conductivity because the additional electrons contributed by the nitrogen atom provide electron carriers for the conduction band.²⁴⁻²⁶ Therefore, a superior performance can be expected by addition N-CNTs into LiFePO_4 (Fig. 1).

Herein we present 3D N-CNTs modified porous LiFePO_4 obtained by using sol-gel approach combined with high-temperature calcinations. An investigation was undertaken into the N-CNTs effects on the electrochemical performance compared with the CNTs modified LiFePO_4 composites and the pristine porous LiFePO_4 .

3.2 Experimental

3.2.1 Synthesis of porous LiFePO_4 /Nitrogen-doped carbon nanotube composite and LiFePO_4 / carbon nanotube composite

Multiwalled carbon nanotubes (CNTs) purchased from Shenzhen Nanotech Port Co. Ltd. were used in this study. The diameter of CNTs is 40-60nm. Nitrogen doped carbon nanotubes (N-CNTs) were prepared by ultrasonic spray pyrolysis reported previously with diameter around 50nm [25].

In situ sol-gel experiments were conducted in aqueous solution under ambient atmosphere. In a typical synthesis, $\text{LiFePO}_4/\text{N-CNTs}$ and $\text{LiFePO}_4/\text{CNTs}$ composites were prepared by using an in situ sol-gel method as follows: first 80mg N-CNTs were dissolved in 30mL of water via strong ultrasonic agitation for 30min, then 1.039g lithium dihydrogen phosphate (LiH_2PO_4) was dissolved in 100 mL of water and stirred at 80 °C for 1 h. Separately, 2.449g iron (III) citrate($\text{FeC}_6\text{H}_5\text{O}_7$) dissolved in 70ml of water by stirring at 70 °C for 1h. The three solutions were mixed together and dried at 70°C for 24 h. After thorough grinding with a mortar and pestle, the obtained material was fired in an inert (argon) atmosphere at 700 °C for 10 h with a heating rate of 10 °C min⁻¹. The procedure was similar for the synthesis of CNTs modified porous LiFePO_4 . For the pristine porous LiFePO_4 , N-CNTs and CNTs were not added.

3.2.2 Physical characterization

The XRD analyses were performed on a Rigaku rotating-anode X-Ray Diffractometer. The diffractometer employs Co Ka radiation, with monochromation is achieved using a curved crystal, diffracted beam, graphite monochromator. The instrument was operated at 45 kV and 160 mA. The experimental diffraction patterns were completed from 2 to 82° two-theta, at a rate of 10 degree/minute.

Scanning electron microscopy (SEM) images were taken on a Hitachi S-4800 microscope, operating at 5 kV. TEM measurements were carried out with a Hitachi H-7000 transmission electron microscopy (TEM). Raman scattering (RS) spectra were recorded on a HORIBA Scientific LabRAM HR Raman spectrometer system equipped with a 532.4 nm laser. N₂ adsorption/desorption isotherms were performed using a Folio Micromeritics TriStar II Surface Area and Pore Size Analyser.

3.2.3 Electrochemical characterizations

The electrochemical performances were carried out using a computer-controlled Arbin BT-2000 Battery Test Station with coin-shape half cells between 2.2 and 4.5 V at different rates. The electrolyte was 1M LiPF_6 solution in a 1:1 mixture of ethylene carbonate (EC) and dimethyl carbonate (DEC). The working electrode was fabricated by mixing the active material (LiFePO_4)/acetylene black/polyvinylidene fluoride with a

weight ratio 75:15:10, then grinding the mixture in a mortar and pestle. The resultant slurry, pasted on Al foil, was dried at 100 °C under vacuum for 24 h. The coin cells (2352) were assembled in a high purity argon filled glove box.

Charge–discharge testing was conducted galvanostatically at different C rates using a computer controlled battery test system (Arbin BT-2000 Battery Test System) within the voltage range of 2.5-4.2 V (vs. Li^+/Li). Cyclic voltamograms (CV) measurements were performed on an electrochemical workstation (Potentiostat/Galvanostat/EIS (VMP3)) over the potential range 2.5-4.2 V vs. Li^+/Li at a scanning rate of 0.1 mV s⁻¹. All the electrochemical measurements were conducted at room temperature.

3.3 Results and discussion

Typical scanning electron microscopy (SEM) and transmission electron microscopy (TEM) images of CNTS and N-CNTs are shown in Fig. 3.1. From low magnifications micrographs (Fig.3.1a, c), both CNTs and N-CNTS have the length extending 25-30 micrometers. A high magnification (Fig. 3.1b, d) reveals both CNTs and N-CNTs have the diameters around 50 nm. The TEM images (Fig. 3.1 e, f) illustrate that commercial CNTs have tubular morphology, while N-CNTs exhibit bamboo-like structure derived from N atoms doping. And the N content is calculated as 5.2 at.% based on previous work.

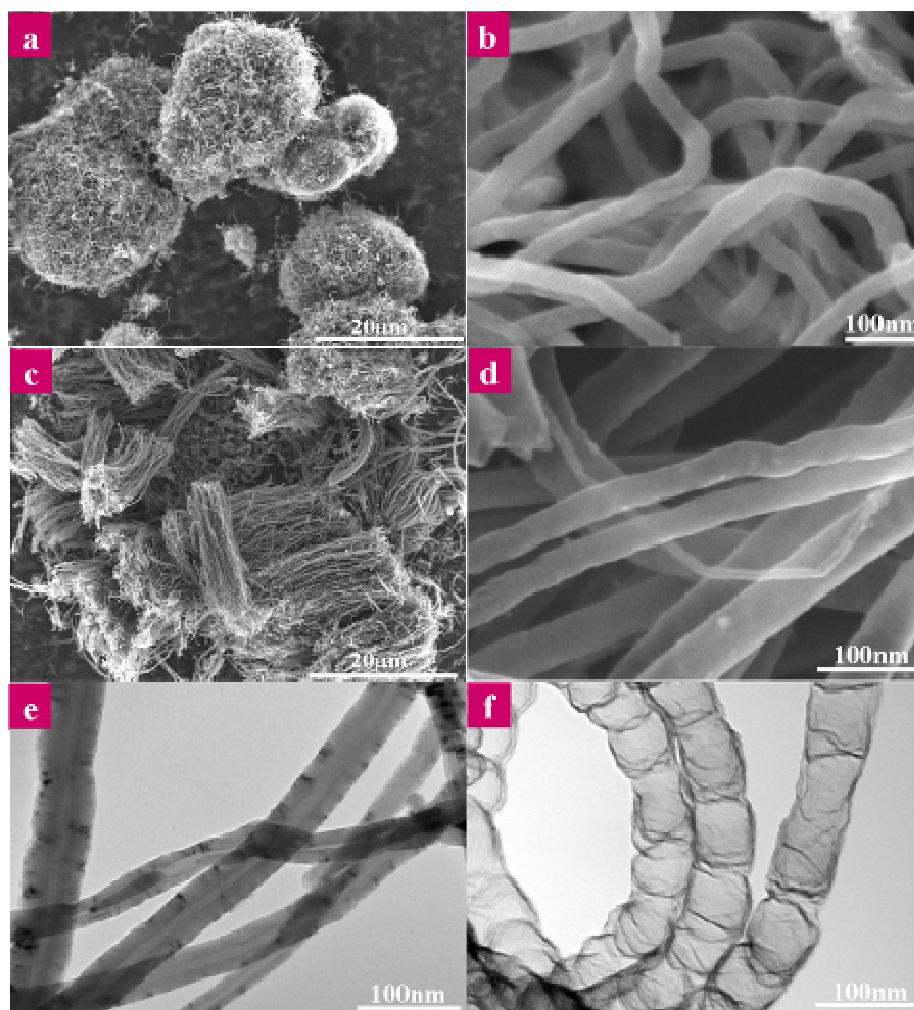


Figure 3.1 SEM and TEM images of CNTs (a, b and e) and N-CNTs (c, d and f).

Elemental maps from N-CNTs were obtained by EDX spectroscopy on the SEM (Fig. 3.2). The instrument was able to detect traces of nitrogen in the N-doped case. It is clear that both carbon and nitrogen are present in the N-CNTs, and nitrogen uniformly dispersed in the N-CNTs. Raman spectra of CNTs and N-CNTs is shown in Fig. 2d. The strong peaks at 1348 and 1584 cm^{-1} are assigned to D-band and G-band, respectively. The G-band stands for the presence of graphite carbon, whereas D-band is attributed to disorders or defects in the graphite structure [27]. The intensity ratio of D and G bands (I_D/I_G) is used to evaluate the disorder in the materials. The ratios I_D/I_G of CNTs and N-CNTs are 0.53 and 0.85, respectively. The higher I_D/I_G ratio implies more defects in N-CNTs.

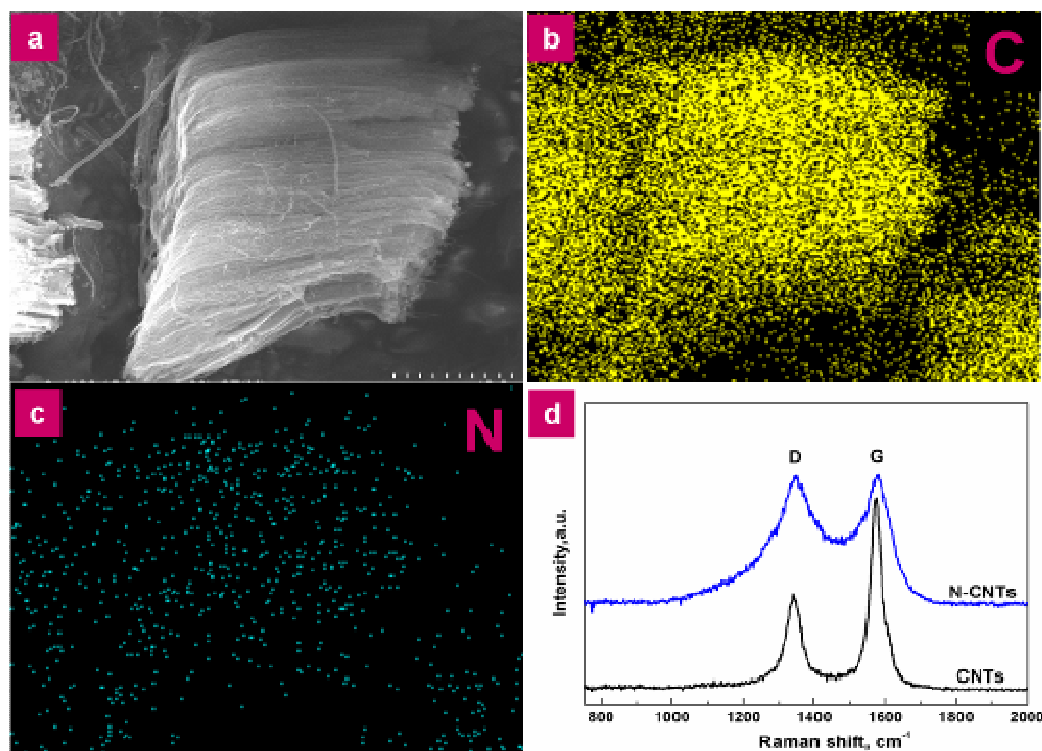
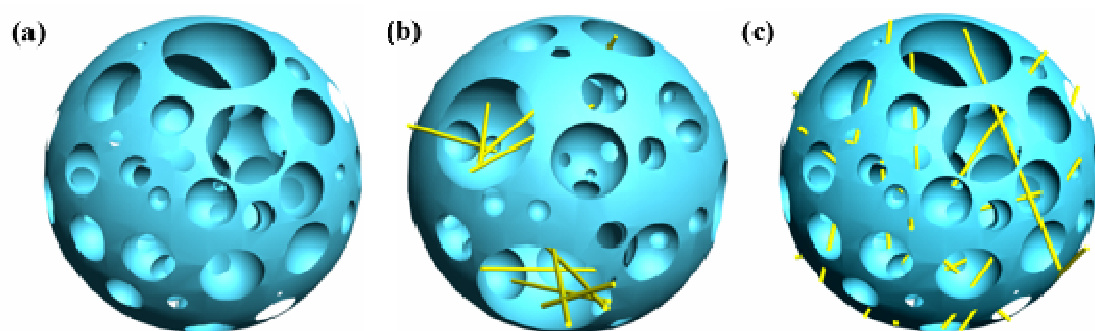


Figure 3.2 EDX elemental mappings (a, b and c) and Raman spectra (d) for N-CNTs.



Scheme 3.1 Schematic image of (a) porous LiFePO_4 ; (b) $\text{LiFePO}_4/\text{CNTs}$ network; (c) $\text{LiFePO}_4/\text{N-CNTs}$ composites.

The modified composites were obtained by using the addition of the dispersed CNTs and N-CNTs into the precursor. Final products were collected by the calcination process. As illustrated in Scheme 3.1, the interconnected pores are formed from vigorous gas

evolution (mainly CO and CO₂) during degradation of a citrate precursor. The interlacing LFP pores can serve as the channel for the penetration of the electrolyte through the electrode. Both CNTs and N-CNTs incorporate into the bulk porous network, leading to improved electrochemical performance. The dispersion of commercial CNTs in the porous structure is not homogenous; in contrast, highly dispersed N-CNTs act as a bridge to connect all pores together for fast electrons transfer.

The phase composition for the as-obtained product has been identified with the X-ray diffraction (XRD) method, as demonstrated in Fig. 3.3. The majority of diffraction lines can be indexed to the orthorhombic phase LiFePO₄ (JCPDS no. 40-1499). It is noted that very small amount of impurity phases are also present in all samples, which can be indentified as Fe₇(PO₄)₆. The minor impurity may appear under the reducing environment during the annealing process [28, 29]. The profiles of the reflection peaks are quite narrow, indicating the high crystallinity of the LFP samples. It is also reveals that the addition of CNTs and N-CNTs has no effects on the main structure and the formation of LFP.

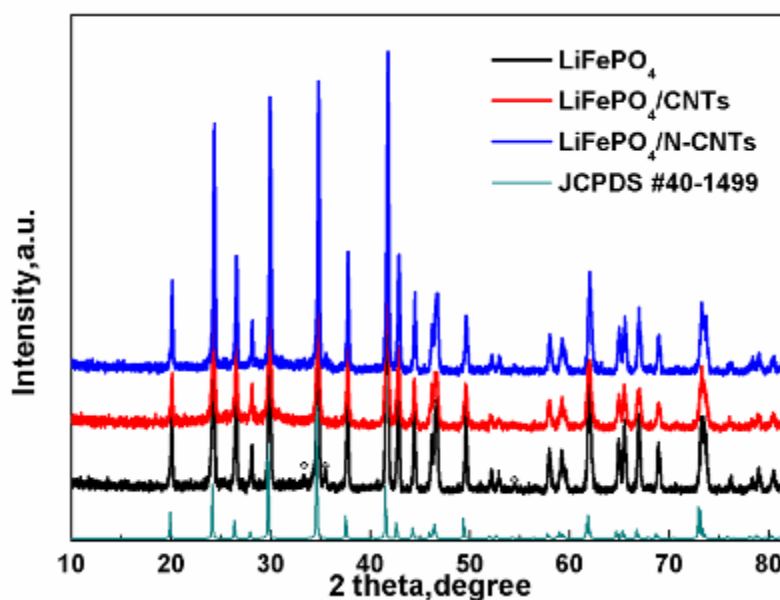


Figure 3.3 Powder X-ray diffraction patterns for porous LiFePO₄ and LiFePO₄ composite. * represents the impurity phase.

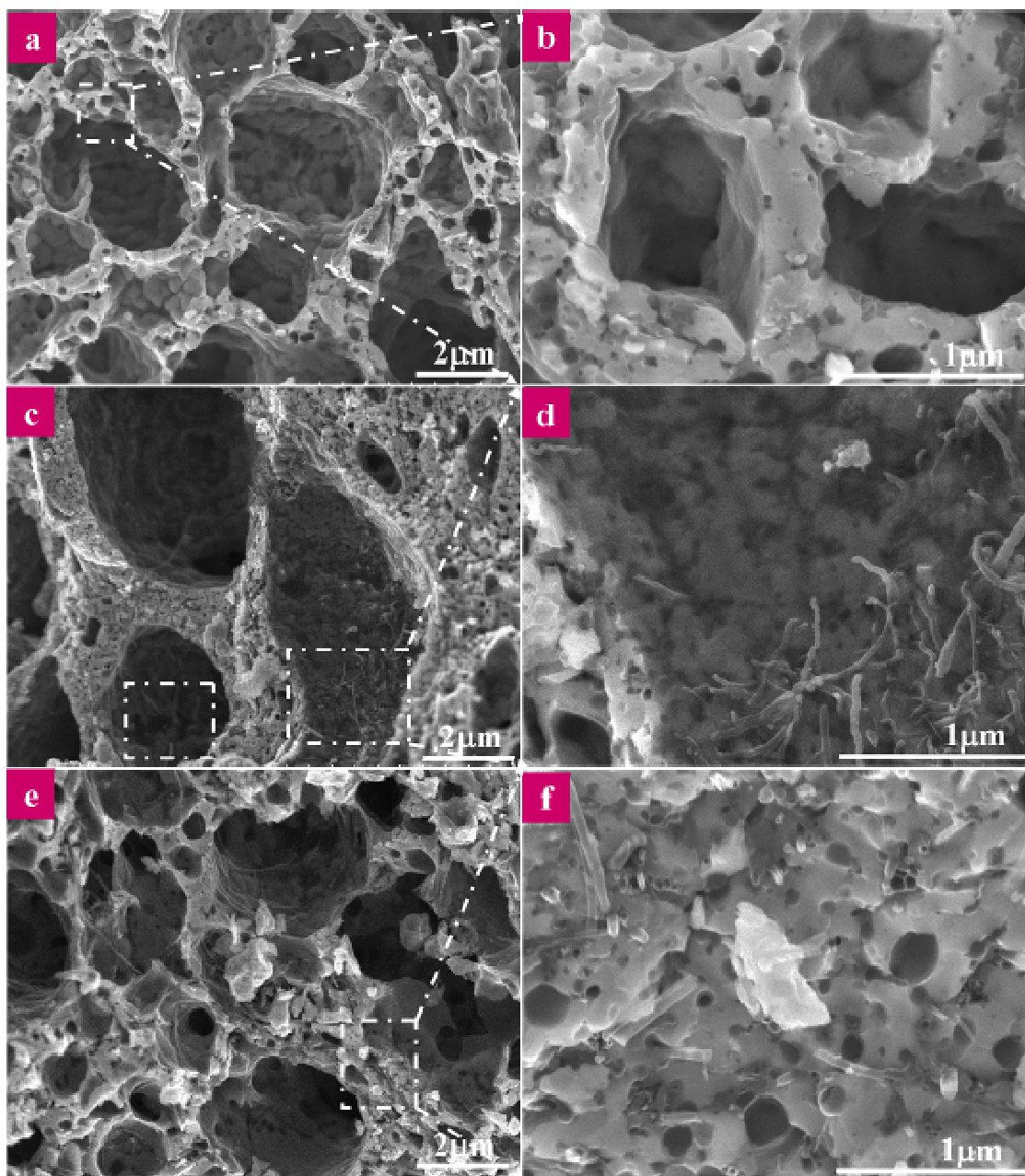


Figure 3.4 SEM images of (a, b) porous LiFePO_4 ; (c, d) $\text{LiFePO}_4/\text{CNTs}$ composite; (e, f) $\text{LiFePO}_4/\text{N-CNTs}$ composite.

Porous LFP was formed during the calcination process. SEM micrographs reveal a porous structure of the pristine LFP (Fig 3.4a). Higher magnification image reveals the presence of numerous sub-micro sized apertures, these small apertures lead into much larger voids inside the particles, indicating the interior pore system is interlaced (Fig.

3.4b). The cross-sectional image of the cracked particle (see details in Fig.S3.1†) reveals that numerous micropores were distributed throughout the interior of the LFP particles, constructing 3D interconnected pore system. Porous LFP/CNTs and LFP/N-CNTs composites are shown in Fig. 3.4c and 3.4e. The 3D CNTs and N-CNTs networks do not change the structure of pristine porous LFP, but the degree of pore size uniformity is different, as shown in the lower magnification images. The distribution of pore sizes in LFP/N-CNTs is more homogenous than that of CNTs, indicating that N-CNTs may regulate and control the uniform porous structure of LFP, which can be attributed to the uniform dispersion of N-CNTs network. From high-resolution SEM images (Fig. 3.4f), the interlaced N-CNTs networks were uniformly incorporated into porous LFP particles, while CNTs were only located in certain big pores (dot dash line squared regions). The EDS elemental mapping for LFP/N-CNTs show a uniform distribution of N, C, Fe, P and O (see ESI† Fig. S3.2). The poor dispersion of CNTs network restricts the formation of the homogeneous pore sizes in LFP during the calcination process, and will bring the nonuniform electron distribution. The specific BET surface area of the LFP/N-CNTs is $11.6 \text{ m}^2 \text{ g}^{-1}$ and the pore diameter is around 90 nm. While for LFP/CNTs and LFP, the surface area is 6.4 and 2.3, respectively. Incorporated N-CNTs can greatly enhance the surface area, favouring the diffusion kinetics of lithium ions.

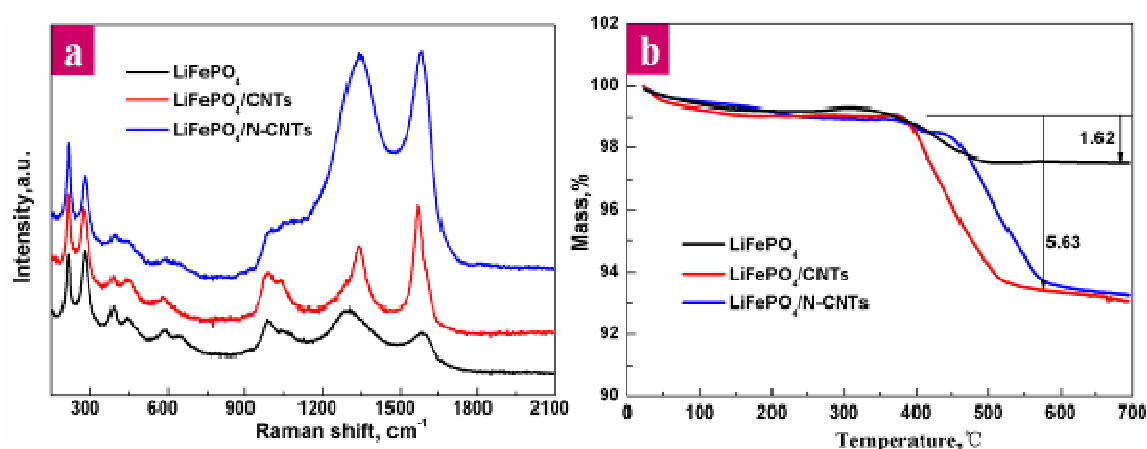


Figure 3.5 Raman spectra and TGA curves of the as synthesized porous LiFePO_4 and LiFePO_4 composites.

The Raman spectra of the pristine LFP and the modified composites are shown in Fig. 3.5a. Intense Raman modes were all observed at 216, 282, 393, 441, 987 and 1078 cm^{-1} in these three samples, which corresponds to the finger print peaks of orthorhombic symmetry LiFePO_4 [30]. Corresponding to the XRD results, the addition of CNTs and N-CNTs have no effects on the main structure of LFP. Carbon lines appeared at pristine LFP is due to residual carbon from the decomposition of citrate. The I_D/I_G ratio for pristine LFP is calculated to 4.97, indicating the large amount of amorphous carbon in the pristine LFP, which delivers low contribution to the electronic conductivity of the cathode material [31]. For modified composites, the I_D/I_G ratios are 0.55 and 0.95, respectively. Higher I_D/I_G ratio of N-CNTs indicated higher defectiveness, manifesting more defects existed in N-CNTs than CNTs.

To confirm the carbon content of the LFP and the modified composites, the thermal gravimetric analysis (TGA) was performed on the LFP composites. Fig. 3.5b compares the TG curves of LFP versus the modified composites. According to the TG curves of LFP composites in air, at low temperature around 230 $^{\circ}\text{C}$, the weight loss is related to the absorbed moisture, then two reactions happens in the range of 340 $^{\circ}\text{C}$ to 550 $^{\circ}\text{C}$, as previous reported, one is the oxidation of LiFePO_4 to $\text{Li}_3\text{Fe}_2(\text{PO}_4)_3$ and Fe_2O_3 , which resulted in a weight gain of 5% [32, 33], the other is the combustion of the carbon to CO_2 . It is noted that a plateau appeared at about 400 $^{\circ}\text{C}$, indicating that the mass of the sample remains constant, which is due to the loss of the weight from the oxidation of carbon comparative to the gain of weight from the formation of Fe (III). The total weight loss for LFP in the TG curve is 1.62%, therefore the carbon content of LFP is 6.62 wt% (1.62 wt% + 5 wt%). For the modified composites, the incorporated CNTs and N-CNTs contributed to the increased carbon amount. Due to the same addition, the carbon content is 10.63 wt% (5.63 wt%+ 5 wt%) for both composites.

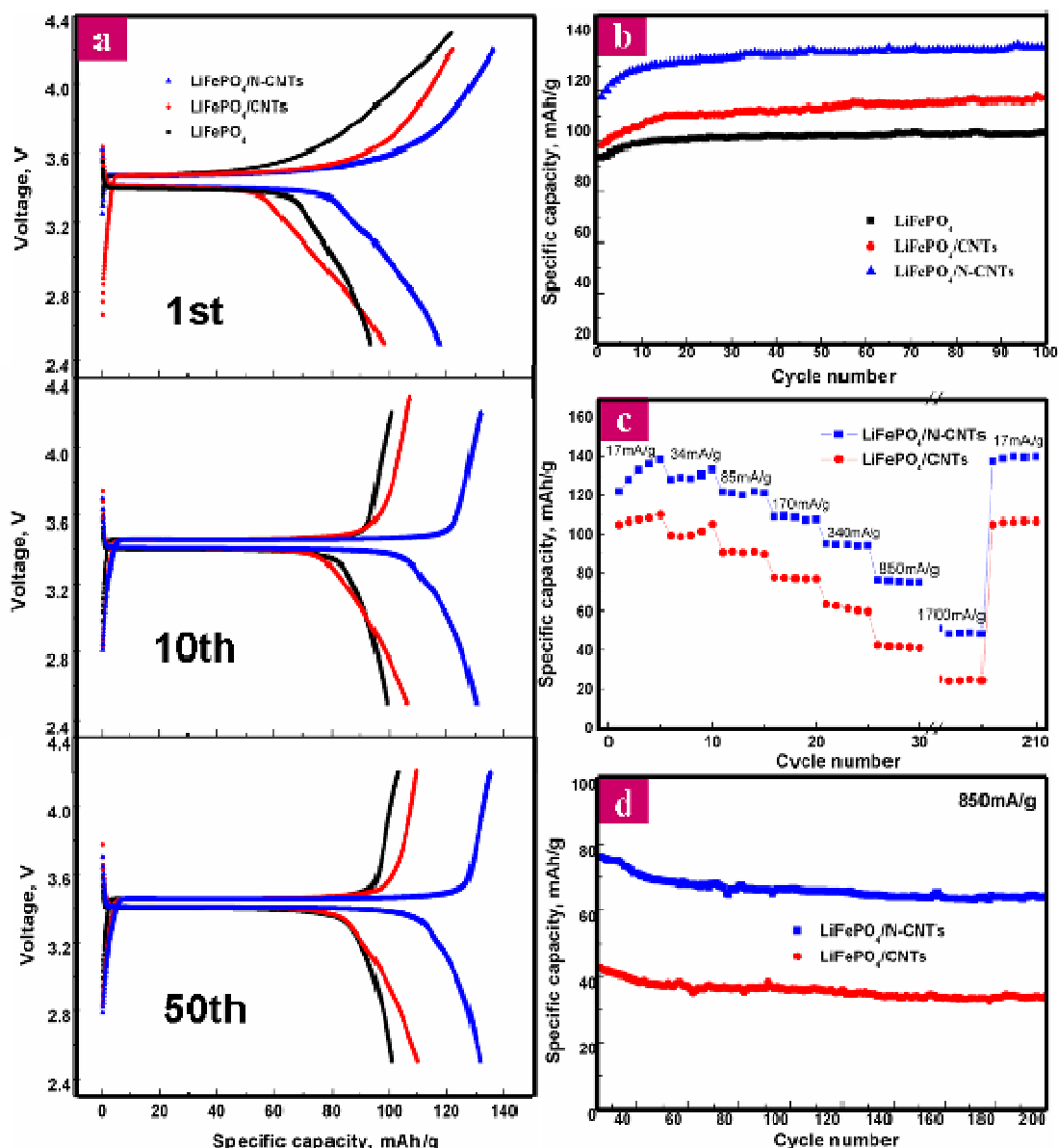


Figure 3.6 (a) Charge-discharge profiles of porous LiFePO_4 , $\text{LiFePO}_4/\text{CNTs}$ and $\text{LiFePO}_4/\text{N-CNTs}$ cycled at a current rate of 17 mA g^{-1} ; (b) Discharge capacities during continuous cycling of lithium ion batteries at 17 mA g^{-1} ; (c) rate performance; (d) cycle performance of $\text{LiFePO}_4/\text{CNTs}$ and $\text{LiFePO}_4/\text{N-CNTs}$ cycled at a current rate of 850 mA g^{-1} .

Fig. 3.6 exhibits electrochemical performance for the pristine LFP and modified composites. Fig. 3.6a shows the charge and discharge curves of LFP, LFP/CNTs and LFP/N-CNTs at a constant current density of 17 mA g^{-1} for the 1st, 10th and 50th cycles.

The initial profiles for all three samples exhibit a flat voltage plateau at around 3.4 V (versus Li^+/Li), which is resulted from the two-phase redox reaction between FePO_4 and LiFePO_4 [6]. From the initial cycle of LFP/N-CNTs, the charge capacity delivery is 137 mAh g^{-1} ($\text{FePO}_4 + \text{Li} \rightarrow \text{LiFePO}_4$) and 119 mAh g^{-1} for discharge ($\text{LiFePO}_4 \rightarrow \text{Li} + \text{FePO}_4$), demonstrating the columbic efficiency is 87%. For LFP/CNTs and LFP, the first columbic efficiency values are 80% and 77%, respectively. High columbic efficiency indicates high conversion of the active materials, which can be attributed to high conductivity of the composites. According to our testing results, the electronic conductivity for the LFP/N-CNTs can reach 105 S m^{-1} , while the electronic conductivity value for LFP/CNTs and LFP are 40 and 10 S m^{-1} , respectively. Besides, 3D network provided by the incorporated N-CNTs into LFP can increase the electrons and lithium ion diffusion rate. On the subsequent cycling, such as 10th and 50th cycles, the charge/discharge efficiency is close to 100%, and the capacity retention is excellent. The voltage profiles of all three samples show a narrow gap between charge and discharge, indicating low electrode resistance. The narrower the gap, the lower electrode resistance is. From these three cycles (1st, 10th and 50th), the LFP/N-CNTs show narrower gap than the other two, indicating lower electrode resistance of the composite, which is in accordance with the conductivity testing results. In addition, the polarization between the charge and discharge curves of the modified LFP composites is less than the pristine porous LFP, since the electrochemical conductivity of LFP is enhanced by addition of CNTs and N-CNTs. Closer examination of the curves shows that the polarization of LFP/N-CNTs is less than that of LFP-CNTs composites because nitrogen can induce defects to lower the activation energy for Li^+ diffusion, thus increase the Li^+ diffusion rate [34]. For this reason, take the 50th cycle for example, LFP/N-CNTs composites exhibits a discharge capacity of 138 mAh g^{-1} at a current rate of 17 mA g^{-1} , while pristine porous LFP and LFP/CNTs composites display discharge capacity of 104 and 113 mAh g^{-1} , respectively.

In order to examine the cycle life of porous LFP and modified composites, long term discharge cycling at 17 mA g^{-1} is performed, as shown in Fig. 3.6b. After 100 cycles, N-CNTs and CNTs modified composites still delivered the capacities of 138 and 113 mAh

g^{-1} respectively, while the pristine porous LFP displays a capacity of 104 mAh g^{-1} , indicating that the incorporated N-CNTs and CNTs drastically enhance the specific capacity. The explanation is as follows: 3D network of the CNTs and N-CNTs combined the porous LFP particles increases the electrons and lithium ion diffusion rate. More importantly, unique cross-linked CNTs and N-CNTs facilitate electrons and lithium ion transfer in the inert zones, leading to high specific capacity. It should be noticed that the specific capacity of N-CNTs modified composites is more superior than that of CNTs modified ones, because N-CNTs owns higher electronic conductivity so that improve the lithium ion and electrons diffusion rate [24]. Moreover, more uniformly dispersion of N-CNTs into the porous network also provides more sufficient electronic conduction, leading to higher specific capacity of LFP. In addition, it was reported that functionalized CNTs could act as a cathode to store some lithium ion and deliver a reversible capacity [35]. In this case, N-CNTs might contribute some capacity as well.

The comparison of rate performance for the LFP and the modified samples at different current densities from 17 mA g^{-1} to 1700 mA g^{-1} is shown in Fig. 3.6c. Under all charge/discharge rates, the discharge capacities of LFP/N-CNTs are higher than those of LFP/CNTs, highlighting N-CNTs modification is better than that of CNTs. It is noted that at high rates, such as 1700 mA g^{-1} , the discharge capacity for LFP/N-CNTs composites still remains stable, but the capacity of LFP/CNTs fades significantly even at a lower rate of 340 mA g^{-1} . Under high current density of 850 mA g^{-1} , as shown in Fig. 3.6d, after 200 cycles, the LFP/N-CNTs still delivers a capacity of 68 mAh g^{-1} , which is twice of that of LFP/CNTs. As the observation from the above SEM images, more uniformly dispersed N-CNTs into the porous networks and inherent higher electronic conductivity facilitate the lithium ions and electrons diffusion, resulting in the excellent electrochemical performance at high-rate cycling. Another important feature is that as long as the current rate reverses back to a low current density of 17 mA g^{-1} , the discharge capacity can recover to the original value for both modified samples, demonstrating that our 3D porous architecture is tolerant to varied charge and discharge currents, which is a highly desirable property required for lithium ion batteries applied in hybrid vehicle and electric vehicle markets.

3.4 Conclusions

In summary, 3D LFP/N-CNTs with hierarchically structure can be fabricated by a two-step process, sol-gel and calcination. Interpenetrating conductive N-CNTs and CNTs networks in the porous composites play the role of electron transport path in LFP. In comparison with LFP/CNTs, LFP/N-CNTs present higher specific capacity and excellent rate performance, which is resulted from the improved lithium ions and electrons accessibility provided by the well dispersed N-CNTs in the porous LFP network and inherent superior electronic conductivity of N-CNTs. Our results demonstrated that LFP/N-CNTs is a promising cathode material for lithium ion battery. This novel strategy can be extended to other cathode (or anode) materials of advanced batteries applied in electric vehicles.

3.5 Acknowledgements

This work is supported by Natural Sciences and Engineering Research Council of Canada (NSERC), Phostech Lithium Inc., Canada Research Chair (CRC) Program and the University of Western Ontario. The authors express their sincere thanks to Dr Henry Huang for their kind help and discussions.

3.6 Supporting Information

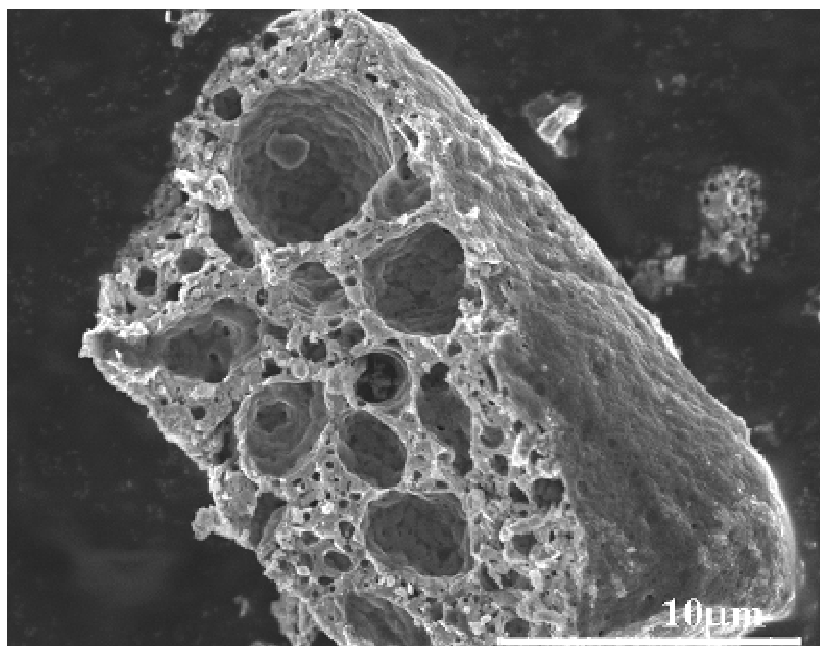


Figure S 3.1 The cross-sectional image of the cracked LiFePO_4 particle.

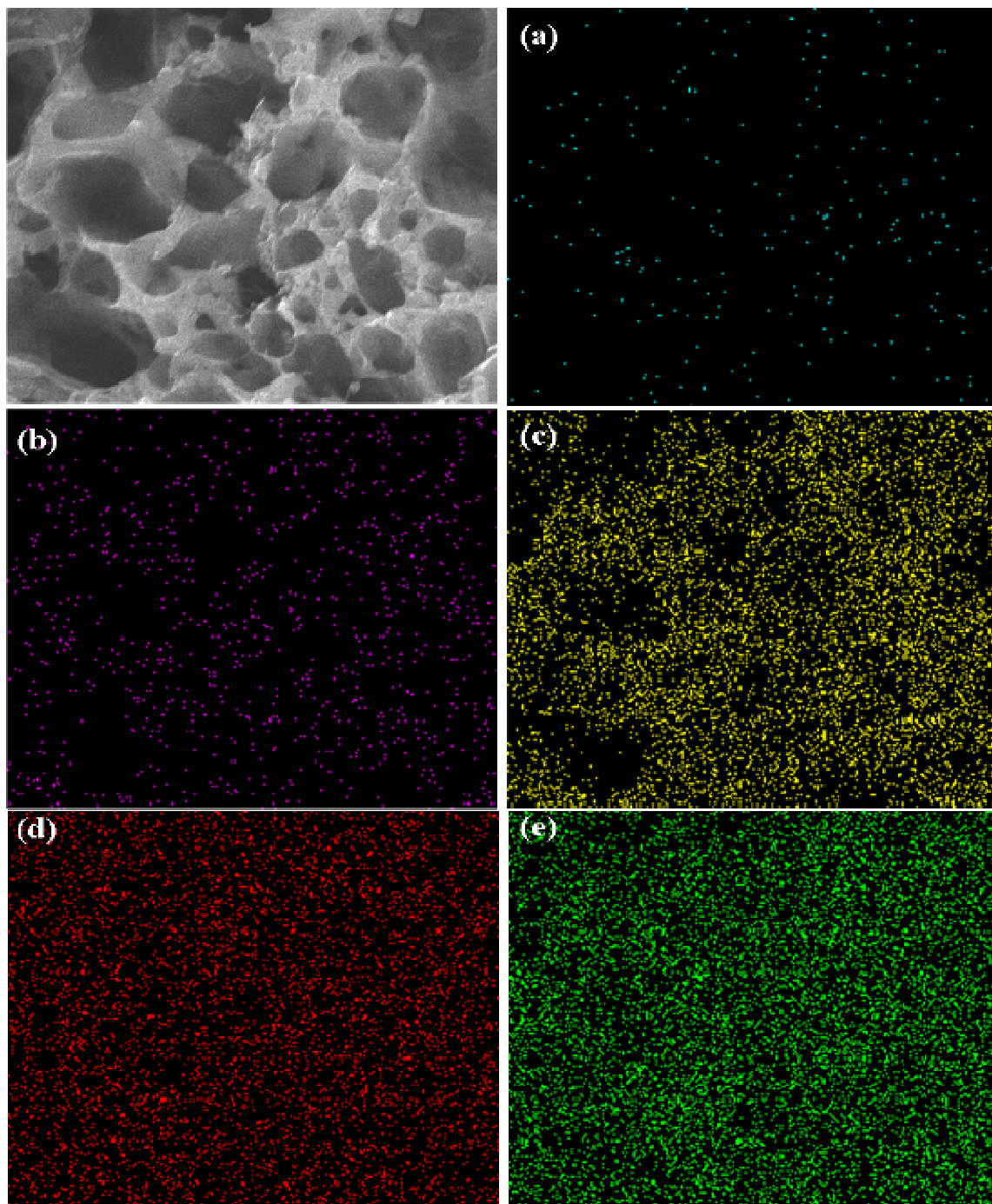


Figure S 3.2 Elements mapping in LiFePO₄/N-CNTs composites: (a) N element; (b) C element; (c) O element; (d) Fe element; (e) P element.

3.7 Reference

- [1] P. G. Bruce, B. Scrosati and J. -M. Tarascon, *Angew. Chem., Int. Ed.*, 2008, **47**, 2930;
- [2] M. Armand and J. -M. Tarascon, *Nature*, 2008, **451**, 652.
- [3] K. Saravanan, M. V. Reddy, P. Balaya, H. Gong, B. V. R. Chowdari and J. J. Vittal, *J. Mater. Chem.*, 2009, **19**, 605.
- [4] Y. S. Hu, Y. G. Guo, R. Dominko, M. Gaberscek, J. Jamnik and J. Maier, *Adv. Mater.*, 2007, **19**, 1963.
- [5] L.-F. Cui, R. Ruffo, C. K. Chan, H. Peng and Y. Cui, *Nano Lett.*, 2009, **9**, 491.
- [6] A. K. Padhi, K. S. Nanjundaswamy and J. B. Goodenough, *J. Electrochem. Soc.*, 1997, **144**, 1188.
- [7] A. S. Andersson, J. O. Thomas, B. Kalska and L. Haggstrom, *Electrochem. Solid-State Lett.*, 2000, **3**, 66.
- [8] A.S. Andersson and J.O. Thomas, *J. Power Sources*, 2001, **97–98**, 498–502.
- [9] B. Kang and G. Ceder, *Nature*, 2009, **458**, 190.
- [10] A. V. Murugan, T. Muraliganth and A. Manthiram, *Electrochem. Commun.*, 2008, **10**, 903.
- [11] P. S. Herle, B. Ellis, N. Coombs and L. F. Nazar, *Nature materials*, 2004, **3**, 147.
- [12] K. L. Harrison and A. Manthiram, *Inorg. Chem.*, 2011, **50**, 3613.
- [13] N. Ravet, J.B. Goodenough, S. Besner, M. Simoneau, P. Hovington and M. Armand, Abstract 127, 196th ECS, Honolulu, Hawaii, 1999, 17.
- [14] Y. -H. Huang and J. B. Goodenough, *Chem. Mater.*, 2008, **20**, 7237.
- [15] K. Zaghib, J. Shim, A. Guerfi, P. Charest and K. A. Striebel, *Electrochem. Solid-State Lett.*, 2005, **8**, A207.

- [16] R. Dominko, M. Bele, J. M. Goupil, M. Gaberscek, M. Remskar, D. Hanzel, I. Arcon and J. Jamnik, *Chem. Mater.*, 2007, **19**, 2960.
- [17] C.A. J. Fisher, V. M. Hart Prieto and M. S. Islam, *Chem. Mater.*, 2008, **20**, 5907.
- [18] J. Liu, M. Kunz, K. Chen, N. Tamura and T. J. Richardson, *J. Phys. Chem. Lett.*, 2010, **1**, 2120.
- [19] F. Yu, J. Zhang, Y. Yang and G. Song, *J. Power Sources*, 2009, **189**, 794.
- [20] S. W. Oh, S. -T. Myung, S.-M. Oh, K. H. Oh, K. Amine, B. Scrosati and Y.-K. Sun, *Adv. Mater.* 2010, **22**, 4842.
- [21] S. W. Oh, S.-T. Myung, H. J. Bang, C. S. Yoon, K. Amine, Y.-K. Sun, *Electrochem. Solid-State Lett.*, 2009, **12**, 181.
- [22] C. M. Doherty, R. A. Caruso, B. M. Smarsly, P. Adelhelm and C. J. Drummond, *Chem. Mater.*, 2009, **21**, 5300.
- [23] Y. Zhou, J. Wang, Y. Hu, R. O'Hayreb and Z. Shao, *Chem. Commun.*, 2010, **46**, 7151.
- [24] H. Liu, Y. Zhang, R. Li, X. Sun, D. Désilets and H. Abou-Rachid, *Carbon*, 2010, **48**, 1498.
- [25] J. Liu, Y. Zhang, M. Ionescu, R. Li and X. Sun, *Appl. Surf. Sci.*, 2011, DOI: 10.1016/j.apsusc.2011.04.041.
- [26] Y. T. Lee, N. S. Kim, S. Y. Bae, S. -C. Yu, H. Ryu, H. J. Lee and J. Park, *J. Phys. Chem. B*, 2003, **107**, 12958.
- [27] H. Hiura, T. W. Ebbesen, K. Tanigaki and H. Takahashi, *Chem., Phys. Lett.*, 1993, **202**, 509.
- [28] A. A. Salah, A. Mauger, C. M. Julien and F. Gendron, *Mater. Sci. Eng. B*, 2006, **129**, 232.

- [29] S. P. Ong, L. Wang, B. Kang and G. Ceder, Chem. Mater., 2008, **20**, 1799..
- [30] A. A. Salah, A. Mauger and K. Zaghib, J. Electrochem. Soc., 2006, **153**, 1692
- [31] M. M. Doeff, J. D. Wilcox, R. Kostecki and G. Lau, J. Power Sources, 2006, **163**, 180.
- [32] I. Belharouak, C. Johnson and K. Amine, Electrochem. Commun., 2005, **7**, 983.
- [33] X. Lou and Y. Zhang, J. Mater. Chem., 2011, **21**, 4156.
- [34] Z. Liu, X. Huang and D. Wang, Solid State Commun., 2008, **147**, 505.
- [35] S. W. Lee, N. Yabuuchi, B. M. Gallant, S. Chen, B. S. Kim, P. T. Hammond and Y. S. Horn, Nature Nanotechnology, 2010, **5**, 531.
- [36] X. Li, J. Liu, Y. Zhang, Y. Li, H. Liu, X. Meng, J. Yang, D. Geng, D. Wang, R. Li and X. Sun, J. Power Sources, 2012, **197**, 238.

Chapter 4

4 3D Porous LiFePO₄/Graphene Hybrid Electrodes with Enhanced Performance for Li-ion Batteries

Based on last chapter (3), the N-CNTs modified composites deliver higher specific capacity than CNTs modified and pristine ones. Graphene nanosheet is another carbon additive since it also possesses superior conductivity. Besides this, flexible structure and high surface area (theoretical value of $2630 \text{ m}^2 \text{ g}^{-1}$) can offer an improved interfacial contact with active material. Such promising advantages make graphene a great potential material for use in LFP.

In this chapter, three-dimensional porous self-assembled LiFePO₄/graphene (LFP/G) composite was successfully fabricated using a facile template-free sol-gel approach. Graphene nanosheets were incorporated into the porous hierarchical network homogeneously, which greatly enhances the electrical conductivity and efficient use of the LiFePO₄ (LFP), leading to an outstanding electrochemical performance of the hybrid cathodes. The obtained LFP/G composite has a reversible capacity of 146 mAh g^{-1} at 17 mA g^{-1} after 100 cycles, which is more than 1.4 times greater than that of porous LFP (104 mAh g^{-1}). Moreover, the porous LFP/G composite also exhibits a desirable tolerance to varied charge/discharge currents.

Keywords: Graphene nanosheet, Hierarchical network, LiFePO₄, Lithium ion batteries

Note: This work has been published.

J. Yang, J. Wang, D. Wang, X. Li, D. Geng, G. Liang, M. Gauthier, R. Li, X. Sun, **J. Power Sources**, 2012, 208, 340-344.

4.1 Introduction

Recently, Li-ion batteries (LIB) have been recognized as alternative energy sources for electrical vehicles (EVs) and hybrid electrical vehicles (HEVs) [1, 2]. The pioneering work of Goodenough [3], demonstrated that LiFePO_4 is a desirable cathode material with outstanding features, such as low cost, environmental compatibility, high theoretical specific capacity, and especially, superior safety performance. Unfortunately, the slow rate of lithium ion diffusion and poor electrical conductivity ($\sim 10^{-9} \text{ S cm}^{-1}$) limits the practical use of LiFePO_4 in LIB for EVs and HEVs [4]. To improve Li-ion diffusion within LiFePO_4 and the $\text{LiFePO}_4/\text{FePO}_4$ interface, one effective approach is to design nanosized LiFePO_4 particles, which shorten the Li-ion insertion/extraction pathway [5-13].

However, this strategy adversely affects the tap density and volumetric energy density, hampering its use in industrial-scale technologies. Therefore, the development of unique geometrical structures, such as micro-sized three-dimensional (3D) porous architectures, is a feasible strategy because such networks provide a high tap density, and a porous structure facilitates the fast and efficient transport of mass and charge [14]. In addition, the interconnected open pores of this structure favor electrolyte percolation into active materials and hence efficiently use electrode material [15, 16].

Carbon coating is the most common and effective way to enhance the electrical conductivity of LiFePO_4 (LFP) [13]. Various conductive additives have been reported in carbon/LFP to enhance its electrical conductivity [17-19]. For example, carbon nanotubes (CNT) were used as a novel carbon source because of their excellent electrical conductivity and network structure [20]. In comparison with CNTs, graphene can offer an improved interfacial contact because of its superior conductivity, flexible structure, and more important, high surface area (theoretical value of $2630 \text{ m}^2 \text{ g}^{-1}$) [21]. Such promising advantages make graphene a great potential material for use in LFP. Su et al. directly mixed graphene with LFP particles mechanically and produced a composite mixture with an improved electrochemical performance, but the graphene was not well dispersed within the mixture, which limited the enhancement in electrical conductivity [22].

Consequently, the creation of effective graphene conductive networks is crucial for fully utilizing this unique carbon material.

By combining the advantages of porous LFP and unique properties of graphene, herein, we develop a novel 3D hierarchical LiFePO_4 -graphene (LFP/G) hybrid cathode with a porous structure using a facile template-free sol-gel route. Graphene nanosheets, integrated with porous LFP, create an effective electronically conducting network. The development of this network in LFP/G yields a much better electrochemical performance as compared with pristine LFP.

4.2 Experimental

4.2.1 The procedures of materials synthesis

Graphene sheets used in this study were prepared through the thermal expansion of graphite oxide. The preparation methodology for these sheets has been described in another research paper [23]. In a typical sol-gel route of LFP/G, 20 mg of graphene nanosheets were firstly dissolved in 30 mL of water via strong ultrasonic agitation for 30 min. Then, 1.039 g of lithium dihydrogen phosphate and 2.449 g of iron (III) citrate were dissolved separately in 170 mL of water by stirring at 70 °C for 1h. The two solutions were mixed together and dried at 70 °C for 24 h. The obtained xerogel was subsequently fired in an argon atmosphere at 700 °C for 10 h. For the preparation of pristine porous LFP, graphene nanosheets were not added, but all other preparation methods followed the route used to obtain LFP/G.

4.2.2 Physical characterization

Scanning electron microscopy (SEM) imaging was carried out using a Hitachi S-4800 microscope with an operation voltage of 5 kV. Transmission electron microscopy (TEM) observations were performed with a Hitachi H-7000 microscope at an accelerating voltage of 100 kV. Raman scattering (RS) spectra were recorded on a HORIBA Scientific LabRAM HR Raman spectrometer system. The XRD analyses were conducted using a Rigaku rotating-anode X-ray diffractometer, which employs $\text{Co K}\alpha$ radiation.

Thermogravimetric analysis (TGA) curves were collected by using a Netzsch system with a heating rate of $10\text{ }^{\circ}\text{C min}^{-1}$ in air.

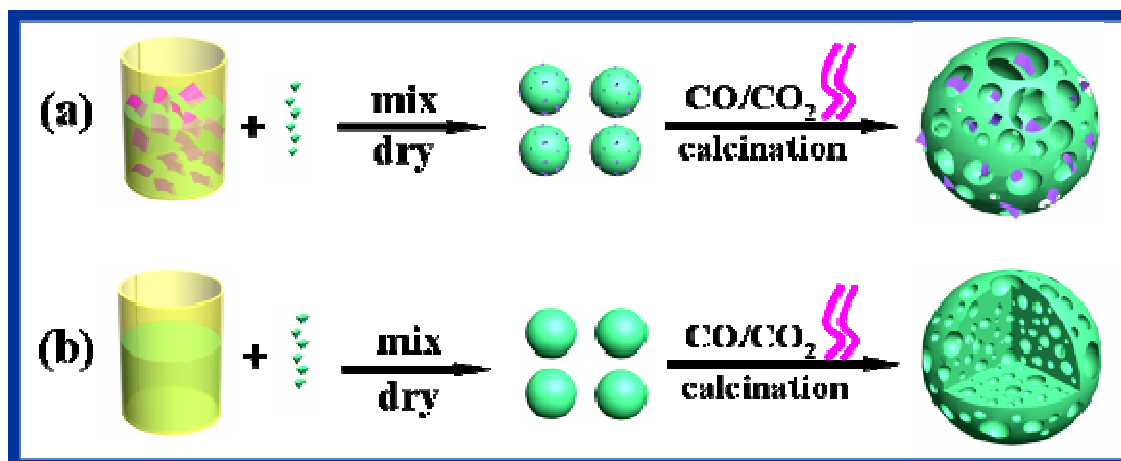
4.2.3 Electrochemical measurements

The LFP/G powder was mixed with acetylene black and polyvinylidene fluoride (PVDF) with a weight ratio of 75:15:10 in N-Methyl-2-pyrrolidone (NMP) solvent to produce the slurry. The resultant slurry, pasted on Al foil, was dried at $100\text{ }^{\circ}\text{C}$ under vacuum for 24 h to form the working electrode. The coin cells (2032) were then assembled in a high purity argon-filled glove box using lithium metal as the anode and 1 M LiPF_6 (dissolved in a solvent consisting of 50% ethylene carbonate and 50% dimethyl carbonate by volume) as the electrolyte.

The electrochemical performance of the as-obtained samples was conducted galvanostatically at various rates at room temperature using a computer-controlled battery test system (Arbin BT-2000 Battery Test System) within a voltage range of 2.5-4.2 V (vs. Li^+/Li). Cyclic voltamograms (CV) measurements were performed on an electrochemical workstation (Potentiostat/Galvanostat/EIS (VMP3)) over the potential range of 2.5-4.2 V (vs. Li^+/Li) at a scanning rate of 0.1 mV s^{-1} .

4.3 Results and discussion

The approach for LFP/G composite, schematically illustrated in Scheme 4.1a, starts with the dispersion of graphene sheets in deionized water, proceeds with the self-assembly of graphene with the LFP precursor, and ends with the crystallization of the LFP/G precursors. CO and CO_2 were evolved from the degradation of these precursors through annealing, resulting in the formation of a porous 3D network to obtain the final LFP/G product. A 3D cross-sectional view of LFP formation is shown in Scheme 4.1b. Porous LFP was also prepared by the same procedure for the sake of comparison.



Scheme 4.1 Scheme of 3D porous (a) LiFePO₄/graphene and (b) LiFePO₄ formation process

Figures 4.1a and 4.1b display the transmission electron microscopy (TEM) and scanning electron microscopy (SEM) images of graphene, respectively. As shown in the figures, the typical wrinkled graphene is composed of layered platelets. The micrographs of porous LFP composite are shown in Figures 4.1c-d. The cross section SEM images of pristine LFP demonstrate its porous structure (See Figure S4.1).

Because of the production of gases generated during the citric anion degradation and their subsequent expulsion from the LFP structure, the surface of the LFP particles demonstrates the formation of a porous architecture (Figure 4.1c). A close view shows the presence of abundant small nanometer-sized apertures (Figure 4.1d), indicating the formation of an interlaced pore system network. Figures 4.1e-f show the SEM images of self-assembled hybrid LFP/G composite. The incorporation of graphene nanosheets does not seem to affect the interlaced channels. Moreover, graphene nanosheets are embedded into the LFP uniformly (Figure 4.1e), resulting from the homogeneous dispersion of graphene within the LFP precursor suspension. The SEM images obtained under increased magnification further demonstrate that graphene is intimately incorporated into porous LFP particles (Figure 4.1f).

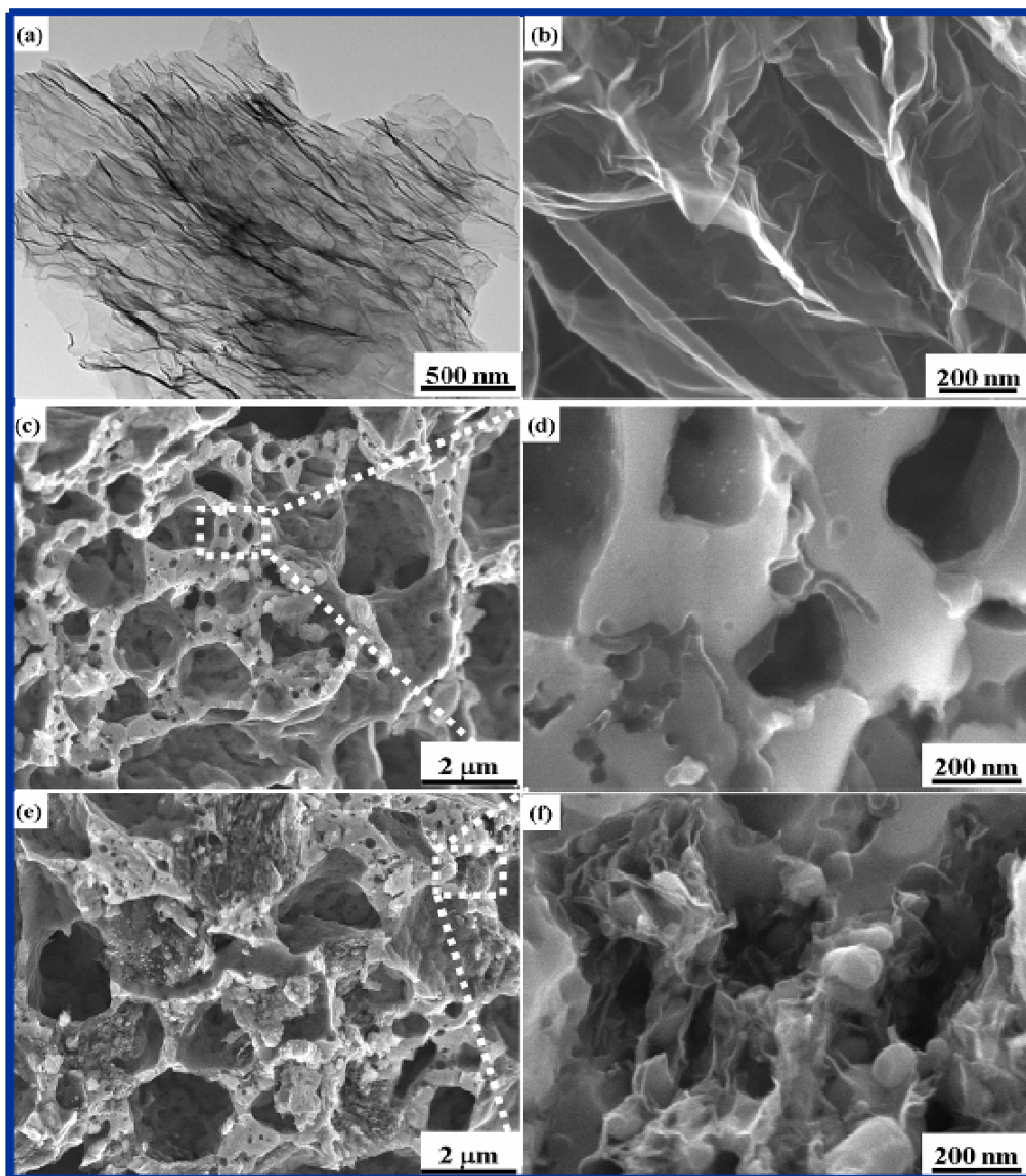


Figure 4.1 TEM image of (a) Graphene; SEM images of (b) Graphene, (c) and (d) Porous LiFePO₄ at different magnifications, (e) and (f) LiFePO₄/graphene composite at different magnifications.

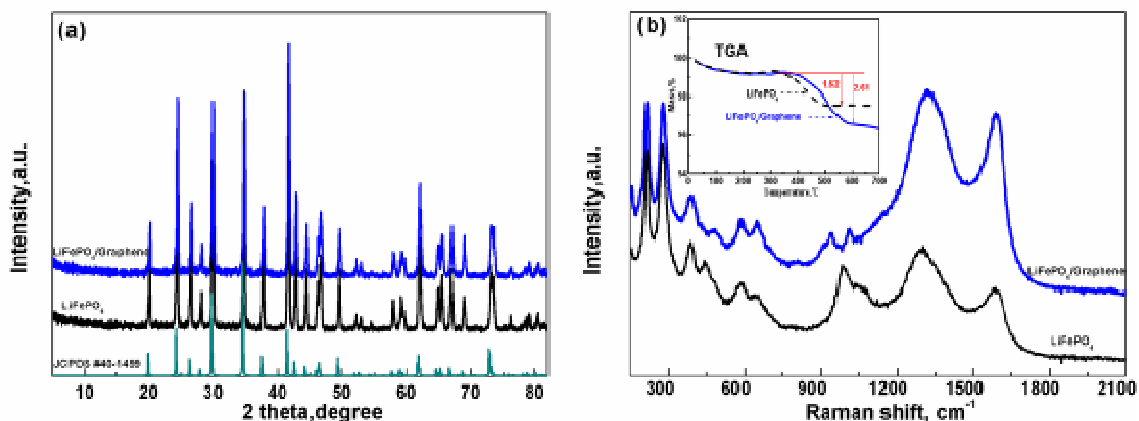


Figure 4.2 Powder X-ray diffraction (XRD) pattern (a), Raman spectra (b) and TGA curve of the inset of (b): porous LiFePO_4 and LiFePO_4 -Graphene composite.

Figure 4.2a compares the XRD patterns of the porous LFP with the LFP/G. Both patterns perfectly match the standard orthorhombic LiFePO_4 (JCPDS #40-1499), indicating that the obtained samples are of a high purity and exhibit a high crystallinity. Moreover, the addition of graphene has no effects on the crystal structure of LFP through Raman spectroscopy. The Raman spectra of both samples are shown in Figure 4.2b. Strong Raman peaks at 213, 280, 393, 441, 587 and 650 cm^{-1} can be detected for LFP and LFP/G, which are assigned to the fingerprint peaks of orthorhombic symmetry LFP [24]. Two broad peaks at 1315 and 1584 cm^{-1} are attributed to the D band and the G band, respectively [25]. The calculated peak intensity ratio (I_D/I_G) is an indicator of the degree of disordering in the carbon found in the samples, where a higher I_D/I_G ratio indicates a greater degree of disorder in the carbon arrangement [26]. Compared with the I_D/I_G ratio of 1.63 for LFP, the LFP/G shows a ratio of 1.08, indicating that the presence of graphite carbon in LFP/G is higher than in the pristine LFP, which will result in an increased electrical conductivity of pristine LFP.

The TGA curve is shown in the insert of Figure 4.2b. The weight changes of the pristine LFP and LFP/G are 1.62% and 2.61%, respectively. Combining the weight gain from the formation of $\text{Li}_3\text{Fe}_2(\text{PO}_4)_3$ and Fe_2O_3 upon heating in air [27], the weight loss gives a carbon content of 6% in LFP and 7% in LFP/G.

To examine the effectiveness of graphene nanosheets in improving the electrochemical performance of the electrode, the Li-ion insertion/extraction properties in LFP/G and LFP are compared, as shown in Figure 4.3. A single pair of oxidation and reduction peaks is observed for both samples, confirming the occurrence of a single electron transfer reaction in all samples during cycling, as demonstrated in Figure 4.3a. For porous LFP, the anodic oxidation occurs at 3.55 V, and the cathodic reduction appears at 3.32 V, corresponding to a 0.23 V potential interval. For LFP/G, the potential interval is 0.2 V. The reduced potential interval value represents improved reversibility and reactivity.

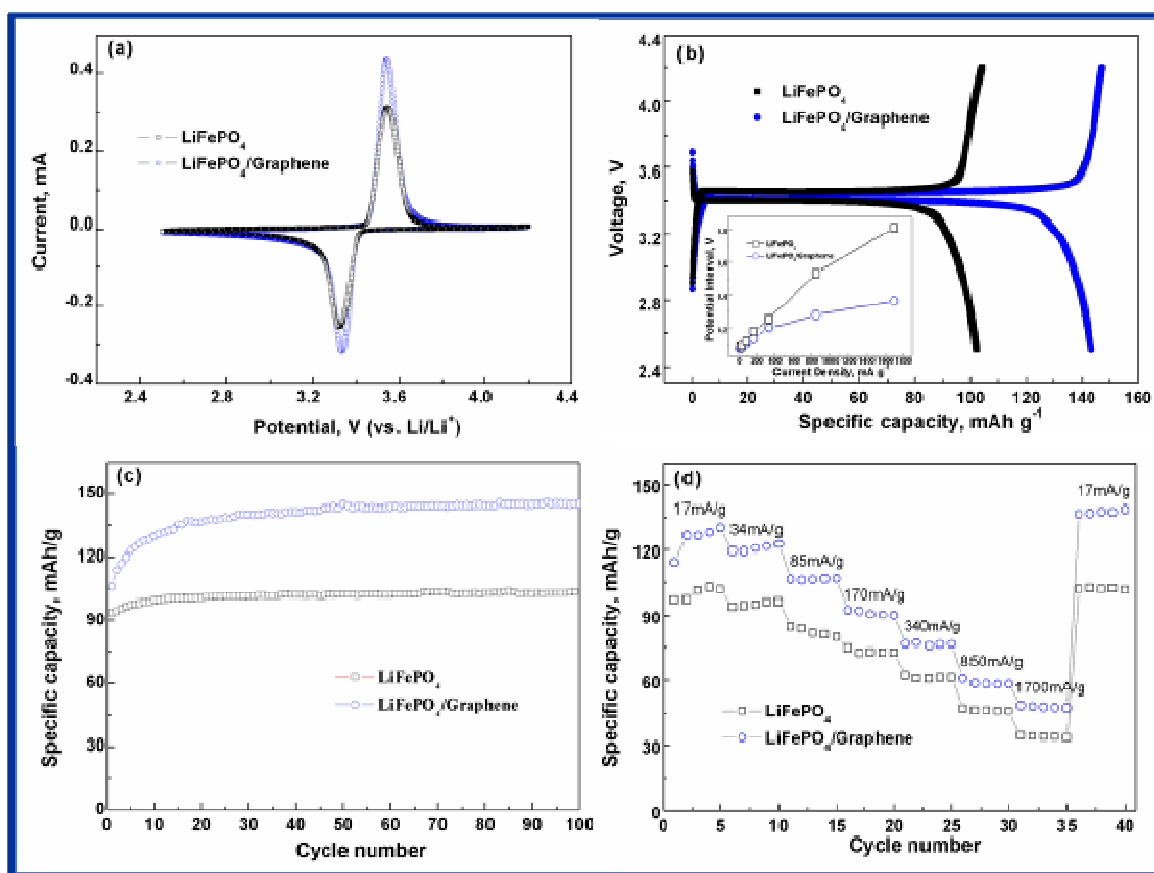


Figure 4.3 (a) Cyclic voltammograms (0.1 mV s^{-1}); (b) Charge-discharge profiles of porous LiFePO_4 , $\text{LiFePO}_4/\text{graphene}$ cycled at a current rate of 17 mA g^{-1} ; (c) Discharge capacities during continuous cycling of lithium cells at 17 mA g^{-1} ; (d) rate performance.

The charge–discharge profiles of the samples at 17 mA g^{-1} cycled in a potential window of 2.5–4.2 V (versus Li^+/Li) at room temperature are shown in Figure 4.3b. The performance discussed here is related to stable cycles. Typical flat plateaus over the voltage range of 3.4–3.5 V were obtained for both samples. Compared with porous LFP, LFP/G delivers higher charge and discharge capacities and a lower potential interval, indicating that porous LFP suffers from a larger polarization loss. The polarization between the charge and discharge plateau of the two samples increases along with an increase in the current density, as shown in the insert of Figure 4.3b. More important, the potential interval is higher for LFP than LFP/G under various current densities, especially at higher current densities. As an example, the potential interval for LFP and LFP/G at a current density of 1700 mA g^{-1} is 812 mV and 362 mV, respectively. As an electrode has a lower electrical resistance with a lowered potential interval, these results indicate that graphene could potentially alleviate the polarization loss of LFP/G during the cycling. To examine the cyclic performance of porous LFP and LFP/G, long-term discharge cycling was performed at 17 mA g^{-1} . The capacity stability was reached only after carrying out several initial cycles, and no detectable decline in capacity was observed over 100 discharge cycles for both samples, demonstrating that they have an excellent cycling performance, as shown in Figure 4.3c. After 100 cycles, LFP/G still delivered a capacity of 146 mAh g^{-1} , which is more than 1.4 times the capacity (104 mA h g^{-1}) of LFP, demonstrating that the incorporated graphene greatly enhances the specific capacity throughout the cycle process.

Figure 4.3d compares the rate performance of porous LFP and LFP/G at different current densities. Under all charge/discharge rates, the specific capacities of LFP/G are higher than those of the porous LFP. The discharge capacity for LFP/G still remains stable at an extremely high current density of 1700 mA g^{-1} , while the capacity of LFP decreases significantly even at a lower rate of 340 mA g^{-1} . As long as the current density reverts back to a low current density of 17 mA g^{-1} , the original discharge capacity of LFP/G can be recovered, demonstrating that our 3D porous architecture LFP/G is tolerant to varied charge and discharge currents, which is a highly desirable property for electrode materials in lithium ion batteries.

The improvement can be ascribed to two main factors: graphene nanosheets possess a higher degree of graphitization than amorphous carbon, which increases the speed of electron migration, and embedded graphene nanosheets act as a bridge to increase the area that is simultaneously accessible to electrons and lithium ions, thus significantly reducing the inert zones and leading to high specific capacity [22].

4.4 Conclusions

In summary, we have successfully prepared a 3D hierarchical self-assembled LFP/G hybrid network using a facile template-free sol-gel method. Graphene nanosheets were dispersed uniformly into the porous structure, which led to the efficient use of the active materials. In comparison with porous LFP, the hybrid LFP/G composite shows significantly enhanced Li-ion insertion/extraction kinetics, which demonstrates that graphene nanosheets are promising conductive additives for Li-ion battery electrode materials. The self-assembly hybrid systems can also be applied to other hybrid structures to optimize the performance of electrodes in the energy storage system of electric or hybrid electric vehicles.

4.5 Acknowledgments

We appreciate the support from Natural Sciences and Engineering Research Council of Canada (NSERC), Phostech Lithium Inc., Canada Research Chair (CRC) Program and the University of Western Ontario.

4.6 Supporting Information

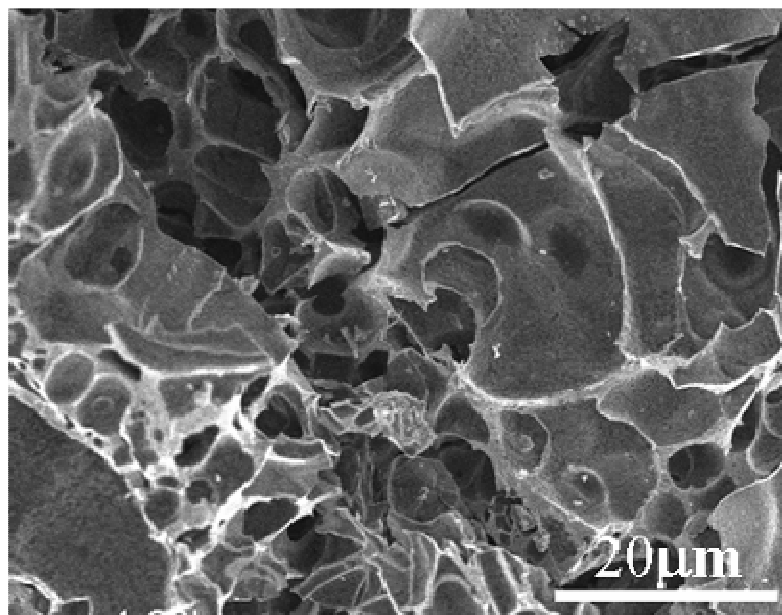


Figure S 4.1 Cross section SEM image of pristine LFP.

The cross section SEM images of pristine LFP demonstrate its porous structure.

4.7 References

- [1] J. Maier, Nat. Mater. 2005, **4**, 805.
- [2] J. M. Tarascon, M. Armand, Nature, 2001, **414**, 359.
- [3] A. K. Padhi, K. S. Nanjundaswamy, J. B. Goodenough, J. Electrochem. Soc., 1997, **144**, 1188.
- [4] B. L. Ellis, W. R. M. Makahnouk, Y. Makimura, K. Toghill, L. F. Nazar, Nature Mater., 2007, **6**, 147.
- [5] Y. Wu, Z. Wen, J. Li, Adv. Mater., 2011, **23**, 1126.
- [6] J. S. Sakamoto, B. Dunn, J. Mater. Chem., 2002, **12**, 2859.
- [7] M. S. Islam, D. J. Driscoll, C. A. J. Fisher, P. R. Slater, Chem. Mater., 2005, **17**, 5085.
- [8] C. Delmas, M. Maccario, L. Croguennec, F. L. Cras, F. Weill, Nat. Mater., 2008, **7**, 665.
- [9] R. Dominko, M. Bele, J. M. Goupil, M. Gaberscek, M. Remskar, D. Hanzel, I. Arcon, J. Jamnik, Chem. Mater., 2007, **19**, 2960.
- [10] Z. H. Chen, J. R. Dahn, J. Electrochem. Soc., 2002, **149**, A1184.
- [11] F. Yu, J. Zhang, Y. Yang, G. Song, J. Power Sources, 2009, **189**, 794.
- [12] S. W. Oh, S. T. Myung, S. M. Oh, K. H. Oh, K. Amine, B. Scrosati, Y.K. Sun, Adv. Mater., 2010, **22**, 4842.
- [13] J. Wang, X. Sun, Energy Environ. Sci., 2012, **5**, 5163.
- [14] A. Magasinski, P. Dixon, B. Hertzberg, A. Kvit, J. Ayala, G. Yushin, Nat. Mater., 2010, **9**, 353.
- [15] Y. S. Hu, P. Adelhelm, B. M. Smarsly, S. Hore, M. Antonietti, J. Maier, Adv. Func. Mater., 2007, **17**, 1873.

- [16] W. Zhou, M. Yao, L. Guo, Y. M. Li, J. H. Li, S. H. Yang, *J. Am. Chem. Soc.*, 2009, **131**, 2959.
- [17] C. M. Doherty, R. A. Caruso, B. M. Smarsly, P. Adelhelm, C. J. Drummond, *Chem. Mater.*, 2009, **21**, 5300.
- [18] P. S. Herle, B. Ellis, N. Coombs, L. F. Nazar, *Nat. Mater.*, 2004, **3**, 147.
- [19] D. Lepage, C. Michot, G. X. Liang, M. Gauthier, S. B. Schougaard, *Angew. Chem. Int. Ed.*, 2011, **50**, 6884.
- [20] Y. Zhou, J. Wang, Y. Hu, R. O'Hayreb, Z. Shao, 2010, **46**, 7151.
- [21] A. Peigney, C. Laurent, E. Flahaut, R. R. Bacsa, A. Rousset, *Carbon*, 2001, **39**, 507.
- [22] S. Fang-Yuan, Y. Conghui, H. Yan-Bing, L. Wei, C. Wei, J. Fengmin, L. Baohua, Y. Quan-Hong, K. Feiyu, *J. Mater. Chem.*, 2010, **20**, 9644.
- [23] W. S. Hummers, R. E. Offeman, *J. Am. Chem. Soc.*, 1958, **80**, 1339.
- [24] A. A. Salah, A. Mauger, K. Zaghib, *J. Electrochem. Soc.*, 2006, **153**, A1692.
- [25] H. Hiura, T. W. Ebbesen, K. Tanigaki, H. Takahashi, *Chem. Phys. Lett.*, 1993, **202**, 509.
- [26] T. Muraliganth, A. V. Murugan, A. Manthiram, *J. Mater. Chem.*, 2008, **18**, 5661.
- [27] I. Belharouak, C. Johnson, K. Amine, *Electrochem. Commun.*, 2005, **7**, 983.

Chapter 5

5 Stacked Graphene and Unfolded Graphene Impact on Morphology of LiFePO_4 as Superior Cathode Material for Rechargeable Lithium Batteries

In Chapter 4, stacked graphene nanosheets were used as a 3D network to incorporate LFP particles, and this modification improved the performance of the composite (146 mA h g^{-1} at 0.1C). The wrinkled graphene nanosheets were distributed uniformly into the LFP particles. However, on a large scale, the stacked graphene nanosheets combined in a limited way with LFP, only the surface portion of the stacked graphene nanosheets can be used to increase the electronic conductivity, as the interior layers were not utilized. In addition, the unattached LFP particles were not sufficiently used during cycling. Compared with stacked graphene, unfolded graphene with thinner and smaller size will allow a more uniform dispersion of the LiFePO_4 precursor and a larger contact area between the graphene and the LFP active material and thereby full utilization of the unfolded graphene. Further, unfolded graphene, which has a higher surface area than stacked graphene, provides more nucleation sites to anchor LFP nuclei.

In this chapter, we describe the use of unfolded graphene as a three dimensional (3D) conducting network for LiFePO_4 nanoparticle growth. Compared with stacked graphene, which has a wrinkled structure, the use of unfolded graphene enables better dispersion of LiFePO_4 and restricts the LiFePO_4 particle size at nanoscale. More importantly, it allows each LiFePO_4 particle to be attached to the conducting layer, which could greatly enhance the electronic conductivity and thereby realizing the full potential of the active materials. Based on its superior structure, after post treatment for 12 hours, the LiFePO_4 /unfolded graphene nanocomposite achieved a discharge capacity of $166.2 \text{ mA h g}^{-1}$ in the 1st cycle, which is 98% of the theoretical capacity (170 mAh g^{-1}). The composite also displayed stable cycling behavior up to 100 cycles, whereas LiFePO_4 /stacked graphene composite with a similar carbon content could deliver a discharge capacity of only 77 mA h g^{-1} in the 1st cycle. X-ray absorption near-edge spectroscopy (XANES) provided spectroscopic

understanding of the crystallinity of LiFePO_4 and chemical bonding between LiFePO_4 and unfolded graphene.

Key words: Nanostructured LiFePO_4 , Unfolded Graphene, High Specific Capacity, Lithium ion Batteries.

Note: This work has been published. (**Back Cover Page, highlighted by "Green Car Congress"**)

J. Yang, J. Wang, Y. Tang, D. Wang, X. Li, Y. Hu, R. Li, G. Liang, T.-K. Sham, X. Sun, **Energy Environ. Sci.** 2013, 6, 1521-1528.

5.1 Introduction

The use of lithium ion batteries (LIBs) for electrical vehicles (EVs) and hybrid electrical vehicles (HEVs) has been pursued in an attempt to displace fossil fuel and address environmental issues [1-3]. Cost, life time and safety are the major issues in the successful application of LIBs for electrical energy storage involved in transportation [4, 5]. Moreover, the high storage performance of electrical energy at high charge and discharge rates is essential for EVs and HEVs [6]. LiFePO_4 (LFP) has garnered the most interest because of its environmental benignity, high safety, acceptable operating voltage (3.4 V vs. Li^+/Li), and reasonable theoretical capacity of 170 mA h g^{-1} [7]. However, the challenge for the application of LFP in EVs and HEVs is the sluggish diffusion of lithium ions and the poor electrical conductivity of LFP ($\sim 10^{-9} \text{ S cm}^{-1}$) [8]. To overcome the ionic and electronic transport limitations, a variety of methods have been attempted, including metal doping [9, 10], surface coating or admixing with electronically conductive materials [11-16], and controlling the particle-size [17,18]. Of these methods, carbon coating and conductive additives are the most effective and facile for improving the conductivity of LFP [12, 13]. However, uniform coating of LFP is difficult to achieve [19, 20], so the electrode performance is limited in terms of rate capability and lifetime.

To enhance the performance of the electrode materials, graphene has recently been used as a 3D conducting matrix to grow and anchor insulating materials because of its superior conductivity, high mechanical strength, structural flexibility, and more importantly, high surface area (theoretical value of $2630 \text{ m}^2 \text{ g}^{-1}$) [21-23]. Therefore, the application of 2D graphene nanosheets to allow the effective use of the active materials is essential in high-power batteries.

Some recent studies have focused on graphene-modified LFP. Ding et al. fabricated a LFP/graphene composite using a co-precipitation method [24]. In their work, the graphene suspension was prepared first, followed by the addition of a precursor into the solution, and finally the graphene-modified LFP was obtained by post-heat treatment. However, there were some unattached and aggregated LFP particles in the composites. In this case, the unattached LFP was not sufficiently utilized, thereby resulting in a limited

enhancement of the specific capacity. Su et al. mechanically mixed graphene with LFP particles. This method did not adequately combine LFP and graphene because the graphene was not well dispersed, resulting in limited utilization of LFP active material (150 mA h g^{-1} at 0.1C) [25]. Our previous work also investigated graphene-modified LFP in which graphene nanosheets were used as a 3D network to incorporate LFP particles, and this modification improved the performance of the composite (146 mA h g^{-1} at 0.1C) [26]. The wrinkled graphene nanosheets were distributed uniformly into the LFP particles. However, on a large scale, the stacked graphene nanosheets only combined in a limited way with LFP.

Based on the above studies, only the surface portion of the stacked graphene nanosheets can be used to increase the electronic conductivity, as the interior layers were not utilized. In addition, the unattached LFP particles were not sufficiently used during cycling [26]. Compared with stacked graphene, unfolded graphene possesses fewer layers and is smaller, allowing a more uniform dispersion of the LiFePO_4 precursor and a larger contact area between the graphene and the LFP active material and thereby full utilization of the unfolded graphene. In addition, unfolded graphene, which has a higher surface area than stacked graphene, provides more nucleation sites [22, 23] to anchor LFP nuclei, further restricting the size and agglomeration of the LFP particles.

In this paper, we applied unfolded graphene as a conducting matrix in order to sufficiently utilize the LFP active materials. To demonstrate good dispersion of LFP on the unfolded graphene, stacked graphene was used for comparison. Unfolded graphene improved the dispersion and greatly enhanced the utilization of LFP in comparison with stacked graphene nanosheets. Nano-sized LFP particles were dispersed uniformly and tightly anchored to the unfolded graphene network, whereas larger sized (micro-scale) LFP particles were loosely attached on the stacked graphene. Furthermore, the unfolded graphene matrix acted as a 3D network, enabling Li^+ and electrons to migrate and reach each LFP particle and resulting in a high discharge capacity of $166.2 \text{ mA h g}^{-1}$, which is close to the theoretical capacity. Various advanced characterization techniques including field-emission scanning electron microscopy (SEM), transmission electron microscopy

(TEM), high-resolution TEM (HRTEM), X-ray diffraction (XRD), Raman and synchrotron analysis, were used to understand and explain the results.

5.2 Experimental

5.2.1 Preparation of LiFePO_4 /Stacked graphene and LiFePO_4 /unfolded graphene composites

Stacked graphene used in this study was prepared through the thermal expansion of graphite oxide (GO). And unfolded graphene was obtained by hydrazine reduction of GO. In detail, we first use concentrated sulfuric acid (23 ml) and sodium nitrate (NaNO_3 , 0.5g) to oxidize the graphite powder (1g) to GO, after 2 hours, potassium permanganate (3g) was then added into the suspensio with stirring for 5 days. Thereafter, 100 ml of diluted sulfuric acid was added in the above suspension, followed by the addition of hydrogen peroxide (140 ml) with 1 h stirring. The suspension was subsequently filtered and washed until reaching a neutral pH, after dried at 60 °C in a vacuum oven, GO was obtained. The stacked graphene was prepared by 30 seconds thermal treatment of the as-obtained GO around 1050 °C in the furnace.

The unfolded graphene was reduced by hydrazine reduction of GO as-obtained in the distilled water. After ultrasonication of GO (0.02 g mL^{-1}) in 2 L batches bath ultrasound (VWR B2500A-MT) for 3 h and following centrifugation, the centrifugate was collected. Single and few-layer graphene sheets were readily prepared, homogeneously and stably suspended in the good solvent medium.

The following describes a typical synthesis for LFP/SG composites. First: 22.5 mg of stacked graphene was dissolved in 30 mL of water via strong ultrasonic agitation for 30 min. Next, 1.039 g lithium dihydrogen phosphate (LiH_2PO_4 , Sigma) was dissolved in 100 mL of water and stirred at 80 °C for 1 h. Separately, 1.739 g iron (II) acetate ($\text{Fe}(\text{AC})_2$, Sigma) was dissolved in 70 mL of water by stirring at 70 °C for 1 h. The two solutions and the stacked graphene suspension were mixed together and dried at 70 °C for 24 h. For the LFP/UG composites, the procedure was similar, except that the stacked graphene solution was replaced with the unfolded graphene suspension (0.2 g L^{-1}). After thorough

grinding of the xerogel followed by annealing in a furnace filled with an argon atmosphere at 700 °C and a heating rate of 10 °C min⁻¹, the composites were obtained.

5.2.2 Physical Characterization

The synthesized material was then characterized by various methods. Powder X-ray diffraction (XRD, Rigaku, Japan) using a Co K α radiation source was used to identify the crystalline phase. FE-SEM (S-4800, Hitachi) with an operating voltage of 5 kV, TEM (H-7000, Hitachi) and HRTEM (JEOL 2010F) was used to determine the morphology and microstructure of the samples. A Raman scattering spectroscopy apparatus (HORIBA) equipped with a 532.4 nm laser was performed to study the phonon modes of Fe, P, O and C. The Fe K-edge XANES spectra were obtained on the Soft X-ray Microcharacterization Beamline (SXRMB, $\Delta E/E$: 10⁻⁴), and C K-edge were conducted on the undulator Spherical Grating Monochromator (SGM) beamline at the Canadian Light Source (CLS) located at the University of Saskatchewan in Saskatoon.

5.2.3 Electrochemical measurements

The electrochemical cell used in our study was a CR 2032 coin cell. The electrolyte used in our experiment was 1 M LiPF₆ in a mixture of ethylene carbonate/dimethyl carbonate (1: 1 v/v) solvents. All electrochemical tests were performed in an Arbin BT-2000 Battery Test Station within a voltage range of 2.5-4.2 V (versus Li⁺/Li). The composites were mixed with acetylene black and poly-(vinylidene fluoride) (PVDF) binder with a weight ratio of 75:15:10, using N-methyl-2-pyrrolidene (NMP) as the solvent, and then the mixture was ground in a mortar and pestle and pasted onto pure Al foils. The coin cells were assembled in a high-purity argon filled glove box, and all of the electrochemical measurements were conducted at room temperature.

5.3 Results and Discussion

The stacked graphene was prepared by thermal reduction of graphene oxide, whereas unfolded graphene was synthesized by hydrazine reduction of graphene oxide in solution [27-29]. The LiFePO₄/unfolded graphene (LFP/UG) and LiFePO₄/stacked graphene

(LFP/SG) nanocomposite were obtained by a facile method combining a sol-gel route and a solid-state reaction approach.

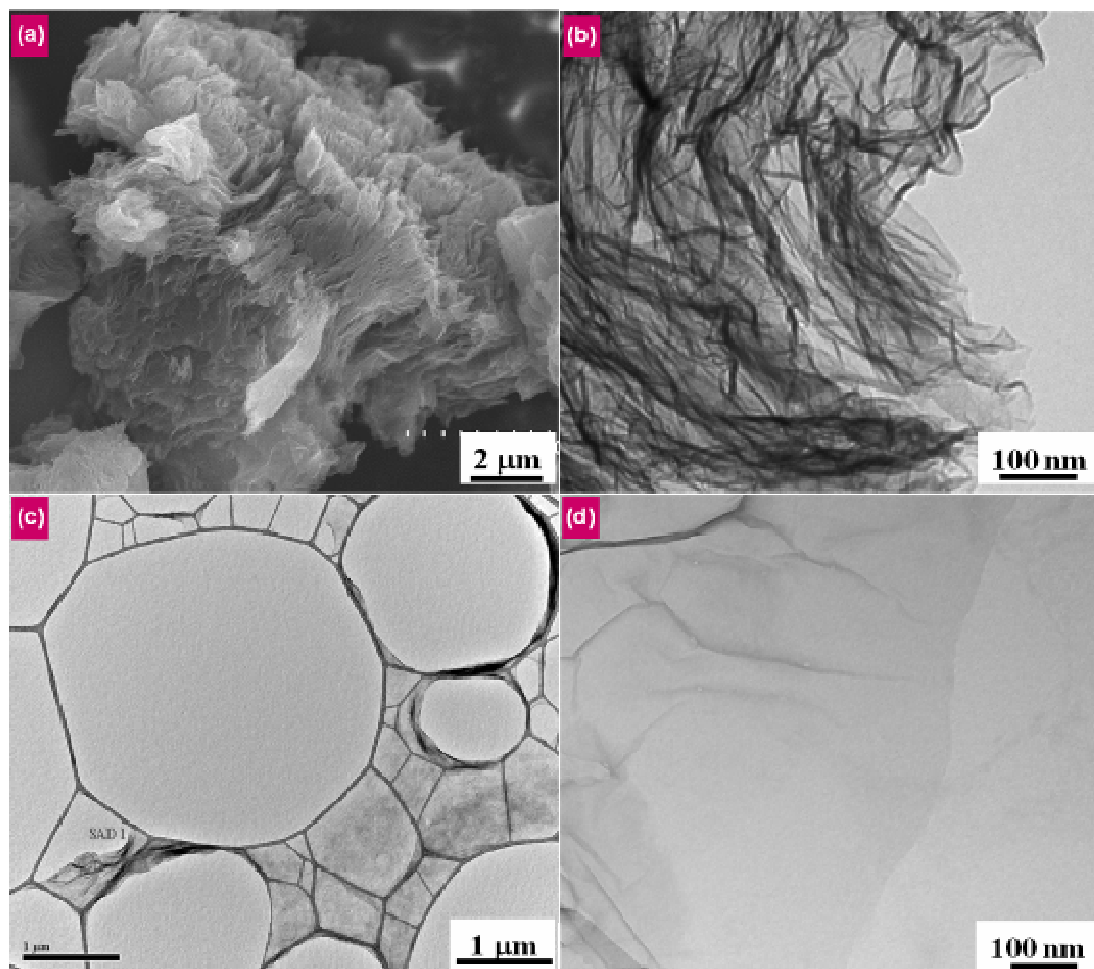


Figure 5.1 (a) SEM image and (b) TEM image of stacked graphene, (c) and (d) TEM images of unfolded graphene.

Typical SEM and TEM images of stacked graphene and unfolded graphene are shown in Figure 5.1. From low magnification micrographs (Figure 5.1a, c), the stacked graphene consists of multiple flakes that are closely packed in perpendicular direction to the basal plane of graphene sheets. These closely packed flakes make the size of stacked graphene up to 10 μm , whereas the size of the unfolded graphene is approximately 500 nm, which is 20 times smaller than that of stacked graphene. In addition, the unfolded graphene has fewer flakes than the stacked graphene. TEM images (Figure 5.1b, d) clearly reveal the

difference in morphology. The stacked graphene has multiple wrinkled layers, whereas the unfolded graphene exhibits an even and flat structure with individual flakes, resulting in a higher surface-to-volume ratio.

The LFP/SG and LFP/UG composites were obtained by adding the same amount of dispersed stacked graphene or unfolded graphene suspension to the LiFePO_4 precursor solution. The final products were collected after calcination of the dried xerogel.

SEM and TEM images of the LFP/SG and LFP/UG composites are shown in Figure 5.2. Micro-scale LFP particles were obtained when stacked graphene was used, and only a few LFP particles were attached to the stacked graphene (Figure 5.2a). In contrast, many nano-scale LFP particles dispersed uniformly in the unfolded graphene network (Figure 5.2b). TEM images revealed that the LFP nanoparticles in the range of 30-100 nm were firmly anchored to the unfolded graphene matrix (Figure 5.2c). It should be noted that unfolded graphene provides active sites for LFP nuclei, thereby restricting the aggregation and in-situ crystallite growth of anchored LFP nanoparticles. HRTEM image showed the crystal lattice fringes of the LFP nanoparticles with a d-spacing of 0.29 nm (Figure 5.2d), corresponding to the (020) plane of orthorhombic LFP crystals and indicating that the LFP nanoparticles were single crystals with high crystallinity. The selected area electron diffraction (SAED) pattern (inset of Figure 5.2c) of the transparent area shows typical rings of graphene, indicating that no LFP phase exists in this region. The SAED pattern of the LFP nanoparticles (inset of Figure 5.2d) indicates the single crystallinity of the LFP nanoparticle. The XRD patterns of the as-obtained LFP/SG and LFP/UG composites (Figure 5.2e) demonstrated that highly pure LFP with an orthorhombic olivine structure was successfully obtained, and no impurity phase was detected. No obvious peaks corresponding to graphene were found owing to the low graphene content.

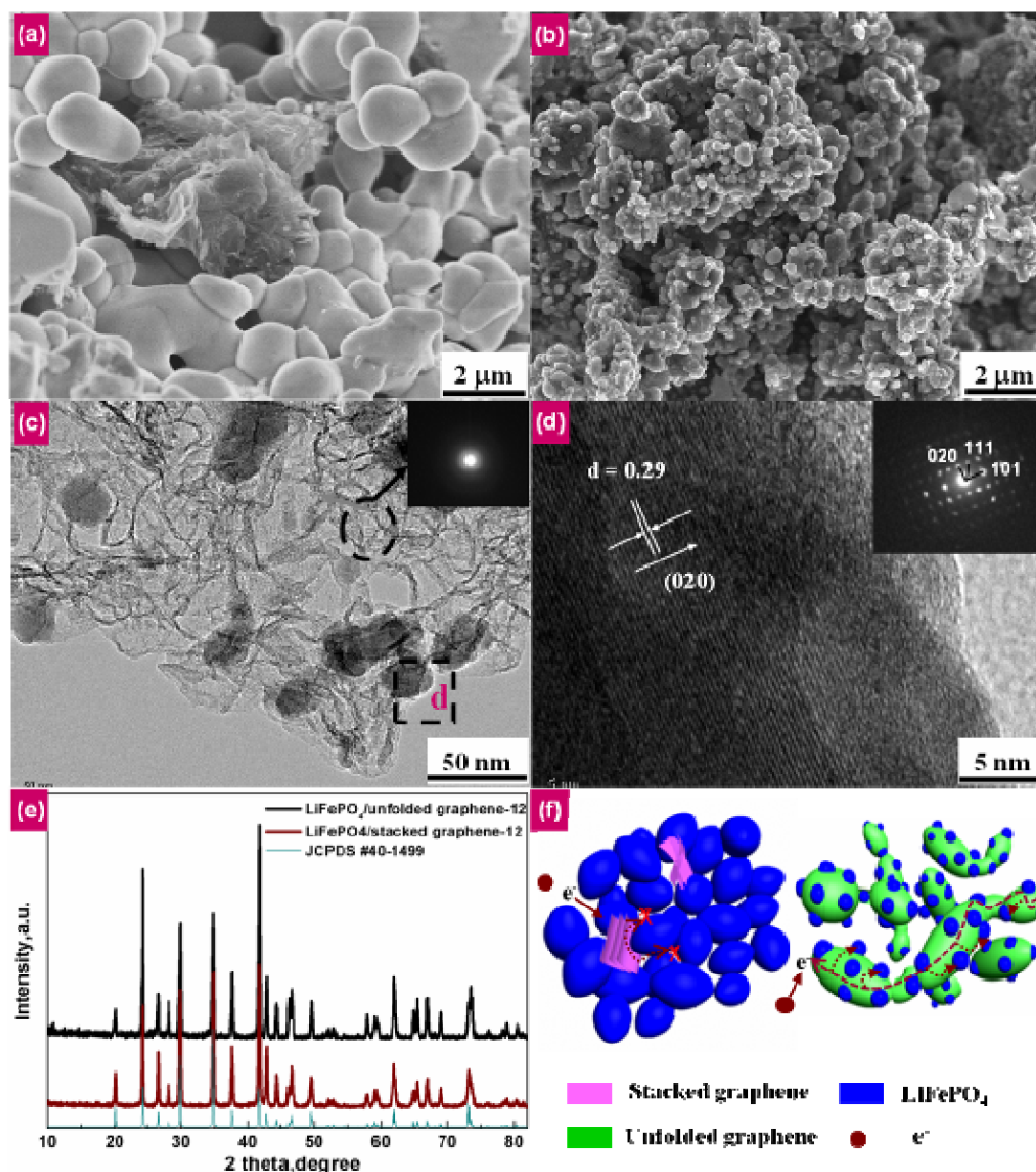


Figure 5.2 SEM images of (a) LiFePO₄/stacked graphene composites and (b) LiFePO₄/unfolded graphene composites; (c) TEM image of LiFePO₄/unfolded graphene composites. (Inset showing selected area electron diffraction (SAED) pattern of unfolded graphene (circle area)); (d) High-resolution TEM image and SAED pattern (inset) of an individual LiFePO₄ nanoparticle on unfolded graphene (boxed area in (c)); (e) XRD spectrum of the LiFePO₄/unfolded graphene and LiFePO₄/stacked graphene composites; (f) Electron-transfer pathway for the LiFePO₄/stacked graphene and LiFePO₄/unfolded graphene composites.

The carbon content of LFP/UG and LFP/SG composites can be calculated from the thermogravimetric (TGA) curves (see supporting Figure S5.1). As reported, the oxidation of LiFePO_4 to $\text{Li}_3\text{Fe}_2(\text{PO}_4)_3$ and Fe_2O_3 can result in a weight gain of 5.07% [30-32]. After calculation from the TGA curves, the total weight gain for LFP/UG and LFP/SG in the TGA curve is 3.57 wt % and 3.6 wt %, respectively. Therefore, the carbon content of LFP/UG and LFP/SG is 1.5 wt % ($5.07\% - 3.57\%$) and 1.47 wt % ($5.07\% - 3.6\%$), respectively. The results demonstrate that the carbon content of the two composites is comparable.

Figure 5.2f schematically illustrates the structure of LFP/UG and LFP/SG composites. During the entire preparation process, no other carbon source except graphene was introduced. Therefore, only graphene contributes to the improvement of the electronic conductivity of LFP. In this case, the manner in which LFP and graphene are combined is crucial for the Li-ion intercalation and de-intercalation processes. Owing to the limited contact area between LFP and stacked graphene, the electrons can only reach certain LFP particles that are attached to the stacked graphene during the cycling process. Therefore, electrons are not able to reach LiFePO_4 particles from all directions (as indicated by the “ \times ”), resulting in low utilization of LFP and polarization of the electrode.

For LFP/UG composites, the unfolded graphene acts as the conductive network, not only restricting the LFP size to nano-scale, which decreases the Li^+ ion diffusion path, but also enabling all of the electrons from all directions to reach all the LFP particles. The red arrows in Figure 5.2f indicate that electrons can reach each of the LFP particles with the aid of the unfolded graphene. Therefore, in comparison with stacked graphene, application of unfolded graphene in electrodes can significantly enhance the utilization of the LFP.

To study the effects of annealing time on the morphology of the LFP growth on unfolded graphene, time-dependent controlled experiments were performed, as shown in Figure 5.3. After 2 h of annealing (Figure 5.3a), very fine LFP nanoparticles were dispersed homogeneously on unfolded graphene nanosheets. As annealing time progressed to 6 h (Figure 5.3b), the nanoparticles had grown larger and were uniformly dispersed on the

unfolded graphene. When the annealing time was increased to 12 h (Figure 5.3c), the graphene nanosheets were crimped and connected to form a conducting 3D network, and spherical-shaped LFP nanoparticles were anchored to the graphene matrix. The nanoparticles had grown larger, with the sizes up to 100 nm. A further increase in the annealing time to 24 h (Figure 5.3d), resulted in larger, irregular particles. As shown by TEM images (inset in Figure 5.3a, 5.3b, 5.3c and 5.3d), with an increase in the annealing time, the particle size increased as follows: 3 nm for 2 h of annealing (LFP/UG-2), and 5 nm for 6 h of annealing (LFP/UG-6), 70 nm for 12 h of annealing (LFP/UG-12), and 200 nm for 24 h of annealing (LFP/UG-24). The results presented above reveal that the morphology and the size of the LFP nanoparticles can be tailored by adjusting the annealing time. The longer the annealing time, the larger the LFP particles size is.

The successful preparation of the LFP/Graphene (LFP/G) composite was confirmed by the XRD spectrum. The XRD patterns of LFP/G nanocomposite treated for various annealing times are shown in Figure 5.4a. All of the intense peaks can be well indexed as the olivine LiFePO_4 phase (JCPDS Card No. 40-1499, space group Pmnb (62), $a_0 = 6.018 \text{ \AA}$, $b_0 = 10.34 \text{ \AA}$, $c_0 = 4.703 \text{ \AA}$), except for a small diffraction peak at 34° for the LFP/G composite annealed for 24 h, which corresponds to $\text{Fe}_7(\text{PO}_4)_6$. In addition, the crystallinity was observed to increase with the annealing time.

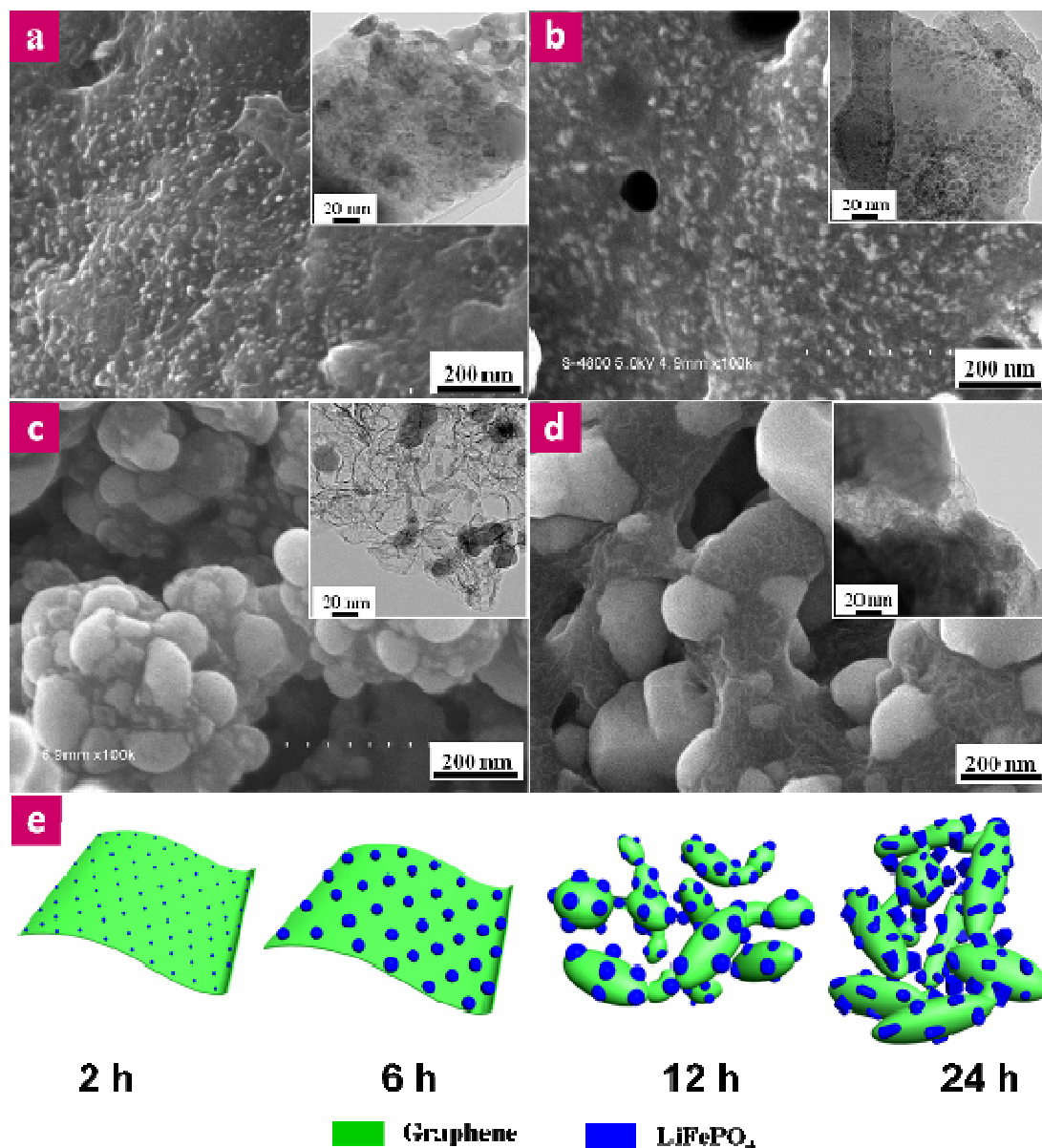


Figure 5.3 SEM and TEM (inset) images of LiFePO₄/unfolded graphene nanocomposite obtained with different annealing time: (a) 2 h. (b) 6 h. (c) 12 h. (d) 24 h; (e) Schematic image of LiFePO₄ growth on the unfolded graphene.

To further identify the effect of the annealing time effect on the crystallinity of the as-obtained products, HRTEM and SAED were conducted (see supporting information, Figure S5.2). The presence of the lattice fringes indicates the single crystal nature of the nanoparticles (Figure S5.2a, S5.2c and S5.2e). The widths of the neighboring lattice fringes for LFP/UG-6 and LFP/UG-24 were 2.9 Å and 5.2 Å, respectively; these widths

corresponded to the (020) and (200) planes, respectively, of LiFePO_4 . SAED spots were random (Figure S5.3b), confirming the low crystallinity of LFP/UG-2. For the LFP/UG-6 and LFP/UG-24 nanocomposites, the crystallinity gradually increased. These observations are consistent with the XRD results.

The Raman spectra of LFP/G nanocomposites are shown in Figure 5.4b. Intense Raman modes were observed at 216, 282, 393, 441, 987 and 1078 cm^{-1} in three samples (LFP/UG-6, LFP/UG-12 and LFP/UG-24), corresponding to the finger print peaks of LiFePO_4 with orthorhombic symmetry [33]. For the LFP/UG-2 nanocomposites, there were no obvious peaks in the $200\text{--}1100\text{ cm}^{-1}$ region. This phenomenon is ascribed to the low crystallinity of the LFP/UG-2 composites, which is in accordance with the XRD and SAED results. The addition of graphene nanosheets had no effects on the main structure of LFP. Carbon peaks from unfolded graphene nanosheets appeared in all composites. Two strong peaks at 1342 and 1581 cm^{-1} were assigned to the D-band and G-band, respectively. The G-band denotes the presence of graphite carbon, whereas the D-band is attributed to disorders or defects in the graphite structure [34]. The I_D/I_G (disordered/graphite) ratio of the Raman spectra was used to evaluate the disorder in the materials. With the increase of the annealing time, the I_D/I_G ratio decreased from 1.19 for LFP/UG-2 to 1.07 for LFP/UG-24. A lower I_D/I_G ratio indicates a larger amount of graphitized carbon; i.e., the amount of graphitized carbon increases with the increasing annealing time.

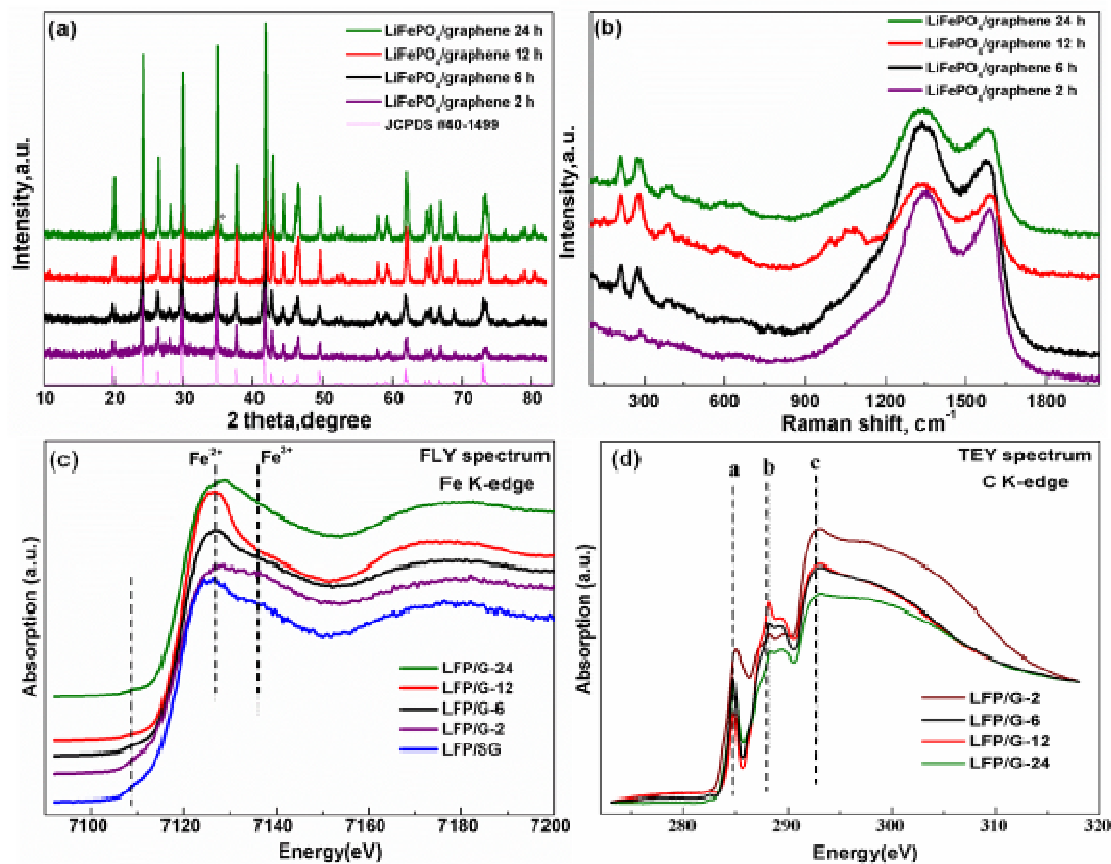


Figure 5.4 XRD patterns (a), Raman spectra (b), normalized absorption of Fe K-edge (c) and C K-edge (d) XANES spectra for LiFePO₄/unfolded graphene composites annealed at 700 °C for various time.

To investigate the chemical states and local chemistry environment of elemental Fe in the LFP/SG and LFP/UG composites and the interaction (chemical bonding) between unfolded graphene and LFP particles, Fe K-edge and C K-edge XANES spectra were performed (Figure 5.4c and 5.4d). The Fe K-edge XANES spectra consist of two main edge jumps, the pre-edge and the main edge regions. The pre-edge peak was centered at the lower energy side of the sharply rising absorption edge (white line), corresponding to the 1s to 3d electronic transition of Fe [35]. As demonstrated in Figure 5.4c, all of the LFP composites exhibited a distinct increased white line located at ~7126 eV, which corresponds well with the results of other groups [35, 36]. For LFP/UG-2, the spectrum was broader than that of the other composites, indicating the low crystallinity of LFP/UG-2. With increasing annealing time, the spectral features became sharp,

illustrating increased crystallinity of LFP/UG. The LFP/SG composites also exhibited sharp features, indicating good crystallinity. It should be noted that for LFP/UG-24 composites, the position of the Fe *K*-edge in the XANES spectra slightly shifted toward the higher energy side. The shift in the edge position originated from the high valence of the Fe ions, which is related to the appearance of impurity in LFP/UG-24, as shown in the XRD patterns. This shift phenomenon was also observed in Suzuki's and Yang's work [37-39].

Two patterns in the C *K*-edge XANES spectra located at ~285 eV and 291 eV (a and c positions) corresponded to graphitic π^* and σ^* transitions, respectively (Figure 5.4d) [40], which indicated that the graphitic framework existed in all of the LFP/UG nanocomposites. Therefore good electronic conductivity in LFP/UG nanocomposites was expected. Further analysis of the XANES spectra showed several interesting features. First, π^* transition intensity (a position) for LFP/UG-12 was reduced compared with other composites. Lower intensity indicates more charge transfer from LFP to C 2p-derived π^* states in unfolded graphene [41], indicating stronger chemical bonding between LFP and interface of unfolded graphene. Second, the intensity of resonance at ~288 eV (b position) from LFP/UG-12 was stronger than the other LFP/UG composites. Many groups attribute this resonance to the chemical bonding between active materials and carboxylate groups [41, 42]. The observation in the spectra further demonstrated the stronger carboxylate bonding in the LFP/UG-12 composites.

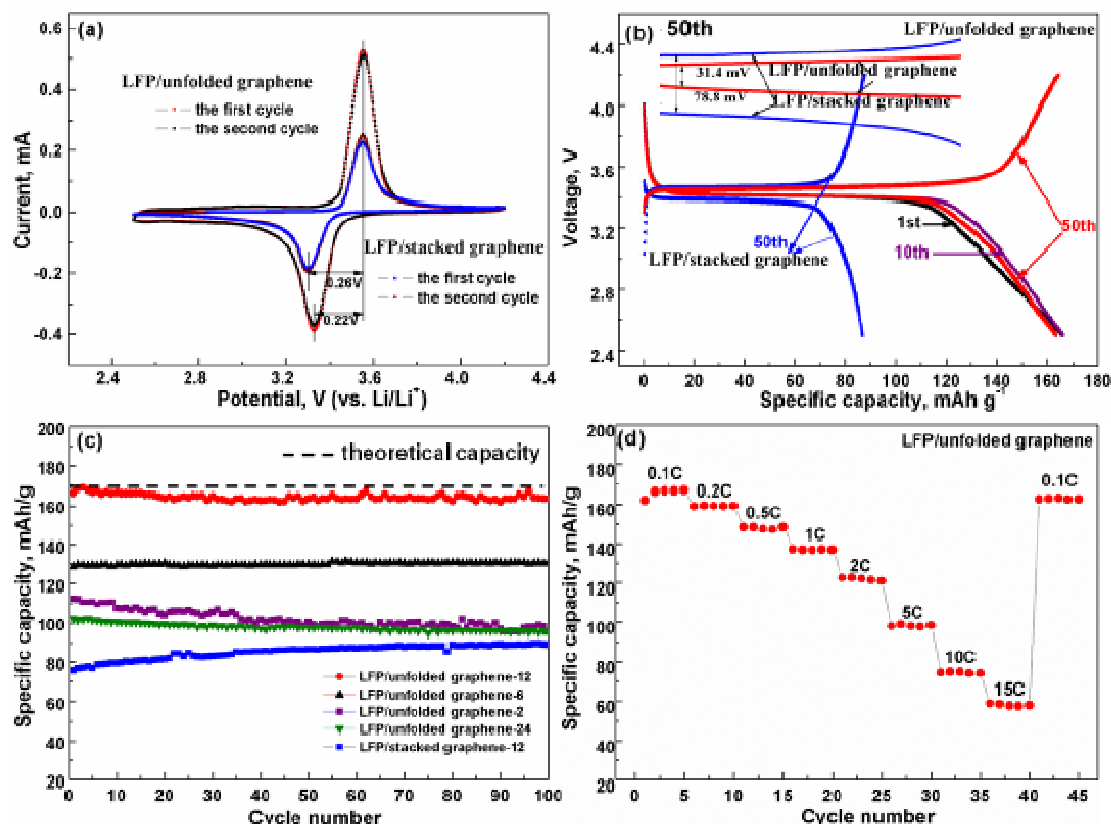


Figure 5.5 (a) Cyclic voltammograms (0.1 mV s^{-1}); (b) charge-discharge curves at different cycle number for LFP/UG-12 and LFP/SG at a current rate of 17 mA g^{-1} ; (c) cycling profile tested at a current density of 17 mA g^{-1} between 2.5 and 4.2 V for LFP/UG and LFP/SG; (d) rate performance for LFP/UG-12.

Cyclic voltammograms (CV) of LFP/UG-12 and LFP/SG composites were shown in Figure 5.5a. Both electrodes exhibited a couple of redox peaks of $\text{Fe}^{2+}/\text{Fe}^{3+}$ at a scan rate of 0.1 mV s^{-1} . For LFP/SG, the anodic peak at 3.55 V corresponded to the oxidation of Fe^{2+} to Fe^{3+} , and the reduction of Fe^{3+} to Fe^{2+} appeared at 3.29 V, where the potential interval between the two redox peaks was 0.26 V. By contrast, this interval was 0.22 V for LFP/UG-12 nanocomposites, which was approximately 40 mV smaller than that for LFP/SG composites. This difference is due to the unfolded graphene matrix, which serves as a highly conducting 3D network that allows both Li^+ and electrons to migrate and reach the LFP nanoparticles that are grown on the graphene, thereby leading to efficient use of the active materials. In the subsequent cycle, the position and the currents of the

two peaks were quite similar to those of the first cycle, revealing the superior stability of the LFP/UG-12 nanocomposite.

Figure 5.5b showed the charge–discharge curves of the prepared LFP/SG and LFP/UG-12 composites at different cycle numbers. The cell exhibited a typical plateau at 3.41 V (versus Li^+/Li) associated with the Fe^{3+} to Fe^{2+} redox process for both electrodes. In the 1st cycle, the discharge capacity of LFP/UG-12 was $166.2 \text{ mA h g}^{-1}$, which is 98% of the theoretical capacity. The exceptionally high capacity is due to full usage of the active material. At the end of 10th cycle and 50th cycle, the delivered capacities were 166.4 and $164.1 \text{ mA h g}^{-1}$, respectively, demonstrating the superior high conversion of the active LFP/UG-12 material. By contrast, for LFP/SG composites, the discharge capacity was only 86 mA h g^{-1} in 50th cycle, which is approximately half that of the LFP/UG nanocomposites. As shown in the inset of Figure 5.5b, the ΔE evaluated from the difference between the charge potential and the discharge potential is different for both electrodes at the 50th cycle. The polarization value was 31.4 mV and 78.8 mV for LFP/UG-12 and LFP/SG composites, respectively, which is in good agreement with the results in Figure 5.4a.

The long cycling performance of LFP/UG-12 nanocomposites was investigated at a constant current density of 17 mA g^{-1} , as illustrated in Figure 5.5c. No obvious decline was observed in the discharge capacity after 100 charge-discharge cycles at room temperature. For example, the discharge capacity loss was less than 1.3% over 100 cycles and the coulombic efficiency was close to 100%. For comparison, the LFP/SG composites that had been annealed for the same duration were also tested at the same current density. With approximately 1.5 wt % carbon content, the LFP/SG composites also exhibited stable cycling behavior, but with low Li^+ storage capability as a result of insufficiently usage of the active LFP material (caused by the limited contact area between LFP and stacked graphene). The products annealed for various durations were also tested. For LFP/UG-2, the capacity faded significantly at a current density of 17 mA g^{-1} . The discharge capacity in the 100th cycle was 96 mA h g^{-1} , which was only 84% of its initial capacity. Compared with LFP/UG-2, LFP/UG-6 and LFP/UG-12 exhibited better lithium intercalation/deintercalation properties. For LFP/UG-24, the initial

discharge capacity delivery was $102.4 \text{ mA h g}^{-1}$, and a capacity fade of 6% was observed after 100 cycles. The electrochemical performance is related to the crystallinity and purity of the LFP [43]. The low crystallinity of LFP/UG-2 led to low electronic conductivity, which is apparent in the Fe K-edge XANES spectra, thereby resulting in poor lithium storage behavior. According to the HRTEM and XANES results, the crystallinity of LFP and chemical bonding between the LFP and the surface of unfolded graphene increases with an increase in the treatment duration to 12 h. Therefore, the Li^+ diffusion rate in the nanocomposite was improved in samples with a 6 h and 12 h annealing duration, leading to better cycle performance. However, when the annealing duration was extended to 24 h, the discharge capacity significantly decreased. The poor electrochemical performance of LFP/UG-24 can be ascribed to the presence of $\text{Fe}_7(\text{PO}_4)_6$ impurity in the nanocomposite and reduced chemical interaction between LFP and the unfolded graphene, which can be identified by the XRD patterns and XANES spectra.

The LFP/UG-12 nanocomposite was cycled at different current densities, and an excellent rate performance was observed (Figure 5.5d). It should be noted that the discharge capacity of the nanocomposite remained stable at an extremely high rate of 5 C (850 mA g^{-1} , completing the discharge and charge process in 12 min), and the delivered discharge capacity was approximately 100 mA h g^{-1} . When the current density was increased to 10 C (1700 mA g^{-1}) and 15 C (2550 mA g^{-1}), the discharge capacity remained relatively high, at 75 and 60 mA h g^{-1} , respectively. It is worth to mention that as long as the current rate was reversed back to a current density of 17 mA g^{-1} , the discharge capacity could be recovered to its original value, demonstrating that homogeneously embedded LFP nanoparticles in a superior conducting matrix can be tolerant to high charge and discharge currents, and thereby satisfying one of the mandatory electrochemical features for LIBs used in EVs and HEVs.

5.4 Conclusions

In summary, a novel nanocomposite with uniformly dispersed LFP nanoparticles anchored to unfolded graphene matrix was developed for high-power electrode materials in LIBs. The use of an unfolded graphene matrix, which serves as a conducting 3D nano-network, enables both Li^+ and electrons to migrate and reach each of LFP particles, hence

realizing the full potential of the active materials. In comparison with the LFP/SG composites, the LFP/UG-12 nanocomposites delivered a much higher discharge capacity (close to the theoretical capacity) and a superior rate capability with low graphene content of 1.5 wt%. In LFP/UG composites, the crystallinity of LFP and the chemical bonding between the LFP and unfolded graphene are improved by lengthening the annealing duration to 12 h, which can be demonstrated by the XANES spectra. The unique structure, the superior conducting properties of the graphene matrix and strong chemical interaction between LFP and the unfolded graphene enable the LFP/UG-12 nanocomposite to achieve excellent Li storage behavior. The success of this electrode design was demonstrated by the superior characteristics of the LFP/UG nanocomposite. This design could also be extended to other cathode and anode materials, which promises to promote the development of next-generation LIBs applied in EVs and HEVs with both high-power and high-energy densities.

5.5 Acknowledgements

This work was supported by the Natural Sciences and Engineering Research Council of Canada (NSERC), Phostech Lithium Inc., Canada Research Chair (CRC) Program, and the University of Western Ontario.

5.6 Supporting Information

Supporting Information Available: Experimental part, TGA curves of LFP/UG and LFP/SG composites, HRTEM and SAED of LFP/UG composites annealed at 2h, 6h and 24h.

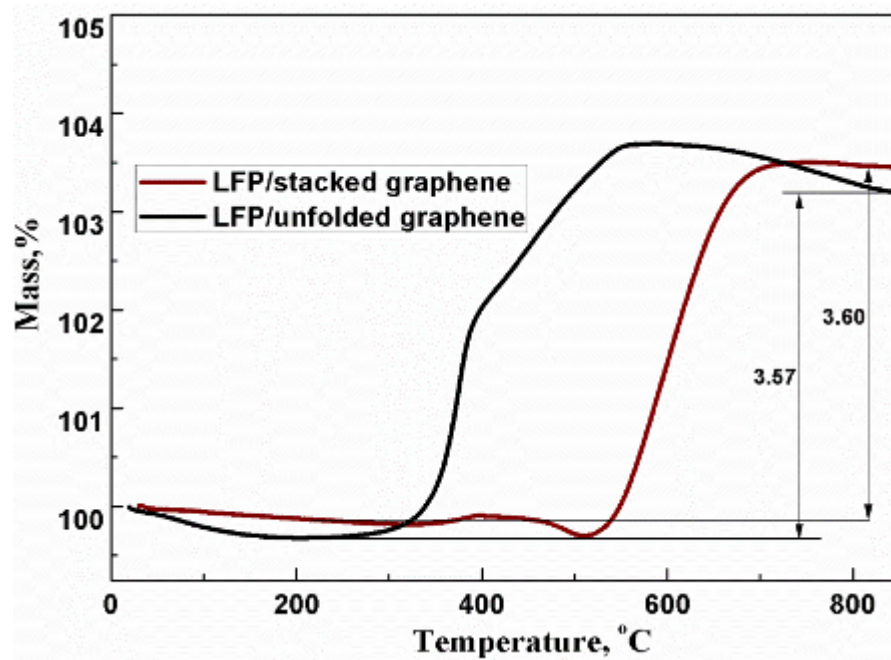


Figure S 5.1 TGA curves of the LiFePO_4 /stacked graphene and LiFePO_4 /unfolded graphene compistes.

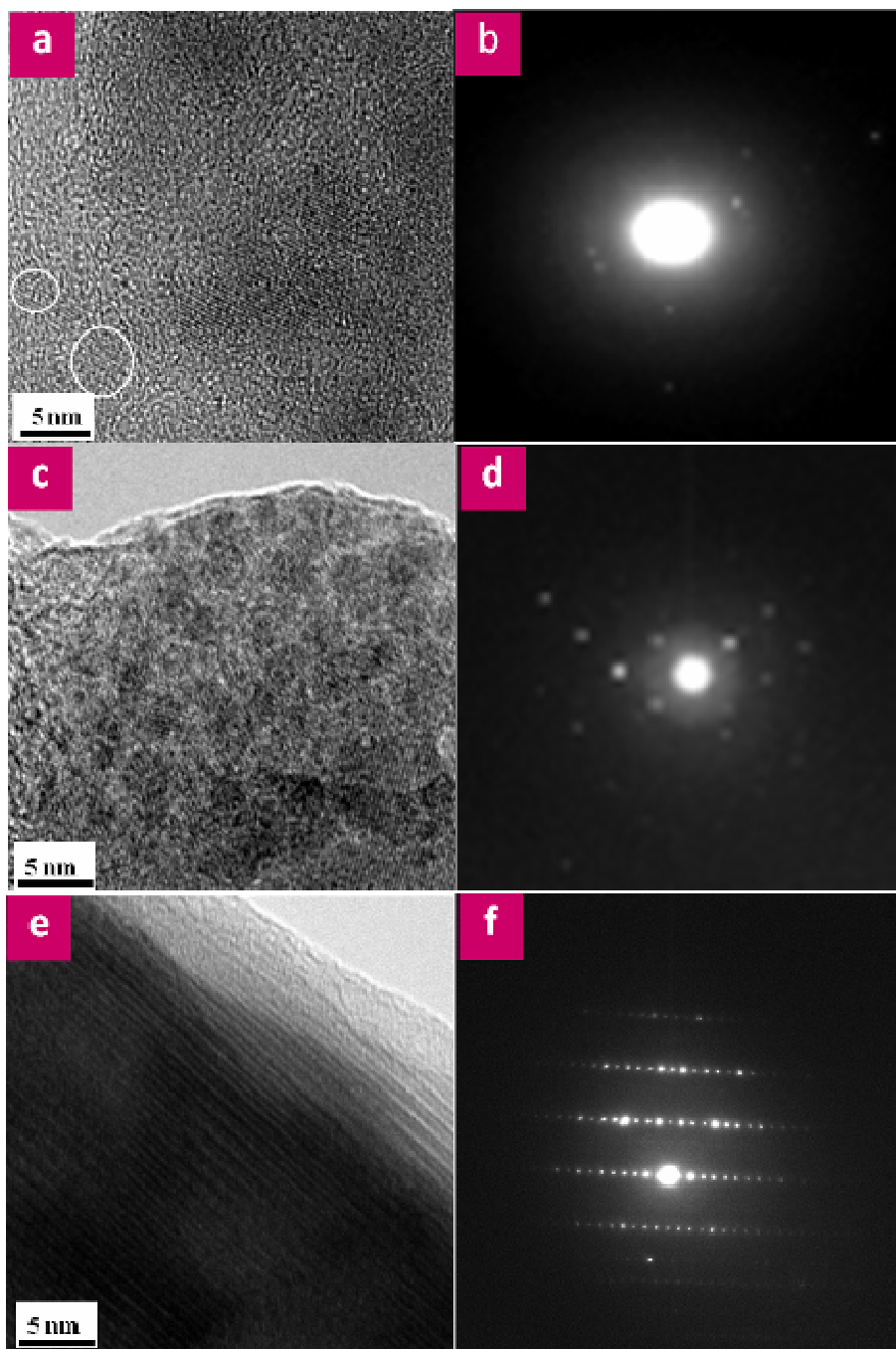


Figure S 5.2 HRTEM and SAED of LiFePO_4 /unfolded graphene composites annealed at different time. (a) and (b) 2h; (c) and (d) 6h; (e) and (f) 24h.

5.7 References

- [1] M. Armand and J. M. Tarascon, *Nature*, 2008, **451**, 652-657.
- [2] P. G. Bruce, B. Scrosati and J. M. Tarascon, *Angew. Chem. Int. Ed.*, 2008, **47**, 2930-2946.
- [3] Y. G. Guo, J. S. Hu and L.J. Wan, *Adv. Mater.*, 2008, **20**, 2878-2887.
- [4] H. Huang, S. C. Yin and L. F. Nazar, *Electrochem. Solid-State Lett.*, 2001, **4**, A170-A172.
- [5] A. S. Arico, P. Bruce, B. Scrosati and J. M. Tarascon and W. van Schalkwijk, *Nat. Mater.*, 2005, **4**, 366-377.
- [6] F. Cheng, Z. Tao, J. Liang and J. Chen, *Chem. Mater.*, 2008, **20**, 667-681.
- [7] A. K. Padhi, K. S. Nanjundaswamy and J. B. Goodenough, *J. Electrochem. Soc.*, 1997, **144**, 1188-1194.
- [8] R. Amin, P. Balaya and J. Maier, *Electrochem. Solid-State Lett.*, 2007, **10**, A13-A16.
- [9] S.-Y. Chung, J. T. Bloking, Y.-M. Chiang, *Nat. Mater.* 2002, **1**, 123-128.
- [10] S. B. Schougaard, J. Breger, M. Jiang, C. P. Grey and J. B. Goodenough, *Adv. Mater.*, 2006, **18**, 905-909.
- [11] F. Croce, A. D. Epifanio, J. Hassoun, A. Deptula, T. Olczac and B. Scrosati, *Electrochem. Solid-State Lett.*, 2002, **5**, A47-A50.
- [12] R. Dominko, J. M. Goupil, M. Bele, M. Gaberscek, M. Remskar, D. Hanzel and J. Jamnik, *J. Electrochem. Soc.*, 2005, **152**, A858-A863.
- [13] R. Dominko, M. Bele, M. Gaberscek, M. Remskar, D. Hanzel, S. Pejovnik and J. Jamnik, *J. Electrochem. Soc.*, 2005, **152**, A607-A610.
- [14] J. Wang and X. Sun, *Energy Environ. Sci.*, 2012, **5**, 5163-5185.

- [15] G. Cui, Y.-S. Hu, L. Zhi, D. Wu, I. Lieberwirth, J. Maier and K. Mullen, *Small*, 2007, **3**, 2066-2069.
- [16] G. Cui, L. Gu, L. Zhi, N. Kaskhedikar, P. A. van Aken, K. Mullen and J. Maier, *Adv. Mater.*, 2008, **20**, 3079-3083.
- [17] C. Delacourt, P. Poizot, S. Levasseur and C. Masquelier, *Electrochem. Solid-State Lett.*, 2006, **9**, A352-A355.
- [18] D. H. Kim and J. Kim, *Electrochem. Solid-State Lett.* 2006, **9**, A439-A442.
- [19] Y. S. Hu, Y. G. Guo, R. Dominko, M. Gaberscek, J. Jamnik and J. Maier, *Adv. Mater.*, 2007, **19**, 1963-1966.
- [20] Y. Wang, Y. Wang, E. Hosono, K. Wang and H. Zhou, *Angew. Chem. Int. Ed.*, 2008, **47**, 7461-7465.
- [21] S. Park and R. S. Ruoff, *Nat. Nanotechnol.*, 2009, **4**, 217-224.
- [22] H. Wang, J. T. Robinson, G. Diankov and H. Dai, *J. Am. Chem. Soc.*, 2010, **132**, 3270-3271.
- [23] Y. Liang, H. Wang, H. S. Casalongue, Z. Chen and H. Dai, *Nano Res.*, 2010, **3**, 701-705.
- [24] Y. Ding, Y. Jiang, F. Xu, J. Yin, H. Ren, Q. Zhuo, Z. Long and P. Zhang, *Electrochem. Commun.*, 2010, **12**, 10-13.
- [25] F. Y. Su, C. H. You, Y. B. He, W. Lv, W. Cui, F. Jin, B. Li, Q. Yang and F. Kang, *J. Mater. Chem.*, 2010, **20**, 9644-9650.
- [26] J. Yang, J. Wang, D. Wang, X. Li, D. Geng, G. Liang, M. Gauthier, R. Li and X. Sun, *J. Power Sources*, 2012, **208**, 3400-344.
- [27] W. S. Hummers and R. E. Offeman, *J. Am. Chem. Soc.*, 1958, **80**, 1339.

- [28] D. Li, M. Muller, S. Gilje, R. Kaner and G. Wallace. *Nat. Nanotechnol.*, 2008, **3**, 101-105.
- [29] D. Geng, Y. Chen, Y. Chen, Y. Li, R. Li, X. Sun, S. Ye and S. Knights. *Energy Environ. Sci.*, 2011, **4**, 760-764.
- [30] I. Belharouak, C. Johnson and K. Amine, *Electrochem. Commun.*, 2005, **7**, 983-988.
- [31] X. Lou and Y. Zhang, *J. Mater. Chem.*, 2011, **21**, 4156-4160.
- [32] J. Yang, J. Wang, X. Li, D. Wang, J. Liu, G. Liang, M. Gauthier, Y. Li, R. Li and X. Sun, *J. Mater. Chem.*, 2012, **22**, 7537-7543.
- [33] H. Hiura, T. W. Ebbesen, K. Tanigaki and H. Takahashi, *Chem. Phys. Lett.*, 1993, **202**, 509-512.
- [34] A. A. Salah, A. Mauger and K. Zaghib, *J. Electrochem. Soc.*, 2006, **153**, A1692-A1701.
- [35] G. X. Wang, S. Bewlay, S. A. Needham, H. K. Liu, R. S. Liu, V. A. Drozd, J. F. Lee and J. M. Chen, *J. Electrochem. Soc.*, 2006, **153**, A25-A31.
- [36] K. Hsu, S. Hua, C. Chen, M. Cheng, S. Tsay, T. Chou, H. Sheu, J. Lee and B. Hwang, *J. Power Sources*, 2009, **192**, 660-667.
- [37] K. Inoue, S. Fujieda, K. Shinoda, S. Suzuki and Y. Waseda, *Mater. Trans.*, 2010, **51**, 2220-2224.
- [38] X. Wang, C. Jaye, K. Nam, B. Zhang, H. Chen, J. Bai, H. Li, X. Huang, D. A. Fischer and X. Q. Yang, *J. Mater. Chem.*, 2011, **21**, 11406-11411.
- [39] F. Omenya, N. A. Chernova, S. Upreti, P. Y. Zavalij, K. W. Nam, X. Q. Yang and M. S. Whittingham, *Chem. Mater.*, 2011, **23**, 4733-4740.
- [40] J. Zhou, J. Wang, H. Fang and T. K. Sham, *J. Mater. Chem.*, 2011, **21**, 5944-5949.

- [41] J. Zhou, J. Wang, H. Fang, C. Wu, J. N. Cutler and T. K. Sham, Chem. Commun., 2010, **46**, 2778-2780.
- [42] D. Wang, X. Li, J. Wang, J. Yang, D. Geng, M. Cai, R. Li, T. K. Sham and X. Sun, J. Phys. Chem. C, 2012, **116**, 22149–22156.
- [43] J. Wang, J. Yang, Y. Zhang, Y. Li, M. N. Banis, X. Li, R. Li, G. Liang and X. Sun, Adv. Funct. Mater., 2012, **23**, 806–814.

Chapter 6

6 In-situ Self-catalyzed Formation of Core-shell LiFePO_4 @CNTs Nanowire for High Rate Performance Lithium-ion Batteries

In the previous three chapters, we introduced superior carbon additive to increase the electronic conductivity, then realizing good electrochemical performance of LiFePO_4 composites. However, as a storage system for large-sized vehicles, the high power density is desired, usually smaller size could obtain good rate capability. Considering the volumetric density, we design to in-situ grow one dimensional LiFePO_4 nanowires encapsulated into CNTs, while 3D CNTs conducting network structure was also obtained simultaneously. Nanometer size can decrease the lithium ion diffusion pathway and increases the contact areas between electrolyte and active materials, 3D network of CNTs can offer good electronic conductivity. Therefore, LFP@CNTs nanowires can give excellent cycling stability and rate capability.

In this chapter, in-situ self-catalyzed core-shell LiFePO_4 @CNTs nanowire can be fabricated by a two-step synthesis, where one-dimensional LiFePO_4 nanowire with a diameter of 20-30 nm encapsulated into CNTs, and 3D conducting networks of CNTs were obtained from in situ carbonization of polymer. The LiFePO_4 @CNTs nanowire delivers a capacity of 160 mA h g^{-1} at 17 mA g^{-1} , and 65 mA h g^{-1} at 8500 mA g^{-1} (50C, 1.2 minutes for charging and 1.2 minutes for discharging).

Key words: core-shell structure, carbon nanotube, LiFePO_4 nanowire, high-rate cathodes, lithium ion batteries

Note: This work has been published.

J. Yang, J. Wang, Y. Tang, D. Wang, B. Xiao, X. Li, R. Li, G. Liang, T.-K. Sham, X. Sun, **J. Mater. Chem. A**, 2013, in press.

6.1 Introduction

LiFePO₄ with olivine structure is an attractive cathode material applied in lithium ion batteries (LIBs) because of its low cost, high thermal and chemical stability, and acceptable operating voltage (3.4 V versus Li⁺/Li) [1]. The poor electronic conductivity ($\sim 10^{-9}$ S cm⁻¹) of LiFePO₄ is usually circumvented by carbon coating on the surface of LiFePO₄ [2, 3]. The current focus for LiFePO₄ applied in large-size batteries (electric vehicles and hybrid electrical vehicles) is on ultrafast battery discharge. This goal can be achieved by decreasing the size of the LiFePO₄ [4, 5]. According to the formula [6], $L = \sqrt{D\tau}$ (where D is the diffusion coefficient, τ is the diffusion time and L is the diffusion distance), the short diffusion lengths could shorten the diffusion time of Li ions in LiFePO₄ during intercalation/deintercalation process, also the relatively high surface area for the nano-sized particles enables fast charge transfer [7, 8]. Unfortunately, more undesirable chemical reactions occurred at electrolyte/electrode interface layer will produce HF, which attacks the surface of LiFePO₄, leading to poor cycle performance [4d]. One effective way to eliminate this problem is complete carbon coating [4b, 9-11]. Insufficient use of LiFePO₄ occurred in place where carbon is unattached during the intercalation process, thus resulting in polarization of the electrode [10]. Full carbon coating plays a bifunctional role (conductivity improvement and protection barrier), ensuring LiFePO₄ particles getting electrons from all directions and avoiding the direct contact with the electrolyte, thus alleviate polarization and improve cycle life [4d, 11].

Another strategy is hierarchical nanostructure design [12-17]. An electrode consisting of carbon-coated, high-crystalline LiFePO₄ in nanoscale with three dimensional (3D) conductive networks is desired for high power LIBs [14, 15]. Wu [12] recently synthesized hierarchical carbon-coated LiFePO₄ nanoplates, which possess a unique geometrical structure is helpful to facilitate the fast transport of mass and charge, hence it exhibits considerable discharge capacity and rate capability. In the case of carbon, carbon nanotubes (CNTs) are superior conducting materials for hybridization of active materials [14]. Incorporation of CNTs into LiFePO₄ has demonstrated improved specific capacity and rate capability of the composites [4c, 16]. Nevertheless, in these composites, the

CNTs were randomly dispersed into micro-sized LiFePO_4 , hence the combination manner of LiFePO_4 and CNTs is limited.

Herein we synthesized, for the first time to our knowledge, one-dimensional LiFePO_4 nanowire with a diameter of 20-30 nm encapsulated into CNTs (LFP@CNTs), and 3D conducting networks of CNTs were simultaneously obtained during the solid state reaction. One-dimensional LiFePO_4 nanowire reduces the diffusion path of Li ions, while the CNTs shell ensures a full coating and a fast electron conduction path. By combining the advantages of one-dimensional core-shell LFP@CNTs and a 3D CNTs conducting network, a hierarchical nanostructure design of electrode materials for high power and high energy LIBs can be realized.

6.2 Experimental part

6.2.1 Synthesis of LFP@CNTs nanowire composites

The following describes a typical synthesis for LFP@CNTs composites. First: 100 mg PMMA was dissolved in 30 mL of water via strong ultrasonic agitation. Next, 1.039 lithium dihydrogen phosphate (LiH_2PO_4 , Sigma) was dissolved in 100 mL of water and stirred at 70 °C for 1 h. Separately, 1.739 M iron (II) acetate ($\text{Fe}(\text{AC})_2$, Sigma) dissolved in 80 ml of water by stirring at 60 °C for 1h. The three solutions were mixed together and dried at 70 °C for 24 h. After thorough grinding of the xerogel followed by annealing in a furnace filled with an argon atmosphere at 700 °C for 6 h, 10 h and 20 h with a heating rate of 10 °C min^{-1} , the core shell LFP@CNTs composites were obtained.

6.2.2 Physical Characterization

The synthesized material was then characterized by various methods. Powder X-ray diffraction (XRD, Rigaku, Japan) using a Co Ka radiation source was used to identify the crystalline phase. FE-SEM (S-4800, Hitachi) with an operating voltage of 5 kV, TEM (H-7000, Hitachi) and HRTEM (JEOL 2010F) was used to determine the morphology and microstructure of the samples. A Raman scattering spectroscopy apparatus (HORIBA) equipped with a 532.4 nm laser was performed to study the phonon modes of Fe, P, O and C. N_2 adsorption/desorption isotherms were performed using a Folio Micromeritics

TriStar II Surface Area Analyser. The Fe K-edge XANES spectra were obtained on the Soft X-ray Microcharacterization Beamline (SXRMB, $\Delta E/E$: 10^{-4}), and C K-edge were conducted on the undulator Spherical Grating Monochromator (SGM) beamline at the Canadian Light Source (CLS) located at the University of Saskatchewan in Saskatoon.

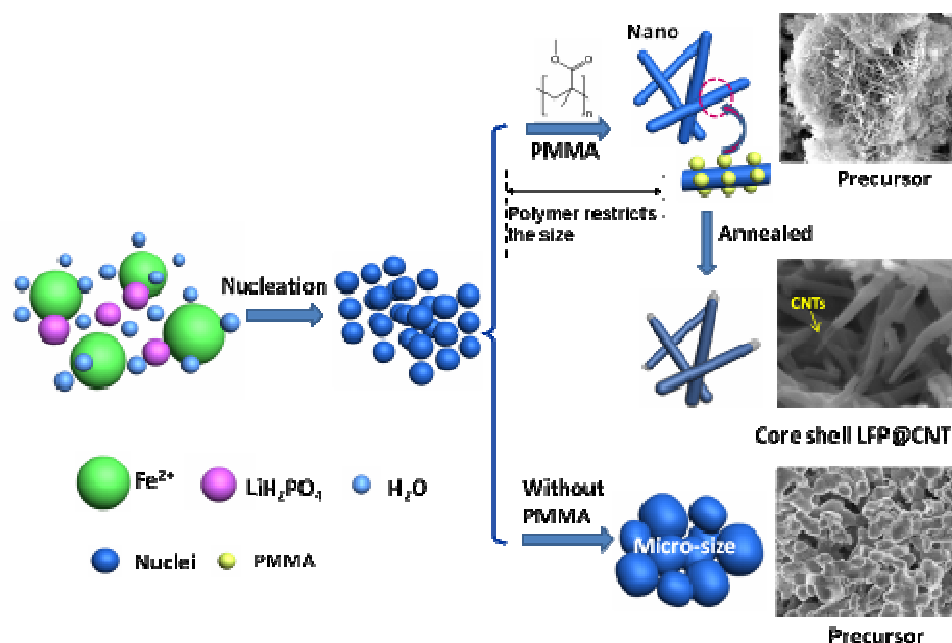
6.2.3 Electrochemical Measurements

The electrochemical cell used in our study was a CR2032 coin cell. The electrolyte used in our experiment was 1 M LiPF_6 in a mixture of ethylene carbonate/dimethyl carbonate (1: 1 v/v) solvents. All electrochemical tests were performed in an Arbin BT-2000 Battery Test Station within a voltage range of 2.5-4.2 V (versus Li^+/Li). The composites were mixed with acetylene black and poly-(vinylidene fluoride) (PVDF) binder with a weight ratio of 75:15:10, using N-methyl-2-pyrrolidene (NMP) as the solvent, and then the mixture was ground in a mortar and pestle and pasted onto pure Al foils. The coin cells were assembled in a high-purity argon filled glove box, and all of the electrochemical measurements were conducted at room temperature.

6.3 Results and discussion

LFP@CNTs core-shell nanowires were fabricated by a two step process: 1) sol-gel route to get one-dimensional LiFePO_4 nanowire precursor; 2) a solid state reaction to obtain core-shell high-crystalline LFP@CNTs nanowires and CNTs networking from in situ carbonization of polymer. The schematic drawing of synthetic procedure is demonstrated in scheme 6.1. First, one-dimensional nanowire structure is induced by polymerization of polymethylmethacrylate (PMMA) during the sol-gel process. It is also noted that PMMA polymer can restrict the size of the LiFePO_4 precursor. This is caused by PMMA being polymerized in situ on the outer surface of the generated LiFePO_4 precursor precipitate, then form a shell to restrict the growth of the LiFePO_4 [9]. In contrast, micro-sized particles are obtained without PMMA. Subsequent heat treatment at 700 °C for 10 h under argon leads to formation of core-shell LFP@CNTs nanowires and CNTs networking (LFP@CNTs-10h). During this step, the Fe^{2+} provided by the composites facilitates the formation of CNTs shell [18] and networking from the PMMA

polymerization. Meanwhile, the CNTs shell restricts the in situ crystallite growth of LiFePO_4 nanowires.



Scheme 6.1 Schematics to illustrate the synthetic procedure of the LFP@CNTs nanocomposites.

The Scanning Electron Microscopy (SEM) image shown in Figure 6.1a suggests that the one-dimensional core-shell LFP@CNTs nanowires can be created on a large scale basis. The corresponding magnified SEM images shown in Figure 6.1b indicate the typical diameter of the prepared LFP@CNTs nanowire is in the range of 20-30 nm, and the needle-like LiFePO_4 nanowire is encapsulated into CNTs, which is in-situ generated by carbonization of the PMMA polymer. Transmission Electron Microscopy (TEM) image (Figure 6.1c) further demonstrates the core-shell structure of LFP@CNTs-10h. It is interesting to note that LFP@CNTs nanowires are inter-connected by 3D CNTs networking (indicated by arrows), which results from in situ carbonization of PMMA (more images are shown in Figure S6.1). The electrons can easily reach the LFP@CNTs nanowires through 3D conducting network. The specific BET surface area of the LFP@CNTs nanowires is $34.3 \text{ m}^2 \text{ g}^{-1}$.

A high-resolution TEM image (Figure 6.1d) clearly reveals that a transparent CNTs shell with a thickness of 3 nm encapsulates LiFePO_4 nanowire, and the number of the walls is around 5-8 layers for typical CNTs as-obtained (Figure S6.1). Lithium ions can easily diffuse in the framework of LiFePO_4 through the thin carbon shell during the intercalation and deintercalation process [19]. The CNTs shell has an approximate diameter of 15 nm and less near the tip. The lattice fringes with a width of 0.18 nm correspond to the (131) plane of LiFePO_4 . The Selected-Area Electron Diffraction (SAED) patterns suggest that the fabricated LiFePO_4 nanowire is highly crystalline (Figure S6.2). Energy-dispersive X-ray (EDX) line scanning (Figure 6.1e) of single LFP@CNTs nanowire (inset in Figure 6.1e) shows the evidence of core-shell structure with the carbon signal peak at the shell of the nanowire and the Fe, P and O signal peaks at the core of the nanowire. As illustrated in Figure 6.1f, Li ions could easily diffuse in and out of the high-crystalline LFP@CNTs nanowire, due to its nanometer scale dimension and large surface area. Electrons could also be effectively supplied into the LiFePO_4 core through the CNT shell and the 3D CNTs networks during cycling.

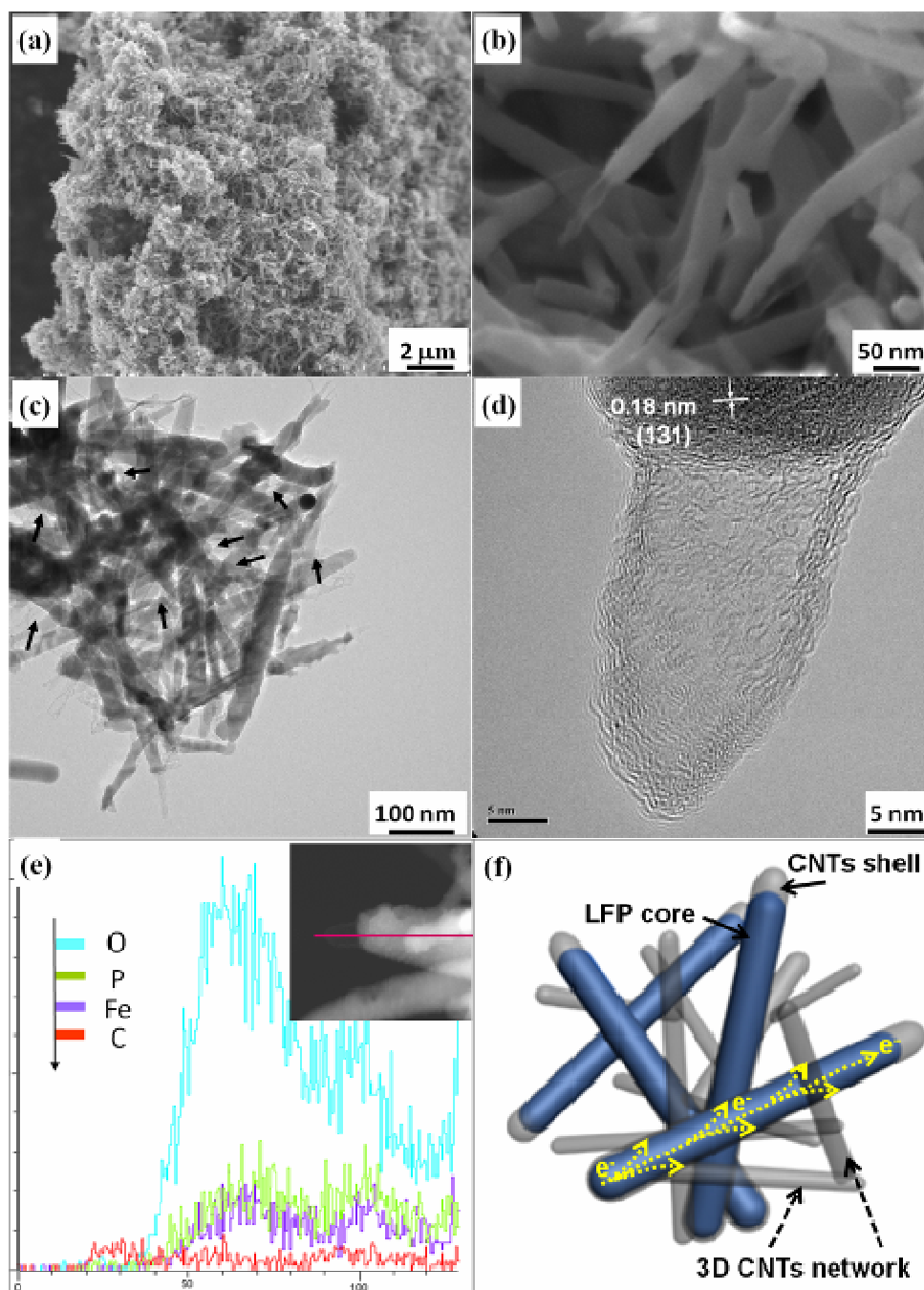


Figure 6.1 (a) and (b) SEM image of the as-prepared needle-like LFP@CNTs; (c) TEM image of the fabricated core-shell nanowire, and (d) the corresponding HRTEM image LFP@CNTs nanowire; (e) EDX Line scanning of LFP@CNTs core-shell nanowire, HRTEM image of single LFP@CNTs nanowire (inset); (f) Schematic illustration of the LFP@CNT core-shell Nanowire.

The crystallite size of the LFP@CNTs-10h is similar to the size of its precursor (Figure S6.3), indicating that the formed CNTs shell effectively restricts the crystallite growth of LiFePO_4 . As we know, carbon can be consumed by the residual oxygen in the Argon-filled tube furnace during the calcination process. In order to further investigate the protective effect of the CNTs shell, we performed the annealing process at 5 h and 20 h. It is noted that core-shell nanowire structure can be obtained for the 5 h treated sample (LFP@CNTs-5h), while for 20 h annealed sample (LFP@CNTs-20h), the LiFePO_4 nanowire was cracked into nanorod and agglomerated within a diameter of 50-100 nm (Figure S6.4). The HRTEM images show a typical example of core-shell LFP@CNTs nanowire annealed at different time (Figure 6.2). It is clearly observed that amorphous CNTs shell (5 h) evolves into graphitized CNTs shell (10 h) and the CNTs tip (20 h) disappears in the core-shell structure, which is consistent with the TGA results (Figure 6.3b). After calculation [4a, 20], the carbon content in LFP@CNTs-5h, LFP@CNTs-10h and LFP@CNTs-20h is about 4.1 wt. %, 3.9 wt. % and 3.1 wt. %, respectively, providing an evidence of carbon loss when prolonging the annealing time. Graphitized carbon shown in Raman spectrum (Figure S6.5) guarantees the high electronic transfer capability of the LFP@CNTs composites [21]. The XRD patterns of the prepared samples can be indexed as olivine LiFePO_4 (JCPDS no. 40-1499), and precursor is completely transformed into the LiFePO_4 (Figure 6.3a), indicating that high-crystalline and pure LiFePO_4 was obtained in calcination step.

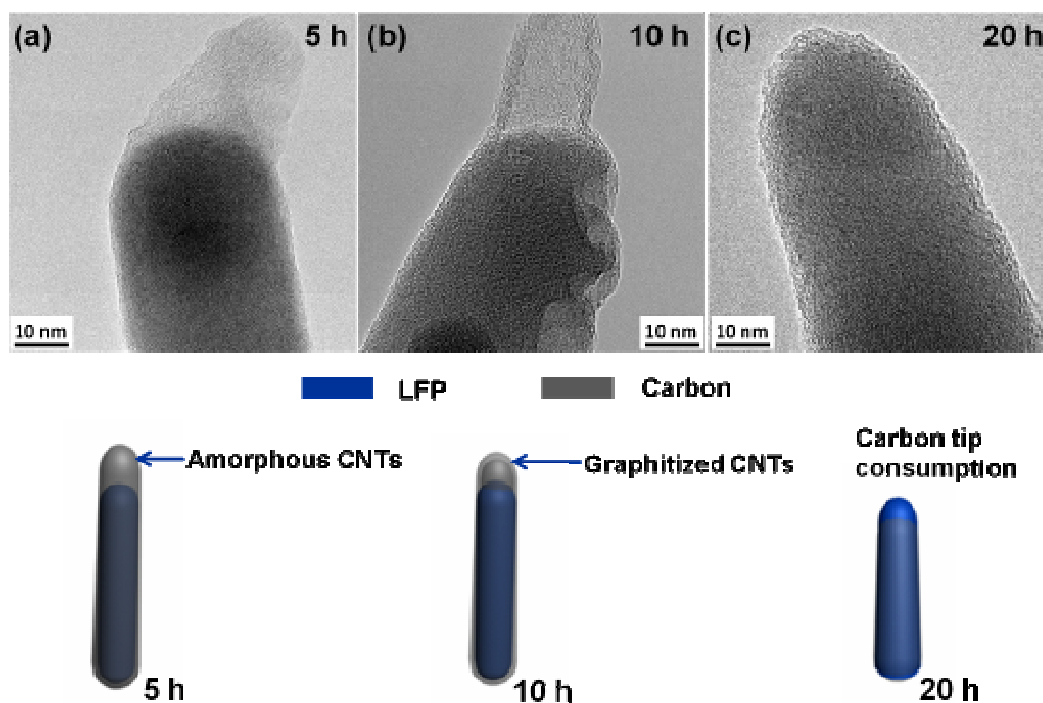


Figure 6.2 TEM images of LFP@CNTs composites annealed for different time: (a) 5 h. (b) 10 h. (c) 20 h. (d) schematics of the morphology evolution.

In order to investigate i) the interaction (chemical bonding) between CNTs shell and LiFePO_4 core; and ii) the local chemistry environment of elemental Fe in LFP@CNTs composites, C K-edge and Fe K-edge X-ray Absorption Near Edge Structure (XANES) spectra were studied (Figure 6.3c, 6.3d). The Fe K-edge XANES spectra exhibit a pre-edge and an edge jump (Figure 6.3c). The pre-edge peak is centered at the lower energy side of the sharply rising absorption edge (white line), corresponding to the $1s$ to $3d$ electronic transition of Fe [22]. All of the LFP@CNTs composites exhibited an edge feature characteristic of Fe(II) and a distinct increased white line located at ~ 7126 eV, indicating an Fe bivalence feature with some depleted p character with increasing annealing time [22, 23]. The gradually increasing resonance at ~ 7141 eV indicates the improved crystallinity of the composites when prolonging the annealing time. Three regions of resonance in the C K-edge XANES spectra can be observed (Figure 6.3d). Two patterns located at ~ 285 eV and 291 eV (at a and c position) correspond to graphitic π^* and σ^* transitions, respectively [24]. The presence of graphitic π^* and σ^* transitions implies that the graphitic framework exists in LFP@CNTs nanocomposites. The most

interesting feature in the spectra is the obvious resonance at ~ 288 eV (at b position), which arises from oxygen containing functional group of carboxylate bonding among other C-O single bond functionalities [24a]. Many groups attribute this resonance to the chemical bonding between active materials and carboxylate groups [24b, 25]. The intensity of peak b from LFP@CNTs-20h is lower than that of the other two composites, suggesting that the weakened carboxylate bonding in the composites. This is accompanied by the increase in intensity of the π^* resonance, pending no countervailing arguments of texture for these random powder sample, this observation strongly indicates that a more order graphitic situation is restored. Considering carboxylate bonding is related to the interaction between the CNTs shell and LiFePO_4 core, this phenomenon provides direct spectroscopic evidence that the interaction between the CNTs shell and LiFePO_4 core is stronger in LFP@CNTs-10h than LFP@CNTs-20h.

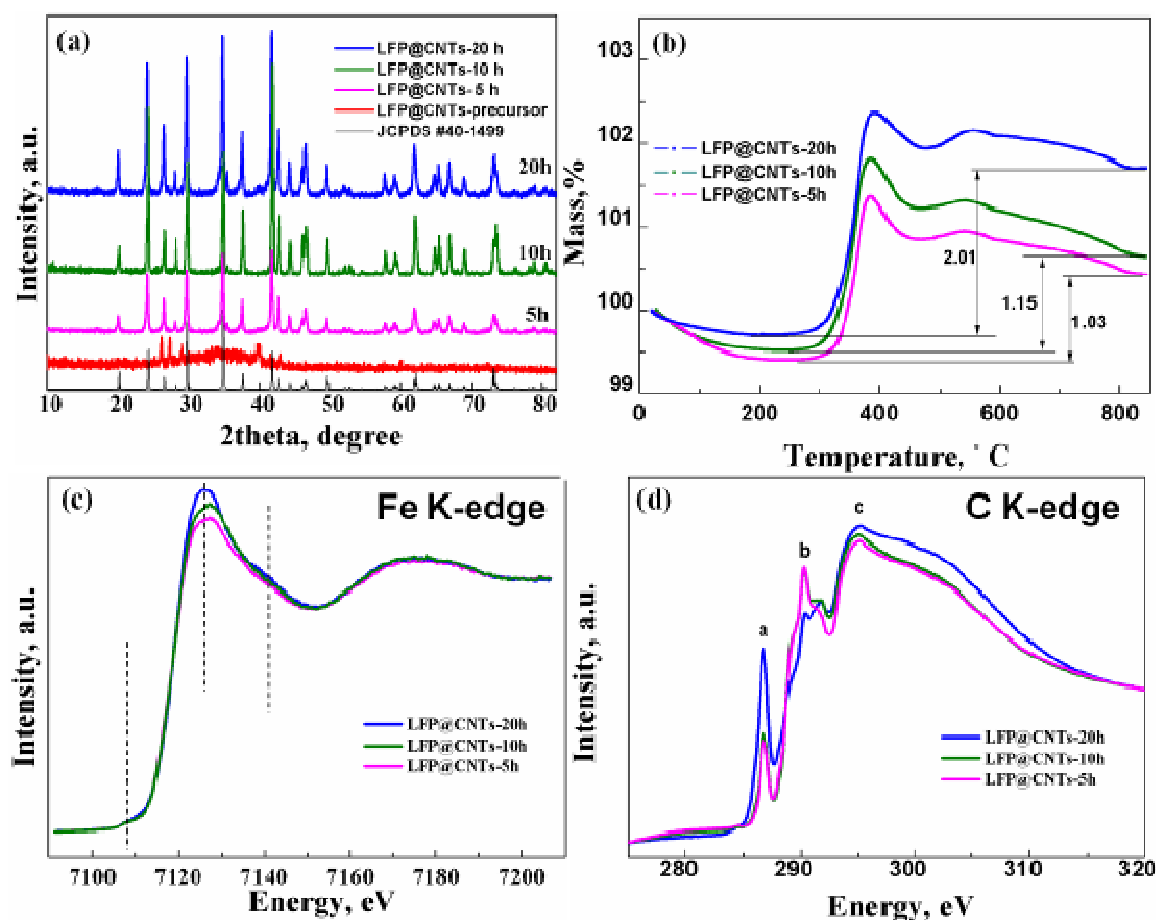


Figure 6.3 XRD patterns (a) and TGA curves (b) of LFP@CNTs composites; normalized XANES spectra for LFP@CNTs composites: (c) Fe K edge; (d) C K edge.

Figure 6.4 shows the electrochemical performance of the LFP@CNTs nanocomposite. A couple of redox peaks are observed for the three cyclic voltammetry (CV) curves (1st, 5th and 10th) of LFP@CNTs-10h (Figure 6.4a). It is noted that the gap between the redox peaks is gradually decreasing and the peaks intensity increases in conjunction with the increase in cycle number (inset zoom in Figure 6.4a), suggesting the kinetics for lithium insertion and extraction improves during cycling. The charge and discharge curves in different cycles (1st, 10th, 50th and 100th) show the same trend (Figure 6.4b). The gap between the redox peaks becomes increasingly narrow from the initial cycle to the 100th cycle, and the value of potential interval (ΔE) decreased from 83 mV in the initial cycle to 52 mV in the 10th cycle, 47 mV in the 50th cycle and 44 mV in the 100th cycle

(Figure S6.6). LFP@CNTs-10h nanocomposite delivers a discharge capacity of 155 mA h g^{-1} in the initial cycle at a current density of 34 mA g^{-1} (0.2C), and the discharge capacity remains almost constant till 100 cycles.

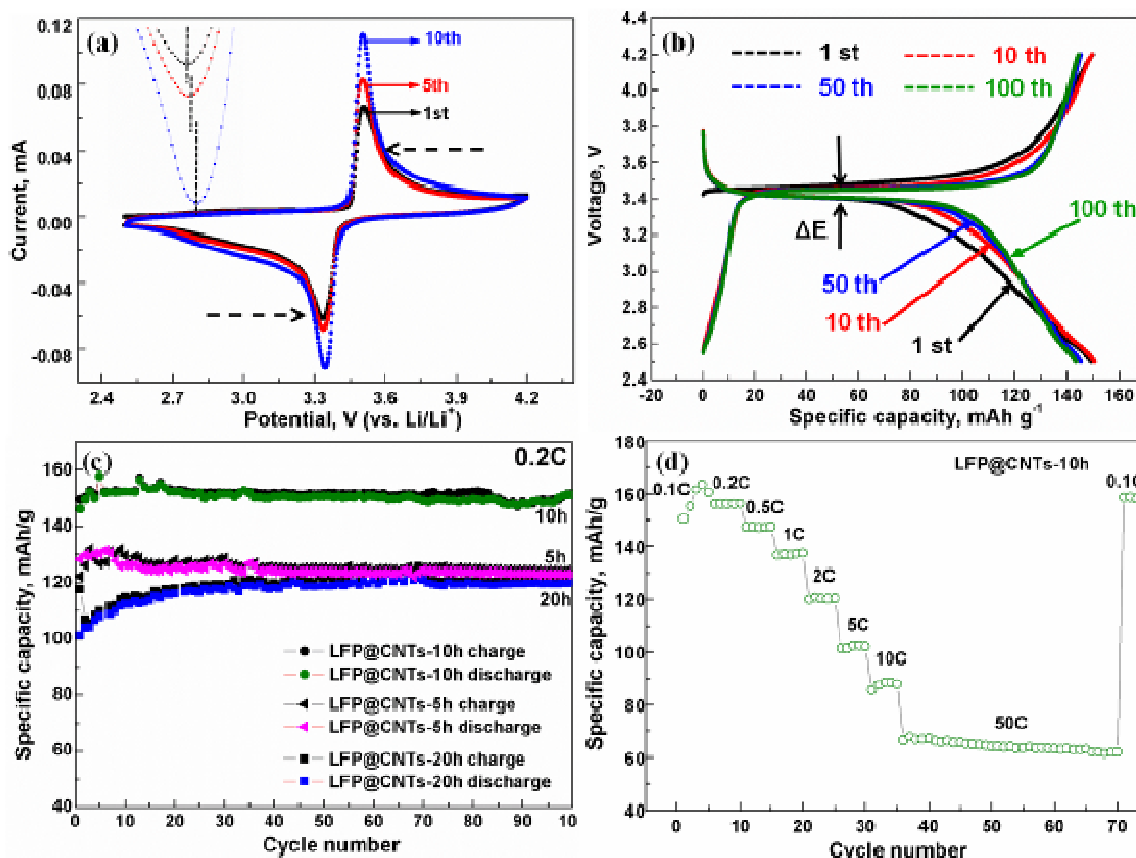


Figure 6.4 (a) Cyclic voltammetry (CV) profiles for LFP@CNTs-10 at a scan rate of 0.1 mV s^{-1} ; (b) Galvanostatic cycle charge-discharge profiles in voltage range of 2.5-4.2 V at 0.2 C; (c) Cyclic performance at 0.2 C prepared at different annealing time and (d) Rate capabilities of LFP@CNTs-10 nanocomposites.

The cycle performance of LFP@CNTs composites at a current density of 34 mA g^{-1} (0.2C) is shown in Figure 6.4c. It is found invisible specific capacity fading over 100 cycles and the coulombic efficiency stays about 100%, demonstrating LFP@CNTs nanocomposites have an excellent cycling performance. Because of amorphous CNTs shell, LFP@CNTs-5h delivers a capacity of 127 mA h g^{-1} . LFP@CNTs-20h displays a

capacity of 120 mA h g^{-1} , which is lower than that of LFP@CNTs-10h, due to the agglomeration of LiFePO_4 nanorods and weak chemical bonding between the CNTs shell and LiFePO_4 core. The discharge specific capacity of LFP@CNTs-10h decreases from 160 to 102 mA h g^{-1} with an increasing current rate from a value of 0.1C to 5C regularly (Figure 6.4d), and it still delivers a capacity of 65 mA h g^{-1} even at a high current density of 8500 mA g^{-1} (50C, 1.2 minutes for charging and 1.2 minutes for discharging) with almost no fading up to 35 cycles, thereby indicating its high power performance. The results shown in Figure 6.4b obviously demonstrates the remarkably electrochemical performance benefiting from the one dimensional core-shell LFP@CNTs nanowire structure and 3D CNTs networking.

6.4 Conclusions

In summary, one-dimensional core-shell LFP@CNTs nanowires composites are successfully synthesized via a facile sol-gel route followed by post-heating treatment. By using PMMA, the core-shell structure is obtained in the calcinations step, and the structures display the encapsulated architecture with LiFePO_4 embedded inside and CNTs outside. The homogenous CNTs shells and 3D networking act as a continuous conductive network since electrons are easily transferred between the surface of LiFePO_4 nanowires and CNTs. The small size of LFP nanowires confined by polymer decreases the lithium ions diffusion path and increases the contact areas between electrolyte and active materials, therefore, our LFP@CNTs nanowires offer excellent cycling stability and rate capability. By conducting calcinations in Argon, the 10 h post-heating time is demonstrated as the optimal time. Longer annealing time leads to agglomeration of LiFePO_4 nanorods and poor interaction, resulting in poor electrochemical performance. In addition, the one dimensional core-shell nanostructures can be easily extended to other cathode or anode materials, then optimize the performance of electrodes in lithium-ion batteries of electric or hybrid electric vehicles.

6.5 Acknowledgements

This work is supported by NSERC, Clariant (Canada) Inc. (former Phostech lithium Inc.), CRC Program and the University of Western Ontario.

6.6 Supporting Information

Supporting Information. TEM images, Selected-area electron diffraction pattern, SEM images, Raman spectrum and charge-discharge galvanostatic curves for different cycles of LFP@CNTs composites.

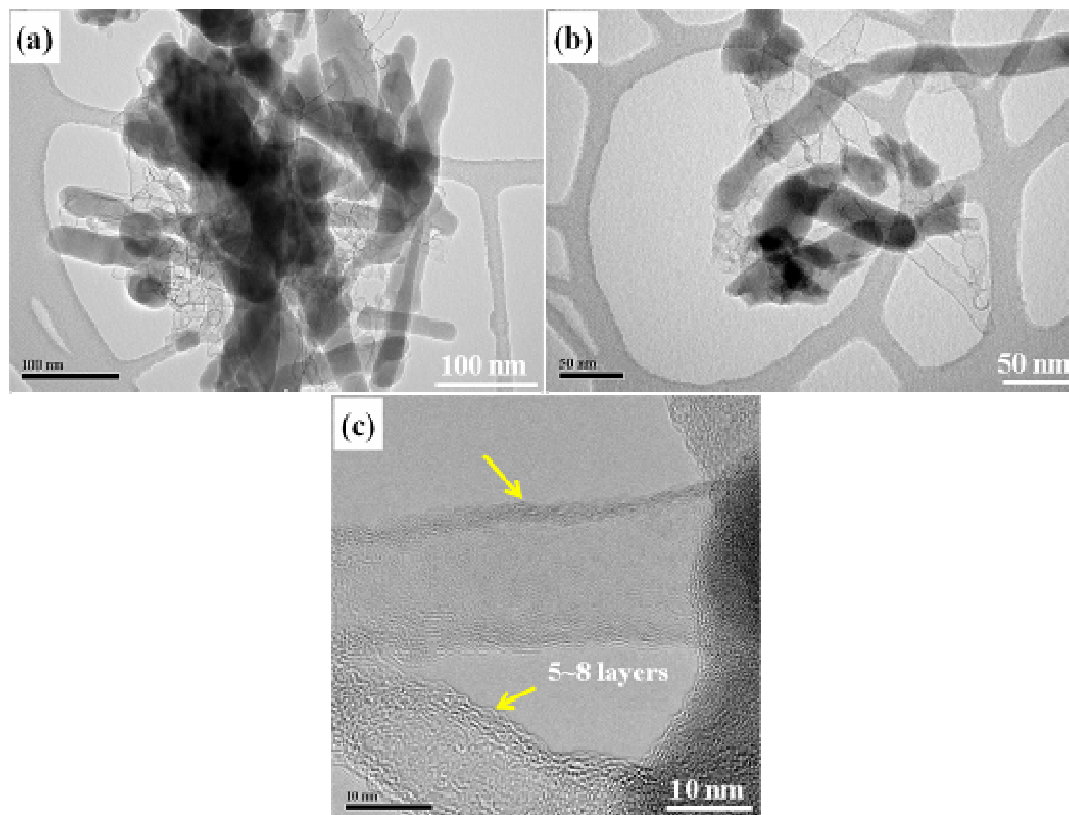


Figure S 6.1 TEM images (a), (b) and HRTEM image (c) of LFP@CNTs nanowires.



Figure S 6.2 Selected-area electron diffraction of core shell LFP@CNTs-10h nanowire.

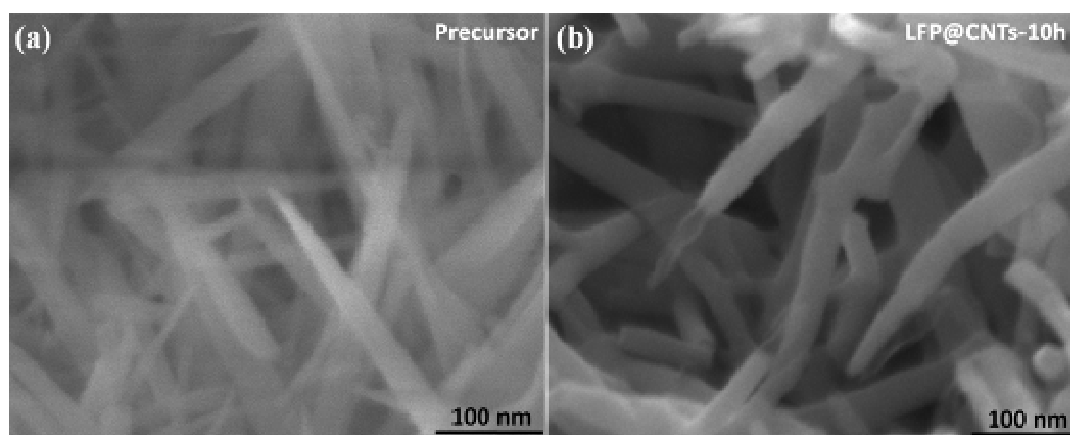


Figure S 6.3 SEM images of (a) LiFePO₄ precursor and (b) LFP@CNTs-10h nanowire.

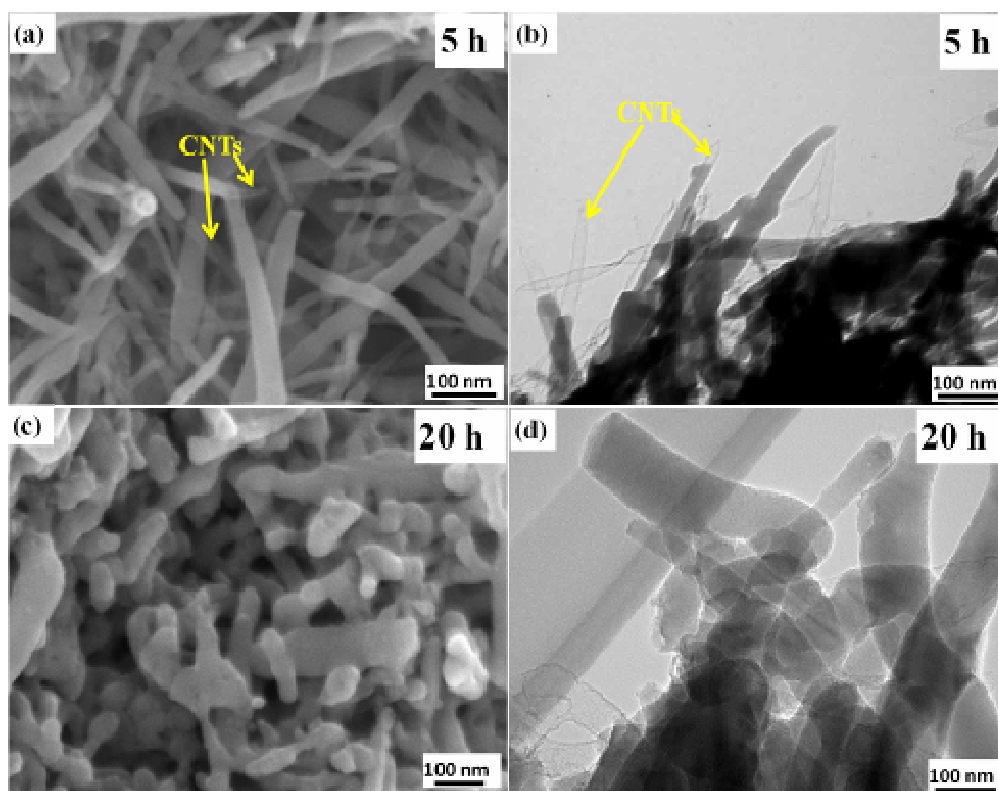


Figure S 6.4 SEM image (a) and TEM image (b) of core-shell LFP@CNTs-5h; SEM image (c) and TEM image (d) of LFP@CNTs-20h nanorod.

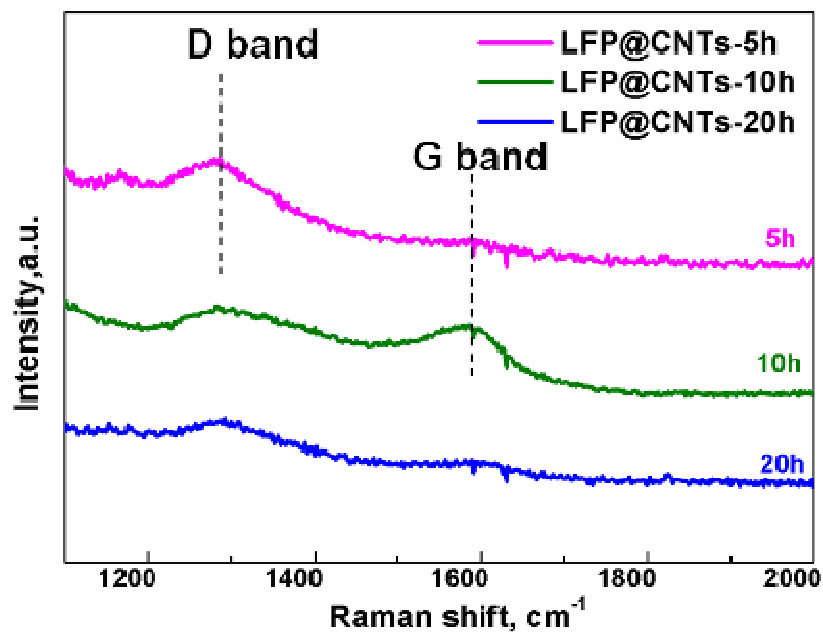


Figure S 6.5 Raman spectra of LFP@CNTs composites annealed at different time.

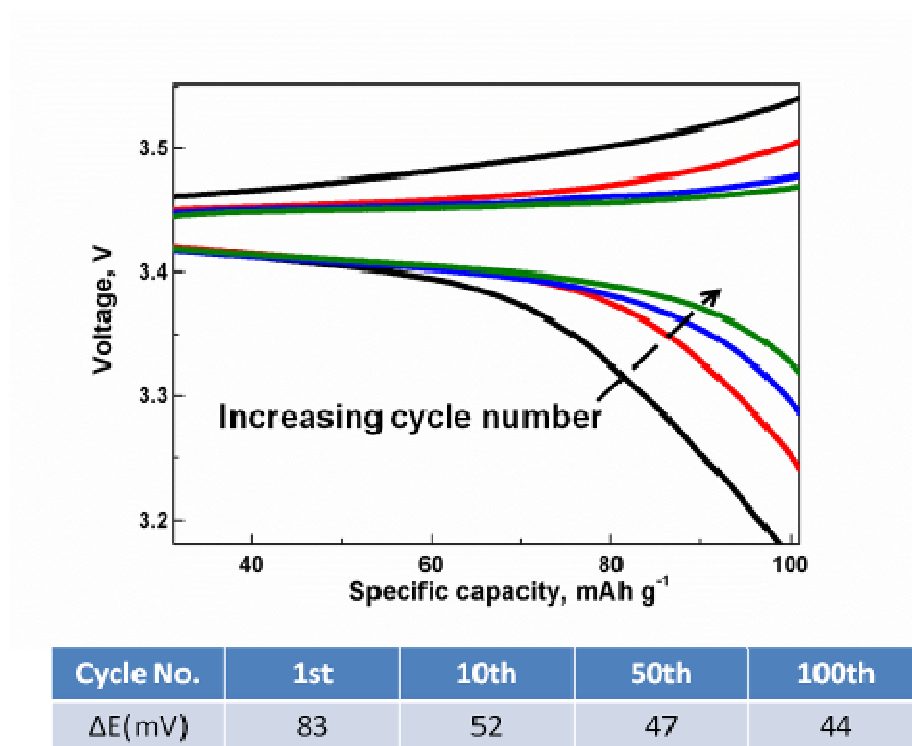


Figure S 6.6 Charge-discharge galvanostatic curves for different cycles (1st, 10th, 50th and 100th).

6.7 References

- [1] A. K. Padhi, K. S. Nanjundaswamy and J. B. Goodenough, *J. Electrochem. Soc.*, 1997, **144**, 1188-1194.
- [2] N. Ravet, J. B. Goodenough, S. Besner, M. Simoneau, P. Hovington and M. Armand, *The Electrochemical Society and The Electrochemical Society of Japan, Meeting Abstracts*, 1999, **99-2**, Honolulu, HI, Oct 17-22.
- [3] A. Yamada, H. Koizumi, S.-I. Nishimura, N. Sonoyama, R. Kanno, M. Yonemura, T. Nakamura and Y. Kobayashi, *Nat. Mater.*, 2006, **5**, 357-360.
- [4] a) J. Yang, J. Wang, D. Wang, X. Li, D. Geng, G. Liang, M. Gauthier, R. Li and X. Sun, *J. Power Sources*, 2012, **208**, 340-344; b) J. Wang and X. Sun, *Energy Environ. Sci.*, 2012, **5**, 5163-5185; c) J. Yang, J. Wang, X. Li, D. Wang, J. Liu, G. Liang, M. Gauthier, Y. Li, R. Li and X. Sun, *J. Mater. Chem.*, 2012, **22**, 7537-7543; d) J. Wang, J. Yang, Y. Tang, R. Li, G. Liang, T.-K. Sham and X. Sun, *J. Mater. Chem. A*, 2013, **1**, 1579-1586.
- [5] K. Zaghib, A. Mauger, F. Gendron and C. M. Julien, *Chem. Mater.*, 2008, **20**, 462-469.
- [6] H. S. Zhou, D. L. Li, M. Hibino and I. Honma, *Angew. Chem.*, 2005, **117**, 807-812; *Angew. Chem. Int. Ed.*, 2005, **44**, 797-802.
- [7] a) M. Gaberscek, R. Dominko and J. Jamnik, *Electrochem. Commun.*, 2007, **9**, 2778-2783; b) R. Dominko, M. Bele, J. M. Goupil, M. Gaberscek, D. Hanzel, I. Arcon and J. Jamnik, *Chem. Mater.*, 2007, **19**, 2960-2969; c) Y. S. Hu, Y. G. Guo, R. Dominko, M. Gaberscek, J. Jamnik and J. Maier, *Adv. Mater.*, 2007, **19**, 1963-1966.
- [8] V. Srinivasan and J. Newman, *J. Electrochem. Soc.*, 2004, **151**, A1517-A1529.
- [9] a) P. S. Herle, B. Ellis, N. Coombs and L. F. Nazar, *Nat. Mater.*, 2004, **3**, 147-152; b) Y.-H. Rho, L. F. Nazar, L. Perry and D. Ryan, *J. Electrochem. Soc.*, 2007, **154**, A283-A289.

- [10] S. W. Oh, S. Myung, S. Oh, K. H. Oh, K. Amine, B. Scrosati and Y. Sun, *Adv. Mater.*, 2010, **22**, 4842-4845.
- [11] A. A. Salah, A. Mauger, K. Zaghib, J. B. Goodenough, N. Ravet, M. Gauthier, F. Gendron and C. M. Julien, *J. Electrochem. Soc.*, 2006, **153**, A1692-A1701.
- [12] Y. Wu, Z. Wen and J. Li, *Adv. Mater.*, 2011, **23**, 1126-1129.
- [13] C. Sun, S. Rajasekhara, J. B. Goodenough and F. Zhou, *J. Am. Chem. Soc.*, 2011, **133**, 2132-2135.
- [14] S. Kim, J. Ryu, C. B. Park and K. Kang, *Chem. Commun.*, 2010, **46**, 7409-7411.
- [15] J. Liu, T. E. Conry, X. Song, M. M. Doeff and T. J. Richardson, *Energy Environ. Sci.*, 2011, **4**, 885-888.
- [16] Y. Zhou, J. Wang, Y. Hu, R. O'Hayreb and Z. Shao, *Chem. Commun.*, 2010, **46**, 7151-7153.
- [17] X. L. Wu, L. Y. Jiang, F. F. Cao, Y. G. Guo and L. J. Wan, *Adv. Mater.*, 2009, **21**, 2710-2714.
- [18] H. Liu, Y. Zhang, R. Li, X. Sun, D. Désilets and H. Abou-Rachid. *Carbon*, 2010, **48**, 1498-1507.
- [19] L. Cheng, X. L. Li, H. J. Liu, H. M. Xiong, P. W. Zhang and Y. Y. Xia, *J. Electrochem. Soc.*, 2007, **154**, A692-A697.
- [20] X. Lou and Y. Zhang, *J. Mater. Chem.*, 2011, **21**, 4156-4160.
- [21] M. M. Doeff, J. D. Wilcox, R. Kostecki and G. Lau, *J. Power Sources*, 2006, **163**, 180-184.
- [22] G. X. Wang, S. Bewlay, S. A. Needham, H. K. Liu, R. S. Liu, V. A. Drozd, J. F. Lee and J. M. Chen, *J. Electrochem. Soc.*, 2006, **153**, A25-A31.

- [23] K. Hsu, S. Hua, C. Chen, M. Cheng, S. Tsay, T.Chou, H.Sheu, J. Lee and B. Hwang, *J. Power Sources*, 2009, **192**, 660-667.
- [24] a) J. Zhou, J. Wang, H. Fang and T. K. Sham, *J. Mater. Chem.*, 2011, **21**, 5944-5949; b) J. Zhou, J. Wang, H. Fang, C. Wu, J. N. Cutler and T. K. Sham, *Chem. Commun.*, 2010, **46**, 2778-2780.
- [25] D. Wang, X. Li, J. Wang, J. Yang, D. Geng, M.Cai, R. Li, T. K. Sham and X. Sun, *J. Phys. Chem. C*, 2012, **116**, 22149-22156.

Chapter 7

7 Peapod-like LiFePO_4 -C Nanowires Synthesised by Hydrothermal Route for Li-Ion Batteries

In last chapter (6), one dimensional LFP@CNTs could be obtained by applying surfactant of PMMA, and excellent electrochemical performance can be achieved based on the successful morphology design. Therefore, we expect to extend this design into hydrothermal system to realize large-scale yield. In this chapter, we try to get LiFePO_4 nanowire structure by applying hydrothermal route.

In this chapter, a two step process has been employed in preparation of one dimensional peapod like LiFePO_4 /carbon nanowires. The diameter of the core LiFePO_4 nanowire is around 50 nm with carbon shell. The discontinuous LiFePO_4 nanoparticles were connected by the carbon shell constituting the nanowire structure. With the help of the PPy conductive network, the LiFePO_4 /C delivers a capacity of 120 mA h g^{-1} . The mechanism for the morphology evolution of nanowire is investigated. When prolonging the hydrothermal reaction time, the octahedral structure is converted into honeycomb morphology, where the nuclei of the nanowires were derived, and then grew into nanowire morphology.

Key words: LiFePO_4 , nanowire, PPy, lithium ion batteries

Note: This chapter will be submitted.

7.1 Introduction

Over the past few years, there is a dramatic increase of interest in large scale batteries demand for energy storage to develop electric vehicle (EV) and hybrid electric vehicle (HEV). Since the pioneer work of Goodenough and co-workers [1], the olivine LiFePO_4 has been recognized as a most promising cathode material for large size lithium-ion batteries due to its low cost, environmental compatibility, high theoretical specific capacity of 170 mA h g^{-1} and especially a superior safe performance. Unfortunately, the main obstacle of LiFePO_4 for its practical applications in vehicles is due to its poor rate capability, which can be attributed to slow kinetics of lithium-ion diffusion through the LiFePO_4 - FePO_4 interfaces and the poor electronic conductivity [2, 3].

In order to overcome this major problem, various approaches have been explored. One way is increasing the overall conductivity of composite electrodes by coating LiFePO_4 with a conducting phase to form core-shell structures. Core-shell structures are composed of double or multilayer, which are expected to combine the functions of both core and shell parts, and then improve the general performance of the composite. The unique structures have been applied to the field of Li-ion batteries recently [4-15]. Up to now, additives were introduced to synthesize LiFePO_4 /conductive material composites, such as dispersed carbon, metal powders, and intrinsically conducting polymers. Among of them, carbon coating and addition have been particularly attractive with respect to its high conductivity, low cost, and simplicity. Coating the LiFePO_4 particle with carbon can increase the charge-discharge rate capability of an electrode [9-13]. Ravet reported that LiFePO_4 with about 1 wt % carbon coating can achieve a capacity of 160 mA h g^{-1} cycled at 1 C rate at 80°C . The intimate contact between carbon and LiFePO_4 facilitates current collection from the particles [16]. Franger found that LiFePO_4 with a carbon content of less than 5 wt% showed a specific discharge capacity of 143 mA h g^{-1} at 0.1 C [17]. Huang first demonstrated that LiFePO_4 with 15 wt % carbon coating has excellent rate capability even cycled at a 5 C rate with a capacity of 120 mA h g^{-1} [18]. Another way is decreasing the particles' size to eliminate lithium diffusion limitations. Yamada reported that small particles of LiFePO_4 by sintering at 550°C which can reach 95% theoretical capacity of LiFePO_4 at room temperature [19].

Numerous studies have been conducted in literatures on C-LiFePO₄ composite material and great progresses have been achieved in this field in the past years [20-22]. A combination of carbon coating and nano particle size have been commercialized by many companies such as Clariant Inc., and improved material utilization at high rate for LiFePO₄ was achieved. One-dimensional nanostructures are novel promising structures used in the electrodes for rechargeable lithium-ion batteries, especially recently great success have been achieved in the anodes part. In this chapter, we aim at designing nanowire cathode material [23] which combines carbon coating and one-dimensional LiFePO₄.

Fine particles of LiFePO₄ can be obtained by using various synthesis methods [24-27], such as a sol-gel process [28], mechanochemical activation [29], solid-state synthesis [30], which involve several mixing-grinding and heating stages. Among the various synthesis methods, hydrothermal process is a useful method for preparing various interesting structures and offers the promise of simplicity and scalability [31-36]. In 2001, Whittingham first reported that LiFePO₄ can be prepared at a relatively low temperature of 120 °C by hydrothermal route [31]. Lee also reported that LiFePO₄ can be obtained at both subcritical and supercritical hydrothermal conditions [37]. In addition, hydrothermal method gives LiFePO₄ with a few of hundreds of nanometers because of the low operating temperature under a certain pressure. Moreover, the particle size can be further decreased with the introduction of carbon. Thus, hydrothermal route demonstrates a facile way in LiFePO₄ fabrication.

Polypyrrole (PPy) has been extensively studied as a cathode material for rechargeable batteries because it has redox couple and allows percolation of the electrolyte into the polymer network [38-40]. Moreover, it possesses good conductivity. Recently, PPy is studied in conjunction with active material for rechargeable batteries, and improved electrochemical performance can be achieved by introducing PPy polymer [41, 42].

Herein, we synthesis one dimensional core-shell LiFePO₄/carbon nanowires (~50 nm) using hydrothermal method, PPy modified LiFePO₄ was prepared thereafter. The mechanism for the morphology evolution of nanowires is also investigated. The nuclei of

the nanowires are derived from the decomposition of the initial octahedral particles. The electrochemical performances of the two composites were further investigated.

7.2 Experimental

7.2.1 Synthesis of pea-pod like LiFePO_4 nanowire

In a typical synthesis process for preparing LiFePO_4 nanowires, lithium hydroxide (LiOH), ammonium dihydrogen phosphate ($\text{NH}_4\cdot\text{H}_2\text{PO}_4$) and ferrous sulfate ($\text{FeSO}_4\cdot 7\text{H}_2\text{O}$) (all from Aldrich) are used as starting materials, the starting precursors of Li:Fe:P are prepared in a molar ratio of 3:1:1.

Metal salts were first dissolved in 8 ml de-ionized water. After stirring, 0.3 g nitrilotriacetic acid (NTA) surfactant and 7 ml isopropanol were added, and then 1.6 mmol ascorbic acid was added to the suspension. The pH value of the mixture was adjusted to 5 by adding concentrated ammonia, and the concentration of LiOH in the precursor solution is 0.2 M. The mixed solution was then transferred into a 50 ml stainless steel Teflon-lined autoclave. After stirring for 5 min followed by Ar gas bubbling for 10 min to get rid of the oxygen, the autoclave was sealed, kept at 200 °C for 20 h, and then naturally cooled to room temperature. After the hydrothermal reaction, the solution was centrifuged and washed with distilled water for a number of times. The gray-white product was dried at 60 °C in vacuum overnight. To get better crystallized LiFePO_4 and the nano carbon layer, the obtained material was treated at 700 °C for 1 h under Ar atmosphere.

For the preparation of PPy modified LiFePO_4/C composites, we mix the LiFePO_4 powder as-obtained above (1 g) with pyrrole (0.08 mol) and FeCl_3 (0.1 mol) in distilled water (100 ml) by stirring at 5 °C for 24 h, then dried the composite at 90 °C for 12 h under vacuum.

7.2.2 Physical characterization

Phase composition were characterized and analyzed by powder X-ray diffraction (XRD, a Bruker D8 Discover diffractometer, operating at 40 kV and 40 mA with Co K α radiation ($\lambda=0.179$ nm)), field-emission scanning electron microscope (FESEM, Hitachi S-4800,

operating at 5 kV equipped with an energy-dispersive X-ray spectrometry (EDX)) and transmission electron microscope (TEM, Philips CM10 microscope, operating at 100 kV) to study the morphology and size distribution.

7.2.3 Electrochemical Measurements

The electrochemical cell used in our study was a CR2032 coin cell. The electrolyte used in our experiment was 1 M LiPF_6 in a mixture of ethylene carbonate/dimethyl carbonate (1:1 v/v) solvents. All electrochemical tests were performed in an Arbin BT-2000 Battery Test Station within a voltage range of 2.5-4.2 V (versus Li^+/Li). The composites were mixed with acetylene black and poly-(vinylidene fluoride) (PVDF) binder with a weight ratio of 75:15:10, using N-methyl-2-pyrrolidene (NMP) as the solvent, and then the mixture was ground in a mortar with pestle and pasted onto pure Al foils. The coin cells were assembled in a high-purity argon filled glove box, and all of the electrochemical measurements were conducted at room temperature.

7.3 Results and discussion

Figure 7.1 shows a SEM image of the as-prepared LiFePO_4 precursor nanowires. The nanowires have a diameter of around 50 nm and a length extending to a few tens of micrometers. Lower magnification image shows the nanowires are quite uniform (Inset in Figure 7.1).

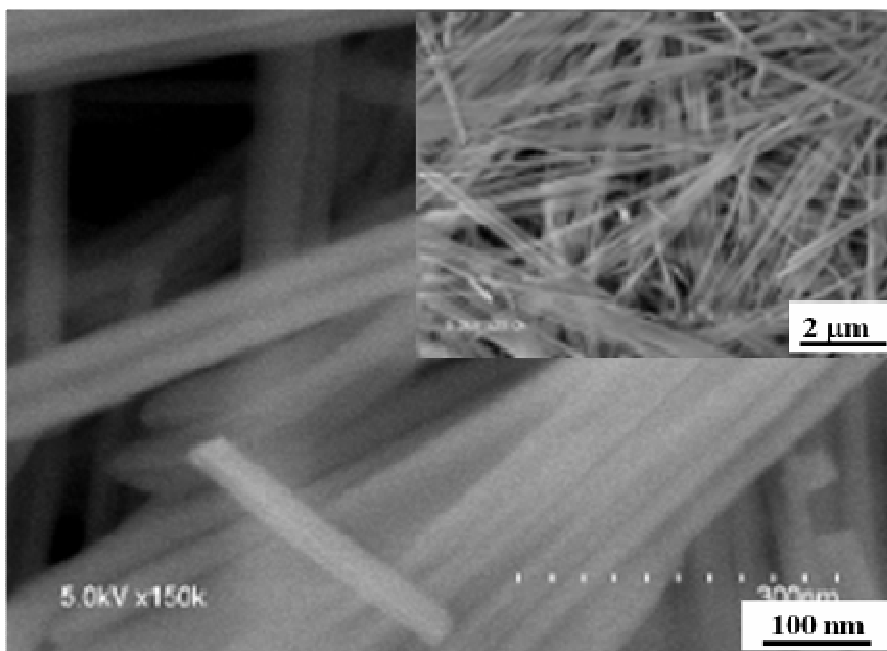


Figure 7.1 SEM images of LiFePO₄ nanowires precursor, inset indicates low magnification graph.

Core-shell LiFePO₄/carbon nanowires can be obtained by heat treatment at 700 °C for one hour. The morphology is shown in Figure 7.2a. After annealing, the nanowires structure is still maintained, and necklace-like structure is composed of discontinued LiFePO₄ particles which are connected by the carbon shell. The diameter of the nanowires is still around 50 nm, and the size distribution is pretty uniform from lower magnification (inset). The core-shell structure can be further demonstrated by the TEM images, as shown in Figure 7.2b. The nanowires present different contrast, where the light part is carbon, and the dark area is LiFePO₄ particles.

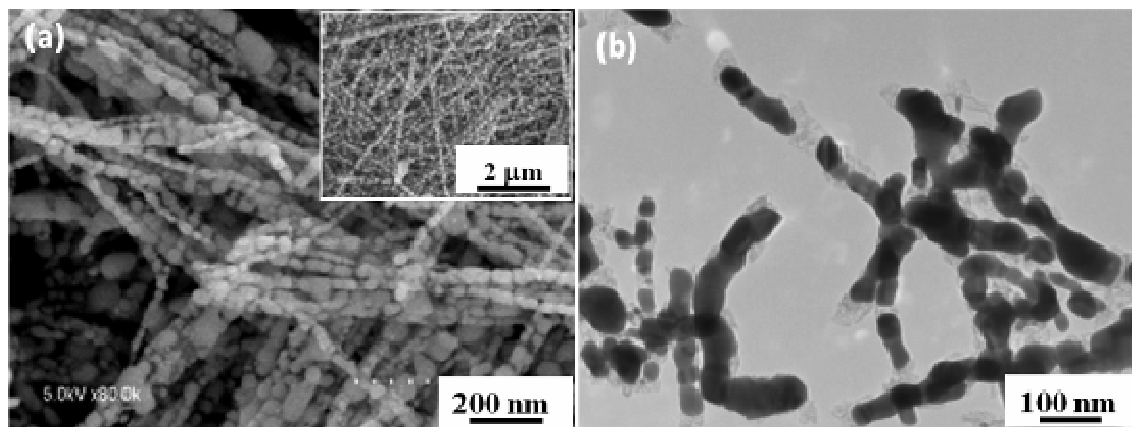


Figure 7.2 SEM (a) and TEM (b) images of core-shell LiFePO_4 /carbon nanowires annealed at 700°C , inset shows the low magnification SEM image.

The mechanism of the morphology evolution of nanowires is further studied. In order to see the morphology evolution, we choose different reaction time (0 min, 5 min, 10 min, 15 min, 20 min, 25 min, 30 min, 40 min, 50 min and 60 min). When the temperature reached 200°C , the big octahedral particles formed immediately, prolong the reaction time to 5 min, the octahedral particles began to decompose along each facet, as shown in Figure S 7.1. With increasing the reaction time, the decomposition is becoming more severe (Figure 7.3a). When the reaction time went to 15 min (Figure 7.3b), the octahedral structure is still maintained, but each facet is fully decomposed to nanorod, as shown in Figure 7.3c. Further prolonging the reaction time, the rod-like structure began to decompose from the edge into honeycomb structure (Figure 7.3d). It is found the octahedral structure gradually changed into honeycomb structure with the increase of reaction time (Figure 7.3e, 7.3f, 7.3g). The nuclei of the nanowires is derived from the decomposition of honeycomb structure, and then the nanowires started to grow at around 50 min, and further the honeycomb structure is fully converted into nanowires structure at 60 min, as shown in Figure 3h. The nanowire grew longer with increasing the reaction time.

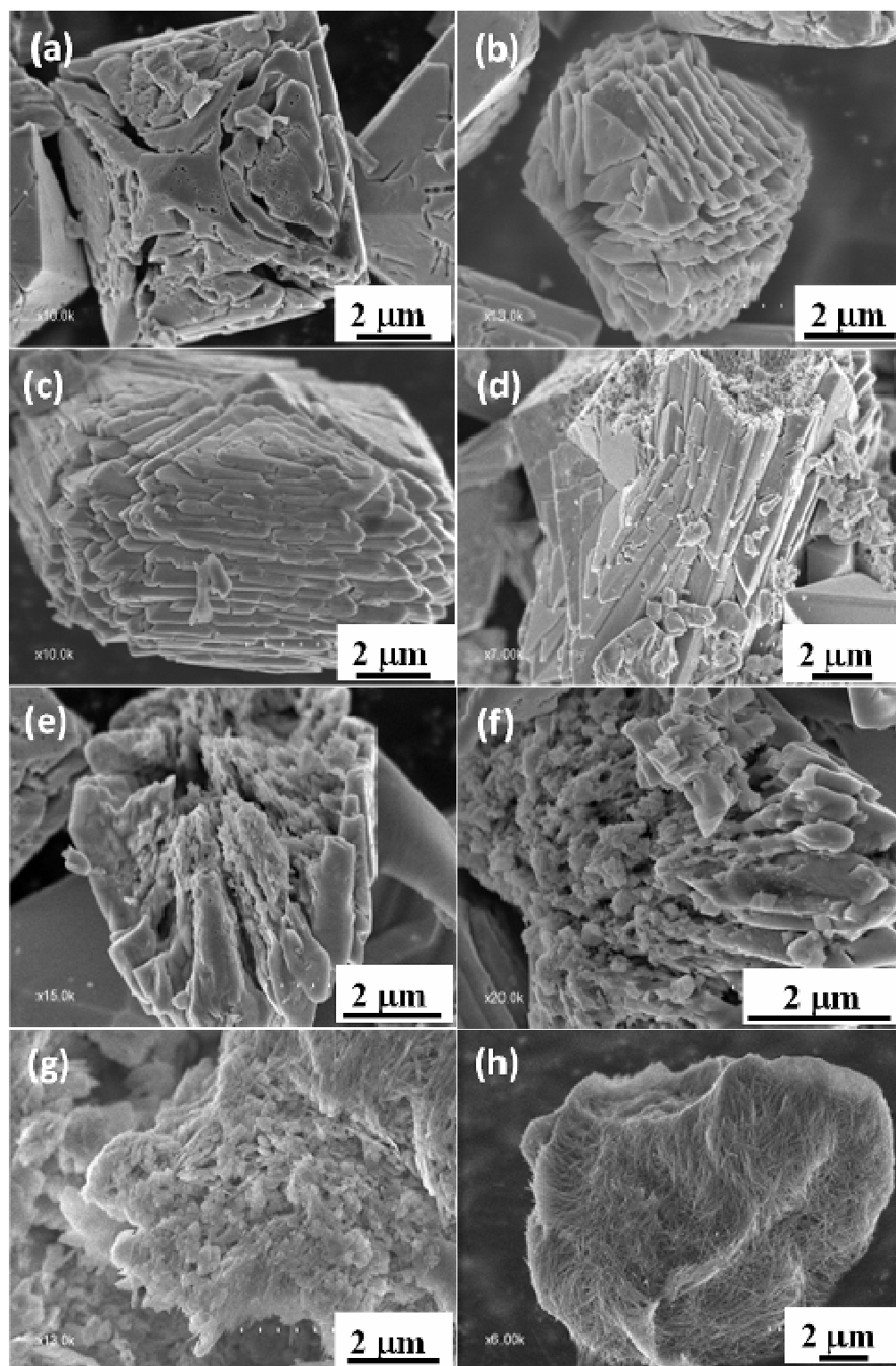


Figure 7.3 The morphology evolution of the of LiFePO_4 precursor nanowires in function of hydrothermal reaction time.

The phase purity of the LiFePO_4 nanowires was analyzed by X-ray powder diffraction. Figure 7.4 shows XRD patterns of the LiFePO_4 /carbon nanowires. Due to the introduction of the surfactant (NTA), some peaks were shown in low angle diffraction. After calcinations, these low angel diffraction peaks disappeared, and the diffraction peaks of the annealed sample can be attributed to an ordered olivine LiFePO_4 structure (JPCDS, no #40-1499).

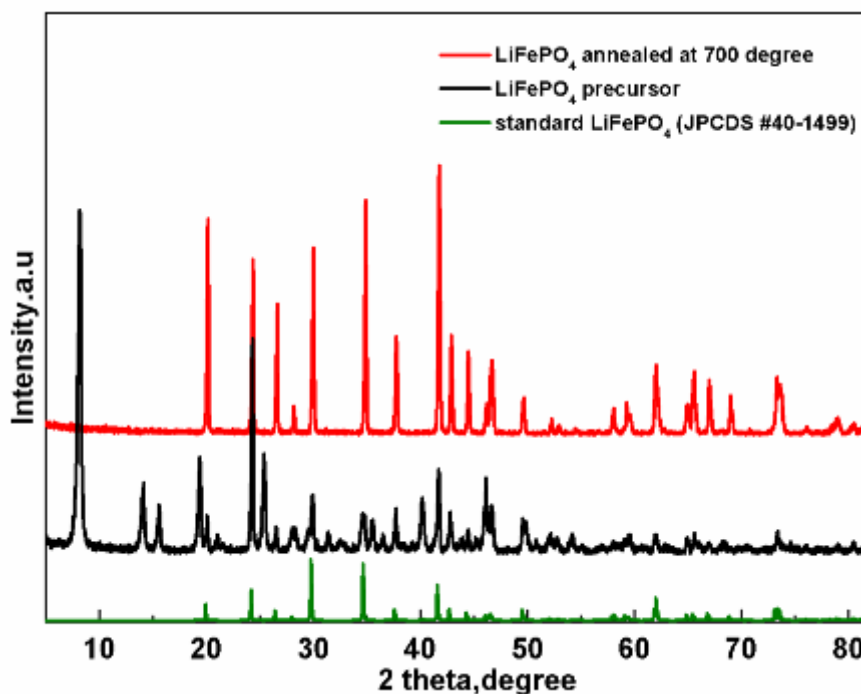


Figure 7.4 XRD patterns of the as-obtained LiFePO_4 /carbon nanowire and its precursor.

The cycle performance of LiFePO_4/C nanowire and PPy modified LiFePO_4/C composites at a current density of 17 mA g^{-1} (0.1 C) is shown in Figure 7.5. It is found no specific capacity fading over the charge/discharge cycles, demonstrating an excellent cycling performance for as-obtained LiFePO_4/C composites. LiFePO_4/C nanowire composites displays a capacity of 100 mA h g^{-1} , while LiFePO_4/C -PPy nanowire shows higher specific capacity (120 mA h g^{-1}), benefiting from high conductivity of PPy polymer and network structure.

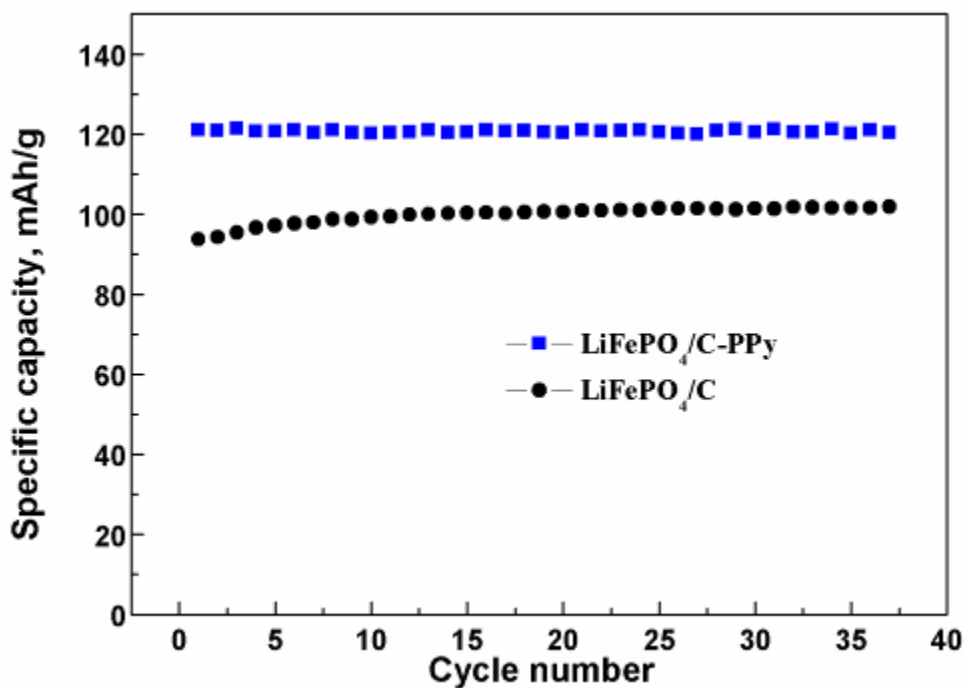


Figure 7.5 Cycle performances of the LiFePO₄/C nanowire and PPy modified composites.

7.4 Conclusions

We have successfully synthesized core-shelled LiFePO₄/carbon nanowires by hydrothermal method. The diameter of the nanowire is around 50 nm. The carbon coating was realized by adding ascorbic acid into the solution. The mechanism of the nanowires evolution is investigated. When prolonging the reaction time, the octahedral structure converted into honeycomb structure, where the nuclei of the nanowires were derived, and then grew into long nanowires structure. Necklace-like structure of nanowire appeared during the heat treatment, discontinued LiFePO₄ nanoparticles were connected by the carbon shell constituting the nanowire structure. PPy modified LiFePO₄/C composites delivers higher specific capacity than the LiFePO₄/C nanowire, which is due to its high conductivity and network.

7.5 Acknowledgements

This work is supported by NSERC, Clariant (Canada) Inc. (former Phostech lithium Inc.), CRC Program and the University of Western Ontario.

7.6 Supporting information

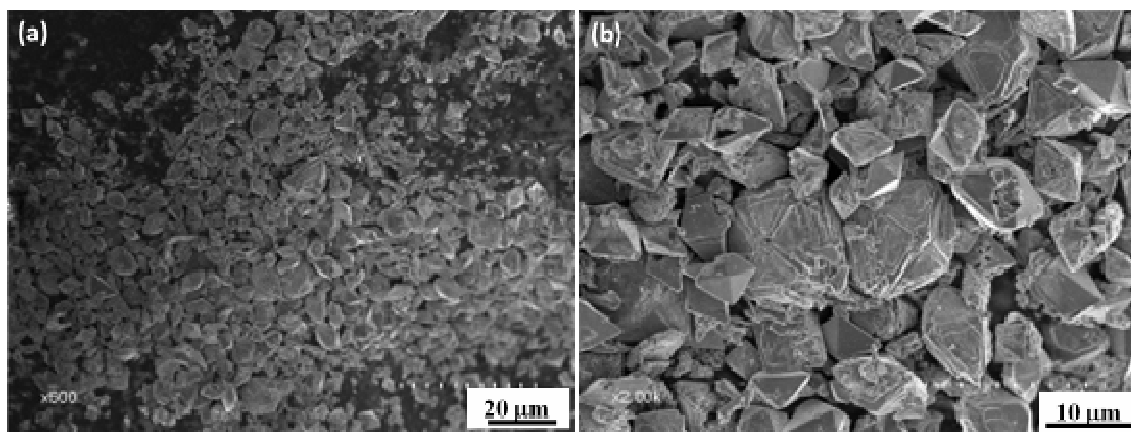


Figure S 7.1 Morphologies of the initial formed products at (a) 0 min; (b) 5 min.

7.7 References

- [1] A. K. Padhi, K. S. Nanjundaswamy, J. B. Goodenough, J. Electrochem. Soc., 1997, **144**, 1188.
- [2] A. S. Andersson, J. O. Thomas, B. Kalska, L. Haggstrom, Electrochem. Solid State Lett., 2000, **3**, 66.
- [3] A. S. Andersson, J. O. Thomas, J. Power Sources, 2001, **97-98**, 498.
- [4] Y. K. Sun, S. T. Myung, M. H. Kim, J. Prakash, K. Amine, J. Am. Chem. Soc., 2005, **127**, 13411.
- [5] K. T. Lee, Y. S. Jung, S. M. Oh, J. Am. Chem. Soc. 2003, **125**, 5652.
- [6] L. J. Fu, H. Liu, H. P. Zhang, C. Li, T. Zhang, Y. P. Wu, R. Holze, H. Q. Wu, Electrochem. Commun., 2006, **8**, 1.
- [7] X. H. Huang, J. P. Tu, C. Q. Zhang, X. T. Chen, Y. F. Yuan, H. M. Wu, Electrochim. Acta, 2007, **52**, 4177.
- [8] M. Li, Q. H. Lu, Y. Nuli, X. F. Qian, Electrochem. Solid State Lett., 2007, **10**, K33.
- [9] B.-C. Park, H. J. Bang, K. Amine, E. Jung, Y.-K. Sun, J. Power Sources, 2007, **174**, 658.
- [10] X. M. Sun, J. F. Liu, Y. D. Li, Chem. Mater., 2006, **18**, 3486.
- [11] K. Wang, X. M. He, L. Wang, J. G. Ren, C. Y. Jiang, C. R. Wan, Solid State Ionics, 2007, **178**, 115.
- [12] Y. S. Jung, K. T. Lee, S. M. Oh, Electrochim. Acta, 2007, **52**, 7061.
- [13] Y. Kwon, H. Kim, S.-G. Doo, J. Cho, Chem. Mater., 2007, **19**, 982.
- [14] H. Lee, J. Cho, Nano Lett., 2007, **7**, 2638.
- [15] Y. K. Sun, S. T. Myung, B. C. Park, K. Amine, Chem. Mater., 2006, **18**, 5159.

- [16] N. Ravet, J. B. Goodenough, M. Armand, Abstract 127, The Electrochemical Society and The Electrochemical Society of Japan Meeting Abstracts, 1999, Vol. 99-2, Honolulu, HI, Oct 17-22.
- [17] S. Franger, F. Le Cras, C. Bourbon, H. Rouanlt, J. Power Sources, 2003, **119–121**, 252.
- [18] H. Huang, S. C. Yin, L. F. Nazar, Electrochem. Solid-State Lett., 2001, **4**, A170.
- [19] A. Yamada, S. C. Chung, K. Hinokuma, J. Electrochem. Soc., 2001, **148**, A224.
- [20] K. Wang, R. Cai, T. Yuan, X. Yu, R. Ran, Z. Shao, Electrochim. Acta, 2009, **54**, 2861.
- [21] Z. Chen, H. Zhu, S. Ji, R. Fakir, V. Linkov, Solid State Ionics, 2008, **179**, 1810.
- [22] C. Lai, Q. Xu, H. Ge, G. Zhou, J. Xie, Solid State Ionics, 2008, **179**, 1736.
- [23] G. Wang, X. Shen, J. Yao, J. Power Sources, 2009, **189**, 543.
- [24] S. Myung, S. Komaba, N. Hirosaki, H. Yashiro, N. Kumagai, Electrochim. Acta, 2004, **49**, 4213.
- [25] C. Delacourt, P. Poizot, S. Levasseur, C. Masquelier, Electrochem. Solid-State Lett., 2006, **9**, A352.
- [26] P. P. Prosini, M. Carewska, S. Scaccia, P. Wisniewski, S. Passerini, M. Pasquali, J. Electrochem. Soc., 2002, **149**, A886.
- [27] B. Wang, Y. Qiu, S. Ni, Solid State Ionics, 2007, **178**, 843.
- [28] J. Barker, M. Y. Saidi, J. L. Swoyer, Electrochem. Solid-State Lett., 2003, **6**, A53.
- [29] S. Franger, C. Benoit, C. Bourbon, F. L. Cras, J. Phys. Chem. Solids, 2006, **67**, 1338.
- [30] M. Konarova, I. Taniguchi, J. Power Sources, 2009, **194**, 1029.

- [31] S. Yang, P. Y. Zavalij, M. S. Whittingham, *Electrochem. Commun.*, 2001, **3**, 505.
- [32] S. Yang, Y. Song, P. Y. Zavalij, M. S. Whittingham, *Electrochem. Commun.*, 2002, **4**, 239.
- [33] J. Chen, M. S. Whittingham, *Electrochem. Commun.*, 2006, **8**, 855.
- [34] S. Franger, F. Le Cras, C. Bourbon, H. Rouault, *Electrochem. Solid-State Lett.*, 2002, **5**, 231.
- [35] S. Tajimi, Y. Ikeda, K. Uematsu, K. Toda, M. Sato, *Solid State Ionics*, 2004, **175**, 287.
- [36] G. Meligrana, C. Gerbaldi, A. Tuel, S. Bodoardo, N. Penazzi, *J. Power Sources*, 2006, **160**, 516.
- [37] J. Lee, A.S. Teja, *J. Supercrit. Fluids*, 2005, **35**, 83-90.
- [38] A. F. Diaz, *Chemica Scripta*, 1981, **17**, 145.
- [39] A. F. Diaz, K. K. Kanazawa, G. P. Gardini, *J. Chem. Soc. Chem. Commun*, 1979, **635**, 528.
- [40] T. F. Otero, I. Cantero, *J. Power Sources*, 1999, **81–82**, 838.
- [41] K. Park, S. B. Schougaard, J. B. Goodenough, *Adv. Mater.*, 2007, **19**, 848.
- [42] J.-K. Kim, J. Manuel, M. Lee, J. Scheers, D. Lim, P. Johansson, J. Ahn, A. Matica, P. Jacobsson, *J. Mater. Chem.*, 2012, **22**, 15045.

Chapter 8

8 Binary Olivine $\text{LiFe}_x\text{Mn}_{1-x}\text{PO}_4/\text{C}$ ($x=0.3, 0.5$ and 0.7) Solid Solution as Cathode Materials for Lithium-ion Batteries

Carbon coating and size reduction are the most common ways to address the sluggish kinetics for LiFePO_4 , while some reports mentioned that doping is another way to increase the electronic conductivity, however, this concept is still controversial. Due to the similar chemical environment of Mn and Fe in LiMPO_4 (M=transition metal), we want to investigate the concentration of Mn effect on the crystal lattice of LiFePO_4 as well as the electrochemical performance.

In this chapter, a series of nanostructured binary $\text{LiFe}_x\text{Mn}_{1-x}\text{PO}_4$ ($x=0.3, 0.5$ and 0.7) solid solution was synthesized via a facile sol-gel route followed by post-heating treatment. It is found that the concentration of Mn substitution not only significantly affect the morphologies of obtained compounds from nanoparticles for Fe-rich phase to nanoplates for Mn-rich phase, but also is highly related to the electrochemical behaviors. It is found that the 50% Mn substitution forming a solid solution with the Fe in the olivine lattice was optimal for achieving the best electrochemical performance. The presented results demonstrate the significant effect of Fe/Mn ratio in binary olivine cathodes on maximizing electrochemical performances.

Key words: solid solution, olivine cathode, nanostructure, lithium ion battery

Note: This work has been submitted.

Jinli Yang, Dongniu Wang, Xifei Li, Yongji Tang, Biwei Xiao, Tsun-Kong Sham, Guoxian Liang, Ruying Li, Xueliang Sun, submitted

8.1 Introduction

Olivine-type phosphate based cathode materials LiMPO_4 ($\text{M}=\text{Fe}$, Mn , Co , and Ni) have recently been extensively studied for rechargeable lithium-ion batteries (LIBs), particularly for large-scale batteries applied in electric vehicles (EVs) and hybrid electric vehicles (HEVs) because of their superior safety, high thermal stability, nontoxicity and low cost [1-3]. However, the intrinsically low ionic and electrical conductivities of LiMPO_4 limit Li^+ insertion and extraction kinetics in these materials [4, 5]. Although this obstacle for LiFePO_4 has been overcome by coating the nano-meter sized particles with conductive carbon [6-11], it still suffered from low energy density caused by low $\text{Fe}^{2+}/\text{Fe}^{3+}$ redox potential (3.4 V vs. Li^+/Li) [12-17]. The other typed LiMPO_4 ($\text{M}=\text{Mn}$, Co , and Ni) cathodes possess higher redox potentials (4.1, 4.8, and 5.1 V vs. Li^+/Li) thus higher energy density can be expected. Since working voltage higher than 4.5 V will cause stability problems of the battery system [12, 18-20], and the 4.1 V voltage plateau is compatible with the commonly used liquid electrolyte [21], LiMnPO_4 is regarded as one of the most exciting cathode material for next generation LIBs.

Similar to the LiFePO_4 electrode, the electrochemical behavior of LiMnPO_4 could also be improved by preparing nano-sized particles and carbon coating [22-26]. Unfortunately, depositing carbon on LiMnPO_4 is more challenging due to the lower catalytic activity of Mn to carbon compared with Fe [27]. Moreover, given the even lower electrical conductivity of LiMnPO_4 ($< 10^{-12} \text{ S cm}^{-1}$) than LiFePO_4 ($1.8 \times 10^{-8} \text{ S cm}^{-1}$), quite a few amount of carbon additives (usually more than 10 wt.%) are required for achieving acceptable capacity and rate performances [28, 29]. In recent studies, $\text{Li}(\text{FeMn})\text{PO}_4$ solid solution systems have been demonstrated that such mixed-transition compounds could have a better electrochemical capability than pure LiMnPO_4 due to that the coexistence of structure could improve the Li^+ diffusion kinetics in these compounds [1, 5, 30]. Applying solvothermal route, Saravanan et al. evidenced that $\text{LiMn}_{0.5}\text{Fe}_{0.5}\text{PO}_4$ exhibited better stability and capability than $\text{LiMn}_{0.75}\text{Fe}_{0.25}\text{PO}_4$ [17]. Under high temperature solid-state reaction, Martha et al. reported that carbon-coated $\text{LiMn}_{0.8}\text{Fe}_{0.2}\text{PO}_4$ nanoparticles could deliver an improved capacity and rate performance [33]. Wang et al. reported that $\text{LiMn}_{0.75}\text{Fe}_{0.25}\text{PO}_4$ nanorods/graphene hybrids could deliver a high specific capacity of

107 mA h g⁻¹ at high discharge rate of 50 C via a two-step approach [34]. By employing co-precipitation route, Oh et al. observed that micro-sized spherical LiMn_{0.5}Fe_{0.5}PO₄ particles showed the better cyclic capability than LiMnPO₄ [23]. It is found that electrochemical behavior of the binary Li(FeMn)PO₄ under various preparation system is very sensitively dependent on the substituted Mn concentration in the solid solution [31, 32]. Nevertheless, study for the effect of different Mn substitutions in solid solution systems on composites performances is still rare.

Herein, we proposed a series of LiFe_xMn_{1-x}PO₄ (x=0.3, 0.5 and 0.7) nanostructures synthesized via a sol-gel route followed by controlled duration of the post heat treatment. The different ratios of Fe/Mn effect on the morphologies and electrochemical performances of LiFe_xMn_{1-x}PO₄ were also investigated. It is revealed that the substitution Mn concentration of 50% in the solid solution of LiFe_xMn_{1-x}PO₄ was optimal.

8.2 Experimental

8.2.1 Preparation of LiFe_xMn_{1-x}PO₄/C (x=0.3, 0.5 and 0.7) series

Synthesis of LiMn_xFe_{1-x}PO₄ series: LiMn_xFe_{1-x}PO₄ (x=0.3, 0.5 and 0.7) composites were synthesized by a sol-gel method. The typical synthesis of LiFe_{0.5}Mn_{0.5}PO₄ was conducted by the following procedures. First, 1.039 g lithium dihydrogen phosphate (LiH₂PO₄, Sigma) was dissolved in 100 mL of water containing 0.4 g citric acid and stirred at 80 °C for 1 h. Separately, 0.869 g iron (II) acetate (Fe(AC)₂, Sigma) and 0.865 g magnesium acetate (Mn(AC)₂, Sigma) was dissolved in 70 mL of water by stirring at 70 °C for 1 h. Then the two solutions were mixed together and dried at 70 °C for 24 h. For the other two LiMn_xFe_{1-x}PO₄ composites, the procedure was similar, except that designed ratio of metal acetate. After thorough grinding of the xerogel followed by annealing in a furnace filled with an argon atmosphere at 700 °C and a heating rate of 10 °C min⁻¹, the composites were obtained. To see the duration effect, the annealing time varies from 3 h, 6 h to 10 h for LiFe_{0.5}Mn_{0.5}PO₄ compound, respectively.

8.2.2 Physical characterization

The crystalline phase of the synthesized products was characterized by powder X-ray diffraction (XRD, Rigaku, Japan) using a Co K α radiation source. The morphology of LiMn_xFe_{1-x}PO₄ (x=0.3, 0.5 and 0.7) series was observed by Field emission scanning electron spectrometry (FE-SEM, Hitachi 4800S) with an operating voltage of 5 kV, transmission electron microscope (TEM, Hitachi H-7000) and high resolution TEM (HRTEM, JEOL 2010F). A Raman scattering spectroscopy apparatus (HORIBA) equipped with a 532.4 nm laser was performed to study the phonon modes of Fe, P, O and C. Fe and Mn K edge spectra and extended X-ray absorption fine structure (EXAFS) data were obtained from the X-ray Science Division (XSD) partnered with the Pacific Northwest Consortium (PNC) at Sector 20 of Advanced Photon Source.

8.2.3 Electrochemical Characterization

The electrochemical cell used in our study was a CR2032 coin cell. The electrolyte used in our experiment was 1 M LiPF₆ in a mixture of ethylene carbonate/dimethyl carbonate (1:1 v/v) solvents. All electrochemical tests were performed in an Arbin BT-2000 Battery Test Station within a voltage range of 2.2-4.5 V (versus Li⁺/Li). The electrodes were fabricated using a mixture of the prepared powders, acetylene black and poly-(vinylidene fluoride) (PVDF) binder with a weight ratio of 75:15:10, using N-methyl-2-pyrrolidone (NMP) as the solvent, and then the slurry was spread onto pure Al foils. The coin cells were assembled in a high-purity argon filled glove box, and all of the electrochemical measurements were conducted at room temperature.

8.3 Results and discussion

The XRD spectra presented in Figure 8.1 shows that all of the composites are well crystallized in the olivine structure, and secondary conductive phase of Fe₂P is also identified. Although the LiFePO₄ and LiMnPO₄ have the isotypical olivine-type structure with a Pnma space group [35-37], the substitution of bigger Mn²⁺ ions with smaller Fe²⁺ ions leads to a linear increase of the cell volume with respect to LiFePO₄ [38]. All the peaks of the composites shift from patterns of LiFePO₄ (JCPDS card no. 40-1499) towards that of LiMnPO₄ (JCPDS card no. 33-0803), demonstrating that Mn forms a

solid solution with Fe in the LiFePO_4 lattice. In addition, upon increasing the Mn concentration from 0.3 to 0.7 (inset in Figure 8.1), the diffraction peaks continuously and slightly shift to lower 2θ values, suggesting a more distortion to unit cell volume of $\text{LiFe}_{0.3}\text{Mn}_{0.7}\text{PO}_4$ than the other two composites.

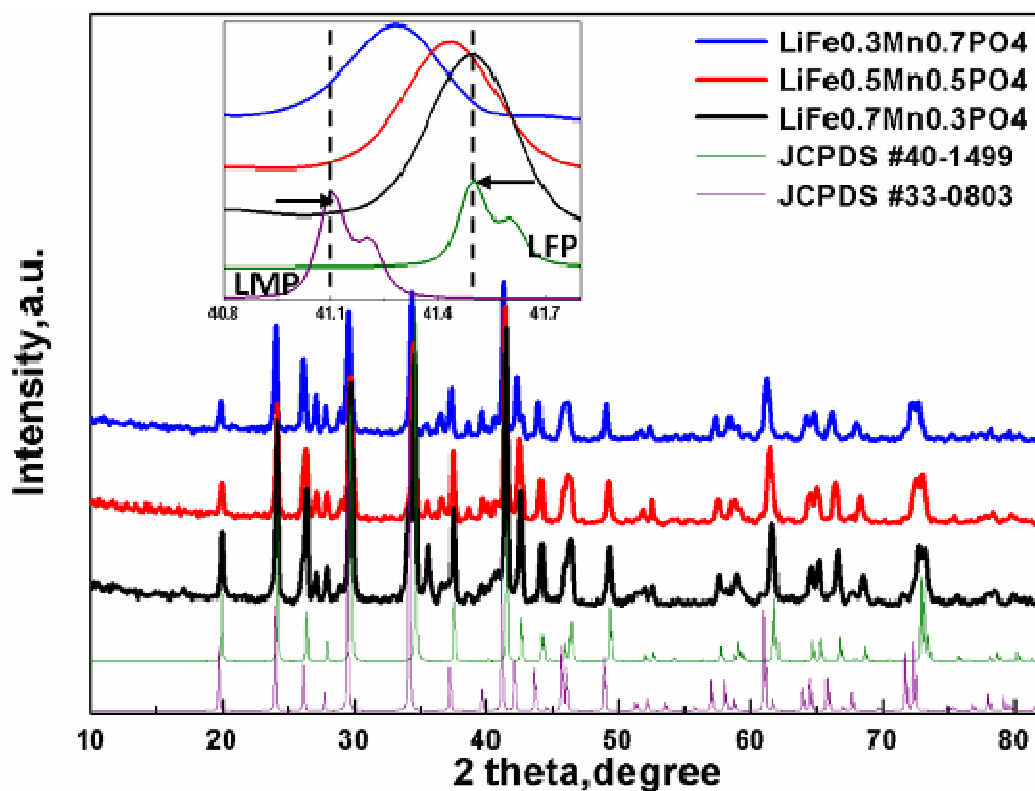


Figure 8.1 XRD spectrum of the $\text{LiFe}_x\text{Mn}_{1-x}\text{PO}_4/\text{C}$ composites. (Inset showing magnified XRD patterns in the range between 40° and 42°).

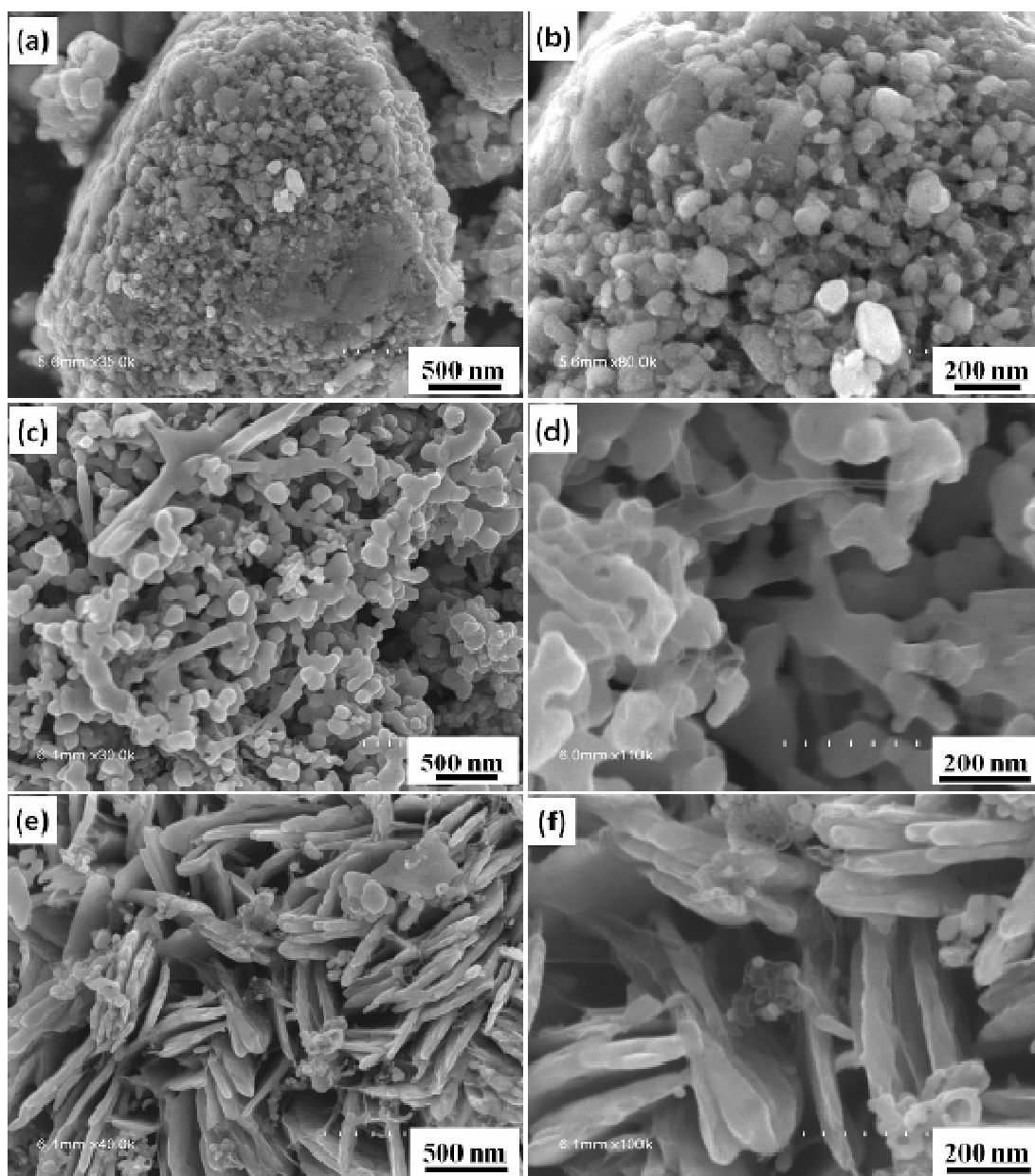


Figure 8.2 SEM images of the obtained $\text{LiFe}_x\text{Mn}_{1-x}\text{PO}_4/\text{C}$ composites: (a), (b) $x=0.3$; (c), (d) $x=0.5$; (e), (f) $x=0.7$.

Figure 8.2 shows the SEM micrographs of the $\text{LiFe}_x\text{Mn}_{1-x}\text{PO}_4$ ($x=0.3, 0.5$ and 0.7). It is clearly observed that the composites exhibit significantly distinct morphologies when different Mn contents were introduced. With increasing of Mn concentration, the morphology changes from nanoparticles to nanorods (Figure 8.2a, 8.2c and 8.2e). For $\text{LiFe}_{0.7}\text{Mn}_{0.3}\text{PO}_4$, it only displays the morphology of spherical nanoparticles with a size

distribution (Figure 8.2b) around 50-100 nm, and the particles agglomerate forming secondary particles. Nanoplates start to appear in the $\text{LiFe}_{0.5}\text{Mn}_{0.5}\text{PO}_4$ composites (Figure 8.2c), and the average plate thickness is around 30-60 nm. When the mol ratio of Mn to Fe increased to 7 to 3, the whole typical morphology of $\text{LiFe}_{0.3}\text{Mn}_{0.7}\text{PO}_4$ is self-assembled nanoplates with a thickness around 50 nm, as estimated from the magnified micrograph (Figure 8.2f). Introducing more Mn atoms in binary Fe-Mn olivine system favors the growth along 2D direction, resulting morphology transformation from nanoparticle to assembled nanoplates.

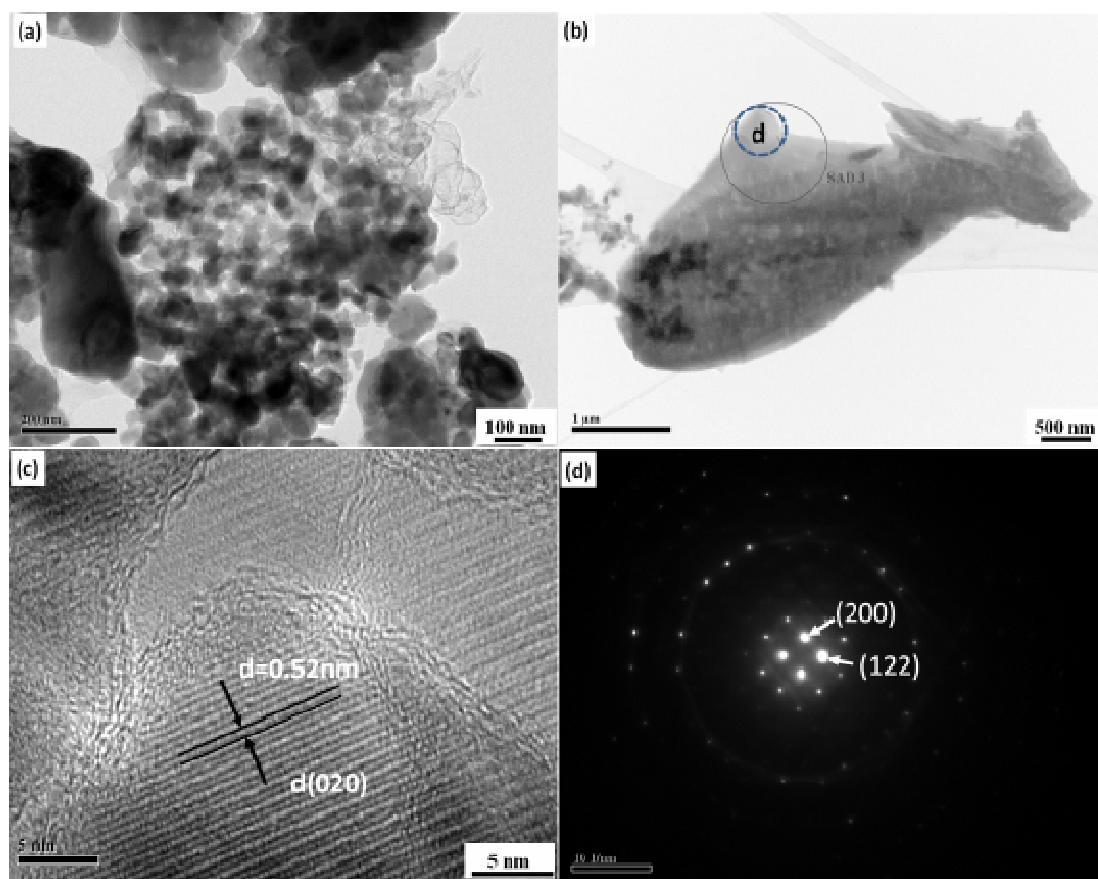


Figure 8.3 Micrographs of $\text{LiFe}_{0.5}\text{Mn}_{0.5}\text{PO}_4/\text{C}$ composites: (a, b) TEM images; (c) High-resolution TEM image and (d) SAED pattern (circle area in (b)).

TEM, HRTEM and SAED images of $\text{LiFe}_{0.5}\text{Mn}_{0.5}\text{PO}_4$ composites are shown in Figure 8.3. An overview of the sample as depicted in the TEM image (Figure 8.3a) shows that nanoparticles and nanoplates co-exist in $\text{LiFe}_{0.5}\text{Mn}_{0.5}\text{PO}_4$, which is consistent with the

SEM results. Morphology of a single piece of 2D nanoplate is shown in Fig. 8.3b, and the size of the plate is extended to micrometers. Moreover, it is clearly found that uniform carbon coating is present on the surface of nanoparticles and nanoplate from the magnified TEM images originated from the pyrolysis of citric acid (Figure S8.1). From the HRTEM image (Figure 8.3c), the presence of clear lattice fringes indicates high crystallinity of $\text{LiFe}_{0.5}\text{Mn}_{0.5}\text{PO}_4$. The observed width with 0.52 nm from the neighboring lattice fringes matches well with the (020) plane of $\text{LiFe}_{0.5}\text{Mn}_{0.5}\text{PO}_4/\text{C}$, illustrating its single crystalline feature. SAED spots in Figure 8.3d further confirm that the nanoplates are indeed single crystalline in nature. For other two ratios of $\text{LiFe}_x\text{Mn}_{1-x}\text{PO}_4$ composites, the morphologies are similar to nanoparticles/nanoplates in $\text{LiFe}_{0.5}\text{Mn}_{0.5}\text{PO}_4$.

In order to probe the annealing time effect on the morphology of the $\text{LiFe}_{0.5}\text{Mn}_{0.5}\text{PO}_4$ composites, various annealing time controlled experiments were carried out. The products calcinated for 3 h and 10 h were examined using SEM (Figure 8.4). Nanoparticles and nanoplates of $\text{LiFe}_{0.5}\text{Mn}_{0.5}\text{PO}_4$ also formed associated with annealing process (Figure 8.4a and 8.4c). For $\text{LiFe}_{0.5}\text{Mn}_{0.5}\text{PO}_4$ annealed at 700 °C for 3 h, the thickness of the nanoplates is around 30 nm, while the size of the particle is 30-100 nm (Figure 8.4b). As mentioned above, 6 h annealing gives narrower particle size distribution of 50-100 nm which may be due to prolonged growth time for crystals. As time progresses to 10 h, a certain amount of nanoparticles tends to agglomerate forming secondary particles of about 250 nm in diameter as indicated in the circle area of Figure 8.4d, which is resulted from the Ostwald ripening process [39]. It is revealed that the duration of the annealing time could affect the morphology of the obtained $\text{LiFe}_{0.5}\text{Mn}_{0.5}\text{PO}_4$.

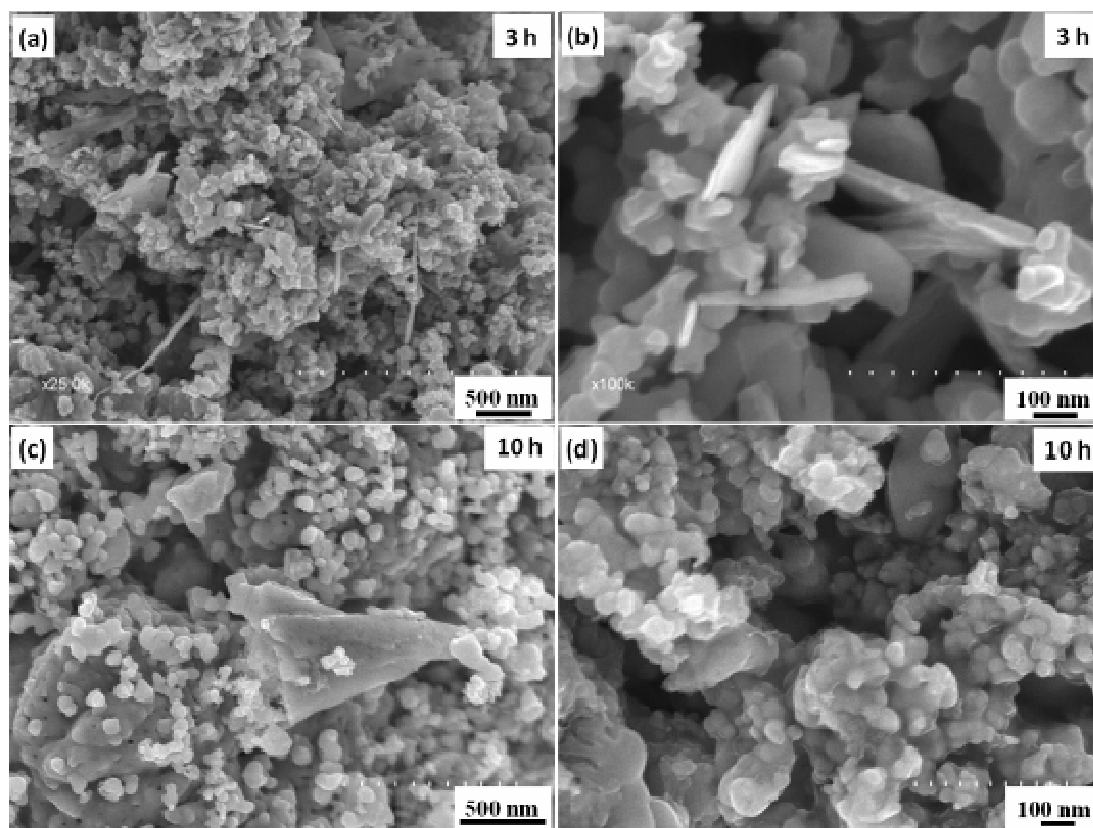


Figure 8.4 SEM images of obtained $\text{LiFe}_{0.5}\text{Mn}_{0.5}\text{PO}_4/\text{C}$ with different annealing time. (a, b) 3 h; (c, d) 10 h.

X-ray absorption near edge structure (XANES) was performed at Fe and Mn K edge to further identify the oxidation states and local chemical environments of iron and manganese in the solid solutions, as shown in Figure 8.5a and 8.5b. The Fe and Mn K-edge XANES spectra are quite similar; they both exhibit a pre-edge and an edge jump followed by a more broadened peak due to multiple scattering. The pre-edge peaks are located at the lower energy side of the sharply rising absorption edge (white line), which can be referred to the 1s to 3d electronic transition of Fe or Mn [40, 41]. All of the $\text{LiFe}_x\text{Mn}_{1-x}\text{PO}_4$ solid solutions exhibited characteristics of Fe (II) or Mn (II) and distinct edge jump located at ~ 7126 eV and 6550 eV, respectively. It should be noted that the spectra for Mn K edge XANES and Fe K edge XANES could be totally overlapped after normalized to edge energy (E-E₀) as shown in Figure S8.2, indicating the same chemical environmental of Fe and Mn atoms in octahedral MO_6 (M= Fe, Mn) upon substitution at different levels in the olivine structure as well as an unchanged valence state (II).

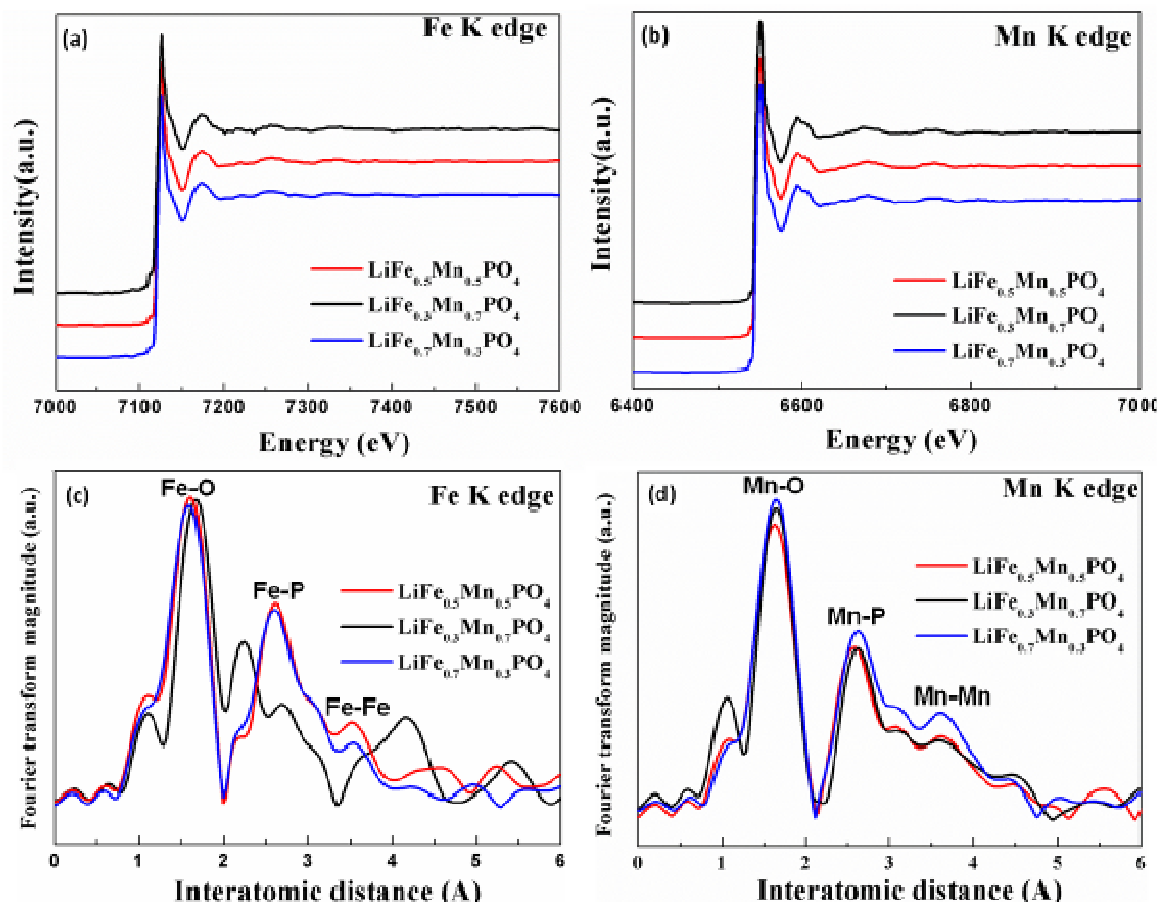


Figure 8.5 XANES spectrum (transmission) of (a) Fe K edge and (b) Mn K edge spectra of $\text{LiFe}_{1-x}\text{Mn}_x\text{PO}_4$ solid solutions; FT magnitudes of (c) Fe K edge and (d) Mn K edge k^3 -weighted EXAFS spectra of $\text{LiFe}_{1-x}\text{Mn}_x\text{PO}_4$ solid solutions.

The Fourier-transformed (FT) extended X-ray absorption fine structure (EXAFS) oscillations for $\text{LiFe}_x\text{Mn}_{1-x}\text{PO}_4$ solid solutions are shown in Figure 8.5c and 8.5d. The FT features of the first several shells around the Fe atoms or Mn atoms are analogous, further confirming its same local environment and chemical states for Mn and Fe atoms. Typical bonds representing M-O, M-P, M-M (M=Fe, Mn) interactions for olivine typed structure are distinct, which matched well with previously reported results [42]. Further examination of the Fe and Mn K edge EXAFS, it could be tracked that the distortion degree of Mn are lower than that of Fe at different Fe/Mn ratios. It is conducted that Mn atoms may favor to occupy the site in octahedral MO_6 while extrude Fe atoms, leading to

lattice mismatching. The EXAFS spectra for $\text{LiFe}_{0.7}\text{Mn}_{0.3}\text{PO}_4$ and $\text{LiFe}_{0.5}\text{Mn}_{0.5}\text{PO}_4$ are quite similar, while for $\text{LiFe}_{0.3}\text{Mn}_{0.7}\text{PO}_4$, an enhanced resonance at 2.1 angstrom and 4.1 angstrom as well as suppressed Fe-P magnitudes in Fe K edge EXAFS demonstrate the alternated bond interactions due to the large amount of substitute Mn atoms. The XANES data observed here correspond well with the XRD results and provide a spectroscopic view of different lattice distortion degree in three $\text{LiFe}_x\text{Mn}_{1-x}\text{PO}_4$ solid solutions.

The effect of various Mn concentration on electrochemical properties of solid solutions is further examined, are illustrated in Figure 8.6. All the CV curves for $\text{LiFe}_x\text{Mn}_{1-x}\text{PO}_4/\text{C}$ ($x=0.3, 0.5$ and 0.7) nanocomposites (Figure 8.6a) show oxidation and reduction peaks for $\text{Fe}^{2+}/\text{Fe}^{3+}$ and $\text{Mn}^{2+}/\text{Mn}^{3+}$, respectively. During the oxidation process, two peaks appear at 3.54 and 4.11 V for $\text{LiFe}_{0.7}\text{Mn}_{0.3}\text{PO}_4/\text{C}$, corresponding to the oxidation of Fe^{2+} to Fe^{3+} and Mn^{2+} to Mn^{3+} respectively. Consequent reduction reaction of Mn^{3+} to Mn^{2+} and Fe^{3+} to Fe^{2+} occurred at 3.93 and 3.42 V, respectively. When increasing the Mn content from 0.3 to 0.5, and to 0.7, the peak intensity of $\text{Mn}^{2+}/\text{Mn}^{3+}$ (Vs. $\text{Fe}^{2+}/\text{Fe}^{3+}$) increases, indicating the successfully substitution of Mn concentration to Fe [43-45]. For $\text{LiFe}_{0.5}\text{Mn}_{0.5}\text{PO}_4/\text{C}$ and $\text{LiFe}_{0.3}\text{Mn}_{0.7}\text{PO}_4/\text{C}$, the current densities of anodic peaks and cathodic peaks for both redox increase in the subsequent cycles such as 5th and 10th cycle, as marked by arrow in Figure 8.5a, suggesting the activation process in initial cycles and good reversibility of these two systems. Whereas in the $\text{LiFe}_{0.7}\text{Mn}_{0.3}\text{PO}_4/\text{C}$, the current density of $\text{Mn}^{2+}/\text{Mn}^{3+}$ peak decreases with the cycles, indicating the poor electrochemical activity of the redox couple. Besides the variation of the peak current, the potential interval also alters in the $\text{LiFe}_x\text{Mn}_{1-x}\text{PO}_4/\text{C}$ ($x=0.3, 0.5$ and 0.7) series upon cycling. The potential interval decreases for both redox couple ($\text{Fe}^{2+}/\text{Fe}^{3+}$ and $\text{Mn}^{2+}/\text{Mn}^{3+}$) in $\text{LiFe}_{0.5}\text{Mn}_{0.5}\text{PO}_4/\text{C}$ and $\text{LiFe}_{0.3}\text{Mn}_{0.7}\text{PO}_4/\text{C}$. Take $\text{LiFe}_{0.5}\text{Mn}_{0.5}\text{PO}_4/\text{C}$ for example, the value of potential interval of redox $\text{Fe}^{2+}/\text{Fe}^{3+}$ decreased from 118 mV in the 1st cycle to 82 mV in the 10th cycle (see Table S8.1), and from 223 mV for $\text{Mn}^{2+}/\text{Mn}^{3+}$ in the 1st cycle to 188 mV in the 10th cycle. In contrast, for the $\text{LiFe}_{0.7}\text{Mn}_{0.3}\text{PO}_4/\text{C}$, the potential interval value increases upon cycling, illustrating ever-increasing polarization in this composite.

The galvanostatic charge and discharge profiles of $\text{LiFe}_x\text{Mn}_{1-x}\text{PO}_4/\text{C}$ ($x=0.3, 0.5$ and 0.7) at $\text{C}/100$ between 2.3 and 4.5 V at 25°C are shown in Figure 8.6b. All electrodes exhibit two reversible plateau regions around 3.5 V and 4.1 V vs. Li/Li^+ , corresponding to the redox couple of $\text{Fe}^{2+}/\text{Fe}^{3+}$ and $\text{Mn}^{2+}/\text{Mn}^{3+}$, respectively. The first charge capacity for $\text{LiFe}_{0.7}\text{Mn}_{0.3}\text{PO}_4/\text{C}$ is $110.4 \text{ mA h g}^{-1}$, and the corresponding discharge capacity is 88 mA h g^{-1} with a coulombic efficiency of 80% . Upon cycling, the discharge capacity gradually increases from the initial cycle to 10th cycle, which is in agreement with increased current densities in CV curves. At the end of 10th cycle, the discharge capacity is around 98 mA h g^{-1} , and the coulombic efficiency increased to 96% . In the case of $\text{LiFe}_{0.5}\text{Mn}_{0.5}\text{PO}_4/\text{C}$, it can be further confirmed that more Li extraction occurs at the Mn plateau region than $\text{LiFe}_{0.7}\text{Mn}_{0.3}\text{PO}_4/\text{C}$. The initial charge capacity is 128 mA h g^{-1} , and the discharge capacity can reach 97 mA h g^{-1} with a coulombic efficiency close to 77% . At the end of 10th cycle, the delivered charge capacity is 106 mA h g^{-1} with the coulombic efficiency of 98% , revealing that most of the lithium ions were reversibly extracted from the electrode material.

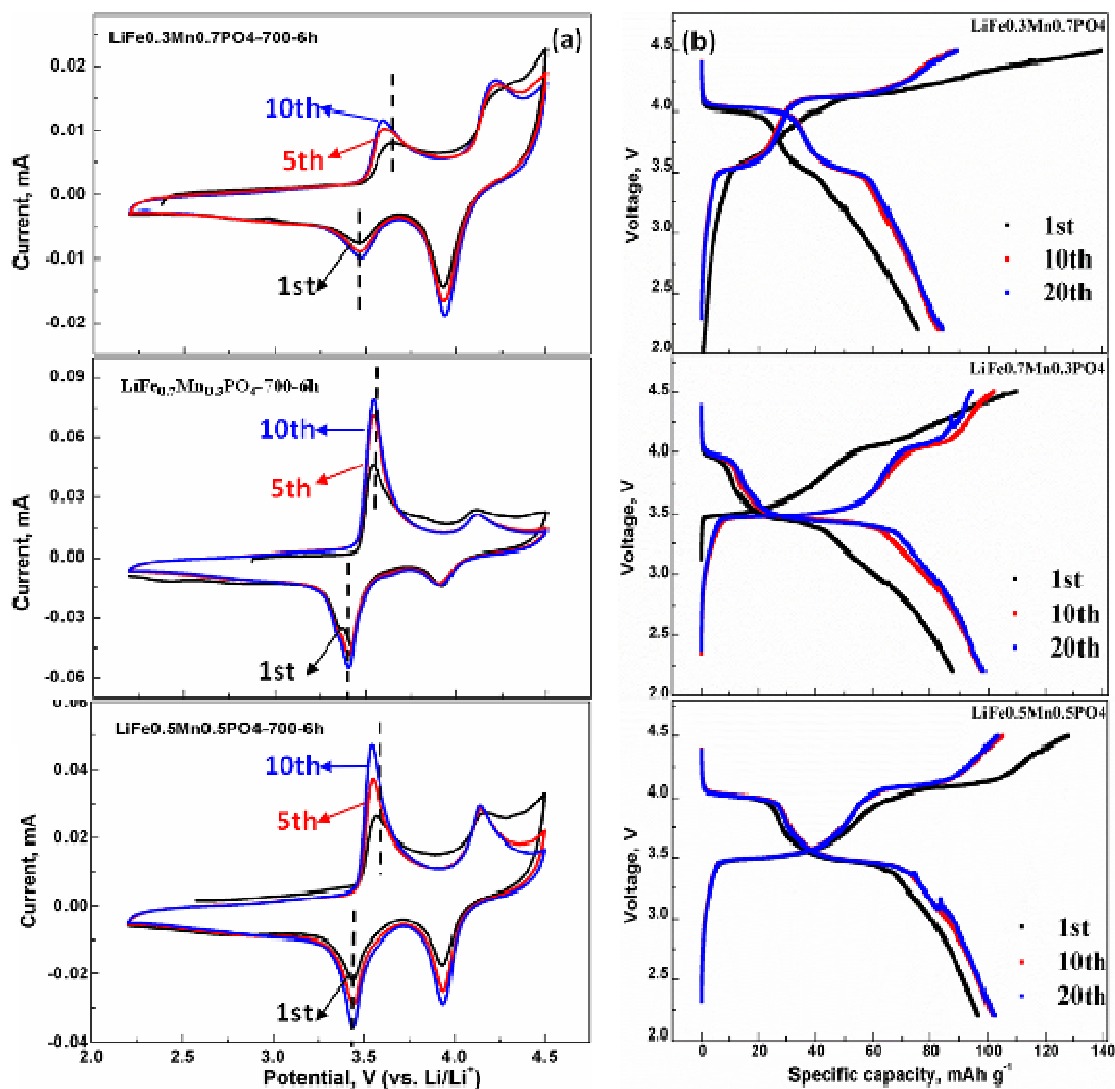


Figure 8.6 (a) Cyclic voltammograms (0.1 mV s^{-1}) and (b) charge-discharge curves at different cycle number for $\text{LiFe}_x\text{Mn}_{1-x}\text{PO}_4/\text{C}$ ($x=0.3, 0.5$ and 0.7) at a current rate of 17 mA g^{-1} .

For comparison, the 1st charge capacity for $\text{LiFe}_{0.3}\text{Mn}_{0.7}\text{PO}_4/\text{C}$ is $140.6 \text{ mA h g}^{-1}$. However, on subsequent discharge, Li insertion is found to be poor with a discharge capacity of 76 mA h g^{-1} with a coulombic efficiency of 54%. At the end of 10th cycle, the discharge capacity is around 83 mA h g^{-1} , and the coulombic efficiency increased to 95.4%. The increasing Mn content affected the electrochemical behavior of $\text{Mn}^{2+}/\text{Mn}^{3+}$ redox couple is ascribed to the huge lattice distortion in the olivine system [46-48]. As we

mentioned above, substitution of bigger Mn^{2+} ions with smaller Fe^{2+} ions leads to a lattice distortion, therefore, only optimized Mn content can retain lattice stability during cycling.

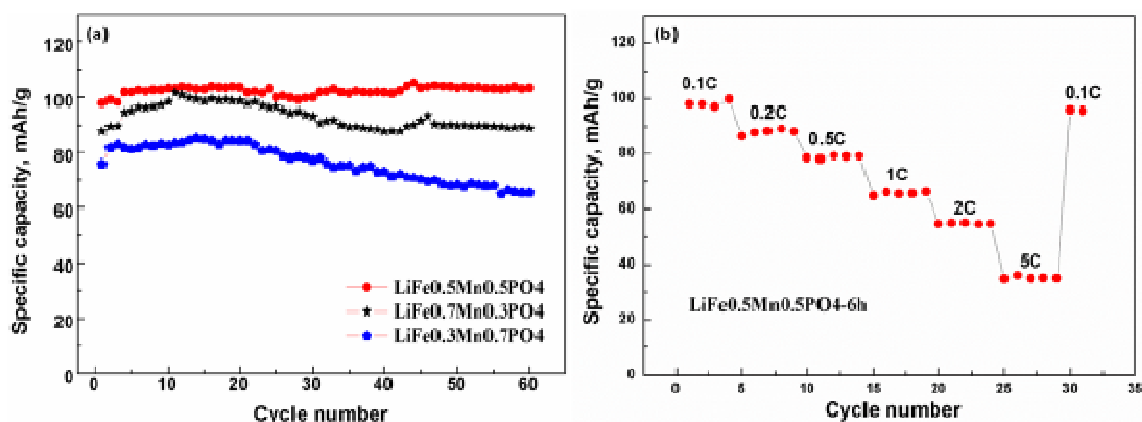


Figure 8.7(a) Cycling profile tested at a current density of 17 mA g^{-1} between 2.2 and 4.5 V for $\text{LiFe}_x\text{Mn}_{1-x}\text{PO}_4/\text{C}$ ($x=0.3$, 0.5 and 0.7) composites; (d) rate performance for $\text{LiFe}_{0.5}\text{Mn}_{0.5}\text{PO}_4/\text{C}$.

Cyclic performances of all of three samples at $1/10 \text{ C}$ are shown in Figure 8.7a. The $\text{LiFe}_{0.5}\text{Mn}_{0.5}\text{PO}_4/\text{C}$ exhibits the best cycle stability, maintaining a discharge capacity of 106 mA h g^{-1} after 60 cycles. Contrastively, the lithium insertion/extraction behavior is poorer in the $\text{LiFe}_{0.3}\text{Mn}_{0.7}\text{PO}_4/\text{C}$ and $\text{LiFe}_{0.7}\text{Mn}_{0.3}\text{PO}_4/\text{C}$ electrodes, which is owing to the structure instability [48] and the lattice mismatching in the two phase reactions (MnPO_4 and LiMnPO_4) [46]. For $\text{LiFe}_{0.3}\text{Mn}_{0.7}\text{PO}_4/\text{C}$, the capacity starts fading from the 25th cycle, and the discharge capacity loss between the 60th cycle and initial cycle is close to 16 mA h g^{-1} . The improved stability of $\text{LiFe}_{0.7}\text{Mn}_{0.3}\text{PO}_4/\text{C}$ can be ascribed to the less distortion of lattice as shown in EXAFS spectrum. It is concluded that the optimized stoichiometric ratio of Mn to Fe is 1 to 1 for maximized electrochemical performances in the sol-gel system conducted in this study. The cycling behavior of $\text{LiFe}_{0.5}\text{Mn}_{0.5}\text{PO}_4/\text{C}$ annealed at different time (see Figure S8.3) was further conducted and it is demonstrated that under the same stoichiometric ratio of Mn to Fe, all prepared samples exhibit high stability. The 6 h annealed sample delivers the best lithium storage capacity of 106 mA h g^{-1} in the 60th cycle, while 3 h and 10 h treated samples deliver capacities of 97 and 95 mA h g^{-1} , respectively. The lithium ions are not fully charged in the 3 h and 10 h treated

samples, which hampers the complete oxidation of Mn^{2+} ions. In another way, the agglomerated large-sized particles in 10 h annealed samples will lead to sluggish lithium ions diffusion kinetics. All these factors will lead to decreased lithium storage capabilities for 3 h and 10 h annealed samples.

Rate capability of $\text{LiFe}_{0.5}\text{Mn}_{0.5}\text{PO}_4$ annealed at 6 h is presented in Figure 8.7b. The cell is cycled at different current densities from 0.1 C to 5 C at 25 °C. It is found that $\text{LiFe}_{0.5}\text{Mn}_{0.5}\text{PO}_4$ compound delivers a reversible discharge capacity of 100, 89 and 80 mA h g^{-1} , corresponding to relatively low current densities at 0.1 C, 0.2 C and 0.5 C. When the C-rate stepped to high current densities from 1 C to 5 C, the capacity gradually decreases from 66 to 35 mA h g^{-1} , due to the intrinsic sluggish mass transfer of Li^+ and electrons in olivine cathodes. Intriguingly, once the current density is reversed back to 0.1 C, a discharge capacity of 96 mA h g^{-1} was obtained, indicating that the fabricated $\text{LiFe}_{0.5}\text{Mn}_{0.5}\text{PO}_4$ nanostructures can tolerate various current densities with almost no capacity loss under the same current rate. The stable capacities at each current rate further demonstrate the highly stable structure of $\text{LiFe}_{0.5}\text{Mn}_{0.5}\text{PO}_4$ upon cycling.

8.4 Conclusion

In summary, highly crystallized solid solution of $\text{LiFe}_x\text{Mn}_{1-x}\text{PO}_4/\text{C}$ ($x=0.3, 0.5$ and 0.7) was successfully prepared using sol-gel route. The Mn concentration significantly affects the final morphology of the obtained samples: with increasing the Mn content, the morphology evolves from nanoparticles to self-assembled nanoplates. EXAFS results demonstrate the lattice distortion of Mn to Fe in the binary olivine system. $\text{LiFe}_{0.5}\text{Mn}_{0.5}\text{PO}_4/\text{C}$ composites exhibited a highest reversible discharge capacity of 106 mA h g^{-1} and best rate performance compared with other two compounds of different stoichiometric Fe/Mn ratios, which is assigned to the high structure stabilities of $\text{LiFe}_{0.5}\text{Mn}_{0.5}\text{PO}_4$. The presented results demonstrate the significant effect of Fe/Mn ratio in binary olivine cathodes on maximizing electrochemical performances.

8.5 Acknowledgements

This work was supported by the Natural Sciences and Engineering Research Council of Canada (NSERC), Clariant Inc. (former Phostech Lithium Inc.), Canada Research Chair (CRC) Program, and the University of Western Ontario.

8.6 Supporting information

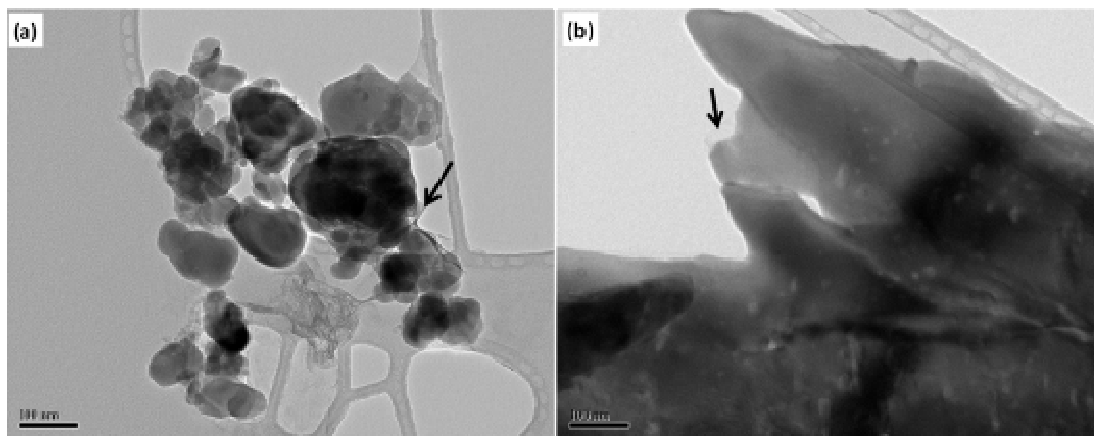


Figure S 8.1 Magnified TEM images of $\text{LiFe}_{0.5}\text{Mn}_{0.5}\text{PO}_4/\text{C}$ composites: (a) nanoparticles, (b) nanoplates.

Table S 8.1 The value of potential interval from $\text{Fe}^{2+}/\text{Fe}^{3+}$ and $\text{Mn}^{2+}/\text{Mn}^{3+}$.

ratio	cycle	3:7	1:1	7:3
Potential interval of $\text{Fe}^{2+}/\text{Fe}^{3+}$ (V)	1st	0.225	0.118	0.115
	5th	0.118	0.095	0.138
	10th	0.102	0.082	0.14
Potential interval of $\text{Mn}^{2+}/\text{Mn}^{3+}$ (V)	1st	0.317	0.223	0.189
	5th	0.247	0.199	0.206
	10th	0.222	0.188	0.207

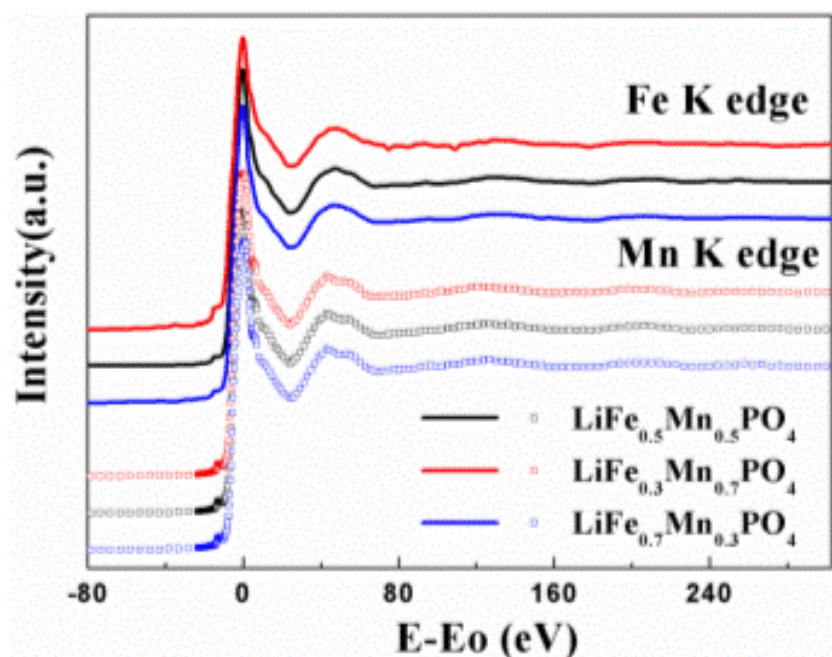


Figure S 8.2 XANES spectra (transmission) of Fe K edge and Mn K edge spectra of $\text{LiFe}_{1-x}\text{Mn}_x\text{PO}_4$ solid solutions (normalized to $E - E_0$).

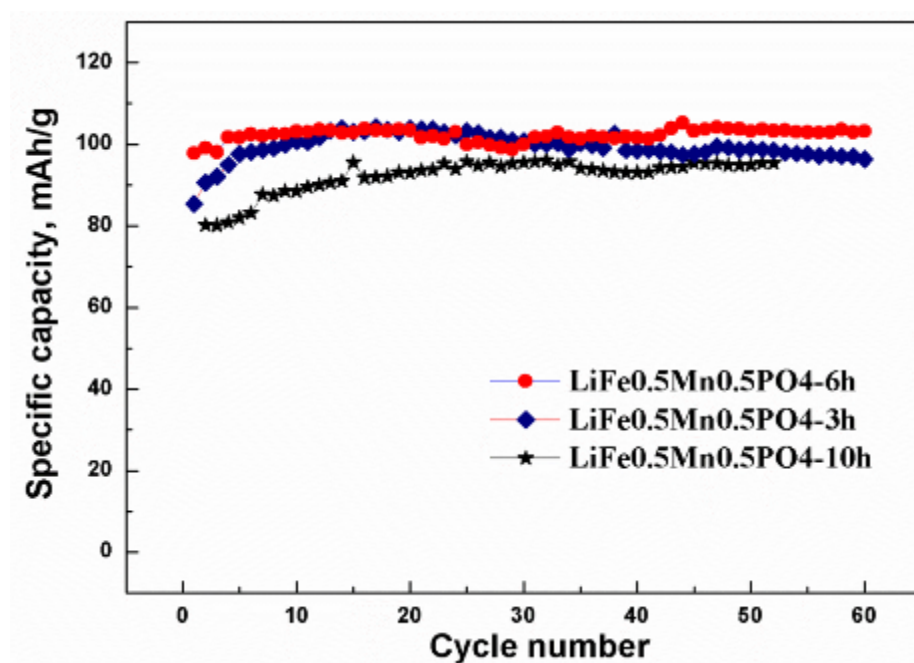


Figure S 8.3 Cycling performances for $\text{LiFe}_{0.5}\text{Mn}_{0.5}\text{PO}_4/\text{C}$ tested at a current density of 17 mA g^{-1} between 2.2 and 4.5 V.

8.7 References

- [1] A. K. Padhi, K. S. Nanjundaswamy, J. B. Goodenough, *J. Electrochem. Soc.*, 1997, **144**, 1188.
- [2] S. Y. Chung, J. T. Bloking, Y. M. Chiang, *Nat. Mater.*, 2002, **1**, 123.
- [3] H. Huang, S. C. Yin, L. F. Nazar, *Electrochem. Solid-State Lett.*, 2001, **4**, A170.
- [4] N. Ravet, Y. Chouinard, J.F. Magnan, S. Besner, M. Gauthier, M. Armand, *J. Power Sources*, 2001, **97-98**, 503.
- [5] A. Yamada, S. C. Chung, K. Hinokuna, *J. Electrochem. Soc.*, 2001, **148**, A224.
- [6] J. Yang, J. Wang, D. Wang, X. Li, D. Geng, G. Liang, M. Gauthier, R. Li, X. Sun, *J. Power Sources*, 2012, **208**, 340.
- [7] P. S. Herle , B. Ellis , N. Coombs, L. F. Nazar , *Nat. Mater.*, 2004, **3**, 147.
- [8] J. Yang, J. Wang, X. Li, D. Wang, J. Liu, G. Liang, M. Gauthier, Y. Li, R. Li, X. Sun, *J. Mater. Chem.*, 2012, **22**, 7537.
- [9] Y. G. Wang, Y. Wang, E. Hosono, K. X. Wang, H. S. Zhou, *Angew. Chem. Int. Ed.*, 2008, **47**, 7461.
- [10] X. L. Wu, L.Y. Jiang, F. F. Cao, Y. G. Guo, L. J. Wan, *Adv. Mater.*, 2009, **21**, 2710.
- [11] J. Wang, J. Yang, Y. Zhang, Y. Li, M. N. Banis, X. Li, R. Li, G. Liang, X. Sun, *Adv. Funct. Mater.*, 2012, **23**, 806.
- [12] K. Zaghib, M. Trudeau, A. Guerfi, J. Trottier, A. Mauger, R. Veillette, C. M. Julien, *J. Power Sources*, 2012, **204**, 177.
- [13] P. Gibot, M. Casas-Cabanas, L. Laffont, S. Levasseur, P. Carlach, S. Hamelet, J. M. Tarascon, C. Masquelier, *Nat. Mater.*, 2008, **7**, 741.

- [14] C. Delacourt, L. Laffont, R. Bouchet, C. Wurm, J. B. Leriche, M. Morcrette, J. M. Tarascon, C. Masquelier, J. Electrochem. Soc., 2005, **152**, A913.
- [15] T. Drezen, N. H. Kwon, P. Bowen, I. Teerlinck, M. Isono, I. Exnar, J. Power Sources, 2007, **174**, 949.
- [16] D. Y. Wang, H. Buqa, M. Crouzet, G. Deghenghi, T. Drezen, I. Exnar, N. H. Kwon, J. H. Miners, L. Poletto, M. Graetzel, J. Power Sources, 2009, **189**, 624.
- [17] K. Saravanan, V. Ramar, P. Balaya, J. J. Vittal, J. Mater. Chem., 2011, **21**, 14925.
- [18] C. Delacourt, P. Poizot, M. Morcrette, J. M. Tarascon, C. Masquelier, Chem. Mater., 2004, **16**, 93.
- [19] B. Ellis, P. S. Herle, Y. H. Rho, L. F. Nazar, R. Dunlap, L. K. Perry, D. H. Ryan, Faraday Discuss., 2007, **134**, 119.
- [20] G. H. Li, H. Azuma, M. Tohda, Electrochem. Solid-State Lett., 2002, **5**, A135.
- [21] B. Kang, G. Cedar, J. Electrochem. Soc., 2010, **157**, A808.
- [22] S.-W. Oh, S. T. Myung, S.-M. Oh, K. H. Oh, K. Amine, B. Scrosati, Y.-K. Sun, Adv. Mater., 2010, **22**, 4842.
- [23] S.-W. Oh, S. T. Myung, Y. S. Choi, K. H. Oh, Y.-K. Sun, J. Mater. Chem., 2011, **21**, 19368.
- [24] Y. S. Choi, S. Kim, S. S. Choi, J. S. Han, J. D. Kim, S. E. Jeon, B. H. Jung, Electrochim. Acta, 2004, **50**, 833.
- [25] S. Kuroda, N. Tabori, M. Sakuraba, Y. Sato, J. Power Sources, 2003, **119-121**, 924.
- [26] Z. Bakenov, I. Taniguchi J. Electrochem. Soc., 2010, **157**, A430.
- [27] N. Ravet, M. Gauthier, K. Zaghib, J. B. Goodenough, A. Mauger, F. Gendron, C. M. Julien, Chem. Mater., 2007, **19**, 2595.

- [28] S.-M. Oh, H.-G. Jung, C. S. Yoon, S.-T. Myung, Z. Chen, K. Amine, Y.-K. Sun, J. Power Sources, 2011, **196**, 6924.
- [29] S.-M. Oh, S.-W. Oh, C.-S. Yoon, B. Scrosati, K. Amine, Y.-K. Sun, Adv. Funct. Mater., 2010, **20**, 3260.
- [30] Y.-K. Sun, S.-M. Oh, H.-K. Park, B. Scrosati, Adv. Mater., 2011, **23**, 5050.
- [31] A. Yamada, Y. Takei, H. Koizumi, N. Sonoyama, R. Kanno, Chem. Mater. 2006, **18**, 804.
- [32] J. Kim, K.-Y. Park, I. Park, J.-K. Yoo, J. Hong, K. Kang, J. Mater. Chem., 2012, **22**, 11964.
- [33] S. Martha, J. Grinblat, O. Haik, E. Zinigrad, T. Drezen, J. Miners, I. Exnar, A. Kay, Markovsky, D. Aurbach, Angew. Chem., 2009, **121**, 8711.
- [34] H. Wang, Y. Yang, Y. Liang, L. Cui, H.-S. Casalongue, Y. Li, G. Hong, Y. Cui, H. Dai, Angew. Chem. Int. Ed. 2011, **50**, 7364.
- [35] A. Yamada, S.-C. Chung, J. Electrochem. Soc., 2001, **148**, A960.
- [36] C. A. Burba, R. Frech, J. Power Sources, 2007, **172**, 870.
- [37] A. Yamada, Y. Kudo, K.-Y. Liu, J. Electrochem. Soc., 2001, **148**, A747.
- [38] J. Molenda, W. Ojczyk, K. Swierczek, W. Zajac, F. Krok, J. Dygas, R. S. Liu, Solid State Ionics, 2006, **177**, 2617.
- [39] D. Chen, W. Wei, R. Wang, X. Lang, Y. Tian, L. Guo, Dalton Trans., 2012, **41**, 8822..
- [40] G. X. Wang, S. Bewlay, S. A. Needham, H. K. Liu, R. S. Liu, V. A. Drozd, J. F. Lee, J. M. Chen, J. Electrochem. Soc., 2006, **153**, A25.
- [41] J. Yang, J. Wang, Y. Tang, D. Wang, X. Li, Y. Hu, R. Li, G. Liang, T.-K. Sham, X. Sun, Energy Environ. Sci., 2013, **6**, 1521.

- [42] F. Omenya, N. A. Chernova, S. Upreti, P. Y. Zavalij, K. W. Nam, X. Q. Yang, M. S. Whittingham, *Chem. Mater.*, 2011, **23**, 4733.
- [43] J. Molenda, W. Qjczyk, J. Marzec, *J. Power Sources*, 2007, **174**, 689.
- [44] M. R. Roberts, G. Vitins, G. Denuault, J. R. Owen, *J. Electrochem. Soc.*, 2010, **157**, A381.
- [45] D. H. Baek, J. K. Kim, Y. J. Shin, G. S. Chauhan, J. H. Ahn, K. W. Kim, *J. Power Sources*, 2009, **189**, 59.
- [46] N. Meethong, H. Y. Huang, S. Speakman, W. Carter, Y. M. Chiang, *Adv. Funct. Mater.*, 2007, **17**, 1115.
- [47] G. Kobayashi, A. Yamada, S. Nishimura, R. Kanno, Y. Kobayashi, S. Seki, Y. Ohno, H. Miyashiro, *J. Power Sources*, 2009, **189**, 397.
- [48] G. Y. Chen, T. J. Richardson, *J. Power Sources*, 2010, **195**, 1221.

Chapter 9

9 High-Performance Carbon-LiMnPO₄ Nanocomposite as Cathode for Lithium Ion Batteries

In the previous chapters, we discussed the limitations and solutions of LiFePO₄ candidate as positive electrode. The successful achievement from LiFePO₄ encouraged the great interest to other olivine typed LiMnPO₄ cathodes materials with higher theoretical energy density, which is required for high power batteries applied in large-sized vehicles.

In this chapter, pure LiMnPO₄/C nanoparticles are fabricated by a two step synthesis. In the first step, Mn₂P₂O₇ with size of 10-15 nm is prepared; in the following step, Li source is mixed with Mn₂P₂O₇ by ball milling, followed by the calcinations process, the crystalline LiMnPO₄/C particles is obtained with the size slightly larger than Mn₂P₂O₇. The final product delivers an initial charge capacity and discharge capacity of 150 mA h g⁻¹ and 87 mA h g⁻¹, respectively. Benefiting from the carbon matrix, the cycling behavior is quite stable at the initial 10 cycles.

Keywords: LiMnPO₄, nanoparticles, carbon matrix, ball milling, lithium ion batteries

Note: The work in this chapter is in preparation.

9.1 Introduction

Recently Lithium-ion rechargeable batteries (LIBs) are being recognized as the alternative energy sources for large scale energy storage in electric vehicles (EV), hybrid electrical vehicles (HEVs) and plug-in hybrid electric vehicles (PHEV) [1, 2]. Challenges remain in making low cost, high-performance and high-safety lithium ion batteries. Since the pioneering work of Goodenough [3], polyanion framework materials are considered as prospective cathodes for LIBs. Among them LiFePO_4 has been proven to be an appealing cathode material with outstanding features such as low cost, environmental compatibility, high theoretical specific capacity of 170 mAh g^{-1} and especially a superior safety performance. The limitations for LiFePO_4 in large scale application are its intrinsically low ionic and electrical conductivity [1, 4], and this obstacle for LiFePO_4 has been overcome by coating the nano-meter sized particles with conductive carbon [5-10]. Nowadays, LiFePO_4 cathode material was commercialized by A123 Inc., Sony Inc., and Clariant Inc. in high-power lithium ion batteries.

The successful achievement from LiFePO_4 encouraged the great interest to other olivine typed LiMPO_4 ($\text{M}=\text{Mn}$, Co , and Ni) cathodes materials, which is even more attractive than LiFePO_4 because of higher theoretical energy density (energy density = specific capacity \times operating voltage) [11-16]. High energy density could be achieved for olivine typed LiMPO_4 such as Mn , Co , and Ni cathodes which have higher redox potentials (4.1, 4.8, and 5.1 V vs. Li^+/Li). However, working voltage higher than 4.5 V will lead to decompose of electrolyte [11, 17-19], and the 4.1 V voltage plateau is compatible to electrolyte [20]. Therefore, for next generation LIBs, LiMnPO_4 is more attractive than Ni and Co based olivines.

Similar to the LiFePO_4 electrode, the electrochemical behavior of LiMnPO_4 could also be improved by preparing nano-sized particles, carbon coating and cation doping [21-25]. Unfortunately, depositing carbon on LiMnPO_4 is more challenging due to the lower catalytic activity of Mn to carbon compared with Fe [26]. Moreover, given the even lower electrical conductivity of LiMnPO_4 ($< 10^{-12} \text{ S cm}^{-1}$) than LiFePO_4 ($1.8 \times 10^{-8} \text{ S cm}^{-1}$), quite a few amount of carbon additives (usually more than 10 wt.%) are required for

achieving acceptable capacity and rate performances [27, 28]. Besides, Mn will dissolve into the electrolyte during the cycling, which will lead to very poor cycle performance.

Recently, many studies have been conducted to mitigate lithium diffusion limitations in LiMnPO_4 by reducing particle size to shorten the diffusion length. The common way to decrease the size of LiMnPO_4 is ball-milling route, which is a mechanical way to decrease the size. Drezen et al. [29] prepared LiMnPO_4 by a sol-gel route followed by ball milling; the size can be decreased to 140 nm, and this material achieved a reversible capacity of 134 mAh g^{-1} at C/10. Oh et al. [28] synthesized LiMnPO_4 with 10-50 nm by ultrasonic spray pyrolysis followed by ball milling, which delivered discharge capacities of 155 mAh g^{-1} and 107 mAh g^{-1} at 0.1 C and 2 C. Ni et al. [30] preformed a high-energy ball-milling method to decrease the size of LiMnPO_4 to nanoscale, and a high capacity of 135 mAh g^{-1} can be obtained, which is more than 50% of that of the pristine one.

It has to be pointed out that the nano-sized LiMnPO_4 do not necessarily give good electrochemical performance [2, 31-33]. For instance, Doi et al. [34] prepared LiMnPO_4 nanoparticles, even if the particle size is down to 7 nm, the sample only presented a capacity of 65 mA h g^{-1} . Delacourt et al. [18] reported that directly precipitated LiMnPO_4 (100 nm) delivered a discharge capacity of 70 mA h g^{-1} at the rate of C/20. It is also noted that the cycling behavior for LiMnPO_4 is not stable [35]. Therefore, an optimum particle size combined with other approaches to enhance the electronic conductivity is crucial to realize high-performance LiMnPO_4 in the practical applications.

For LiMnPO_4 , it is quite challenging to get carbon layer due to the low activities of Mn to carbon. Even by post treatment, very low amount of carbon can be obtained. Ball milling is a useful way to make carbon precursors attached to the as-obtained LiMnPO_4 . Qin [36] prepared LiMnPO_4/C by using ball-milling with different carbon precursors, demonstrating the graphitized carbon can be obtained on LiMnPO_4 . It is interesting to mention that carbon precursor also has effect on rate capability, where pyrolytic carbon from ball-milling with graphene can have better rate performance than with glucose. Li et al. [37] ball-milled the LiMnPO_4 with different carbon sources, they claimed that the LiMnPO_4 sample ball-milled with beta-cyclcodextrin as the carbon source shows a best

reversible capacity of $153.4 \text{ mA h g}^{-1}$ at a rate of 0.1 C due to more uniform carbon coating than other ones. By applying ball-milling route can deposit carbon layer on LiMnPO_4 , but the uniform carbon coating is often a big challenge.

In this study, we report the synthesis LiMnPO_4/C nanocomposites by using sol-gel approach combined with ball-milling. The electrochemical performance is further investigated.

9.2 Experimental

9.2.1 Synthesis of LiMnPO_4/C nanoparticles

The LiMnPO_4/C was prepared by the following procedures. In the first step, 1.73 g manganese acetate was dissolved in 30 mL of water via strong ultrasonic agitation. Then, 500 mg citric acid was dissolved in the solution by stirring at 70°C for 1 h, followed by the drop of the phosphoric acid. The molar ratio of Mn:P is 1:1. The dried xerogel was treated at 700°C for 1 h. After the calcination process under Ar atmosphere, the $\text{Mn}_2\text{P}_2\text{O}_7$ was collected

In the second step, the composite $\text{Mn}_2\text{P}_2\text{O}_7$ from the first step was mixed with lithium hydroxide by ball-milling (Retsch, PM 200) for 5 h at 350 rpm. The final LiMnPO_4 was obtained through CVD thermal treatment at 700°C for 10 h.

9.2.2 Physical characterization

The XRD analyses were conducted on a Rigaku rotating-anode X-Ray Diffractometer. The XRD patterns were recorded with Co K α radiation equipped with monochromation using a curved crystal, diffracted beam at 45 kV and 160 mA. The experimental diffraction patterns were completed from 2 to 82° two-theta, at a rate of $10^\circ/\text{minute}$. Field emission scanning electron microscopy (FE-SEM) images were carried out on a Hitachi S-4800 microscope, operating at 5 kV.

9.2.3 Electrochemical measurements

The electrochemical performances were evaluated using a computer-controlled Arbin BT-2000 Battery Test Station with coin-shape half cells between 2.2 and 4.5 V. Ethylene

carbonate (EC) and dimethyl carbonate (DEC) mixed with a ratio of 1:1 (v/v) containing 1M LiPF_6 were used as the electrolyte. The test electrode was prepared by mixing the active material (LiMnPO_4)/acetylene black/polyvinylidene fluoride with a weight ratio 70:20:10, then grinding the mixture in a mortar and pestle. The resultant slurry, pasted on Al foil, was dried at 90 °C under vacuum for 24 h. The coin cells (2352) were assembled in high purity argon filled glove box.

The LiMnPO_4 working voltage range is between 2.2 V and 4.5 V (versus Li/Li^+) using a constant current mode (CC-mode). Charge-discharge testing was conducted galvanostatically using a computer controlled battery test system (Arbin BT-2000 Battery Test System) at 1/20 C at room temperature.

9.3 Results and discussions

In the first step, the Li sources are not introduced, which is crucial for the size of the final products. The SEM images of the products obtained in the first step are shown in Figure 9.1. Very fine particles with size of 10-15 nm (Figure 9.1b) were obtained in the absence of Li sources. Low magnification graph (Figure 9.1a) illustrates the uniformity of the samples as-prepared. Carbon acted as a matrix, generated from the decomposition of the citric acid to connect the nanoparticles, which promises the good electronic conductivity.

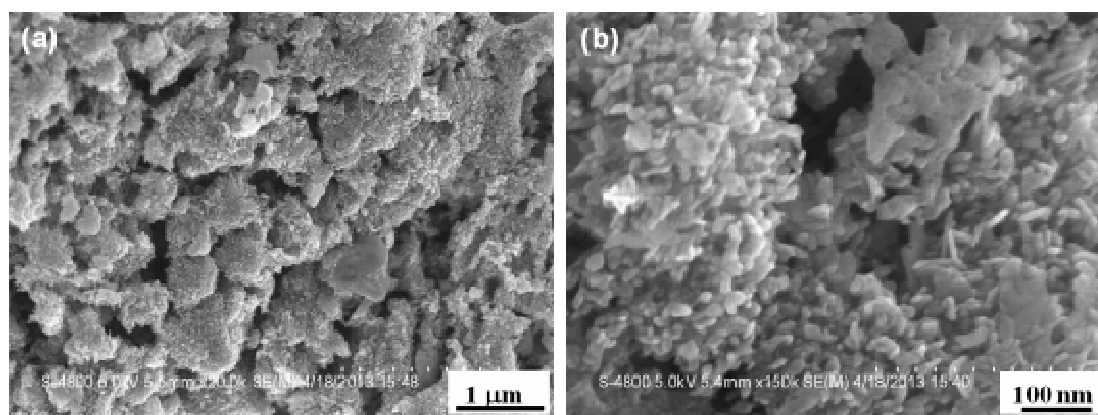


Figure 9.1 SEM images (a) and (b) of the $\text{Mn}_2\text{P}_2\text{O}_7/\text{C}$ with different magnifications.

Figure 2 presents the SEM images of LiMnPO_4/C nanocomposites. In the second step, Li sources were mixed homogeneously with the composites prepared previously by ball-milling. By controlling the heating rate at $100\text{ }^\circ\text{C min}^{-1}$ for the ball-milled sample, the size of final product is around 30 nm, which is slightly larger than that obtained from the first step.

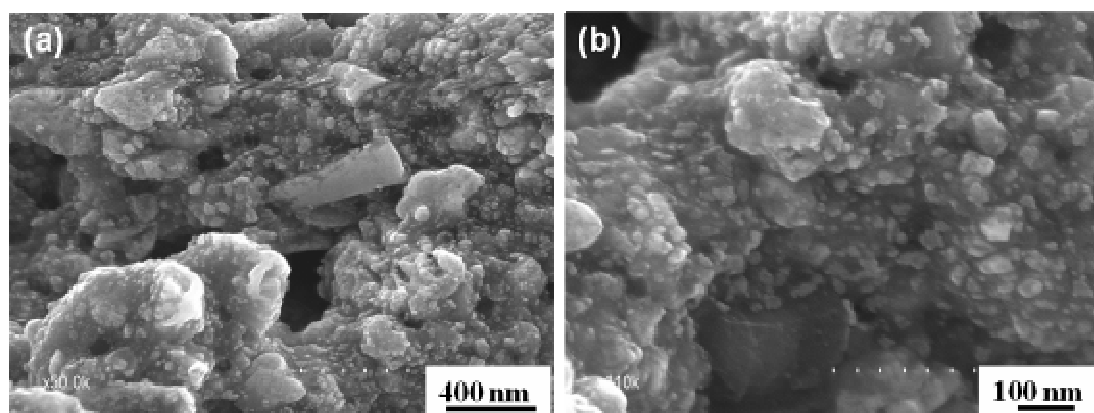


Figure 9.2 SEM images (a) and (b) of the LiMnPO_4/C after annealed at $700\text{ }^\circ\text{C}$.

In order to confirm the formation of the intermediate phase as well as the final product, X-ray diffraction (XRD) was performed on the products obtained at both steps, which is shown in Figure 3. In the first step, pure crystalline $\text{Mn}_2\text{P}_2\text{O}_7$ phase was obtained after $700\text{ }^\circ\text{C}$ annealing, which are in good agreement with the standard PDF card (JCPDs no.35-1497). The broad peaks in the XRD patterns indicate the particle size is in nanoscale. After introducing Li sources in the second step, LiMnPO_4 phase appeared without impurities and all the diffraction peaks can be indexed as olivine-type LiMnPO_4 with a Pnmb space group of the orthorhombic system. The absence phase of LiOH demonstrates that the phase transformation thoroughly performed in the second step and high crystalline LiMnPO_4 is achieved.

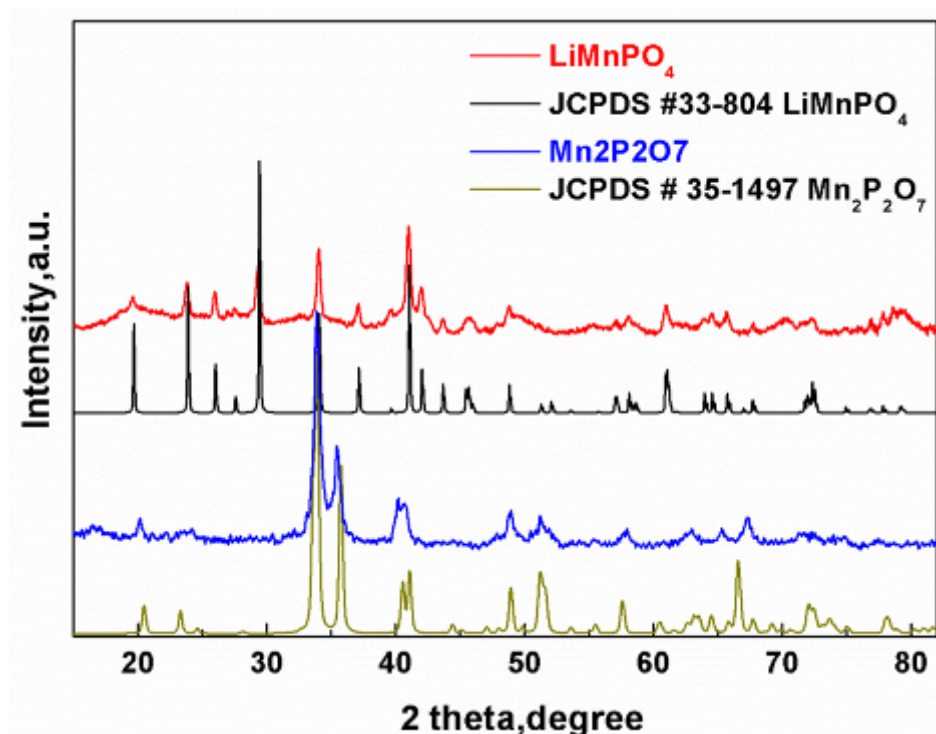


Figure 9.3 X-ray diffraction (XRD) patterns for the obtained products in both steps.

Figure 9.4 illustrates the first two charge-discharge curves of the LiMnPO_4/C using a constant current of $C/20$ with a voltage window of 2.2-4.5 V (Vs. Li^+/Li). The test temperature is 25 °C. The electrode exhibits a reversible plateau around 4.1 V vs. Li^+/Li , which is resulted from the redox couple of $\text{Mn}^{3+}/\text{Mn}^{2+}$ for the LiMnPO_4 . The initial charge and discharge capacities are 150 mA h g^{-1} and 87 mA h g^{-1} , respectively. The coulombic efficiency is around 60%. In the subsequent cycle, the coulombic efficiency is increased to 75%. The low coulombic efficiency is attributed to the low electronic conductivity of the active material, whiel the electrical conductivity could be further enhanced by introducing more conducting (carbon) additives.

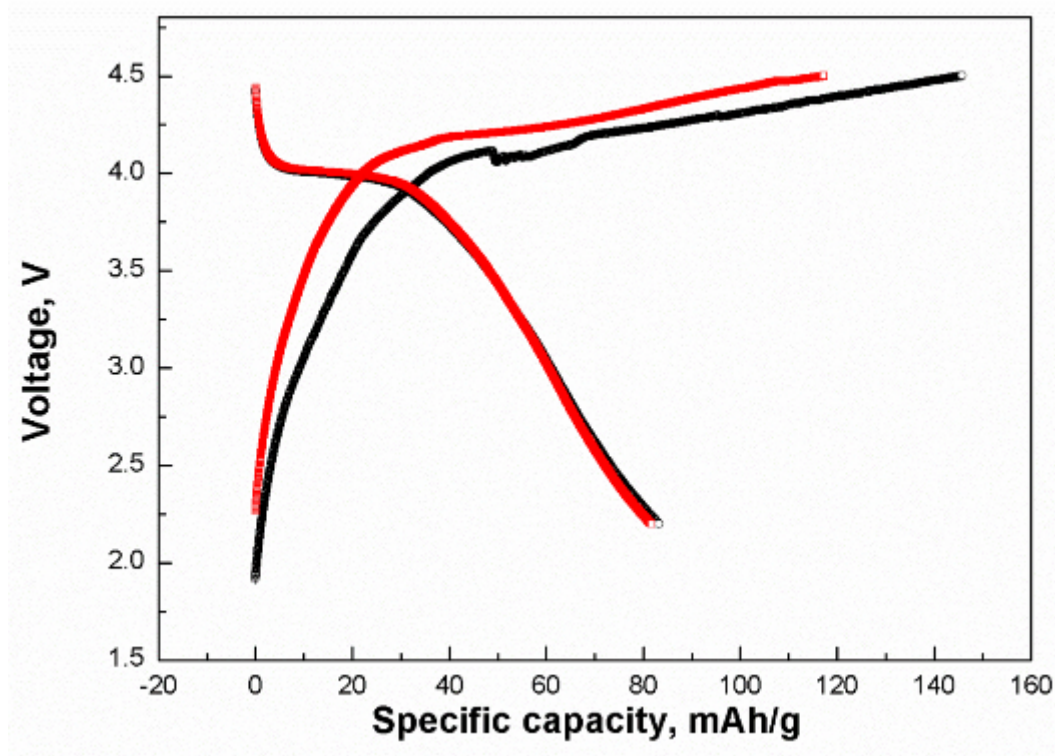


Figure 9.4 The first two charge-discharge curves of LiMnPO_4/C nanocomposites at a rate of $1/20\text{ C}$ at room temperature.

The cycling behavior of LiMnPO_4/C is shown in Figure 9.5. It can be seen that the discharge capacity is almost stable around 87 mA h g^{-1} after 10 cycles at room temperature. Generally, Mn will dissolve in the electrolyte during the charge/discharge cycle, leading to the fade of the capacity upon cycle. Refer to the LiMnPO_4/C nanoparticles obtained in this paper, it is believed that carbon coating could play a bi-functional role to enhance the electronic conductivity and alleviate the Mn dissolution in the electrolyte. Therefore, the design of the nanoparticles in carbon matrix could maintain the stability of the LiMnPO_4 electrodes.

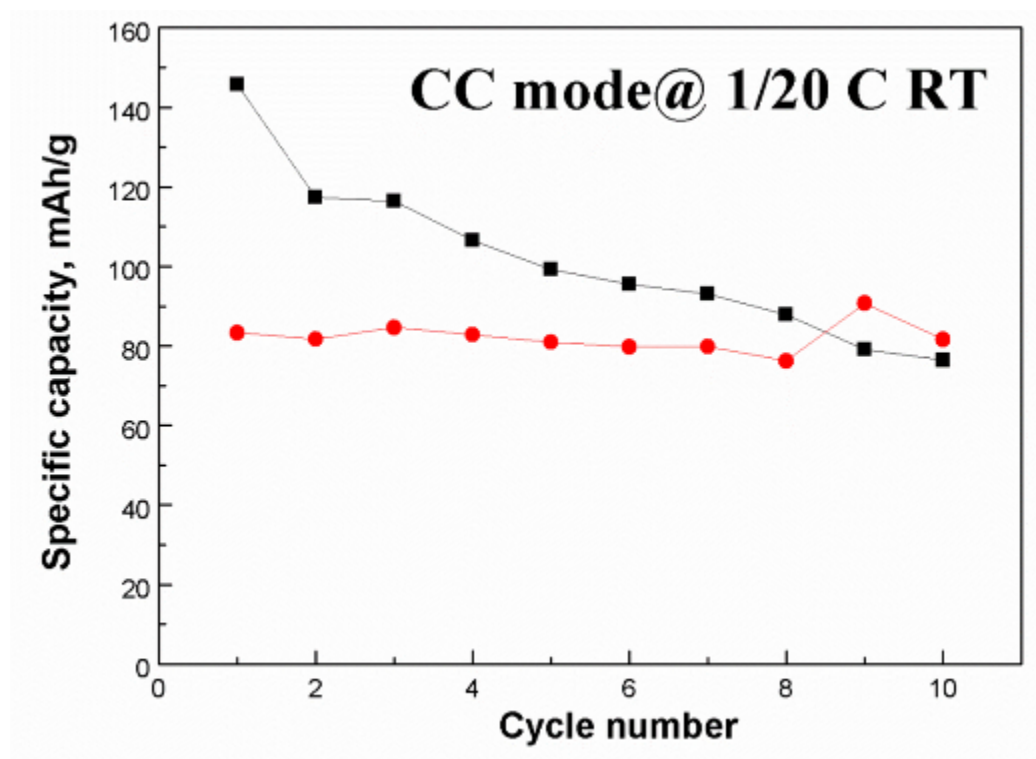


Figure 9.5 The cycle performance of the LiMnPO₄/C nanocomposites at a rate of 1/20 C at room temperature. (top: charge curve; bottom: discharge curve)

9.4 Conclusion

In summary, LiMnPO₄/C nanocomposites can be successfully fabricated by a two step synthesis. With the absence of Li sources in the first step, the particle size of Mn₂P₂O₇ can be restricted to 10-15 nm, while the final product of LiMnPO₄ is slightly larger than Mn₂P₂O₇ after annealing with lithium sources. The LiMnPO₄/C nanoparticles delivers a stable discharge capacity of 87 mA h g⁻¹ up to 10 cycles. The initial charge capacity is 150 mA h g⁻¹, while the subsequent charge is 120 mA h g⁻¹. It is believed that the specific capacity can be enhanced by introducing more carbon additives.

9.5 Acknowledgement

This work is supported by Natural Sciences and Engineering Research Council of Canada (NSERC), Clariant Inc. (former Phostech Lithium Inc.), Canada Research Chair (CRC) Program and the Western University.

9.6 References

- [1] N. Ravet, Y. Chouinard, J. F. Magnan, S. Besner, M. Gauthier and M. Armand, J. Power Sources, 2001, **97-98**, 503.
- [2] H. Huang, S.-C. Yin and L. F. Nazar. Electrochem. Solid State Lett., 2001, **4**, A170.
- [3] A. K. Padhi, K. S. Nanjundaswamy and J. B. Goodenough, J. Electrochem. Soc. 1997, **144**, 1188.
- [4] A. Yamada, S. C. Chung and K. Hinokuna, J. Electrochem. Soc., 2001, **148**, A224.
- [5] J. Yang, J. Wang, D. Wang, X. Li, D. Geng, G. Liang, M. Gauthier, R. Li and X. Sun, J. Power Sources, 2012, **208**, 340.
- [6] P. S. Herle, B. Ellis, N. Coombs and L. F. Nazar, Nat. Mater. 2004, **3**, 147.
- [7] J. Yang, J. Wang, X. Li, D. Wang, J. Liu, G. Liang, M. Gauthier, Y. Li, R. Li and X. Sun, J. Mater. Chem. 2012, **22**, 7537.
- [8] Y. G. Wang, Y. Wang, E. Hosono, K. X. Wang and H. S. Zhou, Angew. Chem. Int. Ed., 2008, **47**, 7461.
- [9] X. L. Wu, L.Y. Jiang, F. F. Cao, Y. G. Guo and L. J. Wan, Adv. Mater., 2009, **21**, 2710.
- [10] J. Wang, J. Yang, Y. Zhang, Y. Li, M. N. Banis, X. Li, R. Li, G. Liang, X. Sun, Adv. Funct. Mater., 2012, **23**, 806.
- [11] K. Zaghib, M. Trudeau, A. Guerfi, J. Trottier, A. Mauger, R. Veillette and C. M. Julien, J. Power Sources, 2012, **204**, 177.

- [12] P. Gibot, M. Casas-Cabanas, L. Laffont, S. Levasseur, P. Carlach, S. Hamelet, J. M. Tarascon and C. Masquelier, *Nat. Mater.*, 2008, **7**, 741.
- [13] C. Delacourt, L. Laffont, R. Bouchet, C. Wurm, J. B. Leriche, M. Morcrette, J. M. Tarascon and C. Masquelier, *J. Electrochem. Soc.*, 2005, **152**, A913.
- [14] T. Drezen, N. H. Kwon, P. Bowen, I. Teerlinck, M. Isono and I. Exnar, *J. Power Sources*, 2007, **174**, 949.
- [15] D. Y. Wang, H. Buqa, M. Crouzet, G. Deghenghi, T. Drezen, I. Exnar, N. H. Kwon, J. H. Miners, L. Poletto and M. Graetzel, *J. Power Sources*, 2009, **189**, 624.
- [16] K. Saravanan, V. Ramar, P. Balaya and J. J. Vittal, *J. Mater. Chem.*, 2011, **21**, 14925.
- [17] C. Delacourt, P. Poizot, M. Morcrette, J. M. Tarascon and C. Masquelier, *Chem. Mater.*, 2004, **16**, 93.
- [18] B. Ellis, P. S. Herle, Y. H. Rho, L. F. Nazar, R. Dunlap, L. K. Perry and D. H. Ryan, *Faraday Discuss.*, 2007, **134**, 119.
- [19] G. H. Li, H. Azuma and M. Tohda, *Electrochem. Solid-State Lett.*, 2002, **5**, A135.
- [20] B. Kang and G. Cedar, *J. Electrochem. Soc.*, 2010, **157**, A808.
- [21] S.-W. Oh, S. T. Myung, S.-M. Oh, K. H. Oh, K. Amine, B. Scrosati and Y.-K. Sun, *Adv. Mater.*, 2010, **22**, 4842.
- [22] S.-W. Oh, S. T. Myung, Y. S. Choi, K. H. Oh and Y.-K. Sun, *J. Mater. Chem.*, 2011, **21**, 19368.
- [23] Y. S. Choi, S. Kim, S. S. Choi, J. S. Han, J. D. Kim, S. E. Jeon and B. H. Jung, *Electrochim. Acta*, 2004, **50**, 833.
- [24] S. Kuroda, N. Tabori, M. Sakuraba and Y. Sato, *J. Power Sources*, 2003, **119-121**, 924.

- [25] Z. Bakenov and I. Taniguchi, J. Electrochem. Soc., 2010, **157**, A430.
- [26] N. Ravet, M. Gauthier, K. Zaghib, J. B. Goodenough, A. Mauger, F. Gendron and C. M. Julien, Chem. Mater., 2007, **19**, 2595.
- [27] S.-M. Oh, H.-G. Jung, C. S. Yoon, S.-T. Myung, Z. Chen, K. Amine and Y.-K. Sun, J. Power Sources, 2011, **196**, 6924.
- [28] S.-M. Oh, S.-W. Oh, C.-S. Yoon, B. Scrosati, K. Amine and Y.-K. Sun, Adv. Funct. Mater., 2010, **20**, 3260.
- [29] T. Drezen, N.-H. Kwo, P. Bowen, I. Teerlinck, M. Isono, I. Exnar, J. Power Sources, 2007, **174**, 949.
- [30] J. Ni, Y. Kawabe, M. Morishita, M. Watada and T. Sakai, J. Power Sources, 2011, **196**, 8104-8109.
- [31] G. Arnold, J. Garche, R. Hemmer, S. Ströbele, C. Vogler and M. Wohlfahrt-Mehrens, J. Power Sources, 2003, **119–121**, 247.
- [32] S.-Y. Chung, J.T. Bloking and Y.-M. Chiang, Nat. Mater., 2002, **1**, 123.
- [33] K. Zaghib, M. Dontigny, A. Guerfy, P. Charest, I. Rodrigues, A. Mauger and C.M. Julien. J. Power Sources, 2011, **196**, 3949.
- [34] T. Doi, S. Yatomi, T. Kida, S. Okada and J. I. Yamaki, Cryst. Growth Des. 2009, **9**, 4990.
- [35] Xiao-Liang Pan, Cheng-Yan Xu and L. Zhen, Cryst. Eng. Comm., 2012, **14**, 6412.
- [36] Z. Qin, X. Zhou, Y. Xia, C. Tang and Z. Li, J. Mater. Chem., 2012, **22**, 21144.
- [37] L. Li, J. Liu, L. Chen, H. Xu, J. Yang and Y. Qian, RSC Adv., 2013, **3**, 6847.

Chapter 10

10 Conclusions and Future Perspectives

10.1 Conclusions

Rechargeable lithium ion batteries (LIBs), as an energy storage system, could offer the highest energy density among the various existing energy storage systems, therefore are considered as the power sources for the future electric vehicles (EVs) and hybrid electric vehicles (HEVs). The challenges facing the development of lithium ion batteries for transportation areas are cost, safety, cell energy density, rate capability, and shelf life. The safety issue is a big concern, thus stable active materials are pursued as electrodes for LIBs fulfill their potential. Olivine LiFePO_4 has been emerging as a positive electrode due to its low cost, environmental compatibility, high theoretical specific capacity of 170 mA h g^{-1} and especially a superior safety performance. However, the main obstacle of LiFePO_4 used for practical applications in vehicles is its low electronic conductivity and low ionic conductivity.

The main objective of the thesis is to develop various hierarchical structure of LiFePO_4 composite, and then good electrochemical performances can be achieved.

The common ways to address the limitations are decreasing the size, coating carbon layers and doping cations. The nanosized strategy will result in low tap density, which hampers the practical application. Therefore, we developed hierarchical structured LiFePO_4 architectures in this research to alleviate this problem. One is three dimensional (3D) porous LiFePO_4 in microscale with superior carbon additives. The porous strategy could allow efficient percolation of the electrolyte through the electrode, favoring the electrolyte access to active materials via the pores, then make full use of electrode material. Another one is nanosized LiFePO_4 anchors in the 3D conducting network, which could achieves fast electronic and ion conduction, lead to high performance of the composites.

A series of carbon additives were applied in 3D porous structure. The first one is carbon nanotubes (CNTs), which possess high conductivity, high surface area and network structure. The second is nitrogen doped CNTs (N-CNTs), due to the additional electrons contributed by the nitrogen atoms provide electron carriers for the conduction band, N-CNTs are more conductive compared with CNTs. Furthermore, N-CNTs also have hydrophilic properties, leading to uniformly dispersion in the solution then intimate contact with active material. The third one is graphene nanosheets. It can offer an improved interfacial contact because of its good electronic behaviors, high surface area (theoretical value of $2630 \text{ m}^2 \text{ g}^{-1}$) and flexible structure.

In this thesis, N-CNTs and CNTs were integrated into porous LiFePO_4 composites. CNTs and N-CNTs were used as carbon additive to increase the electronic conductivity of the active material. Due to its hydrophilic properties, N-CNTs can dispersed uniformly into the 3D interlaced porous LiFePO_4 , which could facilitate the electrons and lithium ions diffusion rate, thus $\text{LiFePO}_4/\text{N-CNTs}$ composites could deliver a reversible discharge capacity of 138 mAh g^{-1} at a current density of 17 mA g^{-1} , demonstrating N-CNTs modified composites can act as a promising cathode for high-performance lithium-ion batteries.

Then we applied graphene nanosheets into porous structure to obtain self-assembled $\text{LiFePO}_4/\text{graphene}$ composite using a facile template-free sol-gel approach. Graphene nanosheets were incorporated into the porous hierarchical network homogenously, which greatly enhances the electrical conductivity and efficient use of the LiFePO_4 , resulting in an outstanding electrochemical performance of the hybrid cathodes. The obtained $\text{LiFePO}_4/\text{graphene}$ composite has a reversible capacity of 146 mA h g^{-1} at 17 mA g^{-1} after 100 cycles, which is more than 1.4 times greater than that of porous LiFePO_4 (104 mA h g^{-1}). Moreover, this porous $\text{LiFePO}_4/\text{graphene}$ composite also exhibits a desirable tolerance to varied charge/discharge currents.

In order to take full advantage of the active material and graphene, we designed the nanosized LiFePO_4 anchored to 3D conducting unfolded graphene network by using a sol-gel approach. The facile designed electrodes exhibit both high specific capacity and

rate performances benefiting from application of unfolded graphene matrix, which serves as a conducting 3D nano-network, enables both Li^+ and electrons to migrate and reach each of LFP particles, hence realizing the full potential of the active materials. Compare with stacked graphene nanosheets, the use of unfolded graphene enables better dispersion of LiFePO_4 and restricts the LiFePO_4 particle size at nanoscale. More importantly, it allows each LiFePO_4 particle to be attached to the conducting layer, which could greatly enhance the electronic conductivity and thereby realizing almost theoretical capacity (171 mA h g^{-1}), the composite also displayed stable cycling behavior up to 100 cycles.

Further, in order to obtain high power density, we designed and synthesized one-dimensional LiFePO_4 @CNTs nanowires with a diameter of 20-30 nm encapsulated into CNTs. The 3D conducting networks of CNTs were simultaneously obtained from in situ carbonization of the PMMA polymer during the solid state reaction. The one-dimensional LiFePO_4 nanowire reduces the diffusion path of Li ions and increases the contact areas between electrolyte and active materials, while the CNTs shell ensures a full coating and a fast electron conduction path. The 3D network of CNTs can offer good electronic conductivity. The LiFePO_4 @CNTs nanowire delivers a capacity of 160 mA h g^{-1} at 17 mA g^{-1} , and 65 mA h g^{-1} at 8500 mA g^{-1} (50C, 1.2 minutes for charging and 1.2 minutes for discharging).

To realize large-scale yield of the nanowire composites, we extended this design into hydrothermal system. By using the surfactant, peapod-like nanowire with a diameter around 50 nm with carbon shell could be obtained after annealed. The discontinued LiFePO_4 nanoparticles were connected by the carbon shell constituted the nanowire structure. With the help of the PPy conductive network, the LiFePO_4/C delivers a capacity of 120 mA h g^{-1} at 17 mA g^{-1} .

Moreover, we investigated the effect of Mn concentration on the crystal lattice of LiFePO_4 as well as the electrochemical performance. The Mn concentration significantly affects the final morphology of the obtained samples. With increasing the Mn content, the morphology evolves from nanoparticles to self-assembled nanoplates. By performed the extended X-ray absorption fine structure (EXAFS), Mn atoms favors to occupy the sites

in octahedral MO_6 while replaces Fe atoms, leading to lattice distortion. $\text{LiFe}_{0.5}\text{Mn}_{0.5}\text{PO}_4/\text{C}$ composites exhibited a highest reversible discharge capacity of 106 mA h g^{-1} and best rate performance compared with other two compounds of different stoichiometric Fe/Mn ratios, which is assigned to the high structure stabilities of $\text{LiFe}_{0.5}\text{Mn}_{0.5}\text{PO}_4$.

We believe that all these studies will provide a better understanding of LiFePO_4 candidates and have an impact on the development of LIBs applied in EVs and HEVs with both high power and high energy densities.

10.2 Future perspectives

Despite the improvement for LiFePO_4 made in this thesis, there are still challenges for LiMnPO_4 candidates. Future work will focus on the following aspects:

- 1) This thesis presented the nanosized LiFePO_4 anchored into unfolded graphene nanosheets, then full potential use of the active material (the specific capacity could reach almost theoretical capacity). For LiMnPO_4 , the even lower electronic conductivity ($< 10^{-10} \text{ S cm}^{-1}$) gives a relatively poor specific capacity. Recently, decreasing the size for LiMnPO_4 could increase the utilization of the Li ions in the olivine structure. Besides, quite large carbon amount is required to alleviate the polarization of the electrodes, then achieving the acceptable capacity. It is expected that to get the similar structure of LiMnPO_4 anchored into unfolded graphene, lower carbon content in this composites will increase the specific capacity, and the 3D network enhances the lithium diffusion kinetics in the electrodes.
- 2) Due to the Mn dissolution of LiMnPO_4 into the electrolyte during the cycling, and especially at relatively high working voltage, the cycle stability is quite low for the LiMnPO_4 . Research reported that atomic layer deposition (ALD) is alternative way to buffer the big volume change in anode materials. In the future, ALD will be a very promising direction to inhibit the dissolution of Mn during charge/discharge cycles. The thin ALD shell on carbon coated LiMnPO_4 is pursued as cathode materials for LIBs.

- 3) Another limitation of the LiMnPO_4 candidates is its annealing temperature. Low annealed temperature will result in low crystalline LiMnPO_4 and also the quality of the carbon nature. Design a gradient materials of core shell structure is an alternative way to compromise this issue. Gradient $\text{LiMnPO}_4/\text{LiFePO}_4$ could be the first case. Then other gradient materials will be synthesized.
- 4) In our research, N-CNTs show better electronic conductivity than CNTs, applying to the composites could improve the utilization of the active materials, then achieving high specific capacity. In our future work, N doped carbon layer on LiMnPO_4 will be further investigated.

Besides this structure design to resolve the limitations for LiMnPO_4 , the focus in the following years is a fully understanding of the kinetics in the batteries by using in-situ synchrotron radiation (SR) techniques (in-situ XANES, in-situ SR XRD, in-situ SR XPS). The relationship between the properties and structure will be further investigated.

Appendices

**Appendix I: PERMISSION FROM ROYAL SOCIETY OF CHEMISTRY (RSC)
FOR PUBLISHED ARTICLE**

Published article: Hierarchically Porous LiFePO₄/Nitrogen-doped Carbon Nanotube Composite for Lithium Ion Batteries Cathodes, **J. Mater. Chem.** 22(2012) 7537-7543.

J. Yang, J. Wang, X. Li, D. Wang, J. Liu, G. Liang, M. Gauthier, Y. Li, R. Li, X. Sun

Link: <http://pubs.rsc.org/en/Content/ArticleLanding/2012/JM/c2jm30380a>

RSC Copyright Policy


(<http://www.rsc.org/AboutUs/CopyrightRightsRetainedbyJournalsauthors.asp>):

When the author signs the exclusive Licence to Publish for a journal article, he/she retains certain rights that may be exercised without reference to the RSC. He/she may:


- *Reproduce/republish portions of the article (including the abstract)*
- *Photocopy the article and distribute such photocopies and distribute copies of the PDF of the article that the RSC makes available to the corresponding author of the article upon publication of the article for personal or professional use only; provided that any such copies are not offered for sale.*

Reproduced by permission of The Royal Society of Chemistry

Appendix II: PERMISSION FROM ELSEVIER FOR PUBLISHED ARTICLE




Copyright
Clearance
Center



Home

Account Info

Help



Title: 3D porous LiFePO₄/graphene hybrid cathodes with enhanced performance for Li-ion batteries

Author: Jinli Yang, Jiajun Wang, Dongniu Wang, Xifei Li, Dongsheng Geng, Guoxian Liang, Michel Gauthier, Ruying Li, Xueliang Sun

Publication: Journal of Power Sources

Publisher: Elsevier

Date: 15 June 2012

Copyright © 2012, Elsevier

Logged in as:
Jinli Yang

LOGOUT

Order Completed

Thank you very much for your order.

This is a License Agreement between Jinli Yang ("You") and Elsevier ("Elsevier"). The license consists of your order details, the terms and conditions provided by Elsevier, and the [payment terms and conditions](#).

[Get the printable license.](#)

License Number	3165990910952
License date	Jun 11, 2013
Licensed content publisher	Elsevier
Licensed content publication	Journal of Power Sources
Licensed content title	3D porous LiFePO ₄ /graphene hybrid cathodes with enhanced performance for Li-ion batteries
Licensed content author	Jinli Yang, Jiajun Wang, Dongniu Wang, Xifei Li, Dongsheng Geng, Guoxian Liang, Michel Gauthier, Ruying Li, Xueliang Sun
Licensed content date	15 June 2012
Licensed content volume number	208
Number of pages	5
Type of Use	reuse in a thesis/dissertation
Portion	full article
Format	both print and electronic
Are you the author of this Elsevier article?	Yes
Will you be translating?	No
Order reference number	
Title of your thesis/dissertation	Development of Hierarchical Structure LiMPO ₄ (M=Fe, Mn) as Cathodes for High Performance Lithium-Ion Batteries
Expected completion date	Sep 2013
Elsevier VAT number	GB 494 6272 12
Permissions price	0.00 USD
VAT/Local Sales Tax	0.00 USD
Total	0.00 USD

ORDER MORE...

CLOSE WINDOW

Copyright © 2013 [Copyright Clearance Center, Inc.](#) All Rights Reserved. [Privacy statement](#).
Comments? We would like to hear from you. E-mail us at customercare@copyright.com

Appendix III: PERMISSION FROM ROYAL SOCIETY OF CHEMISTRY (RSC) FOR PUBLISHED ARTICLE

Published article: LiFePO₄/graphene as a Superior Cathode Material for Rechargeable Lithium Batteries: Impact of Stacked Graphene and Unfolded Graphene, **Energy Environ. Sci.** 6 (2013) 1521-1528. (Back Cover Page, highlighted by "[Green Car Congress](#)")

Link: <http://pubs.rsc.org/en/content/articlelanding/2013/EE/c3ee24163g>

J. Yang, J. Wang, Y. Tang, D. Wang, X. Li, Y. Hu, R. Li, G. Liang, T.-K. Sham, X. Sun

RSC Copyright Policy

(<http://www.rsc.org/AboutUs/CopyrightRightsRetainedbyJournalsauthors.asp>):

When the author signs the exclusive Licence to Publish for a journal article, he/she retains certain rights that may be exercised without reference to the RSC. He/she may:

- *Reproduce/republish portions of the article (including the abstract)*
- *Photocopy the article and distribute such photocopies and distribute copies of the PDF of the article that the RSC makes available to the corresponding author of the article upon publication of the article for personal or professional use only, provided that any such copies are not offered for sale.*

**Appendix IV: PERMISSION FROM ROYAL SOCIETY OF CHEMISTRY (RSC)
FOR PUBLISHED ARTICLE**

Published article: In-situ Self-catalyzed Formation of Core-shell LiFePO₄@CNTs Nanowire for Ultra-high Rate Performance Lithium-ion Batteries, **J. Mater. Chem. A**, 1 (2013) 7306-7311.

Link: <http://pubs.rsc.org/en/content/articlelanding/2013/TA/c3ta11262d>

J. Yang, J. Wang, Y. Tang, D. Wang, B. Xiao, X. Li, R. Li, G. Liang, T.-K. Sham, X. Sun

RSC Copyright Policy

(<http://www.rsc.org/AboutUs/CopyrightRightsRetainedbyJournalsauthors.asp>):

When the author signs the exclusive Licence to Publish for a journal article, he/she retains certain rights that may be exercised without reference to the RSC. He/she may:

- *Reproduce/republish portions of the article (including the abstract)*
- *Photocopy the article and distribute such photocopies and distribute copies of the PDF of the article that the RSC makes available to the corresponding author of the article upon publication of the article for personal or professional use only, provided that any such copies are not offered for sale.*

Reproduced by permission of The Royal Society of Chemistry

Curriculum Vitae

Name:	Jinli Yang
Post-secondary Education and Degrees:	<p>Harbin Institute of Technology Harbin, Heilongjiang, China 2003-2007 B.A.</p> <p>Harbin Institute of Technology Harbin, Heilongjiang, China 2007-2009 M.A.</p> <p>Western University London, Ontario, Canada 2009-2013 Ph.D.</p>
Honours and Awards:	<p>Chinese government award for outstanding self-financed student abroad 2012</p> <p>Principal scholarships 2007-2009</p>
Related Work Experience	<p>Teaching Assistant and Researching Assistant The Western University 2009-2013</p>

Publications:

1. **J. Yang**, J. Wang, Y. Tang, D. Wang, X. Li, Y. Hu, R. Li, G. Liang, T.-K. Sham, X. Sun, *LiFePO₄/graphene as a Superior Cathode Material for Rechargeable Lithium Batteries: Impact of Stacked Graphene and Unfolded Graphene*. **Energy Environ. Sci.**, 2013, 6, 1521-1528. (**Back Cover Page, highlighted by "Green Car Congress"**)
2. **J. Yang**, J. Wang, X. Li, D. Wang, J. Liu, G. Liang, M. Gauthier, Y. Li, R. Li, X. Sun, *Hierarchically Porous LiFePO₄/Nitrogen-doped Carbon Nanotube Composite for Lithium Ion Batteries Cathodes*. **J. Mater. Chem.**, 2012 22, 7537-7543.

3. **J. Yang**, J. Wang, D. Wang, X. Li, D. Geng, G. Liang, M. Gauthier, R. Li, X. Sun, *3D Porous LiFePO₄-graphene Hybrid Electrodes with Enhanced Performance for Li-ion Batteries*. **J. Power Sources**, 2012, 208, 340-344.
4. **J. Yang**, J. Wang, Y. Tang, D. Wang, B. Xiao, X. Li, R. Li, G. Liang, T.-K. Sham, X. Sun, *In-situ Self-catalyzed Formation of Core-shell LiFePO₄@CNTs Nanowire for Ultra-high Rate Performance Lithium-ion Batteries*. **J. Mater. Chem. A**, 2013, 1, 7306-7311.
5. **J. Yang**, D. Wang, X. Li, Y. Tang, B. Xiao, G. Liang, R. Li, X. Sun, Binary olivine solid solution LiFe_xMn_{1-x}PO₄ (x=0.3, 0.5 and 0.7) as cathode materials for lithium ion batteries. (2013) Submitted.
6. J. Wang, **J. Yang**, Y. Zhang, Y. Li, M. N. Banis, X. Li, G. Liang, R. Li, X. Sun, *Interaction of Carbon Coating on LiFePO₄: Local Visualization Study of the Influence of Impurity Phases*. **Adv. Funct. Mater.**, 2013, 23, 806–814.
7. D. Wang, **J. Yang**, X. Li, D. Geng, R. Li, M. Cai, T.-K. Sham, X. Sun, *Layer by Layer Assembly of Sandwiched Graphene/SnO₂ Nanorod/Carbon Nanostructures with Ultrahigh Lithium Ion Storage Properties*. **Energy Environ. Sci.**, 2013, DOI: 10.1039/C3EE40829A.
8. J. Wang, **J. Yang**, Y. Tang, R. Li, G. Liang, T.-K. Sham, X. Sun, *Surface Aging at Olivine LiFePO₄: a Direct Visual Observation of Iron Dissolution and the Protection Role of Nano-carbon Coating*. **J. Mater. Chem. A**, 2013, 1, 1579-1586.
9. X. Li, **J. Yang**, Y. Hu, J. Wang, Y. Li, M. Cai, R. Li, X. Sun, *Novel Approach toward Binder-free and Current Collector-free Anode Configuration: Highly Flexible Nanoporous Carbon Nanotube Electrodes with Excellent Mechanical Strength Harvesting Improved Lithium Storage*. **J. Mater. Chem.**, 2012, 22, 18847-18853.
10. D. Wang, **J. Yang**, X. Li, J. Wang, R. Li, M. Cai, T. K. Sham, X. Sun. *Observation of Surface/Defect States of SnO₂ Nanowires on Different Substrates from X-ray Excited Optical Luminescence*. **Cryst. Growth Des.**, 2012, 12, 397-402.

11. D. Wang, X. Li, **J. Yang**, J. Wang, D. Geng, M. Cai, R. Li, T. K. Sham, X. Sun. Hierarchical Nanostructured Core-Shelled Sn@C Nanoparticles Embedded in Graphene Nanosheets: Spectroscopic View and Its Application for Lithium Ion batteries. **Phys. Chem. Chem. Phys.**, 2013, 15, 3535-3542.
12. Y. Tang, J. Wang, **J. Yang**, Y. Li, B. Xiao, X. Li, G. Liang, R. Li, T.-K. Sham, X. Sun, *Observation of $\text{LiMn}_{0.7}\text{Fe}_{0.3}\text{PO}_4$ Aging in Electrolyte: Effect of impurity phases*. 2013, Submitted.
13. J. Liu, X. Li, **J. Yang**, D. Geng, Y. Li, D. Wang, R. Li, X. Sun, *Microwave-assisted Hydrothermal Synthesis of Nanostructured Spinel $\text{Li}_4\text{Ti}_5\text{O}_{12}$ as Anode Materials for Lithium Ion Batteries*. **Electrochim. Acta**, 2012, 63, 100-104.
14. K. Chang, D. Geng, X. Li, **J. Yang**, Y. Tang, M. Cai, R. Li, X. Sun, *Ultrathin MoS_2 /Nitrogen-doped Graphene Nanosheets with Highly Reversible Lithium Storage*. **Adv. Energy Mater.**, 2013, DOI: 10.1002/aenm.201201108.
15. D. Wang, X. Li, J. Wang, **J. Yang**, D. Geng, R. Li, M. Cai, T.-K. Sham, X. Sun, *Defect-Rich Crystalline SnO_2 Immobilized on Graphene Nanosheets with Enhanced Cycle Performance*. **J. Phys. Chem. C**, 2012, 116, 22149-22156.
16. Y. Tang, Z. Wang, D. Wang, **J. Yang**, B. Xiao, G. Liang, R. Li, X. Sun, T.-K. Sham, *Soft X-ray Absorption Spectroscopy Evidence of LiMPO_4 ($M=\text{Fe}, \text{Mn}$) Aging in Ambient Atmosphere*. 2013, Submitted
17. D. Geng, S. Yang, Y. Zhang, **J. Yang**, J. Liu, R. Li, T.-K. Sham, X. Sun, S. Ye, S. Knights, *Nitrogen Doping Effects on the Structure of Graphene*. **Appl. Surf. Sci.**, 2011, 257, 9193-9198
18. X. Li, J. Liu, Y. Zhang, Y. Li, H. Liu, X. Meng, **J. Yang**, D. Geng, D. Wang, R. Li, X. Sun, *High Concentration Nitrogen Doped Carbon Nanotube Anodes with Superior Li^+ Storage Performance for Lithium Rechargeable Battery Application*. **J. Power Sources**, 2012, 197, 238-245.

19. X. Li, X. Meng, J. Liu, D. Geng, Y. Zhang, M. Banis, Y. Li, **J. Yang**, R. Li, X. Sun, M. Cai, M. Verbrugge, *Tin Oxide with Controlled Morphology and Crystallinity by Atomic Layer Deposition onto Graphene Nanosheets for Enhanced Lithium Storage*. **Adv. Funct. Mater.**, 2012, 22, 1647-1654.
20. Y. Li, J. Wang, X. Li, J. Liu, D. Geng, **J. Yang**, R. Li, X. Sun, *Nitrogen-doped Carbon Nanotubes as Cathode for Lithium-Air Batteries*. **Electrochem. Commun.**, 2011, 13, 668-672.
21. X. Meng, J. Liu, X. Li, M. Banis, **J. Yang**, R. Li, X. Sun, *Atomic Layer Deposited $\text{Li}_4\text{Ti}_5\text{O}_{12}$ on Nitrogen-doped Carbon Nanotubes*. **RSC Adv.**, 2013, 3, 7285-7288.
22. X. Li, J. Liu, X. Meng, Y. Tang, M. Banis, **J. Yang**, R. Li, M. Cai, X. Sun, *Significant Impact on Cathode Performance of Lithium-ion Batteries by Precisely Controlled Metal Oxide Coatings via Atomic Layer Deposition*. 2013, **J. Power Sources**, in press.

Conferences:

1. **J. Yang**, J. Wang, D. Wang, X. Li, , D. Geng, R. Li, G. Liang, X. Sun. " N-CNTs and Graphene Modified LiFePO_4 as Cathode Materials for Lithium Ion Batteries" 223rd ECS meeting. Toronto, Ontario, May 12-16, 2013.
2. **J. Yang**, J. Wang, X. Li, D. Wang, G. Liang, M. Gauthier, X. Sun, "3D Porous LiFePO_4 and its Composites with Nanostructured Carbon as Cathode Materials for Lithium Ion Batteries Used in Electric Vehicles". 24th Canadian Materials Science Conference. London, Ontario, June 5-8. 2012.
3. **J. Yang**, J. Wang, X. Li, D. Wang, G. Liang, M. Gauthier, X. Sun, "3D Porous LiFePO_4 and its carbonaceous composites (graphene, N-CNTs and CNTs) as Cathode Materials for Lithium Ion Batteries Used in Electric Vehicles". 3rd Annual Nano Ontario Conferences, Waterloo, Ontario, October 11-12. 2012.
4. **J. Yang**, J. Wang, D. Wang, X. Li, D. Geng, R. Li, G. Liang, X. Sun, "3D Porous LiFePO_4 and its Carbonaceous Composites (Graphene, N-CNTs and CNTs) as Cathode

Materials for Lithium Ion Batteries Used in Electric Vehicles”. CAMBR (Center for Advanced Materials and Biomaterials Research) Distinguished Lecturer and Research Day, London, Ontario, November 13, 2012.

5. **J. Yang**, J. Wang, X. Li, X. Sun, “Core-Shell LiFePO_4 /Carbon Nanocables by Hydrothermal Route for Li-ion Batteries”. International Meeting on Lithium Batteries (IMLB-2010), Montreal, Quebec, June 27-July 3, 2010

6. **J. Yang**, J. Wang, X. Li, D.Wang, D. Geng, R. Li, X. Sun. “Core-Shell LiFePO_4 /Carbon Nanocables by Hydrothermal Route for Li-ion Batteries.” ECS Canadian Section Fall Symposium, London, Ontario, September 18, 2010.